Study of jet cross-sections and properties in hadronic and heavy-ion collisions with ALICE at the Large Hadron Collider

Thesis submitted for the degree of

Doctor of Philosophy (Science)

by

Rathijit Biswas

Registration no.: 1393/Ph.D.(Sc.)Proceed/2017

in the

Department of Physics

University of Calcutta

Declaration of Authorship

I, RATHIJIT BISWAS, declare that this thesis titled, 'Study of jet cross-sections and properties in hadronic and heavy-ion collisions with ALICE at the Large Hadron Collider' and the work presented in it are my own contributions under the guidance of Prof. Sibaji Raha and joint supervision of Dr. Supriya Das. I confirm that the work is original and has not been submitted earlier as a whole or in part for a degree/diploma at this or any other Institution/University.

Signed:

Rathijit Biswas

Date: 23rd September 2020

Dedicated to every teacher who came into my life to shape me as I am today, starting from the very first ones, my parents

Acknowledgements

At first and foremost I would like to express my gratitude to my supervisor, **Prof. Sibaji Raha** for being the inspirational figure and providing the support in accomplishing my research work. I would like to thank my joint supervisor, **Prof. Supriya Das** for being the close one to the concept of "friend, philosopher and guide" in this journey. Thank you Supriya da for being there for me in academic or non-academic issues that occurred before me in this path from day one to writing this thesis.

I would like to thank **Dr Sidharth K. Prasad** who introduced me to the world of data analysis and from whom I learned a lot in this journey.

I would like to acknowledge the constant support and motivation I got from **Prof. Sanjay Kumar Ghosh** and I thank him for being a friendly guardian in this journey. I would like to acknowledge the constant push, support and motivation I got and still getting from **Dr Saikat Biswas**. I would like to remember at this point the wonderful time that I had spent at CERN with you people. I would like to acknowledge the wonderful time I had while **Prof. Rajarshi Ray** was around- from physics discussions to the plays we staged.

I would like to express my thanks to **Dr Subikash Choudhury** from whom I have learnt a lot and still learning. You were there for me from shaping the paper or preparation of presentations or structuring the thesis. Thank you Subikash da, for you have really widened my level of thinking and experties.

I would like to express my gratitude to my collaborator **Dr Sumit Basu** with whom I spent a very productive time at CERN and learnt a lot of things from technical to physics and beyond.

I would like to express my sincere gratitude to late **Dr Oliver Busch** who was there for me whenever I needed him for the data analysis of ALICE. I would also like to thank every convenor of PWG-JE who was there during my data analysis time for giving constant support in terms of finalising results to prepare for conference presentations. I thank all the PWG-JE members for providing fruitful suggestions toward finalising the results and I thank the whole ALICE collaboration for shaping my work on the data analysis.

I would like to sincerely thank **Prof. Tapan Nayak** for being our guardian both at India and CERN and taking care of us. I would also like to thank **Prof. Subhasis Chattopadhyay**, the current ALICE-India spokesperson, for his guidance and constant motivation while working in ALICE.

I thank my batchmate **Pratap** and **Abhishek**, together we were the three musketeers and always will be the same. I thank all my seniors and juniors with whom I had shared the scholars' room: **Kinkar da, Sudipa di, Soumitra da, Rama da, Subhasis da, Prasenjit da, Saronath da, Avik da, Shyam da, Shreya, Pratik, Arka, Debjani, Prottoy, Abhi**. I had a wonderful time as you guys were there for everything- from academic discussions to designing the departmental t-shirt, organising barbecue and birthday parties.

In this journey I have earned a few good friends for life and Kunal bhai (**Dr Kunal Kothekar**) you are a true brother. We met at SERC school and this friendship grew as we walked the journey from Delhi to CERN to Rome or where not. Thank you for being a wellwisher always.

Talking about friendship, this would not be completed if I don't take your names- Rajjo (**Rajat Gupta**), Prinia (**Priyanka Pathania**) and Genie (**Dr Genius Ahluwalia**). I had the most memorable CERN visit ever with you guys. I will always remember the things we did there with a broad smile, for life.

I would like to acknowledge the constant support I got from Saheli (**Saheli Das**) during the most critical phase of this journey. Thank you Saheli, you were true to the saying - a friend in need, is a friend indeed. We have laughed together and also got frustrated together and those are the things I would cherish forever.

The list of friends will not be completed without you Shreya (**Shreya Thakur**). You have been like a piller in the tough times during this journey. I heartily thank you for being there and providing constant support when I needed that the most.

There is a saying - "it needs a village to raise a child". I thank the people who shaped my primary, nourished my secondary to make me ready to ride the academic caravan. It brings a great joy for me to see my fellow villagers taking pride as their boy reached that far from that small village on the map of West Bengal.

Finally, it was my family for whom I have reached that far. It is not possible to express my gratitude in a few lines. But I will try for the first time to say thank you to my mother (**Supriya Biswas**), my father (**Ranajit Biswas**) and my sister (**Rajasree Biswas**). It was my mother who dreamt of pushing her children towards the top of this

academic tree as she did not get this opportunity during her time and here I am.

Abstract

In ultra-relativistic heavy-ion (AA) collisions, a high density deconfined state of quarks and gluons is produced which is known as the Quark Gluon Plasma (QGP). This state of matter is supposed to have existed microseconds after the Big Bang and resemble the state of the early universe. Attempts have been made to produce this system over a wide range of energy and/or energy-density using facilities such as the Relativistic Heavy Ion Collider (RHIC), the Large Hadron Collider (LHC). This produced system is very short lived and the main challenge of this field of research is to characterise this short lived state of matter. There are few proposed signals to probe the QGP and a family of such probes are termed as the hard probes which are produced at the early stage of the collision and are considered to be the novel probes for the QGP medium. The massive available collision energy at the LHC makes it possible to produce hard probes with increased cross-sections. Jets belong to the family of such hard probes.

A jet is the concentrated collection of hadrons, produced from the fragmentation of a hard scattered parton. In heavy-ion collisions, a deconfined dense medium of free partons is created and the hard initial partons lose their energy while traversing through the medium by the interaction with the medium's partons. This phenomena is termed "jet quenching" and is a smoking gun signature of the QGP production. Though the study of heavy-ion collisions is at the heart of this field, there is also the need for baseline references (in vacuum) to reflect the effects of the medium properly. Study of proton-proton (pp) collisions serves this purpose. The pp collision is also significant in it's own term for providing the testing ground for pQCD processes. The jet study in pp collisions, provides detailed insight on parton fragmentation.

In this thesis, a jet properties study done with ALICE pp data at 2.76 TeV has been presented. The data measurements have also been compared with those obtained from Monte Carlo models to show the agreement with theory predictions. Jet properties study in heavy-ion collisions has also been conducted using the Pb-Pb events generated in the framework of a dynamical jet quenching model, JEWEL. Jet medium interactions have been investigated and the performance of the model against available experimental measurements have been presented in this thesis.

Thesis is partially based on the following publications:

1. **Rathijit Biswas**, Subikash Choudhury, Sidharth Kumar Prasad and Supriya Das, "Study of jet-medium interactions using jet shape observables in heavy ion collisions at LHC energies with JEWEL", Jour. Phys. G:Nucl. Part. Phys 46 (2019) no.9, 095004, arXiv:1906.05513

2. **Rathijit Biswas** (for the ALICE Collaboration),"Measurement of charged jet cross sections and jet shapes in proton-proton collisions at $\sqrt{s}$ = 2.76 TeV with the ALICE detector at LHC", Springer Proc. Phys. 203 (2018) 275-279, arXiv:1702.07646

3. Subikash Choudhury, **Rathijit Biswas**, S.K. Prasad, Supriya Das and Subhasis Chattopadhyay, "Studying Medium Modification of Jets Using Jet Evolution with Energy Loss (JEWEL) Model", Springer Proc. Phys. 203 (2018) 877-879

Publications other than the above mentioned ones

1. S. Roy, R.P. Adak, **R. Biswas**, D. Nag, D. Paul, S. Rudra, S. Biswas and S. Das, "Measurement of angular variation of Cosmic Ray intensity with plastic scintillator detector", Springer Proc. Phys. 201 (2018) 199-204

2. Sumit K. Saha, Sumit Basu, Souvik P. Adhya, **Rathijit Biswas**, Supriya Das, Tapan K. Nayak and Sidharth K. Prasad, "Energy dependence of integrated suppression fraction from R_{AA} and R_{CP} in relativistic heavy-ion collisions", Proceedings of the DAE-BRNS Symp. on Nucl. Phys. 61 (2016) 850-851

"Only a few know, how much one must know to know how little one knows"

- Werner Karl Heisenberg

Contents

Declaration of Authorship i

Acknowledgements iii

Abstract v

List of Figures xii

List of Tables xix

1 Introduction 1
- 1.1 Historical prelude . . . 2
  - 1.1.1 The Standard Model of particle physics . . . 11
- 1.2 Observing and studying particles . . . 15
  - 1.2.1 Natural sources . . . 15
  - 1.2.2 "Trapping" a particle . . . 15
  - 1.2.3 Manipulating particles . . . 18
  - 1.2.4 Particle factories . . . 20
- 1.3 Quantum Chromo Dynamics (QCD): The theory of strong interaction . . . 22
  - 1.3.1 Basic elements of QCD . . . 22
  - 1.3.2 Chiral symmetry: spontaneous breaking and restoration . . . 25
  - 1.3.3 Perturbative QCD . . . 27
    - 1.3.3.1 The strong coupling constant . . . 28
    - 1.3.3.2 Predictions for production cross-sections . . . 30
  - 1.3.4 The QCD phase diagram and Quark Gluon Plasma (QGP) . . . 32
    - 1.3.4.1 Preliminary ideas and the Statistical Bootstrap Model (SBM) . . . 32

1.3.4.2 Critical temperature, QCD Deconfinement and the prediction of the Quark Gluon Plasma (QGP) 34
1.3.4.3 Current understanding of the QCD phase diagram 36
1.4 Relativistic heavy-ion collisions and QGP 40
1.4.1 Experimental programs and facilities 40
1.4.2 Discovery and production of QGP 43
1.4.3 Evolution of relativistic heavy-ion collisions 45
1.4.4 Experimental signatures to probe the produced QGP 51
1.4.4.1 Flow 52
1.4.4.2 Strangeness enhancement 53
1.4.4.3 J/ψ suppression 54
1.4.4.4 High p_T suppression: jet quenching 56
1.5 pp collisions in this scenario 57
1.6 Organization of the thesis 58

2 The LHC and the ALICE experiment 68
2.1 The Large Hadron Collider (LHC) 69
2.1.1 Experiments at the LHC 73
2.1.1.1 A Large Ion Collider Experiment (ALICE) 73
2.1.1.2 A Toroidal LHC Apparatus for Spectroscopy (ATLAS) . 73
2.1.1.3 Compact Muon Solenoid (CMS) 73
2.1.1.4 Large Hadron Collider beauty (LHC-b) 74
2.1.1.5 Large Hadron Collider forward (LHC-f) 74
2.1.1.6 TOTal Elastic and diffractive cross-section Measurement (TOTEM) 74
2.1.1.7 Monopole and Exotics Detector At the LHC (MoEDAL) . 75
2.1.1.8 ForwArd Search ExpeRiment (FASER) 75
2.2 A Large Ion Collider Experiment (ALICE) 75
2.2.1 ALICE coordinate system 77
2.2.2 Detector system layout overview 77
2.2.3 Central barrel detectors 79
2.2.3.1 Inner Tracking System (ITS) 79
2.2.3.2 Time Projection Chamber (TPC) 81
2.2.3.3 Transition Radiation Detector (TRD) 84
2.2.3.4 Time-Of-Flight (TOF) 86
2.2.3.5 High-Momentum Particle Identification Detector (HMPID) 89
2.2.3.6 The PHOton Spectrometer (PHOS) 90
2.2.3.7 Electromagnetic Calorimeters (EMCAL and DCAL (Di-Jet Calorimeter)) 91
2.2.3.8 ALICE COsmic Ray DEtector (ACORDE) 93
2.2.4 Muon Spectrometer (Muon Chamber (MCH) and Muon Trigger (MTR) 93
2.2.5 Forward detectors 95
2.2.5.1 ALICE Diffractive detector (AD0) 95
2.2.5.2 Zero Degree Calorimeter (ZDC) 96
2.2.5.3 Photon Multiplicity Detector (PMD) 97

2.2.5.4 Forward Multiplicity Detector (FMD) 98
2.2.5.5 V0 detector 99
2.2.5.6 T0 detector 100
2.2.6 ALICE data taking: Online 100
2.2.6.1 Detector Control System (DCS) 101
2.2.6.2 Trigger system (TRG) 101
2.2.6.3 Data AcQuisition (DAQ) System 103
2.2.6.4 High Level Trigger (HLT) 105
2.2.7 ALICE data analysis and computing: Offline 105
2.2.7.1 Raw data flow 106
2.2.7.2 AliEn framework 107
2.2.7.3 The AliRoot platform 108
2.2.7.4 CERN Analysis Facility (CAF) 113

3 Introduction to Jets 119
3.1 Evolution of jet (in vacuum) 121
3.1.1 Initial conditions 122
3.1.2 Hard scattering and final state conditions 123
3.1.3 Fragmentation and Hadronization 125
3.1.4 Decay of primary particles 131
3.1.5 Detector effects 131
3.1.6 Additional processes 132
3.1.7 Jet reconstruction 134
3.1.7.1 Jet Definition 135
3.1.7.2 Algorithms 136
3.1.7.3 Recombination scheme 147
3.2 Parton (jet)-medium interaction 149
3.2.1 Medium-induced radiative energy loss 152
3.3 Theoretical uncertainties 154

4 Jet properties study in pp events with ALICE 160
4.1 Prelude 161
4.2 Observables 162
4.2.1 Charged particle multiplicity in leading jets, N_{ch} 162
4.2.2 Charged jet size, R_{80} 163
4.2.3 Radial transverse momentum density of charged jet, p_T^{sum} 163
4.3 Analysis overview 164
4.4 Monte Carlo simulation 166
4.5 Measurements with uncorrected raw data 167
4.6 Correction of the raw data 168
4.7 Underlying event (UE) subtraction 174
4.8 Estimation of systematic uncertainties 175
4.8.1 Uncertainties due to finite tracking efficiency and p_T resolution . . 175
4.8.2 Uncertainties due to UE estimation technique 179
4.8.3 Uncertainties due to MC generator dependence of correction factors (CF) 179

4.9 Results . . . 184
4.9.1 Average charged particle multiplicity distribution in leading jet ($\langle N_{ch} \rangle$) . . . 184
4.9.2 Average leading charged jet size ($\langle R_{80} \rangle$) . . . 185
4.9.3 Radial momentum density distribution (dp_T^{sum}/dr) . . . 186

5 Jet properties study in heavy-ion events with JEWEL 189
5.1 Prelude . . . 190
5.2 Jet Evolution With Energy Loss (JEWEL) . . . 191
5.2.1 Introduction to JEWEL . . . 191
5.2.2 Computing the background . . . 193
5.2.3 Analysis details . . . 194
5.3 Results . . . 194
5.3.1 Jet nuclear modification factor, R_{AA}^{jet} . . . 194
5.3.2 Fragmentation function distributions, $FF(z)$ . . . 197
5.3.3 Radial distribution of transverse momentum density, dp_T^{sum}/dr . . . 201

6 Summary and discussions 208

A QA analysis of PMD data 214
A.1 Photon Multiplicity Detector (PMD) . . . 215
A.1.1 Physics goals of PMD . . . 215
A.1.2 Design overview of PMD . . . 215
A.1.3 Working principle of PMD . . . 219
A.2 QA study of PMD data . . . 220
A.2.1 Data cleanup: removal of the hot cells . . . 220
A.2.1.1 Identification of the hot cells . . . 220
A.2.1.2 Removal of the hot cells . . . 224
A.2.2 Calibration: gain normalization . . . 225

B Monte Carlo event generators 230
B.1 PYTHIA . . . 232
B.2 Hadron Emission Reactions With Interfering Gluons, HERWIG . . . 234
B.3 PHOJET . . . 235
B.4 Predictions by the event generators and tuning of them . . . 236

C Dismantling the PMD from ALICE 241

List of Figures

1.1 Discovery of positron by Anderson. It was the first anti-matter discovered. 5
1.2 Discovery of π in cosmic rays by Powell in 1947 (left) and discovery of Kaon by Rochester in 1949 (right). 6
1.3 The "twitter" of Bevatron, the blackboard placed by Wiegand which shows the report on 6th October, 1955 about detecting 38 anti-protons. 7
1.4 Ω^- discovery in 1964. 7
1.5 Structures of baryons and mesons predicted through quark and anti-quark combination. 8
1.6 Basic building blocks of particles and composition of the standard model. Figure taken from [28]. 11
1.7 Three generations of elementary building blocks of particles. Figure courtesy: Wikipedia. 12
1.8 The three interactions of the standard model. Figure taken from [29]. . . . 12
1.9 Comparative descriptions of all the interactions in nature. Figure taken from [30] 13
1.10 The full standard model with the properties of all the constituents. Figure courtesy: Pinterest. 14
1.11 Timeline of particle physics and associated instrumentation. Figure courtesy: David Nygren, EDIT School -FNAL. 16
1.12 The Wilson cloud chamber in 1911 (left) and the Geiger-Muller tube (right). 17
1.13 The detector zoo. Figure courtesy: Erika Garutti. 18
1.14 Fast electron in a magnetic field at the Bevatron, 1940. 20
1.15 Schematic diagrams for: free quark-field (top left), quark-gluon interaction term (top right), free gluon-field (bottom left) and cubic gluon self-interaction term (bottom middle) and quadratic gluon self-interaction term (bottom right). Figure courtesy [34]. 24
1.16 Classical analogy of spontaneous symmetry breaking. 26
1.17 Schematic diagrams for: quark self-energy correction (top left), gluon self-energy correction (top middle and right), and quark-gluon vertex corrections (bottom). Figure courtesy [34]. 28
1.18 Determinations of the strong coupling constant α_s are shown as a function of the relevant energy scale Q of the respective process. Left: running of the strong coupling constant as of 2009 [49, 50] and right: running of the strong coupling constant as of 2012 [51]. 31
1.19 A cartoon of the statistical bootstrap idea. Figure taken from [58]. 33

1.20 The different regions of the statistical parameter plane (temperature, T, and the baryochemical potential, μ_B), according to the statistical bootstrap model of hadronic matter. Figure taken from [58]. 35
1.21 A schematic of the QCD phase diagram of nuclear matter in terms of the temperature (T) and baryo-chemical potential (μ_B). 37
1.22 Dependence of the energy density as a function of the temperature of the hadronic matter at null baryonic potential given by lattice QCD calculations at finite temperature [79]. 38
1.23 The schematic of the QCD phase diagram, as covered by the experiments. 42
1.24 The Bjorken scenario of the hot QCD matter production and the stages of its evolution. 47
1.25 The different stages of evolution of relativistic heavy-ion collision in space-time. Figure courtesy: V.D. Kekelidze. 49
1.26 Schematic diagram for centrality determination through calculating impact parameter and the spectators. Figure taken from [121]. 50
1.27 Two incident nuclei partially overlap, creating an “almond”-shaped collision region, which then expands and generates elliptic flow. Figure taken from [137]. 52
1.28 Debye radius as a function of T/Tc. The lines correspond to the critical Debye radius for different quarkonia states. Figure taken from slides prepared by Marzia Rosati, Iowa State University. 55
1.29 Illustrations of: jet production in pp collision (left) and jet quenching in heavy-ion collision (right). 56
1.30 Quenching of away side jet as seen by the STAR experiment in Au-Au collisions [148] 57

2.1 The aerial view of the LHC accelerator complex. 69
2.2 The schematic diagram of the whole accelerator complex with LHC at CERN. 70
2.3 Schematic diagram of LHC tunnel with the sector divisions and interaction points. 71
2.4 The schematic diagram of the ALICE detector with its sub-systems. . . . 76
2.5 The coordinate system of the ALICE detector. 78
2.6 The hermetic detector system design layout (left) with detection specifications (right). 78
2.7 Layout of the ITS detector. 80
2.8 Schematic view of the TPC. 81
2.9 Layout of the ALICE TPC showing the central electrode, the field cage and the end plates supporting the readout chambers. 82
2.10 Energy loss in the TPC (dE/dx) versus momentum p (GeV/c) with Bethe-Bloch predictions (black lines) for different particles in pp collisions [16] (top), p-Pb collisions (bottom left) and in Pb-Pb collisions [17] (bottom right). 83
2.11 Layout of the ALICE TRD has been shown here with one displaced chamber for clarity. On top of the TRD, the TOF system can be seen and inside TRD, the heat shield of TPC is visible. 84
2.12 Cross-sectional view of TRD. 85

2.13 Layout of the ALICE TOF detector. 87
2.14 Energy loss in the TOF (dE/dx) versus momentum p (GeV/c) for different particles in pp collisions (top left), p-Pb collisions (top right), Pb-Pb collisions (bottom left) and in Xe-Xe collisions [21]. 88
2.15 The working principle of the ALICE HMPID detector with the pad occupancy. 89
2.16 PID performance by HMPID in pp collisions (left) and in p-Pb collisions (right) [23]. 90
2.17 Three calorimeters installed in ALICE at Run2 period: EMCal (upper side), PHOS (bottom, drawn in orange) and DCal (placed on both side of PHOS in z-direction). 91
2.18 All the 3 calorimeters in ALICE with real-time events. In the top side there is EMCal, in the bottom PHOS is shown in orange and on both side of the PHOS, there is DCal. 92
2.19 ALICE cosmic ray detector layout. 94
2.20 Layout of the Muon spectrometer. 95
2.21 Schematic diagram of the AD0 detector. 96
2.22 Schematic diagram of the ZDC detector. 97
2.23 The ALICE Forward Multiplicity Detector layout. 98
2.24 The layout and positions of T0 and V0 detectors.. 99
2.25 The online control system in ALICE. 101
2.26 The DAQ system of ALICE. 104
2.27 Global view of the data flow in ALICE. 106
2.28 A snapshot of the ALICE V0 sites in Europe. A green circle indicates that jobs are running on the site while red and yellow circles indicate sites that are facing trouble. 108
2.29 Schematic diagram of the AliRoot framework. 109
2.30 The schematic diagram of the ALICE reconstruction framework.. 112

3.1 Schematic diagram of parton evolution. Energy axis at the bottom represents the decreasing energy with time starting from the scattering. This diagram represents a four jet events. This figure is reproduced from [1] . . 122
3.2 Leading order hard scatterings: the most dominant process is gluon-gluon scattering (gg→gg) represented by (d), (i) and (j). Rests are quark-gluon scattering, quark-quark scattering and quark-antiquark annihilation. . . . 123
3.3 The s, t and u channel of Mandelstam variables. 124
3.4 Feynman diagrams for LO and NLO processes. (a) represent 2-to-2 LO, (b) is the 2-to-2 process with an internal loop (UV) NLO and (c) stands for 2-to-3 NLO (IR) process. Figure taken from [10] 125
3.5 Schematic diagrams of few splitting functions. Figure taken from [13] . . . 126
3.6 The active area in space-time in the string model. Figure taken from [31] 129
3.7 Illustration of string breaking into pair of partons. Figure taken from [32] 129
3.8 Schematic diagram of a photon decaying into a $q\bar{q}$ pair in two scenario: left represents string model and right one represents cluster model. This figure is reproduced from [2]. 130

3.9 Schematic diagram of a hard collision between two hadrons, h_1 and h_2, each having three partons. One parton from each of the hadrons (a and b) participate in the hard interaction. 132
3.10 Schematic diagram of a proton-proton collision with Underlying Event. . . 133
3.11 Illustration of the division of the $\eta - \phi$ phase space for the measurement of UE. The Toward region is defined by $\Delta\phi < 60^0$ and η <1, while the Away region is located at $\Delta\phi < 120^0$ and η <1. The Transverse region is defined by $60^0 < \Delta\phi < 120^0$ and $\eta < 1$. Each region has an area in $\eta - \phi$ space of $4\pi/3$. 134
3.12 An example of jet event in the CDF (a) calorimeter and (b) central tracking chamber. This figure taken from [44]. 135
3.13 An algorithm should be order independent i.e., the same algorithm must work with the same accuracy at partonic, particle and detector level. This illustration shows different level of a jet reconstruction. 137
3.14 Illustration of infrared sensitivity in jet clustering. The presence of soft radiation between two jets may cause a merging of the jets that would not occur in the absence of the soft radiation. 138
3.15 Illustration of collinear sensitivity in jet clustering. The top case shows an example, where a jet is not being defined due to splitted energy (left) and when the splitted energy is narrower a jet could be defined (right). Another collinear problem is shown in the bottom case where collinear splitting compels the algorithm to change the jet direction and energy and make a new jet. 138
3.16 Plots showing 1D event reconstruction with two different jet resolution parameter: $R = 0.3$ (left) adn $R = 1.4$ (right). With smaller R, number of jets are increased while the reconstructed momenta is smaller [47]. . . . 140
3.17 Illustration showing the co-existence of pile up collision with the primary hard scattering which leads to the additional particle production and energy deposition in the same event. Illustration taken from [48]. 141
3.18 Active area (left) and passive area (right) determination of a jet algorithm. The shaded regions in both the plots stand for the respective jet areas. . . 141
3.19 Flowchart of a sequential recombination jet clustering algorithm. 146
3.20 Jet areas measured by the SIScone and the three widely used recombination algorithm: K_t, Anti-K_t and C/A with the same dataset and input parameters. Figure taken from [56] 148
3.21 Feynman diagrams for hard processes in nucleon-nucleon collision (left) and in heavy ion-heavy ion collision (right). Figure taken from [59]. 150
3.22 Schematic illustration showing medium induced gluon radiation during the propagation of the parton through the medium. Figure taken from [59].151
3.23 Schematic illustration of typical gluon radiation. Figure taken from [76] . 153

4.1 Schematic illustrations showing differential (left) and integrated (right) jet shape measurements. Figure taken from [1] 161
4.2 Radial transverse momentum distribution about jet axis in leading jet. Scalar p_T^{sum} is obtained for each annular regions as a function of distance r in different jet p_T bins. 164
4.3 The analysis flow chart. 165

4.4 Event selection cuts. 166
4.5 Vertex z distribution. 167
4.6 UE measurements with the raw data for $\langle N_{ch} \rangle$ for three different R: 0.2, 0.4 and 0.6 and $\langle \frac{dp_T^{sum}}{dr} \rangle$ for $R = 0.4$ in the four selected jet p_T bins. 168
4.7 Measurements with the raw data: $\langle N_{ch} \rangle$ (top left), $\langle R_{80} \rangle$ (top right). Rest four are radial transverse momentum distribution in four different jet p_T bins, 20-30 GeV/c being the lowest jet p_T bin and 60-80 GeV/c is the highest jet p_T bin. 169
4.8 Comparison of raw measurements of $\langle N_{ch} \rangle$ (top left) and $\langle R_{80} \rangle$ (top right) at $R = 0.4$ for 2.76 and 7 TeV. Comparison of UE for $\langle N_{ch} \rangle$ (bottom) at $R = 0.4$ for 2.76 and 7 TeV. 170
4.9 Correction factors measured at $R = 0.4$ for: $\langle N_{ch} \rangle$ (top left), $\langle R_{80} \rangle$ (top right). Rest four are radial transverse momentum distribution in four different jet p_T bins as indicated. 172
4.10 Correction factors measured at $R = 0.4$ in UE for: $\langle N_{ch} \rangle$ (top left) and rest four are radial transverse momentum distribution in four different jet p_T bins as indicated. 173
4.11 Observables after bin-by-bin correction and UE subtraction for $R = 0.4$: $\langle N_{ch} \rangle$ (top left), $\langle R_{80} \rangle$ (top right) and $\langle p_T^{sum} \rangle$ (bottom). The distributions in $\langle p_T^{sum} \rangle$ have been scaled, as indicated, for distinguishable display. 174
4.12 Tracking efficiency plot from full GEANT simulation with fitting. 176
4.13 Estimation of uncertainties for finite tracking efficiency: $\langle N_{ch} \rangle$ (top left), $\langle R_{80} \rangle$ (top right) and rest four are for $\langle p_T^{sum} \rangle$ in four different jet p_T bins as indicated. 177
4.14 Estimation of uncertainties for finite momentum resolution: $\langle N_{ch} \rangle$ (top left), $\langle R_{80} \rangle$ (top right) and rest four are for $\langle p_T^{sum} \rangle$ in four different jet p_T bins as indicated. 178
4.15 Estimation of uncertainties from evaluation of UE: $\langle N_{ch} \rangle$ (top left) and rest three are for $\langle p_T^{sum} \rangle$ in three different jet p_T bins as indicated. 180
4.16 Estimation of uncertainties from CF dependencies on the choice of MC generator: $\langle N_{ch} \rangle$ (top left), $\langle R_{80} \rangle$ (top right) and rest four are for $\langle p_T^{sum} \rangle$ in four different jet p_T bins as indicated. 182
4.17 $\langle N_{ch} \rangle$ (left) distributions for $R = 0.4$ with theoretical predictions from different MC models. The right plot shows the comparison of $\langle N_{ch} \rangle$ from this measurement to the previous 7 TeV measurement by ALICE. 184
4.18 $\langle R_{80} \rangle$ (left) distributions for $R = 0.4$ with theoretical predictions from different MC models. The right plot shows the comparison of $\langle R_{80} \rangle$ from this measurement to the previous 7 TeV measurement by ALICE. 185
4.19 $\langle R_{80} \rangle$ (left) distributions for $R = 0.4$ with theoretical predictions from different MC models. The right plot shows the comparison of $\langle R_{80} \rangle$ from this measurement to the previous 7 TeV measurement by ALICE. 186

5.1 Transverse momentum dependence of R_{AA}^{jet} from JEWEL at $R = 0.4$ in 0-10% centrality, compared with ALICE [34, 35], ATLAS [36, 37] and CMS [38] measurements. **Left:** $\sqrt{s} = 5.02$ TeV and **Right:** $\sqrt{s} = 2.76$ TeV. . . 195
5.2 Ratios of jet p_T spectra at $R = 0.3$ and 0.4 with respect to $R = 0.2$ in pp and Pb-Pb collisions. **Left:** $\sqrt{s} = 5.02$ TeV and **Right:** $\sqrt{s} = 2.76$ TeV. . 195

5.3 Transverse momentum dependence of R_{AA}^{jet} at $\sqrt{s} = 5.02$ and 2.76 TeV for jet radius $R = 0.2$, 0.3 and 0.4 in 0-10% central events with JEWEL . . . 196
5.4 Transverse momentum dependence of R_{AA}^{jet} from JEWEL in 0-10% centrality Pb-Pb events, compared with CMS [38] measurements. **Left:** $R = 0.2$ and **Right:** $R = 0.4$. . . . 197
5.5 Fragmentation distributions from JEWEL at $R = 0.4$ in 0-10% Pb-Pb central events compared with ATLAS [42] measurement of the same in pp and Pb-Pb collisions for 126< p_T^{jet} <158 GeV/c. **Left:** $\sqrt{s} = 5.02$ TeV and **Right:** $\sqrt{s} = 2.76$ TeV. Proton-proton data points are scaled by 100 for better visibility. . . . 198
5.6 Ratio of fragmentation distributions from Pb-Pb to pp collisions from JEWEL at $R = 0.4$ in 0-10% centrality compared with ATLAS [41, 42] measurements in 126< p_T^{jet} <158 GeV/c. **Left:** $\sqrt{s} = 5.02$ TeV and **Right:** $\sqrt{s} = 2.76$ TeV. . . . 199
5.7 Ratios of fragmentation distributions from Pb-Pb to pp collisions from JEWEL at $R = 0.4$ in 0-10% centrality for three p_T^{jet} ranges: 40< p_T^{jet} <100, 126< p_T^{jet} <158 and 316< p_T^{jet} <398 GeV/c. **Left:** $\sqrt{s} = 5.02$ TeV and **Right:** $\sqrt{s} = 2.76$ TeV. Colored bands show the statistical error in the measurements. . . . 200
5.8 Ratios of fragmentation distributions from Pb-Pb to pp collisions from JEWEL at $R = 0.2$, 0.3 and 0.4 in 0-10% centrality for two p_T^{jet} bins: 40< p_T^{jet} <100 and 316< p_T^{jet} <398 GeV/c. **Left:** $\sqrt{s} = 5.02$ TeV and **Right:** $\sqrt{s} = 2.76$ TeV. . . . 201
5.9 Radial momentum density distributions in PbPb to pp collisions from JEWEL at $R = 0.4$ in 0-10% centrality are presented for three jet p_T intervals: 40< p_T^{jet} <100, 126< p_T^{jet} <158 GeV/c and 316< p_T^{jet} <398 p_T^{jet}. **Left:** $\sqrt{s} = 5.02$ TeV and **Right:** $\sqrt{s} = 2.76$ TeV. Lines are only to guide the eyes. . . . 202
5.10 Radial momentum density distributions in PbPb to pp collisions from JEWEL at $R = 0.2$, 0.3 and 0.4 in 0-10% centrality are presented for jet p_T interval: 40< p_T^{jet} <100. **Left:** $\sqrt{s} = 5.02$ TeV and **Right:** $\sqrt{s} = 2.76$ TeV. Lines are only to guide the eyes. . . . 203
5.11 Ratios of radial momentum density distributions from PbPb to pp collisions from JEWEL at $R = 0.4$ in 0-10% centrality are presented for three jet p_T intervals: 40< p_T^{jet} <100, 126< p_T^{jet} <158 GeV/c and 316< p_T^{jet} <398 p_T^{jet}. **Left:** $\sqrt{s} = 5.02$ TeV and **Right:** $\sqrt{s} = 2.76$ TeV. . . . 204
5.12 Ratios of radial momentum density distributions from PbPb to pp collisions from JEWEL at $R = 0.4$ in 0-10% centrality for 126< p_T^{jet} <158 GeV/c, in different ranges of constituent particle's p_T. **Left:** $\sqrt{s} = 5.02$ TeV and **Right:** $\sqrt{s} = 2.76$ TeV . . . 204

A.1 Schematic view of the PMD as installed in ALICE . . . 216
A.2 Schematic view of a honeycomb chamber in PMD . . . 216
A.3 Schematics of a single PMD module: (1) Top PCB, (2) 32-pin connectors, (3) edge frame, (4) honeycomb of 48 × 96 cells, (5) bottom PCB . . . 217
A.4 PMD in ALICE: (Top) Open configuration and (bottom) data taking configuration. . . . 218

A.5 Working principle of PMD . . . 219
A.6 Flow chart of data reconstruction after QA: (Top) hot cell removal and (bottom) gain normalization. . . . 221
A.7 Full occupancy X-Y plots for a representative run number 133006 from the dataset LHC10f: (top) CPV plane (bottom) PRE plane . . . 223
A.8 Hot cell removal for a representative run number 133006 from the dataset LHC10f computed on the CPV plane in η ring 3 taking $n = 13$: (top) before hot cell removal and (bottom) after hot cell removal. In this particular case one hot cell was found and removed. . . . 224
A.9 Hot cell removal for a representative run number 133006 from the dataset LHC10f computed on the PRE plane in eta ring 5 taking $n = 13$: (top) before hot cell removal and (bottom) after hot cell removal. In this particular case two hot cells were found and removed. . . . 225
A.10 ADC distribution of an isolated cell of module 2 (SM02) for run number 119057 in the dataset LHC10C: PRE plane (top) and the cell-wise mean ADC distribution of the full module which gives the mean ADC of the module (bottom). . . . 227
A.11 Cell wise gain factors for module 3 (SM03) for run number 119057 in the dataset LHC10C: CPV plane (top) and PRE plane (bottom). . . . 228

B.1 Schematics of a MC event generation. Illustration courtesy: S. Gieseke. . . 231
B.2 PYTHIA event generator general structure. Figure taken from [16]. . . . 233
B.3 Few of the physics processes addressed by PYTHIA. Figure taken from [16] 234

C.1 Dismantling PMD in the ALICE cavern: removal of power source, cooling mechanics, support girders. . . . 242
C.2 Dismantling PMD at the surface area: (from top to bottom) PMD moved from cavern to surface area by crane, PMD is placed at the surface area (radiation protected zone) with the help of a support structure (blue frame), electrical cables and gas flow tubes removal and finally module wise dismantling. . . . 243

List of Tables

1.1 Summary of the heavy-ion experimental facilities. 41

2.1 LHC design values[3] for pp and Pb-Pb system 71
2.2 Year-wise summary of the LHC runs [4] up to Long Shutdown-2 (2018) with beam type. 72
2.3 Design parameters of all the six ITS layers 79
2.4 Overview of TRD parameters 86
2.5 Specifications of ALICE electromagnetic calorimeter. 93
2.6 The list of trigger classes with trigger conditions. The symbols $\bigoplus$ and $\bigodot$ indicate OR and AND operations respectively. 103

4.1 Systematic uncertainties on $\langle N_{ch} \rangle$ for $R = 0.4$ (in %) 181
4.2 Systematic uncertainties on $\langle R_{80} \rangle$ for $R = 0.4$ (in %) 181
4.3 Systematic uncertainties on $\langle p_T^{sum} \rangle$ for $R = 0.4$ for 20< p_T^{jet} <30 GeV/c(in %) 181
4.4 Systematic uncertainties on $\langle p_T^{sum} \rangle$ for $R = 0.4$ for 30< p_T^{jet} <40 GeV/c(in %) 183
4.5 Systematic uncertainties on $\langle p_T^{sum} \rangle$ for $R = 0.4$ for 40< p_T^{jet} <60 GeV/c(in %) 183
4.6 Systematic uncertainties on $\langle p_T^{sum} \rangle$ for $R = 0.4$ for 60< p_T^{jet} <80 GeV/c(in %) 183

5.1 Details of the parameters used for JEWEL 194

A.1 Response of the PMD to different particles 220

Chapter 1

Introduction

This chapter gives a formal introduction to the field. The pre-requisites to proceed with a study in this field has been presented here. Introduction starts from a brief historical timeline of this field to emerge as a fundamental physics branch, brief description of the Standard Model (SM), the theory of strong interaction i.e., Quantum Chromo Dynamics (QCD) and an account of the QCD-phase diagram. This chapter also sets the stage for the study of QGP production and describes some of the novel signatures to probe it. This thesis is based on the work with such a probe which has been indicated at the respective section. The final section of this chapter describes the organization of the thesis.

1.1 Historical prelude

Particles are the basic building blocks of everything that we can see or touch around us. *Particle Physics* is the branch of science that investigates the nature and the behavior of these particles to explore and explain nature at its essence. Detailed understanding of how particles behave and interact can shed light on the innermost and invisible mechanisms of our universe. This field aims to enlighten us with the knowledge of how the big bang created matter, how stars behave, how cosmic rays travel from them to Earth and how the universe itself evolves.

In between 6th to 4th century BCE, Indian philosopher Kanada in his 'Vaisheshika Darshana' (his school of Indian philosophy) proposed the idea of 'param-anu' (atom) which he described as the indestructible particle of matter. It was described as the fundamental building blocks of all the matter. In the 4th century B.C., the Greek philosopher Democritus gave the idea that everything around us is composed of 'something' indivisible (read fundamental) and he termed that as *"atomos"*. This idea was left untouched until early 19th century, when John Dalton proposed atomic theory of matter. Next significant idea came from Kelvin in 1867 following ideas of William Rankine (1849) who proposed that atoms might be like knotted stable vortex rings in the hypothetical ether with different knots corresponding to different chemical elements. He was the first to consider atoms to have a stable geometrical structure. But this idea had been largely abandoned even before the electron was discovered. Within this time, Maxwell added in 1875 that atoms have a more complicated structure than that of a rigid body by the possibility of having internal motion. In 1886 Goldstein discovered existence of positively charged rays in the discharge tube by using perforated cathode.

In 1897, J.J. Thomson, in his successive experiments with cathode rays, observed that cathode rays are made up of negatively charged corpuscles with same charge to mass (q/m) ratio[1]. He concluded that the corpuscles are universal constituents of all atoms and this led to the discovery of the first fundamental particle- *electron*. This discovery laid the stepping stone of this field. In 1900 he also proposed a model for the atom where he thought that a number of electrons move in some vaguely specified positive background of indefinite shape. It will be worth mentioning that within this timeline, Mendeleev in 1869 classified the then known elements into a *"periodic table"*, in 1896 Henri Becquerel had recognised radioactivity by accidentally exposing a sensitive photo-plate to Uranium and by 1899 three types of rays: *alpha*, *beta* and *gamma* had been identified. Rutherford later demonstrated that alpha rays are the nuclei of helium atoms.

In 1900, in order to understand the observed black body radiation, Planck suggested the idea of quantization of the radiation. No obvious connection was made in Planck's treatment between the quantum radiation and the structure of matter and only a few physicists paid attention to his theory. Einstein was one of those few and in 1905 he proposed that light consists of discrete energy packets (which later was understood as *photon*, G.N Lewis coined the name) and came up with an explanation of the photoelectric effect which earned him the Nobel prize. In 1911, Rutherford tabled his nuclear model of an atom which was opposed by Thomson at that time. But Rutherford continued his investigation along the same path and in 1919 he observed first nuclear transmutation and also gave the very first estimation of the nuclear size. By that time, Bohr developed a theory of atomic electronic structure based on quantum ideas in 1913. From the time of the discovery of the electron, Rutherford and other scientists had been trying to probe the presence of a positive particle which can make the atom neutral together with the electron. In 1914, he concluded the presence of it and named it *"positive electron"*. It was only in 1920, that it was assigned the name *proton*. This period saw the rapidly growing interests and associated development of quantum physics. In 1921, Chadwick and Bieler predicted for the first time that some kind of strong force exists inside the nucleus. Compton in 1923 concluded about the particle nature of X-rays which was complemented by de Broglie in 1924 when he conjectured the wave aspect of matter. The observation of certain materials (e.g., radium) to emit electrons, led to the understanding of beta decay. But this observation in 1927 could not solve the energy conservation problem that arose with it. The very next year (1928) Dirac gave an equation which made a bridge between quantum mechanics and special relativity. This approach led to the necessity of the existence of corresponding positively charged particle [2] and he incorrectly predicted the positively charged particles in this case to be *protons*.

Following the prescription of Heisenberg's uncertainty principle in 1927, quantum mechanics and special relativity were well established subject within 1930. This also led to the development of particle physics as a subject. By 1930, there were just three fundamental particles: electrons, protons and photons. In this year, to solve the missing energy paradox in beta decay, Pauli suggested the need of another type of particle, the neutrino, to come into the play. In 1931, Dirac concluded his proposed positively charged particles to be *"positrons"* which have identical mass as electrons. This was the first suggestion of any anti-particle. Anderson in the very next year (1932) claimed to have observed the similar positively charged particles (Figure 1.1) in cosmic ray study [3]. This claim was primarily not accepted by Pauli and Bohr, but later they were convinced that the particles seen by Anderson are Dirac's positrons. 1932 proved to be the golden year as Chadwick announced the discovery of *neutron* [4] and described it as elementary as a proton. This lead to the understanding of the composition of the nucleus. In 1933, Fermi solved the beta decay problem. He revolutionised the field by the introduction of *weak interaction* for the first time and used the neutrino explicitly. He presented a theory, in which a fundamental particle changes type, for the first time and added a new interaction in the list containing the then familiar electromagnetic and gravitational interactions.

In 1933, Yukawa combined relativity and quantum theory to give a description of nuclear interactions by the exchange of new type of particles between protons and neutrons. He defined the range of this interaction as the size of the nucleus and predicted the mass of this exchange particles (*mesons*) to be 200 times more than that of the electron. This lead to the beginning of the theory of *strong interaction.* In 1937 a particle of mass about 200 electron masses was discovered in cosmic rays jointly by Neddermeyer and Anderson [5] and by Street and Stevenson. First it was confused with Yukawa's meson [6] and it took almost 10 years to conclude that it was a *muon.* It was found that it does not interact strongly, rather it passes through matter without interacting inspite of being massive. This discovery was sudden and took the community by surprise so much that I.I. Rabi commented: "who ordered that?". The term *"lepton"* was coined as the generic name for such particles which show no strong interaction, and the first ones to be in that list were the electron, muon and neutrinos. Correspondingly *"hadron"* was attributed to the community of particles which undergo the strong interaction, like

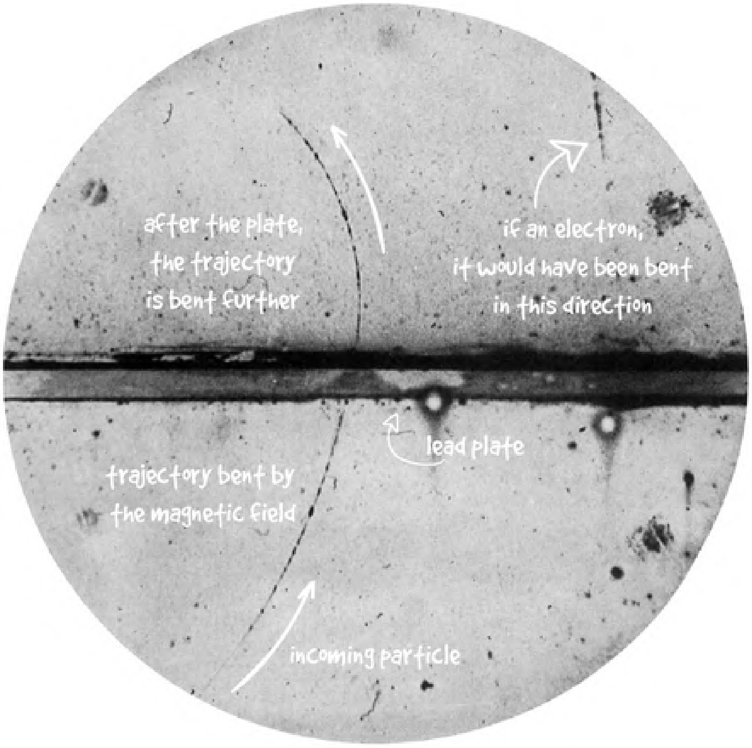

FIGURE 1.1: Discovery of positron by Anderson. It was the first anti-matter discovered.

proton, neutron and till unknown Yukawa's undiscovered meson. In 1947, Powell, Lattes and Occhialini did find the Yukawa's meson which does interact strongly with mass little greater than muon and that decays into a muon and a neutrino [7, 8]. It was given the name *pion*. This year also saw the massive development in the theory with the introduction of the procedures to calculate Quantum Electro Dynamics (QED) processes and Feynmann diagram.

Powell continued to add one more particle in the list, the K^+ via its decay by 1949 shown in Figure 1.2. Rochester and Butler discovered two more particles in 1951 following the same process where the parent particles were neutral but produced two charged daughter. First they were put in the group of particles they termed the *V particles*. These two particles are now known as Λ^0 and K^0. By 1953, particle physics had fully grown and classification of particles and studying their properties, decays had become major activities. Particles were classified by their half-life into two groups: decays involving strong interaction have a half-life of the order of 10^{-24} seconds and the decays involving weak interaction have half-life more than 10^{-13} seconds. Particles were

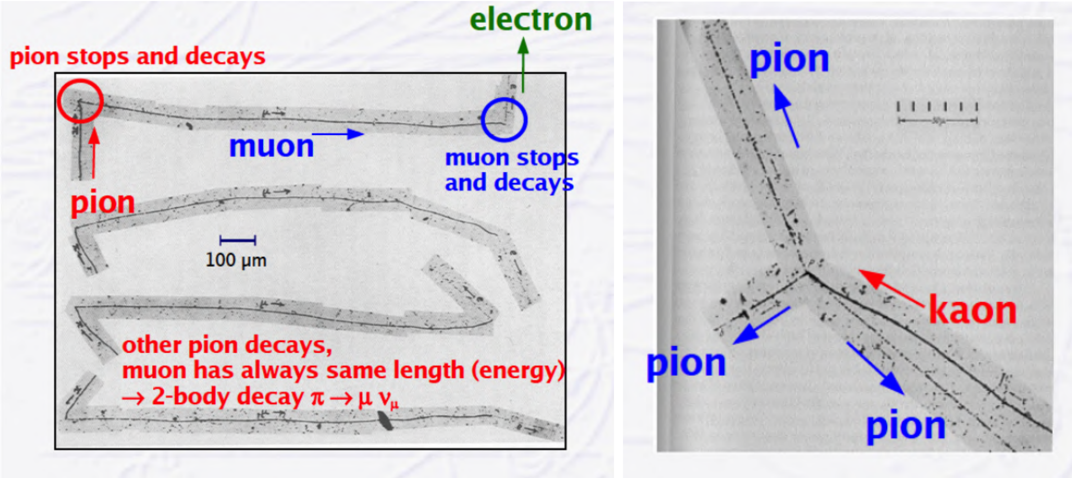

FIGURE 1.2: Discovery of π in cosmic rays by Powell in 1947 (left) and discovery of Kaon by Rochester in 1949 (right).

also classified according to their spin into families of *fermions* or *bosons*. Gell-Mann and Nishijima introduced a new attribute *"strangeness"* to explain the disparity between the time scales of decay between Λ family and K family. It was found that the particles with strangeness decays by relatively slow weak decay process. Though protons and neutrons up to this time were considered as fundamental particles, scattering experiments of electrons by nuclei revealed the possibilities of presence of some internal charge distributions in them. This implies that some kind of internal structure is bestowed upon them. In the fall of 1954, when the Bevatron at the Lawrence Berkeley National Laboratory (LBNL) started working, it was the largest particle accelerator ever built. The antimatter program led by Emilio Segre and Owen Chamberlain, had placed a blackboard, near the Bevatron's entrance and posted daily updates on the group's progress. The snapshot shown in Figure 1.3 revealed that as of October 6, 1955 at 4:30 p.m., the group had detected 38 negatively charged particles with the same mass as protons and the announcement for the discovery of $anti-proton$ came shortly.

In 1957, Schwinger, Bludman and Glashow independently suggested the weak interactions to be mediated by massive charged bosons which Yukawa first predicted 20 years earlier. Lee and Yang named them W^+ and W^- in 1960 [9].

Within a couple of years, there were so many elementary particles in the bucket that it was getting very difficult to find the ordering principle in this *particle zoo*. Gell-Mann in 1961 introduced a new flavor scheme of classification, for which he coined the

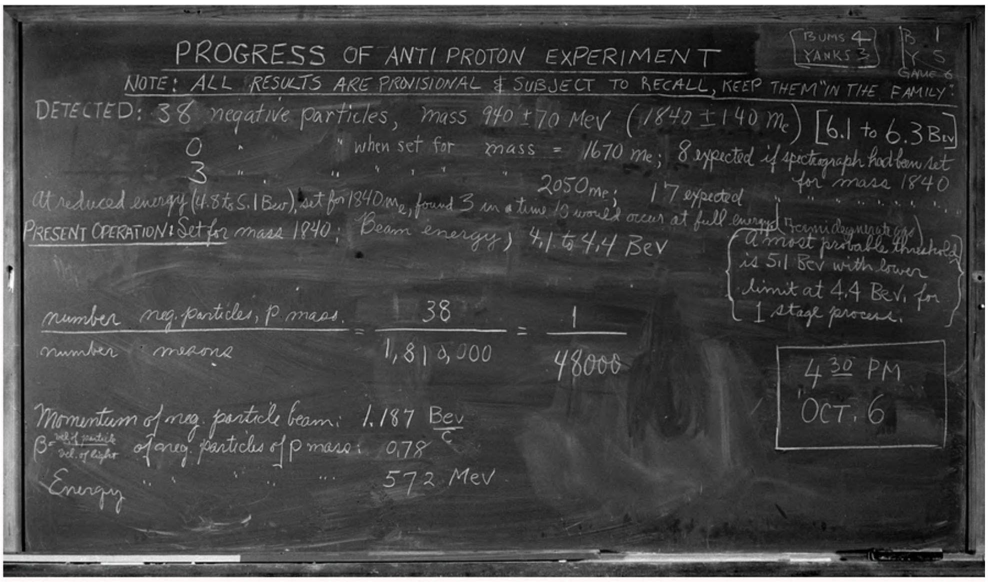

FIGURE 1.3: The "twitter" of Bevatron, the blackboard placed by Wiegand which shows the report on 6th October, 1955 about detecting 38 anti-protons.

term "$Eight-fold\ Way$", to particles having similar mass and spin but differ in charge and strangeness, which was based on the SU(3) grouping. Within this scheme, Gell-Mann and independently Ne'eman predicted at the 1962 Rochester conference that a baryon with strangeness, s = -3 (Figure 1.4) must be there [10] and the discovery of Ω^- [11] in 1964 credited the validity of that scheme.

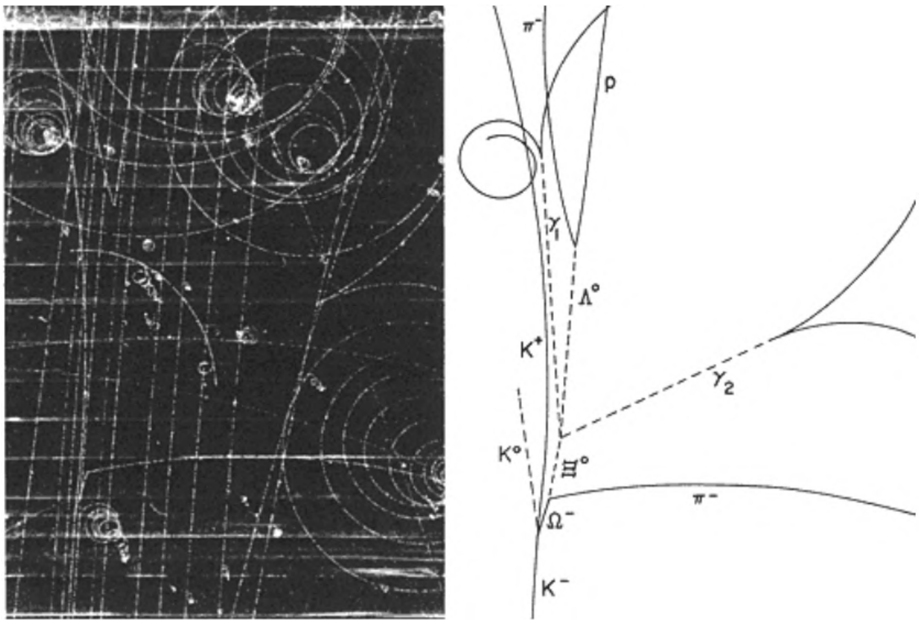

FIGURE 1.4: Ω^- discovery in 1964.

Independently Gell-Mann and Zweig first introduced the revolutionary idea of the *quark* in 1964. This idea complemented Gell-Mann's scheme of flavor dependent classifications of particles with three quarks: *up* (u), *down* (d) and *strange* (s). The introductory idea was that all the hadrons could be composed out of either three such constituents (quark) for the baryons, or out of a constituent- anti constituent pair for the mesons [12–14]. Gell-Mann thought of these constituents as "*kworks*" [15], which he later rewrote into quarks after reading this expression in James Joyce's "Finnegans Wake". This idea was so attractive by the virtue of its simplification in the categorisation of all the particles from a sea of fundamental particles to just three, that it got widely accepted.

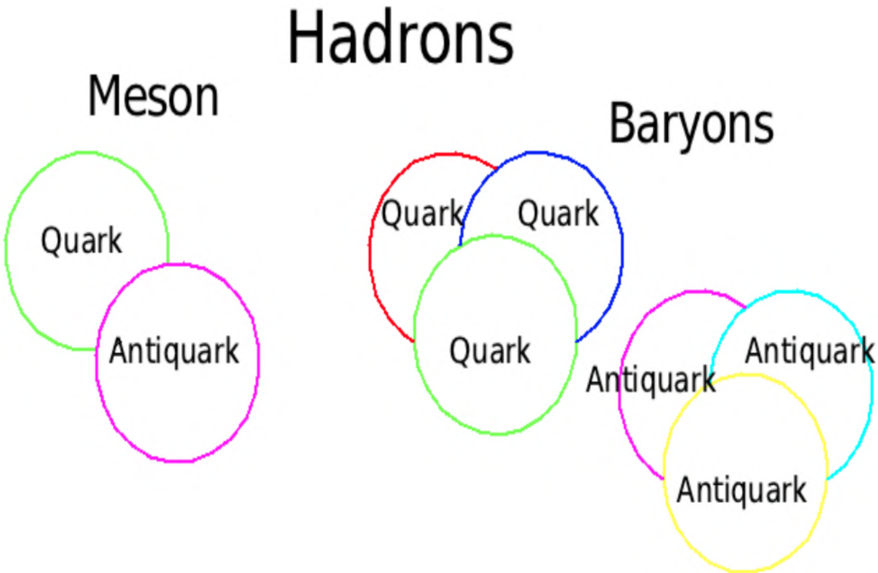

FIGURE 1.5: Structures of baryons and mesons predicted through quark and anti-quark combination.

The observation of repeated patterns of leptons ignited the idea of the presence of a fourth quark which Glashow and Bjorken presented as the *"charm"* (c) quarks. In 1965, Greenberg, Han and Nambu introduced an additional degree of freedom to the quarks which they termed as the *"color charge"* [16] in requiring that the hadrons would be color neutral objects. At that time many physicists were into the unification of the existing theories to bring them under one umbrella. With this vision, Weinberg and Salam independently proposed an idea to unite electromagnetic and weak interactions by postulating a weakly interacting boson, which was later found to be the Z boson. In course of literature survey it was found that it was them who at the same work postulated an additional massive boson to explain the masses of the particles [17]. This idea which is regarded as the most essential part of the *Standard Model* (will be discussed in the next section) was ignored till 1971 and it was found that it was quoted only 5 times though the postulation of it was already made by Higgs, Englert and Brout in 1964.

In 1968 accelerator based experiments entered into the arena and the Stanford Linear Accelerator Centre (SLAC) through the deep inelastic scattering (DIS) programme, indicated the presence of scattering centers inside the proton [4, 19]. They confirmed a conjecture by Bjorken from 1969 that the scattering cross section does not depend on the absolute energy or the squared momentum transfer, Q^2, of the interaction but depends on dimensionless quantities like energy ratios or angles [20]. Analysing the electron-proton scattering data Bjorken and Feynman came up with their idea of constituent particles inside the proton without calling them quarks, but *partons* and a model was developed which took the name of $quark - parton\ model$ (QPM). In 1972, the theory of the strong interaction, *Quantum Chromo Dynamics* [21] was suggested by Gell-Mann and Fritzsch from the original idea of Gell-Mann [22] and was later formally published [23]. Quarks were postulated as real particles with color charge and gluons to be massless mediator quanta of strong interaction with color charge. In 1974, the term *Standard Model* was coined and was endorsed as the soul of modern physics in a report at the international physicists conference by Iliopoulos. By that time only particles with u, d and s were known but c was predicted theoretically. The physics community of that time was low on confidence to find particles with charm quarks, to which Glashow challenged that if it was not found within two years, he would eat his hat! To his rescue, came team SLAC and BNL who discovered a particle J/ψ which is made up of charm and anti-charm pair in the month of November that year. The team at BNL, headed by Samuel Ting found that particle in summer of 1974 and named it J whereas the team at SLAC headed by Richter named it ψ. This discovery came at a point of time when there were two major problems to progress with the quarks: the experimental absence of free quarks and the inconsistency with the Pauli principle. What made J/ψ so special was the fact that this electrically neutral heavy (3 times the mass of a proton) particle has an extraordinarily long lifetime. Typical lifetimes for hadrons in this mass range are of the order of 10^{-23} seconds but the J/ψ lasted fully 10^{-20} seconds before disintegrating

- a lifetime 1000 times greater! The events precipitated by the discovery of J/ψ was so moving that the community started calling it the *November Revolution* [24].

Perl and collaborators analysing SLAC data announced a new charged lepton τ in 1976. The production of particle- antiparticle pair of this lepton arose confusions for having the same energy threshold as charm quark-antiquark production. This confusion was only resolved by the discovery of J/ψ and D mesons. At that time electrons and muons were associated with their types of neutrinos and this suggested that the tau lepton would also have associated neutrinos. By this time the lepton chart was completed by six in numbers. Another new quark was added to the chart in 1977 when Lederman and collaborators discovered a particle called *Upsilon* (Υ). This new quark was named "*bottom*" and this also ignited the idea of having another quark, the sixth, to make them equal in number with the leptons. In 1983, Rubbia with his team including van der Meer used CERN experiments and presented experimental proof in support of $W^{\pm}$ and Z bosons in the exact form as predicted by theory of standard model. By 1989, the extensive studies from CERN and SLAC experimental data, at all the energies expected that time, no more than three low mass neutrino species have been found implying the existence of only three families of fundamental particles. The studies also helped in providing extra tests for the electroweak aspects of the standard model as well as for the strong interaction aspects.

The many experimental programmes that came up during this time led the field by discovering theoretically predicted particles. The QCD and standard model theory was well established and it was only a matter of time to discover the particles to fill the chart. After an extensive search, in 1995 the CDF and D0 experiments at Fermilab discovered the massive top quarks having mass of about 175 GeV. There was no explanation on the reason of this large value of mass, as the standard model can only fit the quarks but not predict them. In 2000, the DONUT collaboration at Fermilab announced the discovery of the *tau neutrino* and the lepton family was full. It was now left with the most important missing link of the standard model, the Higgs boson. It kept hiding from the scientists even after years of search and frustration led the physicists to call it the "$God - damn$" particle. In a book by Lederman in 1993, he first coined the name "*God*" particle for this most important member of the standard model which is still popularly known by the same name. The search came to an end with the discovery of the Higgs boson in 2012 by two experiments at CERN: ATLAS [25] and CMS [26].

In the next section, the current configuration of the standard model will be given.

1.1.1 The Standard Model of particle physics

It took enormous efforts by the scientists over years both in theoretical and experimental sectors to complete the model of the elementary particles [27]. The current building blocks of all the particles in the simplest structure is given in figure 1.6. The structure is described briefly in the following:

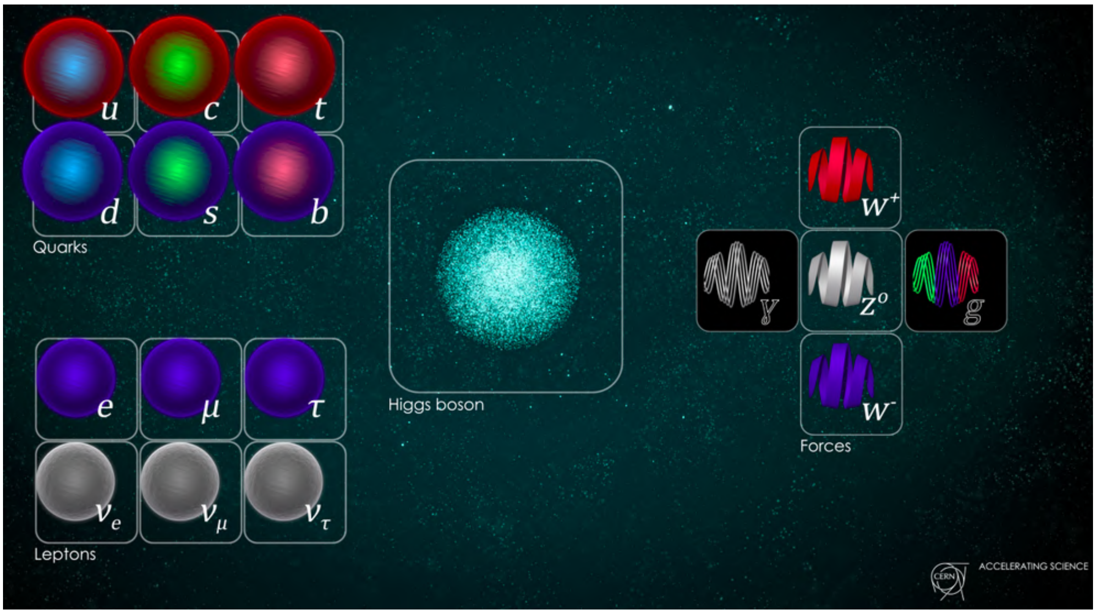

FIGURE 1.6: Basic building blocks of particles and composition of the standard model. Figure taken from [28].

The world of elementary particles are divided into two fundamental groups of *leptons* and *quarks*. All the quarks and leptons are also divided into two broad categories depending upon the statistics they follow related to their spins: the particles following Fermi-Dirac statistics are called the *fermions* and those following the Bose-Einstein statistics are called the *bosons*.

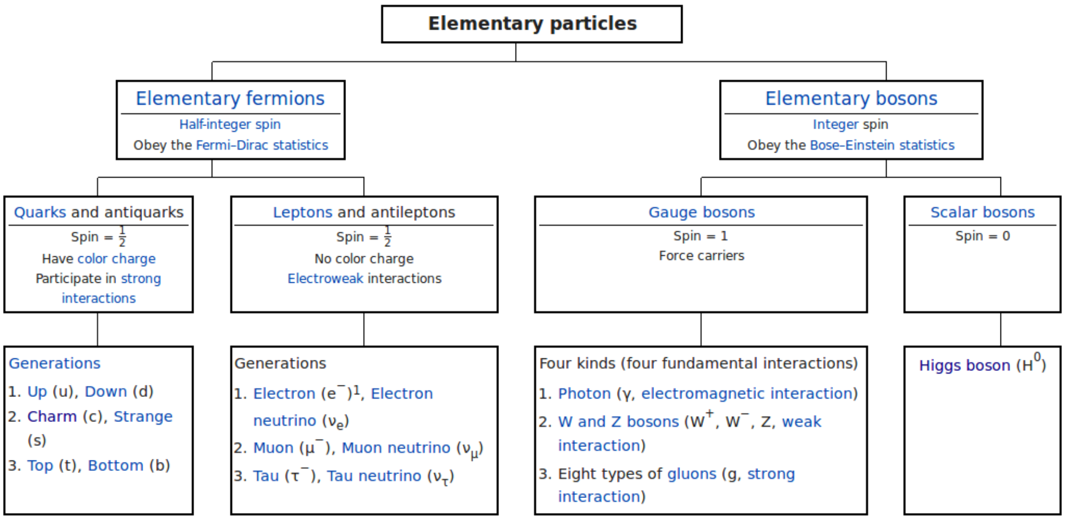

FIGURE 1.7: Three generations of elementary building blocks of particles. Figure courtesy: Wikipedia.

The elementary particles of the standard model come in three generations. From the family of quarks, *up* (u) and *down* (d) quark and from the family of leptons, the *electron* (e) and *electron neutrino* (ν_e) belong to the first generation. The second generation includes the *strange* (s) and *charm* (c) quark and two leptons, *muon* (μ) and *muon neutrino* (ν_{mu}). The third generation consists of *beauty* (b) and *top* (t) from the quark family and *tau* (τ) and *tau neutrino* (ν_τ) from the family of leptons. All these particles are accompanied by their associated anti-particles. Figure 1.7 summarizes these three generations of particles.

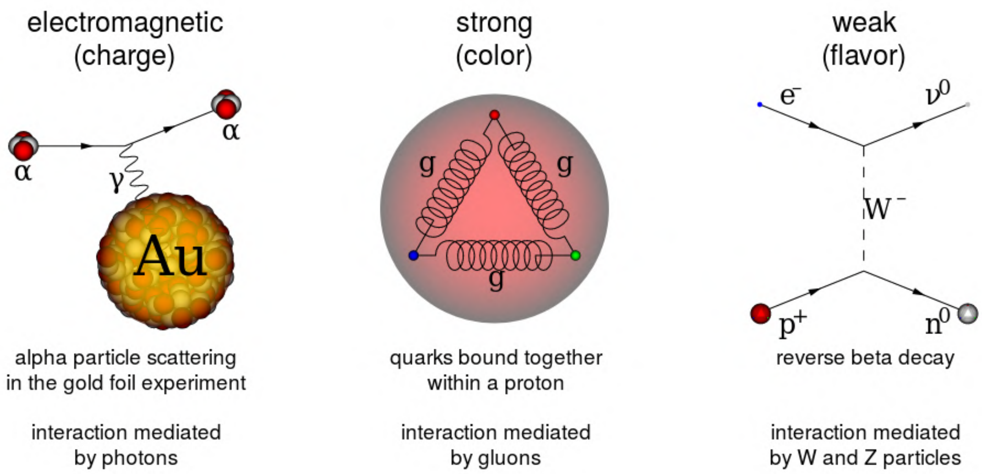

FIGURE 1.8: The three interactions of the standard model. Figure taken from [29].

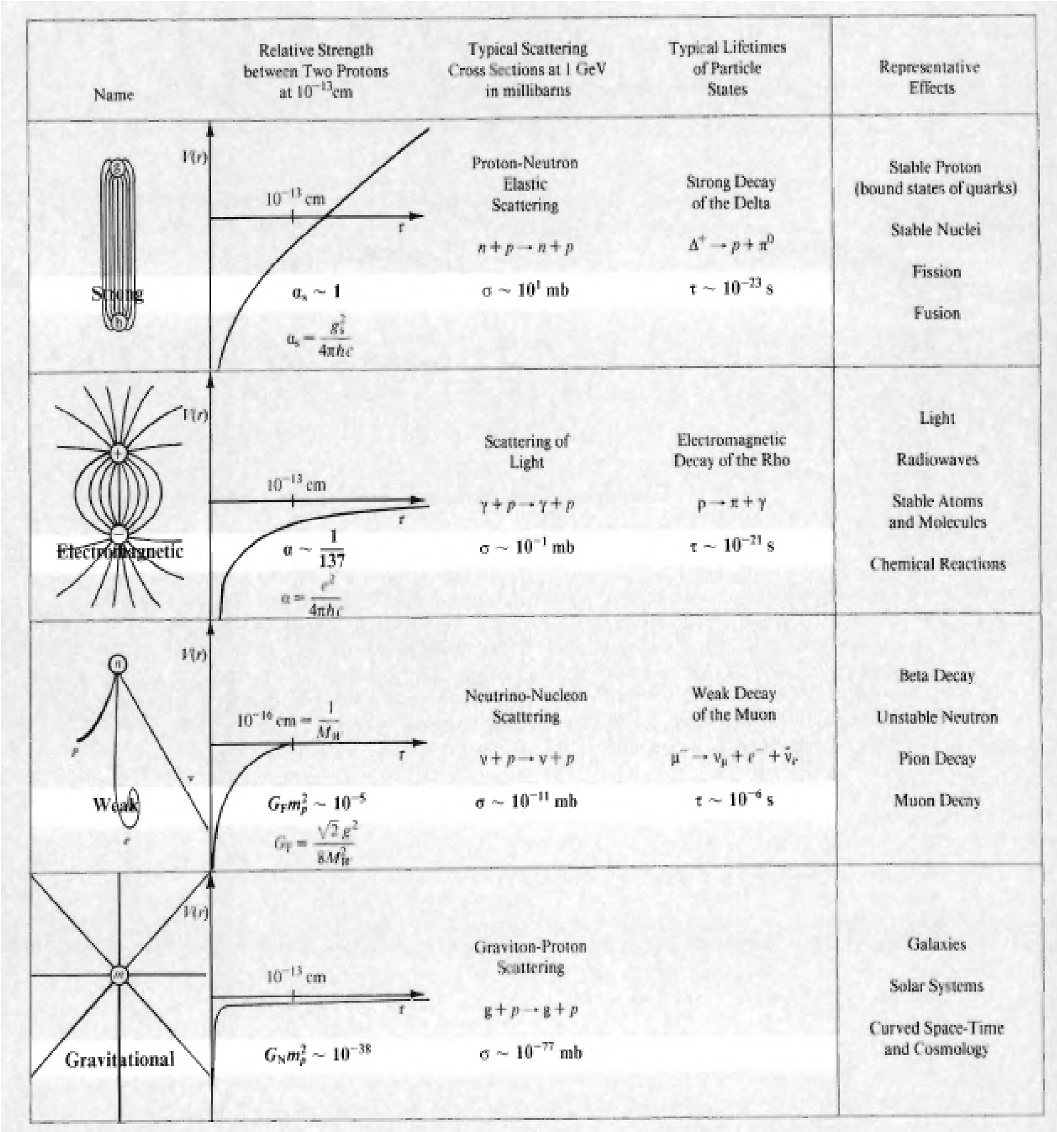

FIGURE 1.9: Comparative descriptions of all the interactions in nature. Figure taken from [30]

There exist four fundamental interactions in nature: strong, weak, electromagnetic and gravitational. But as shown in Figure 1.7, the standard model as of now includes the first three of them due to not only the lack of theoretical work to generalise and unify the gravitational force with the other three interactions but also due to the lack of information on the still hypothetical mediator of this interaction, the *graviton*. As prescribed by the theory, all the interactions are mediated by what could be defined as the force-carrier particles. The strong interaction is mediated by gluons, $W^{\pm}$ and Z bosons are the exchange particles for weak interaction and *photons* (γ) mediate the electromagnetic interaction. Figure 1.8 shows pictorial descriptions of the three interactions acknowledged in the standard model. There is also Figure 1.9 which gives a comparative description of the interactions including the gravitational one.

The *Higgs boson* is the massive elementary particle which gives mass to all the particles [31, 32]. According to the standard model, all the quarks and gluons are associated with color charge but no isolated colored quark or gluon has been seen until now. These colored objects form composite colorless particles that we can detect and they are called the *hadrons*. The hadrons are further classified into two broad groups: *baryons* and *meson*. Baryons (anti-baryons) are made of three quarks (antiquarks) whereas mesons are made of one quark and one antiquark. The complete descriptive structure of the standard model is given in Figure 1.10. Additinonally, the relations between the constituents of the standard model of Physics has been shown in Figure ??.

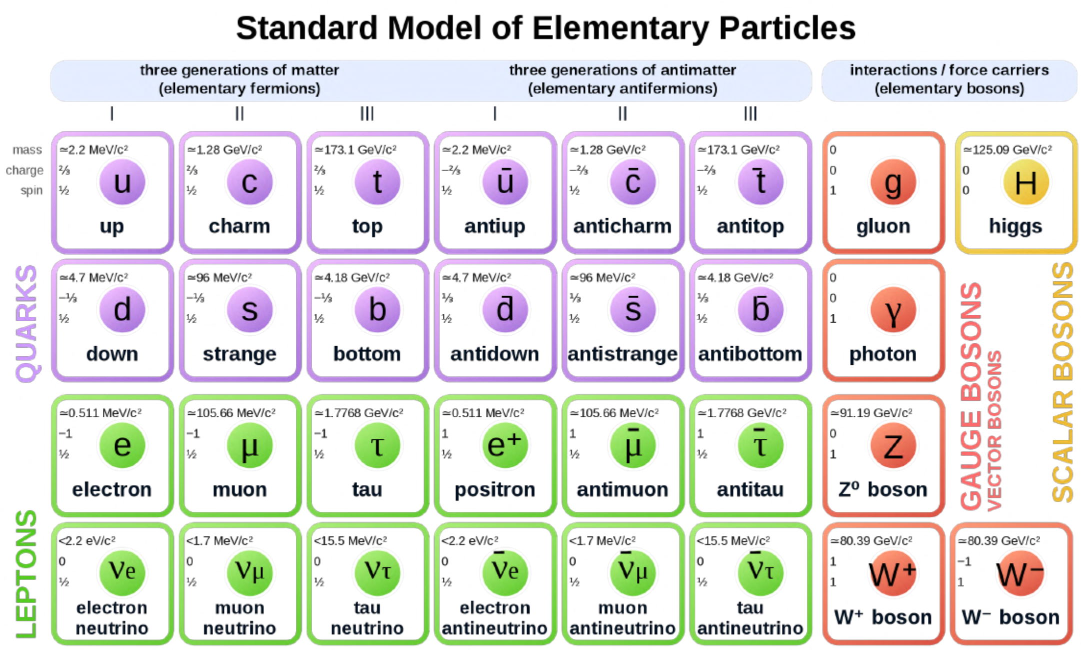

FIGURE 1.10: The full standard model with the properties of all the constituents. Figure courtesy: Pinterest.

The next section will very briefly discuss about the process of observing and studying particles from the beginning of the field to current time.

1.2 Observing and studying particles

1.2.1 Natural sources

At the end of the 19th century, J.J. Thomson discovered the first fundamental particle, the electron. This particular discovery gained so much attention that many scientists in the community started searching for the others. In the early 20th century, physicists observed that particles are abundantly produced by natural phenomena and it was the primary field of experiments in particle physics at that time. In fact, the positron and muon were discovered in this way. One of the natural ways for spontaneous particle production (emission) is radioactivity. Radioactive elements emit particles including the electron, photon and alpha particles as the byproducts of their internal readjustment. This topic was the object of study by particle physics pioneers like Becquerel and Marie Curie.

Enormous streams of particles from the cosmos continuously hits our planet and strike the atoms in the upper atmosphere of the Earth, producing additional particles what we know as the cosmic rays. These contain various particles like photons, electrons, muons, positrons etc. A part of the cosmic ray shower travelling towards the earth's surface get trapped in subsequent collisions, some reach the ground and the rest continue travelling undisturbed. The next relevant question is how to see those particles?

1.2.2 "Trapping" a particle

Particles being the smallest objects, can not be really seen, as no visible light bounces back from an object so tiny, even with the most powerful microscopes. So how is it that scientists can observe, study and manipulate them? The answer is folded in the behaviour of the particles while passing through matter (medium).

All the particles behave differently while travelling through matter. For example, electrons and photons rapidly lose their energy by the continuous collisions they suffer with the atoms of the matter they are passing through, until they get trapped. Whereas, protons travel through matter almost unnoticed until they are close to the end of their journey, when they lose all their energy in a burst and immediately stop. Muons, on the other hand, can travel through layers and layers of any material, even through hundreds of meters of solid rock, without losing much of their energy. Neutrinos, the most notorious among the herd, interact extremely weakly with all other objects: they can pass through an entire planet without stopping.

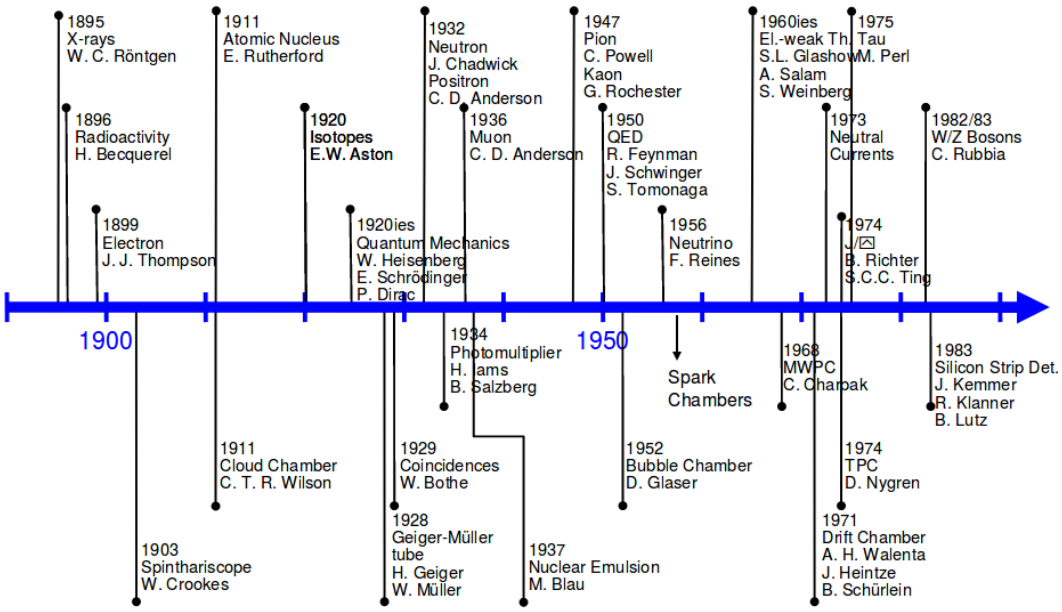

FIGURE 1.11: Timeline of particle physics and associated instrumentation. Figure courtesy: David Nygren, EDIT School -FNAL.

Physicists leverage these different behaviors to develop detectors that detect the particles and study the properties of them. It is something like the setting of a trap to "catch" particles, the other way of "seeing" particles. When a particle passes through a material, it leaves a certain amount of its energy behind. That energy is collected and transferred to another form that helps recording a particle's passage through it. Depending upon the interaction scheme of the particles, the detector technology changes. Modern experiments use a combination of such technologies in order to record all the types of particle moving through it. Using different layers of detectors, scientists can reconstruct particle trajectories and under certain circumstances, measure the exact energy of a particle.

During the earlier time, it was bare human eyes with the help of photographic films and scintillation screens that helped as the light detection system in nuclear physics to decode radioactivity. Figure 1.11 presents a timeline about the progress in particle physics and subsequent advancement in detector technologies.

Photographic emulsions, cloud chambers (Figure 1.12) and later bubble chambers revolutionised the era of non-electronic detectors which led to the discovery of more than 20 particles: $K^{\pm}$, $\pi^{\pm}$, $\bar{\Lambda}^0$, Σ^+ were discovered by the emulsion technique; cloud chamber contributed to the discoveries of e^+, $\mu^{\pm}$, K^0, Λ^0, Σ, Ξ^- and Σ^0, Ξ^0 were discovered by the bubble chamber. Later the energy deposited by the passing particle was used to create electronic signal which in turn helped to detect the particle in real-time. Geiger-M*ü*ller tube shown in Figure 1.12 the first electronic gas ionization detector to detect charged particles.

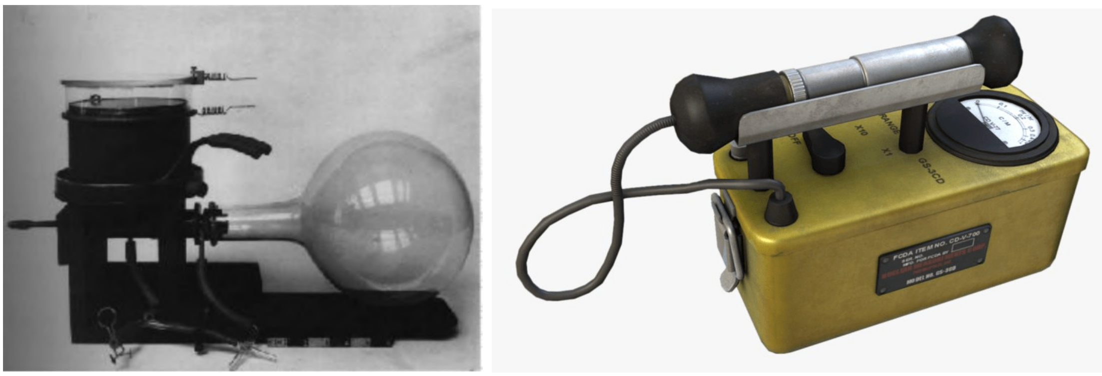

FIGURE 1.12: The Wilson cloud chamber in 1911 (left) and the Geiger-Muller tube (right).

Next came the time of hybridisation, when scintillator detectors were equipped with photo-multiplier tubes (PMTs) for better sensitivity. The rapid evolution of electronic detector technologies by achieving fine granularity, fast data read-out etc. moved the community to the era of electronic detectors and marked the end of the big bubble chamber era. The next generation detectors came just after that with the introduction of the semi-conductor devices. Semi-conductor detectors provide high precision in tracking of particles and were getting introduced in large experiments. Today, these basic detector technologies are even combined into hybrid detector systems such as Silicon PMs, Micro-pattern Gaseous Detectors with Pixel Readout or Silicon Tungsten calorimeters. The modern large-scale detectors used in experiments like there in the LHC, which encompass many forms of tracking chambers and calorimeters that completely surround the interaction point are known as "hermetic detectors" and Figure1.13 represents some of them.

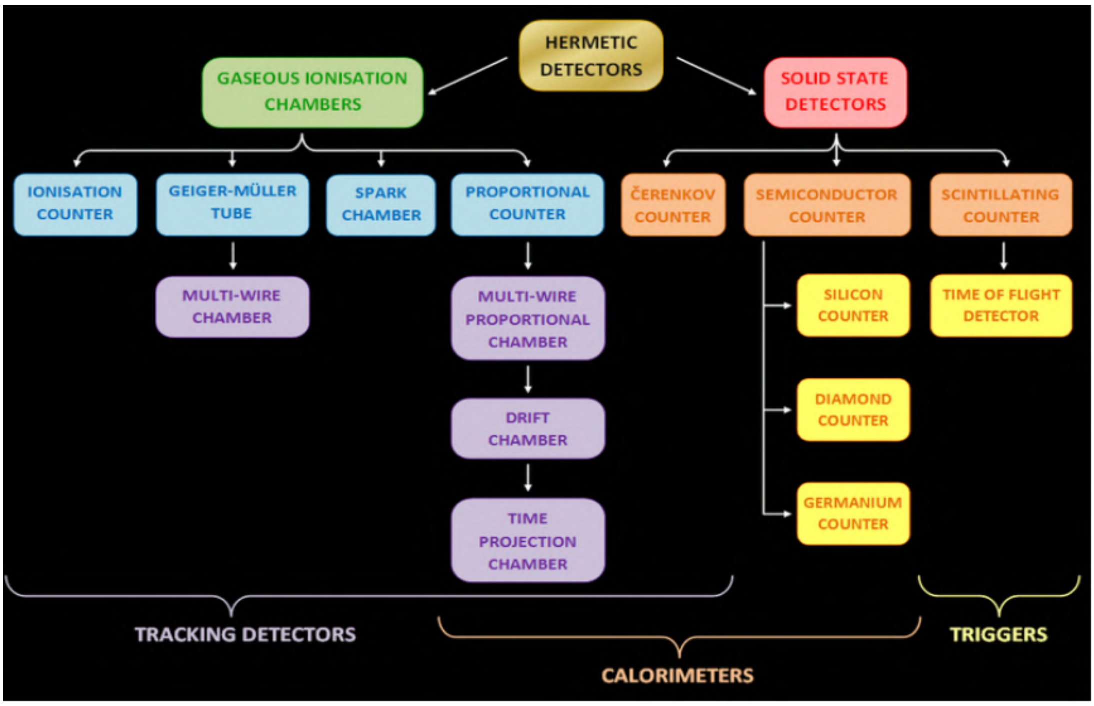

FIGURE 1.13: The detector zoo. Figure courtesy: Erika Garutti.

Detection of particles became less difficult once scientists understood and implemented the idea of manipulating them using an electric or magnetic field. An electric field can push forward the charged particles, like electrons or protons, whereas a magnetic field can change the direction of their trajectories. The next sub-section gives the description of the simple physical laws that help in the process.

1.2.3 Manipulating particles

As discussed in the previous sub-section, electric and magnetic field have the potential to influence the speed and trajectories of any charged particle. The force exerted by an electromagnetic field on a charged particle is called the Lorentz force and it is expressed as follows:

$$\vec{F} = q[\vec{E} + (\vec{v} \times \vec{B})] \tag{1.1}$$

where q is the charge of the particle, $\vec{v}$ is its velocity, $\vec{E}$ and $\vec{B}$ are the electric field and magnetic field applied on the charged particle, respectively. For a given electric and magnetic field, the particle experiences a force $\overrightarrow{F}$, from the field which depends on its charge and speed. By manipulating $\overrightarrow{E}$ and $\overrightarrow{B}$ we can, thus, manipulate the particle's kinematics. If one rewrites the above equation in the following form,

$$v = \sqrt{\frac{2q(V_2 - V_1)}{m}} \tag{1.2}$$

one can see that by creating a potential difference $\Delta V = V_2 - V_1$, the velocity can be modified. The velocity can be increased by applying large potential difference i.e., large electric field.

If one rewrites the first formula to isolate the radius of bending of its trajectory, then the radius of curvature is given by the following formula:

$$r = \frac{mv}{qB} sin\theta \tag{1.3}$$

where θ is the angle between the direction of the particle and direction of magnetic field. This expression shows that the trajectory of a particle can be steered using a magnetic field. Since the magnetic field exerts a force perpendicular to the direction of the particle's direction, the net work done is zero and hence the particle does not lose energy in the process. The direction the particle curves in the magnetic field reveals its charge, since positive and negative charges curve in opposite directions. It can also be seen that the radius is proportional to m/q which implies that if two particles, with one having mass as half of the other one but has twice the charge, come with the same speed, they will both orbit with the same radius. Once the momentum is measured, the energy of the particle can be measured by a calorimeter. With that much information, the mass and hence the identity of the particle can be deduced. Figure 1.14 presents a picture where an electron with 16.9 MeV initial energy spirals about 36 times in the magnetic field. At the end of the visible track the energy decreased to 12.4 MeV and from the visible path length the energy loss by ionization was calculated to be 2.8 MeV. The observed energy loss (4.5 MeV) was concluded therefore because of Bremsstrahlung.

Using the last two expressions, physicists conceived the idea of designing experiments with particles, where the speed of the particles could be increased desirably and the trajectories could be bent to restrict them to follow a designed path. These

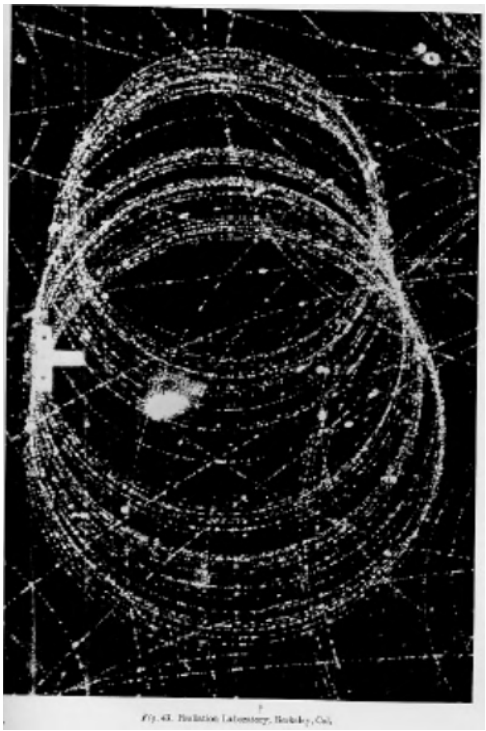

FIGURE 1.14: Fast electron in a magnetic field at the Bevatron, 1940.

ideas helped in designing particle accelerators. The linear accelerator was built using a number of accelerating modules in successive combination. Circular accelerators were built using the combination of accelerating and bending modules in which the particles attain their maximum energy after traversing the path in few cycles depending upon the design.

1.2.4 Particle factories

So far, only the natural sources of particles have been discussed. Now there are many fundamental mechanisms in the universe which involve the particles that have not been discovered yet. This provokes many questions, like, how did the universe form? In the beginning of time according to the Big Bang Theory, in a fraction of a second, a huge amount of energy was released and then the quasi-free quarks and gluons recombined among themselves to create the first glimpse of the matter we see today. And Dark Matter which shares 25% of the total energy of the universe, is produced from which particle, if any? Does there exist any particle which carries gravity?

To answer these and many not asked yet, scientists felt the need for particles interacting at much higher energies and with much more flux to produce the primal universe environment in a controlled way in the laboratories. Natural sources like radioactive elements or cosmic rays are unable to supply that, and one needs controlled sources of particles, the particle factories. At this point Einstein came to the rescue. He proposed a theory on the equivalence of mass and energy, $E = mc^2$, in 1905. This theory roughly states that an object, even if it is at rest, possesess a certain amount of energy based on its mass. Conversely, if a certain amount of energy corresponding to the mass of a certain particle could be created, then it is possible to produce that particle from that energy.

Modern particle colliders have been built to realise this relation where particles are accelerated up to the highest designed energies and then collided. The energy liberated in the collisions produces large number of particles which are detected by detectors and studied. Although today's particle accelerators are impressive, they do not compare to natural particle accelerators found in outer space. Cosmic rays from outside the Milky Way create much more energetic collisions in the Earth's upper atmosphere than our most powerful colliders. But the number of these collisions is not enough to study and characterise the system produced in those.

Modern particle physics accelerators need to be very large to supply the amount of energy required in smashing particles together at relativistic speed. For example the LHC is almost 27 km in circumference and it smashes bunches of particles every 25 nanoseconds producing about 40 million bunch crossings every second. Each of this bunch crossings results in about 30 collisions taking the collision rate to 1 billion per second. Each of these events produce a large numbers of particles and the responsibility of experimental physicists is to record them, study them and decipher the underlying mechanisms associated with their production.

With this, now we have the standard model in our hand and some knowledge of the elementary particles, and how to manipulate them or conduct experiments with them. In the next section, we will try to have some basic idea about what governs the world of elementary particles and how they behave, or how one explains their behaviour a from theoretical perspective.

1.3 Quantum Chromo Dynamics (QCD): The theory of strong interaction

The theory of the strong interaction, between the constituents of the composite hadrons, is known as Quantum Chromo Dynamics (QCD). This theory is closely related to the theory of electromagnetic interactions - Quantum Electro Dynamics (QED) and was in-fact developed initially taking QED as the base. The force carriers in QCD are the gluons and they posses color charge as the quarks. Quarks posses three colors: red, green and blue, whereas there are in total eight color charged gluons. In this section, few of the important aspects of QCD have been briefly presented.

1.3.1 Basic elements of QCD

QCD is based upon gauge field theory and is defined via its Lagrangian density ($\mathcal{L}_{QCD}$), which is composed of four terms [33]:

$$\mathcal{L}_{QCD} = \mathcal{L}_{quarks} + \mathcal{L}_{gluons} + \mathcal{L}_{gauge} + \mathcal{L}_{ghost} \tag{1.4}$$

where,

1. $\mathcal{L}_{quarks}$ describes the interaction of spin $\frac{1}{2}$ quark fields q_a of mass m_q with spin 1 gluon fields $\mathcal{A}^A_\mu$,
2. $\mathcal{L}_{gluons}$ represents the kinetic term of the gluon fields $\mathcal{A}^A_\mu$,
3. $\mathcal{L}_{gauge}$ defines the chosen gauge
   and
4. $\mathcal{L}_{ghost}$ is the so-called ghost term that is a remedy necessary in non-Abelian gauge theories to treat the degeneracy of equivalent gauge field configurations.

If one tries to have a closer look at the first term, it is expressed as,

$$\begin{aligned} \mathcal{L}_{quarks} &= \sum_{q\in u,d,s,c,b,t} \bar{q}_a(i\gamma_\mu(\mathcal{D}_\mu)_{ab} - m_q)q_b \\ \text{where, } (\mathcal{D}_\mu)_{ab} &= \partial_\mu\delta_{ab} + ig_s\mathcal{T}^A_{ab}\mathcal{A}^A_\mu \end{aligned} \tag{1.5}$$

$(\mathcal{D}_\mu)_{ab}$ is known as the co-variant derivative and γ_μ are the *Dirac Matrices*. In the above and also in the others in this section, Greek letters μ,ν,..$\in$\{0,1,2,3\} are the space time indices whereas a,b,c $\in$\{1,2,3\} are the indices of the triplet and A,B,C $\in$\{1,...,8\} are the indices for octet representation. g_s represents the gauge coupling of strong interaction and $\mathcal{A}^A_\mu$ are the eight gluon fields with factors $\mathcal{T}^A_{ab}$ corresponding to the generators of the $SU(3)$ gauge group of QCD. The generator matrices follows the commutation relation:

$$[\mathcal{T}^A, \mathcal{T}^B] = if^{ABC}\mathcal{T}_C \tag{1.6}$$

where f^{ABC} are the corresponding structure constants of $SU(3)$ and take the values:

$$\begin{aligned} f^{123} &= 1 \\ f^{147} &= -f^{156} = f^{246} = f^{257} = f^{345} = f^{367} = \frac{1}{2} \\ f^{458} &= f^{678} = \frac{\sqrt{3}}{2} \end{aligned} \tag{1.7}$$

all the other f^{ABC}s are zero. The second term, $\mathcal{L}_{gluons}$, is expressed as:

$$\mathcal{L}_{gluons} = -\frac{1}{4}\mathcal{G}^A_{\mu\nu}\mathcal{G}^{\mu\nu}_A, \quad \text{with } \mathcal{G}^A_{\mu\nu} = \partial_\mu\mathcal{A}^A_\nu - \partial_\nu\mathcal{A}^A_\mu - g_sf^{ABC}\mathcal{A}^B_\mu\mathcal{A}^C_\nu \tag{1.8}$$

$\mathcal{G}^A_{\mu\nu}$ are called the field strength tensor. Together, $\mathcal{L}_{quarks}$ and $\mathcal{L}_{gluons}$ represent the "classical" part of the Lagrangian and give the free quark field and gluon field terms along with the quark-gluon interaction term. The non-Abelian group structure of QCD also produces cubic and quadratic gluon self-interaction vertices which are proportional to g_s and g_s^2 respectively. The pictorial description for the above lines have been given in Figure 1.15. The generator matrices (for example $\mathcal{T}_A$), play crucial roles for the splitting of quarks and gluons. The relative factors, for the splitting in terms of the various processes like the depicted ones in Figure 1.15, are obtained with conventional normalisation of the $SU(3)$ matrices using the trace Tr[$\mathcal{T}_A$,$\mathcal{T}_B$] = $T_F\delta_{AB}$. Taking the

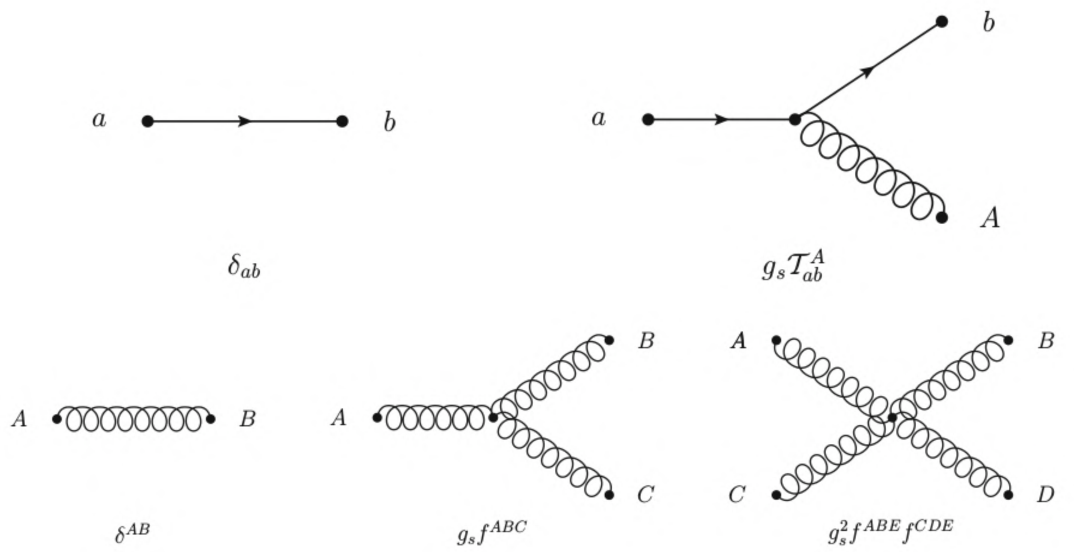

FIGURE 1.15: Schematic diagrams for: free quark-field (top left), quark-gluon interaction term (top right), free gluon-field (bottom left) and cubic gluon self-interaction term (bottom middle) and quadratic gluon self-interaction term (bottom right). Figure courtesy [34].

usual value of $T_F = 1/2$, the relative factors for these processes are deduced as: $C_F = 4/3$ and $C_A = 3$. The implication of these factors can be easily understand via the following examples: if one takes the ratio of a gluon emission by a gluon relative to by a quark, it comes out to be $C_A/C_B = 9/4 = 2.25$ i.e., gluons radiate 2.25 times more than quarks. Similarly, production of a gluon pair from gluon splitting is more than that into a quark-antiquark pair production by a factor $C_A/T_F = 6$.

The local gauge invariance of the QCD Lagrangian imposes a restriction on the gluon field propagator by explicitly specifying a choice of gauge. A popular choice is the covariant Lorentz gauge $\partial_\mu \mathcal{A}^A_\mu = 0$, simplified by the class of R_ξ and this is implemented by simply adding the following term to the classical Lagrangian:

$$\mathcal{L}_{gauge} = -\frac{1}{2\xi}(\mathcal{A}^A_\mu)^2 \tag{1.9}$$

Again the non-Abelian character of the QCD gauge group in addition, introduces a ghost term [35]:

$$\mathcal{L}_{ghost} = \partial_\mu \eta^{A^\dagger}(\mathcal{D}^\mu_{AB}\eta^B) \tag{1.10}$$

The ghosts have no physical meaning and here the ghosts η^A and $\eta^{A^\dagger}$ represent complex scalar fields. The introduction of ghosts is a mathematical trick only, to get rid of the nonphysical degrees of freedom that happen to occur due to calculation with covariant gauges and this completes the Lagrangian for the strong interaction.

1.3.2 Chiral symmetry: spontaneous breaking and restoration

This is one of the most important phenomena that QCD has prescribed. It provides explanation for the production of the pions and gives prediction about the phase transition. Here we will try to understand it through some simple analogy. The total Lagrangian for only three quarks (u, d and s) reduces to following simple form:

$$\mathcal{L} = \sum_{q \in u,d,s} \bar{q}_a (i\gamma_\mu (\mathcal{D}_\mu)_{ab} - m_q) q_b - \frac{1}{4} \mathcal{G}^A_{\mu\nu} \mathcal{G}^{\mu\nu}_A \tag{1.11}$$

This Lagrangian shows a flavor symmetry as the quark interaction does not depend on the quark flavor as long as the masses of the quarks are comparable. The direct consequence of this is the symmetry under isospin transformations and this is reflected in the hadron properties. For light quarks, the QCD Lagrangian additionally exhibits what is known as the *chiral symmetry* (in Greek, *chiral* means hand). Massless spin $\frac{1}{2}$ fermions posses *chirality*: meaning their spin and momentum are either parallel (*right handed*) or anti-parallel (*left handed*) and chooses to remain forever. Naively, this symmetry should have been the consequence that the mesons that are found in nature are of similar mass but with positive and negative parity. However this is not the case in practice and the violation is termed as the "spontaneous" breaking of the symmetry. According to the theorem by Goldstone, spontaneous symmetry breaking results in the creation of a particle, in this case a *pion* [36, 37]. Thus, the pion becomes the main player in the production of the nuclear force. The interaction of pions with nucleons is weak as compared to the interaction of gluons with quarks.

The quark fields can be decomposed in left-hand and right hand fields [38],

$$q_a \sim \Psi_{L,R} = \frac{1}{2}(1 \mp \gamma_5)\Psi \tag{1.12}$$

In this form, the QCD Lagrangian shows symmetry under helicity and flavor transformation and this is represented as the $SU(3)_L \times SU(3)_R$ symmetry. One of the consequences of this symmetry is that the associated parameter, called the condensate, $\langle q\bar{q}\rangle$, becomes zero. But this is not the case and $\langle q\bar{q}\rangle$ is not zero and creation of pion is the proof of that [39]. This is what is referred to as *spontaneous* breaking of the symmetry, and the word *spontaneous* here stands for the fact that this symmetry is respected by the QCD Lagrangian but broken by their state at lower energies. It is also predicted that this symmetry should be restored in high energies.

This phenomena could be easily understood by a simple classical analogy. Let us take a rotating ring along its vertical symmetry axis with angular speed ω in the Earth's gravitational field. A small solid ball has been arranged such that it can move freely along the ring as shown in Figure 1.16.

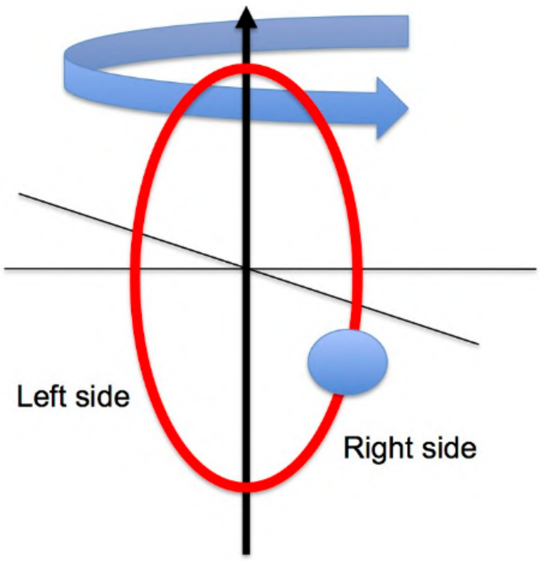

FIGURE 1.16: Classical analogy of spontaneous symmetry breaking.

Here the system has a left-right symmetry which is spontaneously broken by the small ball at low internal energy as it is compelled to choose a side as its equilibrium position due to the centrifugal force. If some energy is supplied to the ball, it will start oscillating around its equilibrium position with an amplitude depending on the energy. Now if the energy supplied crosses a certain threshold value and the ball reaches the other side of the ring, then it will began to move on both the sides. This is the case when one can say that the symmetry of the system is restored. In this analogy, chiral symmetry is restored at high energies (or high temperature), and this restoration actually represents a sufficient condition for the possibility of a QCD phase transition. This can be described by prescribing an analogy with the ferromagnetic phase transition [40]. At high energy, the ferromagnetic system exhibits invariance under rotation due to no preference in the direction of the space. There exists a microscopic magnetisation of the system though, in the presence of thermal agitation at low temperature due to the microscopic magnetic moments of the aligned elementary constituents. This shows that isotropic symmetry is broken spontaneously at low temperature and this is a sufficient condition to predict that there is a phase transition during the generation of the macroscopic magnetisation of the system. In the ferromagnetic case, the magnetisation, M, is the order parameter of the transition, which is the equivalent of the quark-condensate $\langle q\bar{q}\rangle$ in the chiral transition in QCD. Spin waves are the consequences and Goldstone bosons (pions, kaons and eta's) are their analogous partners in QCD. Finally, isotropic symmetry can be explicitly broken via an external magnetic field. The equivalent of a non-zero external magnetic field would be the non-zero masses of quarks, which explicitly breaks the chiral symmetry of the QCD Lagrangian.

Finally, one should keep in mind that the QCD Lagrangian in this case was assumed for massless quarks, which is a reasonable assumption as the masses of the light quarks are small compared to Λ_{QCD} [41]. In this respect the chiral symmetry is broken by the QCD Lagrangian. However, this may not be an appropriate assumption, in particular for the strange quark due to its quite large mass compared to u and d quarks. There should be some threshold mass value at which there will be chiral transition and above which the transition would be a $cross - over$ (described later) but no critical transition point.

1.3.3 Perturbative QCD

There are several approaches within the QCD framework to compute different objectives. To obtain quantitative predictions, a perturbative approach has been prescribed which works wonderfully for high momentum transfer processes or at very small distances, where quarks and gluons are weakly coupled. For the predictions, collisions at very high energies, like at the LHC, stand as an ideal testing ground for a perturbative analysis of the strong interaction. Following are the few features of the pQCD approach:

1.3.3.1 The strong coupling constant

Perturbative expansion of any term needs some parameter to rely on and for $\mathcal{L}_{QCD}$, the relevant one is the gauge coupling constant g_s. This term is related to what is known as the strong coupling constant (α_s) as $\alpha_s = g_s^2/4\pi$. α_s has been defined in the theory in analogy to the fine structure constant α in the QED. The knowledge of α_s along with the quark masses, provides tree-level amplitude calculations with good accuracy as long as $\alpha_s << 1$. Things become complicated if some *loops* arise in the diagrams as shown in Figure 1.17. The loops represent what is known as the *ultraviolet divergences* where emission of soft gluons is introduced in the diagram. The remedy to overcome this is widely known as the $re-normalisation$. Thorough descriptions can be found in [42–44].

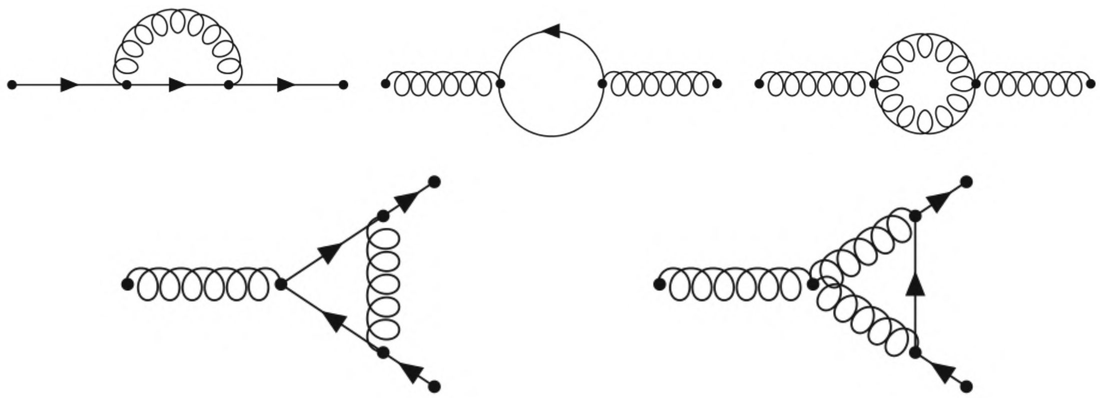

FIGURE 1.17: Schematic diagrams for: quark self-energy correction (top left), gluon self-energy correction (top middle and right), and quark-gluon vertex corrections (bottom). Figure courtesy [34].

An observable $\mathcal{X}$ can be expanded as,

$$\mathcal{X} \; = \; c_0 + c_1\alpha_s + c_2\alpha_s^2 + ... = \sum_{i=0}^{n} c_i\alpha_s^i \tag{1.13}$$

where c_is are the perturbative expansion coefficients. The re-normalization scheme introduces a scale (μ_r) and the predictions in pQCD logarithmically depend on this non-physical scale unless all orders can be summed up. This relation determines the running of the re-normalised coupling constant $\alpha_s(\mu_r^2)$ and is expressed as:

$$\begin{aligned} \mu_r^2 \frac{\partial \alpha_s(\mu_r^2)}{\partial \mu_r^2} &= \beta(\alpha_s(\mu_r^2)), \quad \text{with} \\ \beta(\alpha_s(\mu_r^2)) &= -\alpha_s^2 \cdot (b_0 + b_1\alpha_s + b_2\alpha_s^2 + \mathcal{O}(\alpha_s^3)) \end{aligned} \tag{1.14}$$

In Quantum Field Theory (QFT, the generic theory regarding interacting fields in small realms), the beta function represents the logarithmic dependence of a coupling parameter on the relevant energy scale of a physical process. For example if one takes the coupling parameter to be g and the scale to be μ, then β is expressed as,

$$\beta(g) = \frac{\partial g}{\partial log(\mu)} \tag{1.15}$$

This β function of QCD is a prime example of a quantity that can be evaluated by perturbation theory (which was done by D. Gross, H. Politzer and F. Wilczek in 1973 and 1974 [45–48]) and the first two coefficients are expressed as:

$$b_0 = \frac{33 - 2N_F}{12\pi} \quad \text{and} \quad b_1 = \frac{153 - 9N_F}{24\pi^2} \tag{1.16}$$

where N_F denotes the number of quark flavors with masses m_q smaller than the scale μ_r. It is clear that as long as $N_F \leq 16$, the first term $-b_0 < 0$ and this negative sign in the β function is the manifestation of the non-Abelian nature of the QCD. Retaining only the leading term b_0, we get the strong coupling constant as,

$$\alpha_s(Q^2) = \frac{\alpha_s(\mu_r^2)}{1 + b_0 ln(Q^2/\mu_r^2)\alpha_s(\mu_r^2)} \tag{1.17}$$

This solution gives the strength of the coupling at a scale Q to the one at scale μ_r, within the perturbation regime. This expresses a special property when $b_0 > 0$ implying the weakening of the coupling strength at higher scales Q, or in other words, with decreasing distance the effective color charge gets smaller. This is the consequence of the genuine quantum effect of anti-screening of color charges through gluon self-interactions and the property is known as *Asymptotic Freedom* [45, 46, 48]. This property states that at very small distance, quarks and gluons behave as quasi-free particles.

When the momentum transfer Q is small and it approaches to large distances,

α_s grows beyond the validity of the perturbative regime. An analytic solution exists, defining the value of $\alpha_s(Q)$ when it formally diverges as Λ_{QCD} and is expressed as:

$$\alpha_s(Q) = \frac{1}{b_0 \cdot ln(Q^2/\Lambda_{QCD}^2)} \tag{1.18}$$

where experimentally $\Lambda_{QCD} \approx 200$ MeV for $N_F = 5$. This value is close to the typical hadron masses and sizes, and it draws the dividing line between the pQCD and non-perturbative regime of QCD. This growth of the coupling constant at small scales Q makes QCD the theory of the strong interaction that confines the quarks and gluons into ordinary hadronic matter.

Additionally, there is one more special property of QCD, which is the manifestation of approximately linear growth in strength of the strong force with increasing spatial separation between two color charges that leads to the fact that color charged objects are confined to sub-nuclear dimensions. This property of QCD is called $quark\ confinement$ or $color\ confinement$. It is the property for which free or isolated quarks do not exist. Only entities that are color singlets, i.e. without any net color charge, are not subject to strong interactions and can be observed as free particles. The transition from weakly interacting quarks and gluons inside hadrons to the formation of color-neutral hadrons can not be described by perturbation theory and falls in the non-perturbative regime of QCD.

Unlike the coupling constant (α) in the QED which has a definitive value $\approx 1/137$, the strong coupling constant α_s does not have a fixed value which can be seen in Figure 1.18 and this leads to the name "running coupling constant".

1.3.3.2 Predictions for production cross-sections

Due to confinement, free quarks and gluons are not available, instead in experiments, hadrons with complex internal structure take part in high p_T collisions. But the perturbative treatment is applicable in the partonic realm. This crisis is saved by the factorisation theorem of QCD [52, 53] which separates the cross-section calculation into two parts: a short distance partonic cross-section calculable by pQCD and a non-perturbative long distance part computable through universal functions extractable from measurements in

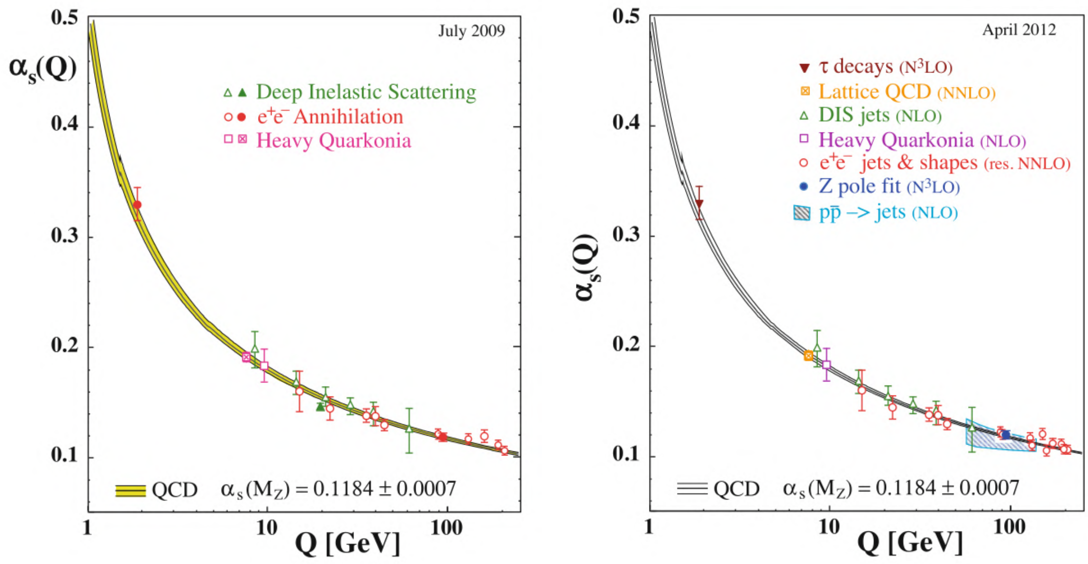

FIGURE 1.18: Determinations of the strong coupling constant α_s are shown as a function of the relevant energy scale Q of the respective process. Left: running of the strong coupling constant as of 2009 [49, 50] and right: running of the strong coupling constant as of 2012 [51].

a process independent way-

$$\sigma_{total} = \sigma_{perturbative} + \sigma_{non-perturbative} \tag{1.19}$$

This approach describes the colliding hadrons in terms of *parton distribution functions* (PDFs), $f_{i/h}(x, \mu_f)$, which represents the probability to find a parton i with longitudinal momentum fraction x within a hadron h at a resolution characterised by the factorisation scale μ_f. Using this, the cross-section of a high p_T scattering process can be written as:

$$d\sigma_(pp \to X) = \sum_{i,j} \int dx dx' f_{i/p}(x, \mu_f) f_{j/h}(x', \mu_f) \times d\hat{\sigma}_{(ij \to X)}(x, x', \mu_f, \mu_r, \alpha_s(\mu_r)) \tag{1.20}$$

where i, j $\in$ q, $\bar{q}$, g are the initial partons, $f_{i/p}$ and $f_{j/p}$ are the respective PDFs with fractional momenta x and x' respectively and μ_f represents the factorisation scale which is also the resolution below which is the domain of non-perturbative QCD. Resolution higher than that is where pQCD comes into play and a physics process can be described in the form of a parton level cross-section d$\hat{\sigma}_{ij \to X}$, factorisation and normalisation scales μ_f and μ_r and the strong coupling constant $\alpha_s(\mu_r)$. The typical scale Q associated with the partonic process is assumed to be in the perturbative domain, i.e., much larger than

Λ_{QCD}.

pQCD gives the most accurate and quantitative predictions by the use of the collinear factorisation. In the partonic domain, the desired cross-sections with the relevant scale Q can be expanded as a power series in α_s. Conventionally, the lowest-order contribution is denoted as leading order (LO), the subsequent ones as next-to-leading order (NLO), next-to-next-to-leading order ($NNLO$) and so forth. More precisely, these terms should be labelled as e.g., *NNLO QCD corrections*. For transverse momenta at the TeV scale or under particular kinematic conditions, tree level effects and loop effects become equally or even more important than a QCD NNLO term. These can be found here [54–56] for further reading.

1.3.4 The QCD phase diagram and Quark Gluon Plasma (QGP)

1.3.4.1 Preliminary ideas and the Statistical Bootstrap Model (SBM)

Collisions of particles at very high energies result in copious production of secondary particles and the very early efforts to explain this were by applying statistical thermodynamics to multi-particle production processes. Many stalwarts like Fermi, Landau, Pomeranchuk worked in this theory but due to difficulties in the explanation this did not see success that time, until Hagedorn came on board. In the 1960s, Hagedorn predicted the probable particle yields at the accelerator energies (keeping Proton Synchrotron at CERN in mind) through his initial work on the statistical particle production. He proceeded with the "fireball" concept in which all the energy of the collision was regarded as being contained within a small space-time volume from which particles radiated, as in a burning fireball. Several observations from the early experiments helped in the process of the development of this approach and one of the most important of them was: the limited transverse momentum of the huge number of secondary particles and the exponential drop of the large angle elastic scattering cross-section with incident energy. Such observations strongly suggested an inherently thermal momentum distribution. Hagedorn worked on this thermal interpretation and understood that the temperature governing particle spectra does not increase, because as more and more energy is poured into the system, new particles are produced.

The entropy rises with collision energy. Also if the number of particles of a given mass (or mass spectrum) increases exponentially, the temperature remains at a limiting value, known as the *Hagedorn temperature* (T_H). Hagedorn predicted this value to be $\approx$ 150 MeV, but it can be as low as the mass of the lightest hadron (the pion), $T_H \approx$ 140 MeV and as high as 160 MeV. Hagedorn further developed the theory and presented a model known as the Statistical Bootstrap Model (SBM) [57] which, in a nutshell, is a theory of successive resonance formation. According to it, the resonance into which hadrons can be excited through a collision, is itself a constituent of a further heavier resonance, whilst also being composed of lighter ones. In this way, a matter cluster when compressed to its natural volume becomes a more massive resonance composed of the lighter resonances as shown in Figure 1.19. Since, the smallest building block of all

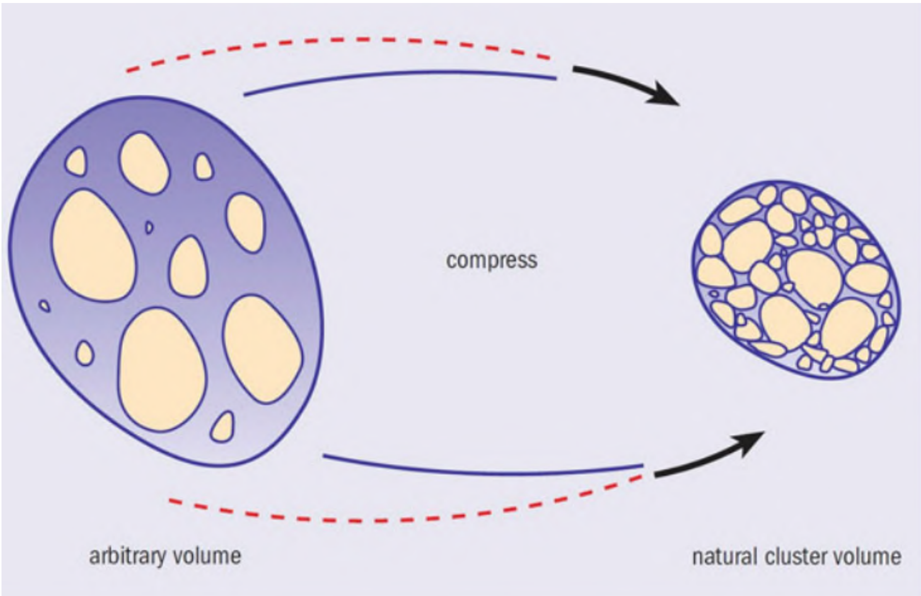

FIGURE 1.19: A cartoon of the statistical bootstrap idea. Figure taken from [58].

hadronic resonances was supposed to be the pion that time, within the SBM, one can also understand why the limiting temperature is of the same magnitude as the smallest hadron mass $T_H \approx m_\pi$.

1.3.4.2 Critical temperature, QCD Deconfinement and the prediction of the Quark Gluon Plasma (QGP)

During the development of the SBM, the concept of quarks and gluons came into the picture as the building blocks of hadrons. These were incorporated into the model by the constant efforts of Hagedorn, Rafelski and Ericson[58]. In the hadronic picture, the compressed hadronic gas was considered as another version, in the quark picture it was given a finite volume of a drop of quark matter. At high temperatures, gluons were also considered in the quark matter and with increasing temperature, asymptotic freedom ensures weak interactions between them. This led a dense assembly of hadrons to deconfine into a soup of quarks and gluons and it was also found that this state of matter could be heated to a very high temperature, with no limit insight [59]. Rafelski found that at the Hagedorn temperature, finite-size hadrons dissolve into a "liquid" of quarks and gluons. They prescribed that a phase transition and a smooth transformation is possible and it should be a first-order transition where the latent heat to dissolve the hadrons, is delivered at a constant T_H [60]. Within the study of hot hadronic matter today, the Hagedorn temperature is understood as the critical temperature (T_c), the phase boundary temperature between the hadron gas state and deconfined state of strongly interacting mobile quarks and gluons as shown in Figure 1.20. This deconfined state of strongly interacting quarks and gluons was later named as the *Quark Gluon Plasma* (*QGP*) [61, 62]. The word *plasma* is used to describe the state of matter when ions and electrons are dissociated in atoms. There is then an analogy when colorless particles dissociate to create deconfined matter. Though the SBM with its exponentially growing mass spectrum of hadrons described many features of the multi-particle production at the energies accessible in the late 1960s, it places a dilemma for cosmology [63]. By 1965, with the discovery of the *cosmic microwave background* (*CMB*) the Big Bang model had unambiguous evidence in support of it, according to which the present universe started approximately 14 billion years ago with a singularity, the so-called "Big Bang". A few microseconds after the Big Bang, the tiny universe was in a state of dense soup made of quark and gluons, the quark gluon plasma (QGP) for a very short time after which QGP ceased to exist due to the rapid cooling of the produced system. By tracing back the cosmic evolution to very early times it was possible to conclude that the universe must have experienced temperatures in excess of 200MeV at times less than 10μs after the

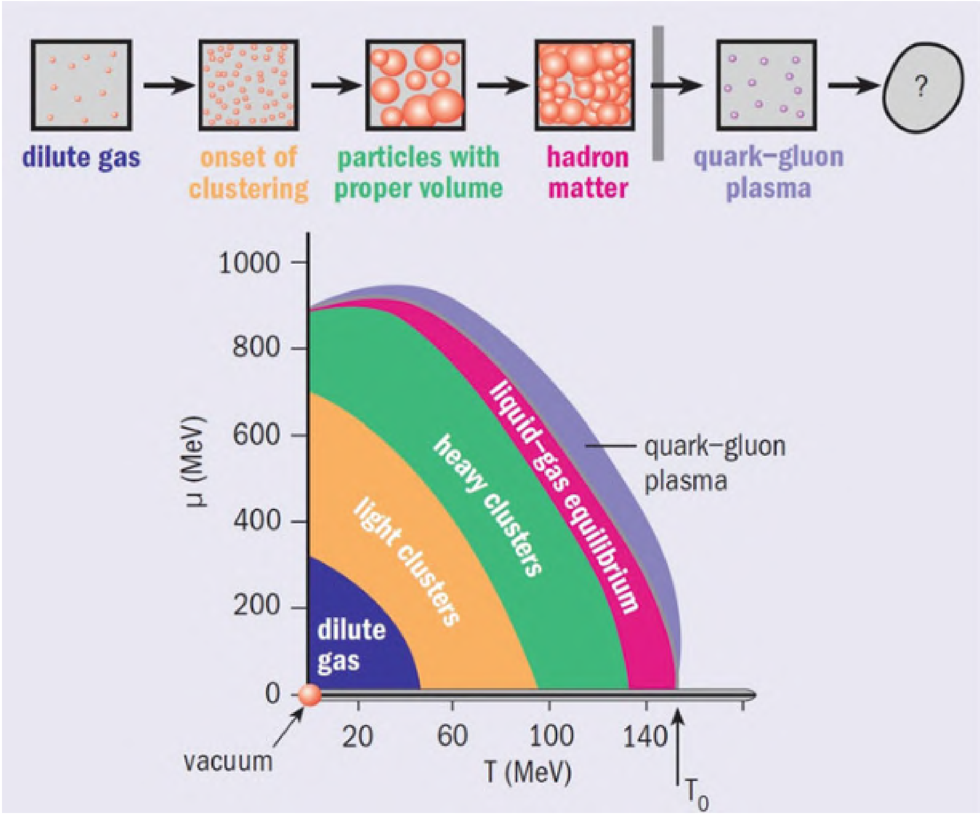

FIGURE 1.20: The different regions of the statistical parameter plane (temperature, T, and the baryochemical potential, μ_B), according to the statistical bootstrap model of hadronic matter. Figure taken from [58].

Big Bang. But it raised some questions on the structure of the matter during the early universe and on its equation of state. The exponential mass spectrum in the SBM put a singularity in the equation of state at the Hagedorn temperature with empirical values in the range 150 MeV $< T_H <$ 200 MeV but the SBM could not give a proper structure of matter beyond the T_H. The quandary of cosmology got its initial resolution in 1975 from the work of Collins and Perry [64], where they showed that due to asymptotic freedom, matter at very large quark densities should be composed of deconfined quarks. Later in that year, Cabibbo and Parisi proposed [65] the singularity as the critical transition point where the hadron gas changes to a strongly interacting colored plasma consisting quarks and gluons. At this point the Hagedorn temperature acquired the name of critical temperature (T_c) where the transition takes place.

1.3.4.3 Current understanding of the QCD phase diagram

In the 1970s, quantitative predictions were not possible due to the lack of reliable mathematical or numerical techniques to solve QCD. In the early 1980s, developments of Monte Carlo simulations based on lattice QCD provided ab initio calculation of the equation of state of strongly interacting matter which have converged to definite results over time [66–68]. These showed that matter composed of hadronic resonances is not separated from the QGP by a discontinuous phase transition in the absence of baryon excess, rather a smooth cross over is expected to turn into a first-order phase transition for matter with a large excess of baryons. The lattice QCD simulations provided support for Hagedorn's model of hadron resonance gas with an exponentially mass spectrum which could describe the equation of state of QCD matter at temperature below T_c and predicted many observable very well. Currently simulations can precisely distinguish the equation of state of hadron gas made up of resonances listed in the Particle Data Book from that of a Hagedorn hadron resonance gas. Numerical results support the exponential continuum mass spectrum of the Hagedorn's SBM [69], in addition the many predicted unknown hadrons by the SBM, according to the models, could be in the strange baryon sector [70]. Above T_c, the density of states grows slowly and eventually approaches a perturbatively interacting QGP composed of massive quasi particles. This implies that the Hagedorn temperature, T_H, indeed is the transition temperature from a hadron resonance gas to a new deconfined state of matter.

Figure 1.21 represents the basic QCD phase diagrams as per our understanding today. The phase transition line has two extremum: high T and low μ_B which implies heating of matter and low T and high μ_B which represents compression of matter. The chemical potential, μ, denotes the change in the system's energy associated with adding a particle to it and describes a system's tendency to create or annihilate particles. Thus a low μ represents freedom to create more particles whereas a high μ denotes the strong aversion of the system to create more particles. In QCD, the net baryon number is a conserved quantity and since we start with some initial net baryon number (colliding nuclei), only their density can change. Therefore the baryo-chemical potential μ_B is a measure of net baryon density. A high μ_B corresponds to a high net-baryon density. Now at higher collision energy, $q\bar{q}$ pairs are produced abundantly and this makes the

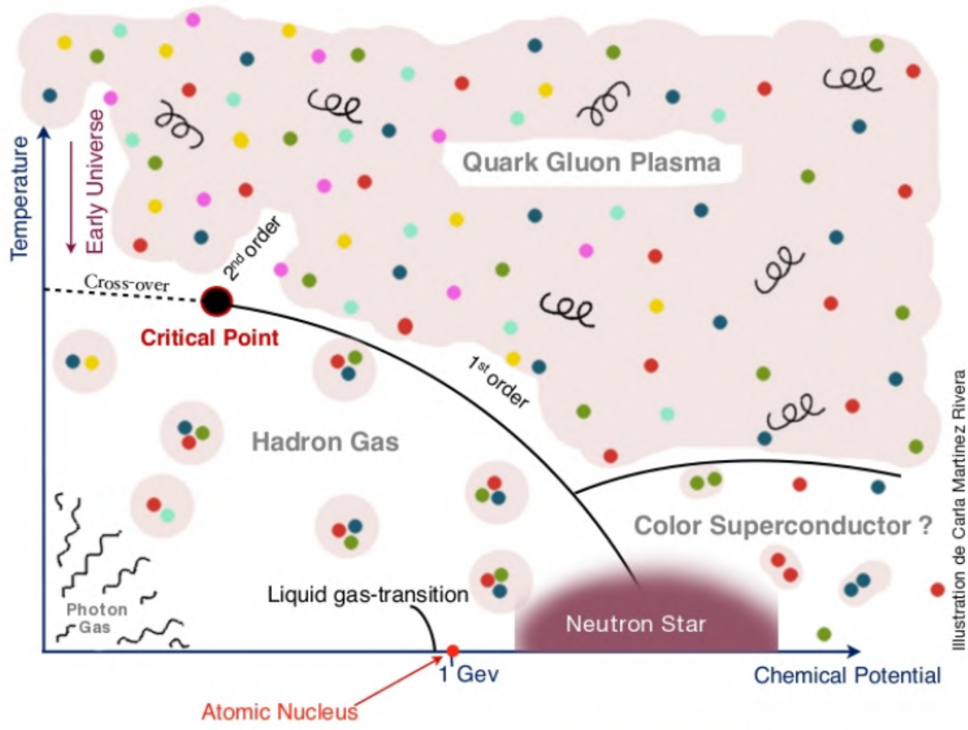

FIGURE 1.21: A schematic of the QCD phase diagram of nuclear matter in terms of the temperature (T) and baryo-chemical potential (μ_B).

baryon density dilute resulting a lower value of μ_B.

The normal nuclear matter sits at the point at very low temperature ($T \sim 0$) and baryo chemical potential of about $\mu_B \sim 1$ MeV. If one moves along the direction of decreasing μ_B, a first order transition is supposed to happen until the QCD critical point is reached. In statistical physics, the phase is defined by the response of the free energy with the temperature. If the first derivative of the free energy is discontinuous with the presence of latent heat, then it is first order phase transition and so on. When the change of phase is continuous i.e., the free energy and its derivatives exhibit continuity, it is called "cross-over" [71]. Beyond the critical end-point, further lowering the value of μ_B with increasing temperature one reaches the cross-over region. The end point of a first order line is a critical point of the second order.This is a very common critical phenomenon in condensed matter physics. All the open region above the phase diagram curve represents the partonic state or the deconfined QGP and the region below the curve represents the hadronic states of matter. If one keeps increasing μ_B beyond the normal nuclear matter, maintaining a low temperature, a state of compressed nuclear matter is formed which exists in cold neutron stars [72]. At ultra-high densities, the color- superconducting quark matter is expected to be found in a color-flavor-locked (CFL) phase [73]. The line separating the CFL phase from the higher temperature disordered phase (QGP) is the most simplified representation of the possible phase structure in this region. This regime is also of particular theoretical interest because analytically controllable calculations are possible, due to asymptotic freedom of QCD [74–78].

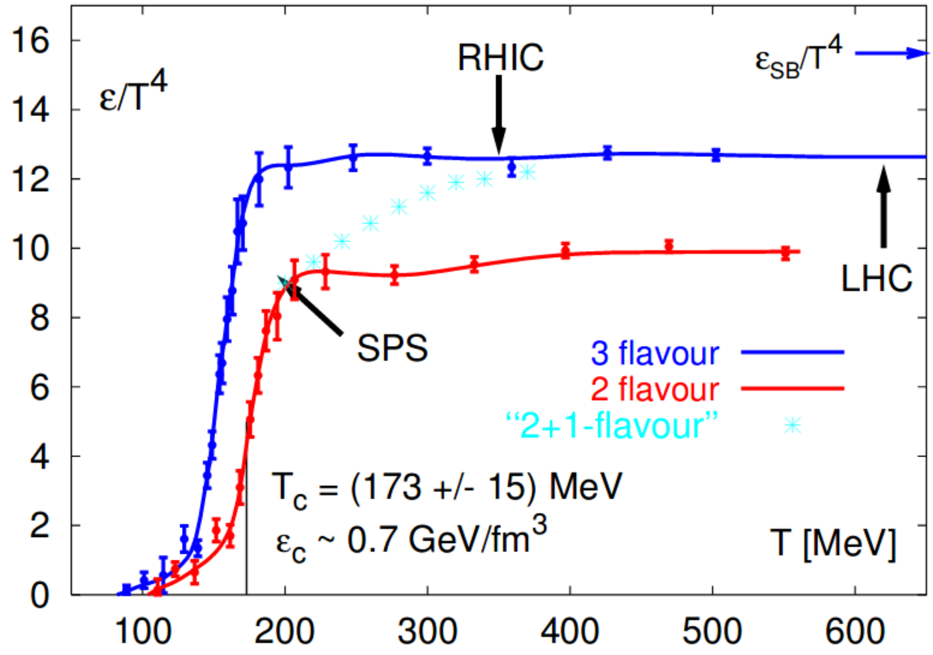

FIGURE 1.22: Dependence of the energy density as a function of the temperature of the hadronic matter at null baryonic potential given by lattice QCD calculations at finite temperature [79].

Since the transition from hadronic matter to deconfined QCD matter occurs in the non-perturbative regime, there is no known way to analytically calculate the transition temperature, T_c or its properties. The lattice QCD calculation has now become a unique tool to test the QCD in the non-perturbative domain: it discretizes space-time, numerically solves the equations of QCD (under certain assumptions, e.g., about the quark masses) and then takes the continuum limit of the lattice spacing $\rightarrow 0$. In particular, it has been used to predict the transition temperature and the nature of the transition in the high T and low μ_B regime. Figure 1.22 shows a calculation of $\frac{\epsilon}{T^4}$ vs T for massless quarks, a transition takes place at $\mu_B = 0$ with the critical temperature, T_c $= 173 \pm$ 15 MeV and the critical energy density, $\epsilon_c = 0.7 \pm 0.3$ GeV/fm^3 [79]. As per the ideal-relativistic gas, the energy density above the critical temperature is proportional to T^4, although the proportionality factor is 20% smaller than the expected value for an ideal gas of gluons and massless u, d and s quarks. $\frac{\epsilon}{T^4}$ is approximately proportional to the number of relativistic degrees of freedom which precisely represents the transition from hadronic degrees of freedom to partonic degrees of freedom. The steepness of the slope of these ratio distributions imply the increase in the number of degrees of freedom when in the deconfined phase. Perturbative calculations at higher temperatures are able to explain the evolution of this factor for $T \geq 2T_c$ [80]. Lattice QCD predictions also state that the high T and low μ_B transition is not a phase transition, but rather a continuous crossover of phases, at which a transition temperature T_c describes a region where the thermodynamic properties of the medium change rapidly. It is prescribed that this becomes a first-order transition at higher μ_B. The lattice QCD is limited to the low μ_B region, the predictions in the higher μ_B and low T region is given by other theories, which actually have calculated that phase transition in this area occur roughly at five times the density of hadronic nuclear matter, $\epsilon_{hadron} \approx \frac{\Lambda_{QCD}}{V_{nucleon}}$.

At this point it is clear from the theoretical calculations that at the temperature of T $\approx$ 170 MeV and energy density of $\approx$ 1 GeV/fm^3, the first-order phase transition occurs, at which the density and temperature of the medium change sharply. Now a relevant question is how did heavy-ion collisions and QGP come together? To produce QGP in laboratory, the first experimental tryouts were with the hadronic collisions. But soon it was realised that the huge amount of energy, required to create QGP, could not be supplied by colliding hadrons with resources available that time. That is when the idea of colliding heavy nuclei came into the project. The origin of the idea came from the never published manuscript by Chapelin and Kerman [81], in March 1978, as mentioned by S. Chin [82] and E. Shuryak [61]. The contents of the manuscript was qualitative and the authors did not pursue it. Though a year later Chin and Kerman presented the idea of cold drops of quark matter containing a large strangeness content (called *strangelets*) [83] which fed the BNL-AGS program with the resources for many years. A few years later, Chapelin suggested the possibility of "warm" high baryon density quark matter being produced in relativistic heavy-ion collisions which the then running experiments did not confirm.

1.4 Relativistic heavy-ion collisions and QGP

1.4.1 Experimental programs and facilities

During the early 1970s, the Lawrence Berkeley Laboratory (LBL, now LBNL- Lawrence Berkeley National Laboratory) was the pioneer in the field of heavy-ion physics with the Bevalac program which used to provide heavy-ion beam for fixed target experiments. At that time the experiments at the Bevalac confined their interest to produce and study the ultra dense matter proposed by Lee and Wick [84]. With the inclusion of QGP in the menu, soon the importance of the heavy-ion collisions program reached sky high and collisions with at-least 10 times larger centre of mass energy than the available Berkeley Bevalac was attempted at CERN with the Intersecting Storage Rings (ISR) by Howel Pugh in 1975. The ISR was a proton-proton collider and its design allowed it to accelerate nuclear beams at about 30 GeV per nucleon pair for light nuclei and about 12 GeV for the typical case for the heavier ones (Au, Pb, U). But due to the unavailability of appropriate heavy-ion source at CERN facility at that time, the ISR program was limited to alpha beams only.

In 1979 Howel Pugh attempted to increase the energy of the heavy-ion beam needed to produce QGP at the Bevalac, LBL. In the next year he proposed VENUS (Variable Energy Nuclear Synchrotron), which envisioned a large synchrotron plus stretcher ring. It was never approved but paved the way for the concept of the future Relativistic Heavy Ion Collider (RHIC). He also proposed TEVALAC, a fixed target program which would increase the energy of Bevalac, but failed to gain approval and he then turned his attention to a concept of "mini-collider" which would take the ion beam from the Bevalac and collide them in a circular ring. It was the stepping stone for the future projects at RHIC and Large Hadron Collider (LHC). By this time the program at CERN also moved forward. After ISR, a heavy-ion program was undertaken which could provide nuclear beams at 20 GeV energy and the *super proton Synchrotron* was born. At the Brookhaven National Laboratory (BNL), a fresh heavy-ion programme was planned and a heavy-ion beam line was planned through the already existing Alternating Gradient Synchrotron (AGS) which was later included in the RHIC.

It was not only the accelerator but the technologies of the detectors were also in need of up-gradation to bring success to the heavy-ion programmes. That is when Howel Pugh proposed using a *time projection chamber* (TPC) detector, introduced by David Nygren of LBL in 1974, in the heavy-ion programmes for the Bevalac experiments and it was a new and revolutionary idea that time. The first inclusion of the TPC in the Bevalac was in 1991 and it was called the EOS TPC that time. The EOS TPC opened a totally new way of analyzing data and was a precursor for the future CERN SPS-NA49 TPC, BNL RHIC-STAR TPC and CERN LHC-ALICE TPC and it was the preeminent legacy of Howel Pugh in the field of relativistic heavy ion physics. During that time (1986-1993) CERN SPS conducted many experiments like NA35, NA36, WA80 etc. SPS started with Oxygen and Sulfur beams and soon it was found that they were not massive enough to assure QGP formation. In 1994, an injector complex for lead ions was commissioned and a totally new experiment with TPC, NA49, was built. In parallel, there were discussions on the future high energy collider experiments at BNL and at CERN with a huge jump in the energy reach from the existing facilities. Finally, in 2000 the RHIC started with four heavy-ion experiments: PHENIX, STAR, PHOBOS, and BRAHMS with a maximum attainable energy of 200 GeV/nucleon. In 1993, a dedicated heavy-ion program was proposed the upcoming LHC at CERN and in 2009 ALICE started taking data. LHC was designed to provide heavy-ion beam at maximum 5.5 TeV centre of mass energy. Table 1.1 summarizes the heavy-ion programs from the time of AGS to that of LHC.

TABLE 1.1: Summary of the heavy-ion experimental facilities.

Facility	Program starting year	Type	Housed by	System	$\sqrt{s_{NN}}$ in GeV/A
AGS	1986	Fixed target	BNL	^{28}Si+^{197}Au	5
SPS	1986	Fixed target	CERN	$^{32}S+^{208}Pb$ $^{16}O+^{208}Pb$	19
AGS	1992	Fixed target	BNL	$^{197}Au+^{197}Au$	5
SPS	1994	Fixed target	CERN	$^{208}Pb+^{208}Pb$	17
RHIC	2000	Collider	BNL	$^{197}Au+^{197}Au$	200
LHC	2008	Collider	CERN	$^{208}Pb+^{208}Pb$	5500
SIS100	–	Fixed target	FAIR	$^{197}Au+^{197}Au$	2.3-9.3

Looking at this table and recalling our previous knowledge of the QCD phase diagram, one can say the LHC produces high T and low μ_B QCD matter, whereas RHIC produces high T and somewhat higher μ_B QCD matter. In particular, the QCD medium should be thought of (approximately) as having a given T and μ_B at each point in space and time. Complementary to the experiments at RHIC and LHC, where μ_B is in the lower side of the axis, a new scientific interest has grown to study the equation of state of highly compressed baryon rich matter (high μ_B). In the highly compressed "cold" matter, as it may exist in the neutron stars, the baryons deconfine into quarks and gluons (though at zero temperature gluons are either virtual or in a condensate). The critical density where this transition takes place is not known and for the entire high density (high μ_B) area of the phase diagram. At very high densities and low temperatures, beyond the deconfinement transition, a new but experimentally unexplored phase is expected where the quarks are correlated and form a color superconductor.

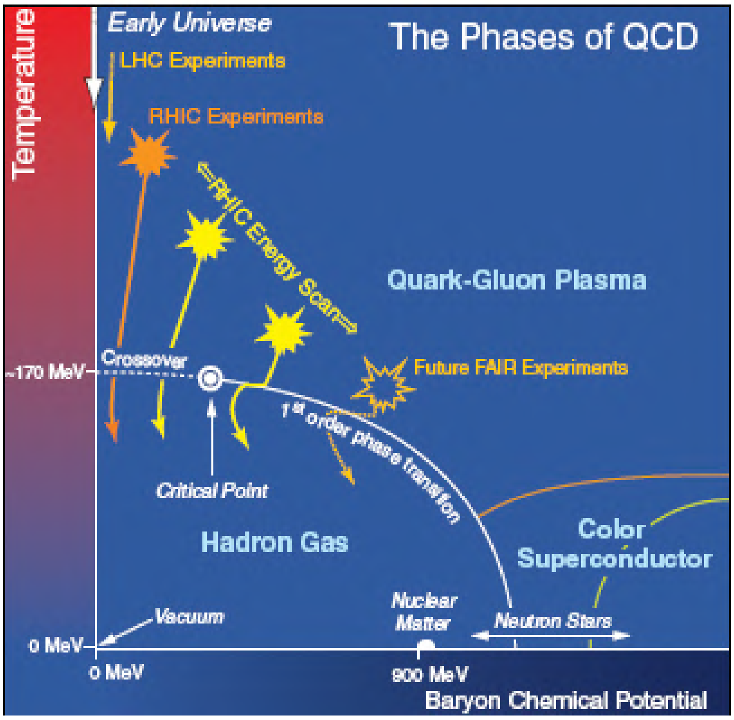

FIGURE 1.23: The schematic of the QCD phase diagram, as covered by the experiments.

Keeping these in mind, the Facility for Antiproton and Ion Research (FAIR) facility at GSI is focusing on hadrons in compressed baryonic matter in the upcoming CBM experiment. A project called Nuclotron-based Ion Collider Facility (NICA) has been taken up in Russia which will study baryon rich systems in a fixed target experiment BMN and in an ion collider experiment MPD. The heavy-ion collisions at FAIR and NICA energies permit the exploration of the ı*terra incognita*ȷ of the QCD phase diagram in the region of high baryon densities. The QCD phase diagram populated by the experimental reach (both existing and futuristic) is shown in Figure 1.23.

The next sub-section tells about how finally QGP was produced using these facilities and experiments after thorough learning from the precursor and implementing those in the successor experiments.

1.4.2 Discovery and production of QGP

After the QCD prediction of the QGP, scientists had prescribed many signatures of this novel state to probe the same, over the years. In the next to next subsection few of them has been described briefly. Conceiving various heavy-ion programs to produce and study this new state of matter, scientists had designed experiments concentrating on certain channels to probe the medium, if produced.

During 1978 to 1981, Hans Gutbrod designed the "plastic ball" experiment at the Bevalac which was equipped with the first electronic detector in relativistic nuclear physics with 4π coverage and particle identification privileges. During 1982-1984, Bevalac accelerated Niobium and later Gold ions at energies starting from 200 MeV to 1 GeV per nucleon. Two nuclear matter flow phenomena in the emission pattern of these collisions were observed: the "$side - splash$" and the "$squeeze - out$". These discoveries for the first time gave evidence for collective phenomena in relativistic heavy ion collisions, which could not be explained by standard nucleon-nucleon cascades in the collisions. Now these phenomena are called the *directed flow* ($v1$) and *elliptic flow* ($v2$). SPS accelerated Oxygen ions in 1986 and the next year Sulphur ions which were used in six experiments to identify the production of QGP through different channels: (a) NA35, NA36 and WA85 looked for the Rafelski's prescribed *strangeness enhancement*, (b) WA80 took on to measure high temperature via direct photon spectroscopy, (c) NA38 set out to measure the J/ψ particle and (d) NA34 addressed spectra of dileptons.

All the experiments had to suffer the limitation of the technology and also the analysis prescriptions which got into shape after years of polishing. But they did confirm some of the ideas conclusively. The chemical composition of the hadrons emitted from the collisions was well described by a gas near chemical equilibrium gas at a temperature close to T_c and a varying baryon chemical potential with the collision energy [85]. The strong enhancement of baryons and anti-baryons containing multiple strange quarks [86, 87] could only be explained if hadrons containing valence quarks of all three light flavors were "born" into thermal abundances [88–90]. However, the programs at SPS also failed to provide other corroborating evidences to probe the production of a thermal phase of matter at temperatures above T_c. CERN announced the assessment of the SPS program in 2000 [91, 92] but it was not published. The necessity of heavy-ion experiments at much higher energies were felt to resolve the ambiguity.

The RHIC on the other hand, with its experimental programmes in 2000, opened the gate to a new kinematic domain in which the produced matter got nearly boost invariant longitudinal flow (first discussed in 1975 [93])from the beginning due to the interactions of the partons inside the colliding nuclei predicted earlier [94]. Bjorken analytically solved this initial conditions [95] which provided the basis for a systematic investigation of the collective properties of the matter produced in the collisions [96–99]. The expanding matter was found to have extraordinarily low shear viscosity, relative to its entropy density [100–103] and thus the matter was found to be a liquid at temperatures well above T_c. A detailed study of the subtle variations of the flow profile between different hadron species revealed that these variations disappeared when all hadrons were assumed to be formed by recombination of deconfined, collectively flowing quarks when the matter cooled below T_c [104, 105]. Together these observations provided strong evidence that the matter formed at RHIC is indeed a plasma of deconfined quarks and gluons which behaves as a nearly inviscid liquid that decays by the emission of hadrons in chemical and thermal equilibrium. To check the threshold, down at which no QGP could be formed and to answer many questions about the critical point or to passively confirm if SPS had it or not, the RHIC took up its *beam energy scan* (*BES*) program in which heavy-ion beams were collided at a centre of mass energy down to 7.7 GeV. The critical assessment of the BES program is summarised in [106, 107]. It was found that the matter produced at the top SPS energy $\sqrt{s_{NN}} = 19.6$ GeV, had some properties similar with that produced at the top RHIC energy, $\sqrt{s_{NN}} = 200$ GeV.

With the availability of unprecedented energy at the LHC, it was confirmed that the nature of the produced QCD matter above T_c is of a strongly coupled system of liquid quark gluon plasma [108]. It was found that the average strong coupling constant, α_s, is slightly weaker in the higher energy density domain at the LHC than at RHIC [109]. This is in accordance with the running of α_s with temperature and it is also reflected in a somewhat larger shear viscosity-to-entropy, η/s, ratio [110]. Officially, RHIC claimed to have created deconfined matter in 2010 at 4×10^{12} K and LHC claimed in 2012 at 5.5×10^{12} K.

The next sub-section tells us about what happens in a heavy-ion collision, what are the intermediate steps to QGP production and how the produced medium evolves with time.

1.4.3 Evolution of relativistic heavy-ion collisions

In 1983, Bjorken imagined a scenario where the QGP would be efficiently formed and described the possible initial energy density and its evolution with time [95]. One of the scenario was that the beam energy, E_b, should be larger than $\sim$ 250 GeV, implying an available energy in the centre of mass larger than 25 GeV per nucleon pair and it was also prescribed in this scenario that QGP would be formed at baryonic potential close to zero. The Bjorken picture is discussed here to have some idea about what happens in the relativistic heavy-ion collision.

At ultra-relativistic energies, nuclei are seen as discs in the center-of-mass system, due to the Lorentz contraction. The crossing time of the nuclei taking part in the collision, can be estimated as

$$\tau_{cross} = \frac{2R}{\gamma} \tag{1.21}$$

where R is nuclear radius and γ is the Lorentz factor. Bjorken assumed the following hypothesis in postulating the QGP evolution scenario:

- τ_{cross} is smaller than the strong interaction time scale, $\tau_{strong} \sim 1/\Lambda_{QCD} \sim$ 1 fm/c. in nucleus-nucleus collision, τ_{cross} is higher than τ_{strong} only if $\gamma < 12$ which is attained when the centre of mass energy is $>$ 25 GeV (and for fixed target experiment, $E_f > 250$ GeV). RHIC and LHC actually has validated the value of γ to be 100 and 1376, respectively.

- The particle multiplicity is uniform in rapidity. This condition implements a rapidity symmetry in the system, allowing to create a uniform energy density in different rapidity slices. This hypothesis was also verified partially by the experiments [95, 111, 112].

Now let us consider the volume centred in the nucleus crossing plane at a time τ after the nuclei crossing to have a cylindrical shape with thickness $2\Delta d$ along the direction of the beam axis and having a radius $R \approx 1.124A^{1/3}$, where Δd is the longitudinal thickness. The particles produced with a speed below $\beta_z \leq \Delta d/\tau$ along the beam axis, will be contained within this volume. As in the limit of rapidity $y \rightarrow 0$, $\beta_z = tanh(y) \approx y$ the rapidity range Δy around $y = 0$ is given by,

$$\Delta y = \frac{2\Delta d}{\tau} \tag{1.22}$$

and the total energy contained within the volume considered is

$$E = |\frac{dE}{dy}|_{y=0} \times \frac{2\Delta d}{\tau} \tag{1.23}$$

For other rapidity domain, the previous expression is generalised and the total energy E is replaced by the transverse energy E_T and finally the energy density in the volume is calculated as:

$$\epsilon(y) = |\frac{dE_T}{dy}|_{y=0} \times \frac{1}{\pi R^2 \tau} \tag{1.24}$$

This expression connects the energy density to the transverse energy produced per unit rapidity.

- ***Initial state and medium formation:*** The initial energy density can then be estimated assuming the time scale needed for the production of particles, as $\tau_{form} \sim \tau_{strong} \sim 1fm/c$. Bjorken actually estimated that initial energy density to be 2-20 GeV/fm^3 for the Sp$\bar{p}$S collider at CERN that was able to deliver ion beam at $\sqrt{s_{NN}} \sim 500$ GeV per nucleon pair. This estimation was well above than the critical energy density for production of QGP. The matter is created in the full

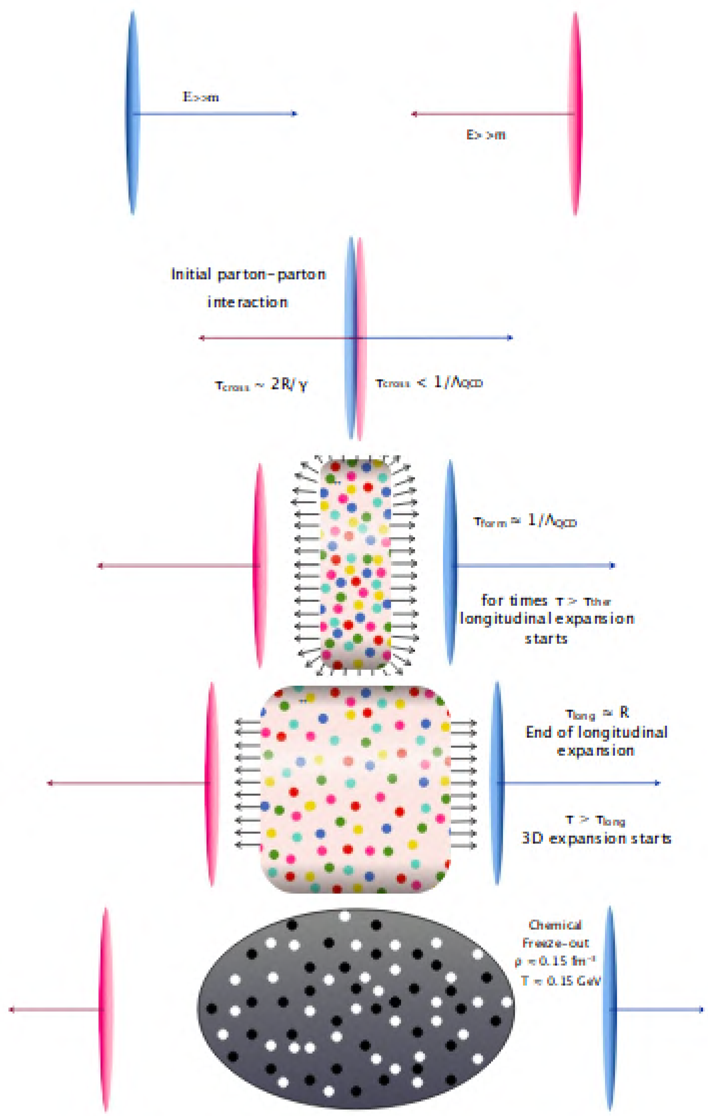

FIGURE 1.24: The Bjorken scenario of the hot QCD matter production and the stages of its evolution.

rapidity range where the particle density is high enough to reach equilibrium and it was found that for RHIC it is about 5 and for LHC it is about 8 units of rapidity. In Figure 1.24 hot nuclear matter production at mid-rapidity is presented with evolution and Figure 1.25 presents space-time $(z-t)$ diagram of the evolution.

The initial conditions are found to be well explained by the viscous hydrodynamics and there are two models which produces significantly good explanations: *Glauber* model and *color glass condensate* (*CGC*) model. There exist different implementations of initial conditions for the evolution, like Optical Glauber for Glauber models [113], IP-Glasma [114] for CGC or others such as Trento [115].

- ***Thermalization:*** If one assumes an average energy, $\langle E\rangle = 500$ MeV, then at this energy density ϵ, $\epsilon/\langle E\rangle \sim$ 8-60 particles per fm^3 could be produced and those particles are supposed to be interacting within the volume. Assuming the interaction cross-section $\sim$ 10 mb, the average path length, λ inside the volume can be estimated as, $\lambda \sim$ 0.02-0.12 fm. One could hope that this might lead to thermalization at a time $\tau = \tau_{thermal}$. This phenomenon has been validated through experimental results but existing theory is not able to yet explain it. In principle, the initial state of the nucleus-nucleus collision is imagined as the interaction of two high-density gluon clouds. In this respect QCD theory in classical limit is supposed to be the best theoretical tool. The typical Bjorken's "x" (fraction of momentum carried by the parton) for two gluon cloud is $\langle x\rangle \sim 10^{-2}$ at RHIC and $\langle x\rangle \sim 10^{-3}$ at the LHC.

- ***Longitudinal expansion:*** At time $\tau \sim \tau_{thermal}$, the produced medium follows relativistic hydrodynamics and evolves like fluid. Due to the larger pressure gradient along the beam direction than in the transverse plane, a longitudinal expansion takes place. As per Bjorken's prescribed hydrodynamic law,

$$\frac{d\epsilon}{d\tau} = -\frac{\epsilon + p}{\tau} \tag{1.25}$$

the energy density in this case evolves as $\epsilon \sim 1/\tau^n$ with $1 \leq n; \leq 4/3$ as in the ultra relativistic limit the ideal gas shows $\epsilon = 3p$ and thus $n = 4/3$. The longitudinal expansion stays as a good approximation for $\tau \leq \tau_{long} \sim R$.

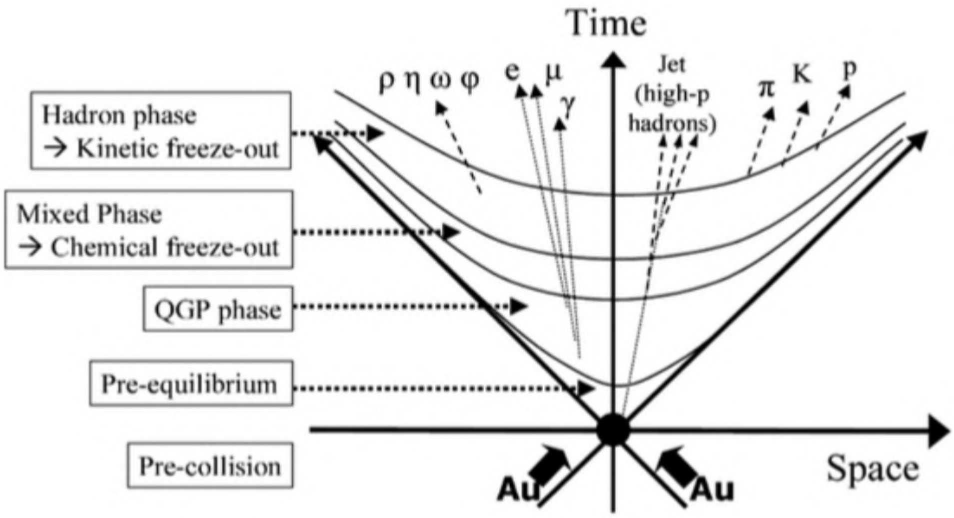

FIGURE 1.25: The different stages of evolution of relativistic heavy-ion collision in space-time. Figure courtesy: V.D. Kekelidze.

- ***3D expansion and freeze-out phase:*** For time $\tau \geq \tau_{long}$, the system will evolve in 3 dimensional expansion until the stage of $freeze-out$ is reached. In $freeze-out$, particle density is very low so as the temperature due to the expansion and successive cooling of the system. Thus the particles are assumed to be non-interacting, they travel in vacuum, can decay and finally reach the detector. It will be worth mentioning that elastic cross-section is larger than the inelastic one and one can expect to observe two $freeze-out$ stages: *chemical* and *kinetic*. The stage when the inelastic collisions between the constituent hadrons of the system stop and the particle abundances get fixed, is called the $chemical\ freeze-out$ phase. The stage when the quasi-elastic collisions between the hadrons cease, is called the $kinetic\ freeze-out$ phase. Naively, the $freeze-out$ is reached once the average path length of particles is similar to the size of the system, $\lambda \sim R$. Keeping in mind our assumption of taking the interaction cross-section as 10 mb, one gets 0.15 particles per fm^3 which corresponds to the energy density,

$$\epsilon_{freeze} \sim 0.15 \text{ fm}^3 \times 0.5 \text{ GeV} \sim 0.075 \text{ GeV/fm}^3 \tag{1.26}$$

This value suggests that $freeze-out$ is expected in the hadron gas phase. Calculation shows, for a $freeze-out$ temperature, $\tau_{freeze} = 150$ MeV, one gets $\epsilon/T^4 \sim$ 1.2 - this value fits very well with the QCD predictive calculation of Figure 1.22.

There are dedicated packages to solve the numerical equations that arise from this phase i.e., the hydrodynamic evolution and some of them are MUSIC [116], iEBE-VISHNU [117], and CLVisc[118]. One alternative model to hydrodynamic expansion is that of transport model. These are microscopic models which describe the evolution of partons throughout the expansion, and unlike hydrodynamics are able to describe non-equilibrium dynamics. Common transport models are AMPT [119] and BAMPS [120].

Before moving to the next sub-section, it will be worthwhile to describe the concept of *centrality* in heavy-ion collisions here. In relativistic heavy-ion collisions, initially two partons from the colliding nuclei undergo hard scattering i.e., a large momentum transfer between them takes place. But the momentum transfer between them is controlled by how the two nuclei collide. It is defined by the *impact parameter* (b) which is the perpendicular distance between the centres of the colliding nuclei as shown in Figure 1.26.

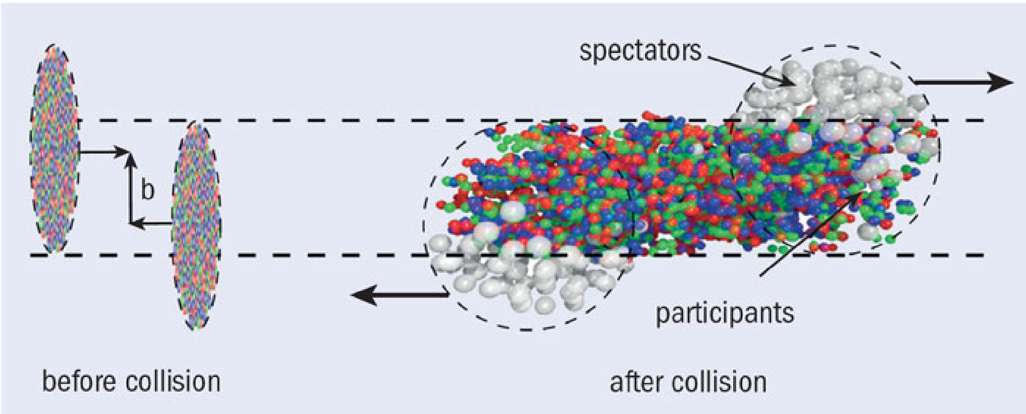

FIGURE 1.26: Schematic diagram for centrality determination through calculating impact parameter and the spectators. Figure taken from [121].

When a collision happens with $b \to 0$ i.e., the nuclei collide head-on, then the collision is called a *central* one whereas the collision in which $b \sim 2R$, is termed as a *peripheral* one. It is difficult to measure the impact parameter directly in the experiment though and thus the concept of "participants" and "spectators" were prescribed in the collisions for that. The nucleons that participate in the collisions are identified as the *participants* and the ones that do not take part are called the *spectators*. For a central collision, number of participants is large with respect to that for a peripheral collision.

Until now we have gathered the knowledge that heavy-ion collisions with critically high energy can produce QGP. In the last subsection, we have also seen how the heavy-ion collisions evolve with time. In a heavy-ion collision that produces quark-gluon plasma, the deconfined phase is populated for only a short time (10 fm/c), before expanding and cooling back to the hadronic phase. For this there is no way it can be "caught red-handed" directly but with probes that are sensitive to the medium formation and carry the medium information one is able to know its presence. This is the most important stage of the whole journey, to probe if there is any medium produced and characterise it. In the next sub-section we will learn about few of the prescribed signatures to probe the QGP medium formation.

1.4.4 Experimental signatures to probe the produced QGP

Over the years, physicists have prescribed many observable to probe QGP medium indirectly as there is no way one can directly probe the medium due to its extreme short lifetime $\sim 10^{-23}$ s. Some of the most important signatures are listed below:

- Estimation of energy density of the medium [95]
- Collective phenomena:
  - Identified particle spectra and particle ratio [122–125]
  - Anistropic flow [126]
  - Multiplicity dependence of particle production [127]
- Enhanced production of strange baryons [128–133]
- J/ψ suppression [134, 135]
- Jet quenching [136]

Description of all the signatures is beyond the scope of this thesis and therefore only four of them: flow, strangeness enhancement, J/ψ suppression and jet quenching will be discussed briefly in this sub-section. It would also be appropriate to mention at this point that this thesis covers the jet quenching phenomenon in more specific and detailed way.

1.4.4.1 Flow

In mid-central heavy-ion collisions, an oblong volume of QCD matter is produced by the overlap region of the colliding nuclei and the produced volume expands mainly in the direction of the steepest pressure gradient as shown in Figure 1.27. The medium is supposed to expand not only radially but also in the plane transverse to the major axis of the volume, containing the impact parameter and beam axis. This rapid expansion near this "reaction plane" enhances the p_T of the particles in the region implying the translation of the initial spatial anisotropy of the collision geometry into a final-state momentum anisotropy. As the p_T spectrum steeply falls, an enhancement in the momentum means that for a particular p_T this will be reflected in the enhancement of particle yields which in turn will enhance the back-to-back particle detection in the azimuth (ϕ). This type of anisotropy in the azimuth is called the *elliptic flow*. This anisotropy is expected to be the largest for the most peripheral collisions and is expected to be present at low p_T region where particles thermalize and produce the bulk of the medium.

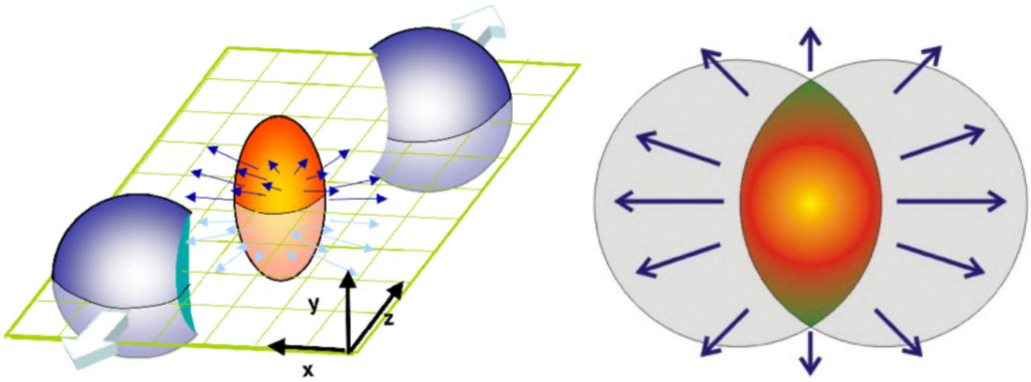

FIGURE 1.27: Two incident nuclei partially overlap, creating an "almond"-shaped collision region, which then expands and generates elliptic flow. Figure taken from [137].

This effect is measured experimentally by constructing azimuthal distribution of particles relative to the reaction plane. One can get the following expression if this distribution is expanded in Fourier expansion along ϕ:

$$E\frac{d^3N}{dp^3} = \frac{1}{2\pi}\frac{d^2N}{p_T dp_T dy}\left[1 + 2\sum_{n=1}^{\infty} v_n cos\left(n[\phi - \Psi_n]\right)\right] \tag{1.27}$$

where $\phi - \Psi_n$ is the azimuthal angle relative to the nth order reaction plane, v_n and

n represent the magnitude and direction of the nth order harmonic respectively. The *sine* term vanishes in the expansion due to the symmetry with respect to the reaction plane. By modeling the initial state and hydrodynamic evolution of the medium, one can calculate the magnitude of v_n in a given system by averaging the angular difference over the particles, summed over all events in the (p_T, y) bin of interest. Each harmonic corresponds to the shape of the flow, like v_1 corresponds to the *directed flow*, v_2 denotes the *elliptic flow*, v_3 corresponds to the *triangular flow* and so on. There have been a lot of experimental efforts dedicated to the measurement of these coefficients from RHIC to LHC energies and some of them can be found here [138–141].

1.4.4.2 Strangeness enhancement

The nuclei that are collided contain only u and d quarks and since valence strange quarks are not present in the nucleons, therefore the production of strange particles out of the medium provides information about the reaction dynamics in partonic and hadronic phase. In the equilibrated QGP medium (both thermally and chemically), the u and d quarks are almost filled up to the *Fermi level*, and Pauli's principle states that the creation of additional $u\bar{u}$ or $u\bar{d}$ pair would cost $2E_F$ (E_F being the *Fermi energy* of the light quarks) from the system. At the same time, due to the chiral symmetry restoration, $s\bar{s}$ could be produced with the expense of maximum energy $\sim\ 2m_s\ \sim 300$ MeV.

Now in purely hot hadronic medium, the production probability is suppressed for strange particles due to their higher mass in comparison to particles with u and d quarks. The dominant channels for the creation of strange hadrons are:

$$N + N \rightarrow N + \Lambda + K \quad \text{and} \quad \pi + \pi \rightarrow K + \bar{K} \tag{1.28}$$

with Q values $\sim$ 670 and 700 MeV respectively which are larger than the threshold value for strange-antistrange pair production. Whereas in the QGP medium, production of strange-antistrange pair production predominantly takes place through the following two channels:

$$q + \bar{q} \rightarrow X + \bar{X} \quad \text{and} \quad g + \bar{g} \rightarrow X + \bar{X} \tag{1.29}$$

The first one is through the collisions of light quark-antiquark, q represents u or d and X

denotes a moderate or heavy quarks like c or s whereas the second one is gluon fusion. The masses of deconfined s and $\bar{s}$ are found to be around 350 MeV, which is less than the mass when those are confined within hadrons. Hence, in the deconfined medium the production of strangeness should be enhanced as the mass goes down to a value comparable with $T_c \sim 170$ MeV. This leads to an increased number of strange hadrons once the plasma cools down and hadronizes.

1.4.4.3 J/ψ suppression

Quarkonia are bound states between two heavy quarks $Q\bar{Q}$: $c\bar{c}$ for the family of η_c, J/ψ, $\psi(2S)$, χ_c etc and $b\bar{b}$ for the family of Υ's and χ_c. Generally, the vacuum spectrum of quarkonia states can be described via non relativistic models by describing a interaction potential like,

$$V(r) \;=\; \sigma r \;-\; \frac{\alpha}{r} \tag{1.30}$$

where σ is the string tension between $Q\bar{Q}$ and α is a Coulomb-like constant. For simplicity if one chooses a Coulombian potential, then σ vanishes. Now if $Q\bar{Q}$ is within a QGP medium, the interaction potential between $Q\bar{Q}$ will be affected by the available free color charges and this phenomena is called the screening of the potential. That is why the potential for this colored plasma is needed to be replaced with a potential with a screening constant:

$$V(r) \;=\; -\frac{\alpha}{r} \times e^{-r/\lambda_D} \tag{1.31}$$

where λ_D is the Debye screening length or radius. If one tries to write the average distance between the heavy quarks in quarkonia, say for J/ψ, using the Bohr radius expression, then one gets,

$$r_B \;=\; \frac{1}{\alpha m_Q} \tag{1.32}$$

and as a numerical exercise, if one considers J/ψ, $m_c = 1250$ GeV and $\alpha(m_c) = 0.36$ [142] then $r_B = 0.44$ fm. Similarly considering $\Upsilon(1S)$, $m_b = 4200$ GeV and $\alpha(m_b) = 0.22$ then one can get $r_B = 0.22$. For the case $r_B \ll \lambda_D$, the bound states exhibit same properties as in the vacuum. But when $r_B \geq \lambda_D$, the medium affects the quarkonium state, leaving it unstable and thus it could melt in the medium. Taking the dependence of the Debye length as in the electromagnetic plasma [143], λ_D for a plasma with temperature

T and charge density ρ could be written as,

$$\lambda_D = \sqrt{\frac{T}{8\pi\alpha(T)\rho}} \tag{1.33}$$

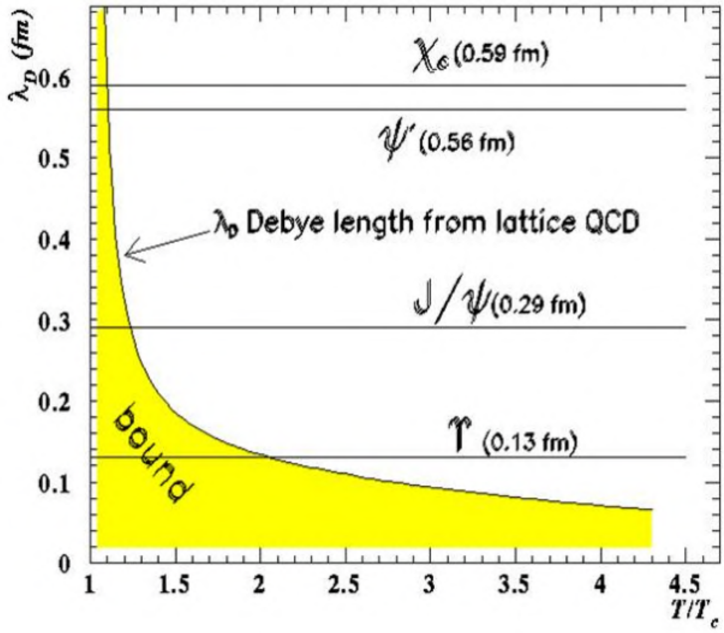

FIGURE 1.28: Debye radius as a function of T/Tc. The lines correspond to the critical Debye radius for different quarkonia states. Figure taken from slides prepared by Marzia Rosati, Iowa State University.

For QGP, taking $\rho \approx T^3$, one could get

$$\lambda_D \sim \frac{1}{T}\sqrt{\frac{1}{8\pi\alpha(T)}} \tag{1.34}$$

and rewriting the above equation, one can get T_D:

$$T_D \sim \frac{1}{\sqrt{8\pi\alpha(T)r_B}} \tag{1.35}$$

and this is temperature above which a quarkonia state could melt. Taking $\alpha(T) \sim 0.2$, for J/ψ one can get $T_D \sim 200$ MeV ($1.3T_c$) and for $\Upsilon(1S)$, $T_D \sim 400$ MeV ($2.6T_c$). Figure 1.28 shows different Debye radius for different quarkonia states.

1.4.4.4 High p_T suppression: jet quenching

Jet is the collimated spray of hadrons produced from a hard scattered parton, after its fragmentation and hadronization. When the jets propagate through the hot and dense medium produced in the relativistic nuclear collisions, they not only undergo interactions with the medium constituents but also experience gluon radiation and suffer loss of energy. As a result of this, the hadrons resulting from the hadronization of the hard parton contain lower energy or even disappear. This phenomenon is called ı*jet quenching*ȷ as shown in Figure 1.29. QCD predicts that high energy partons will lose energy via

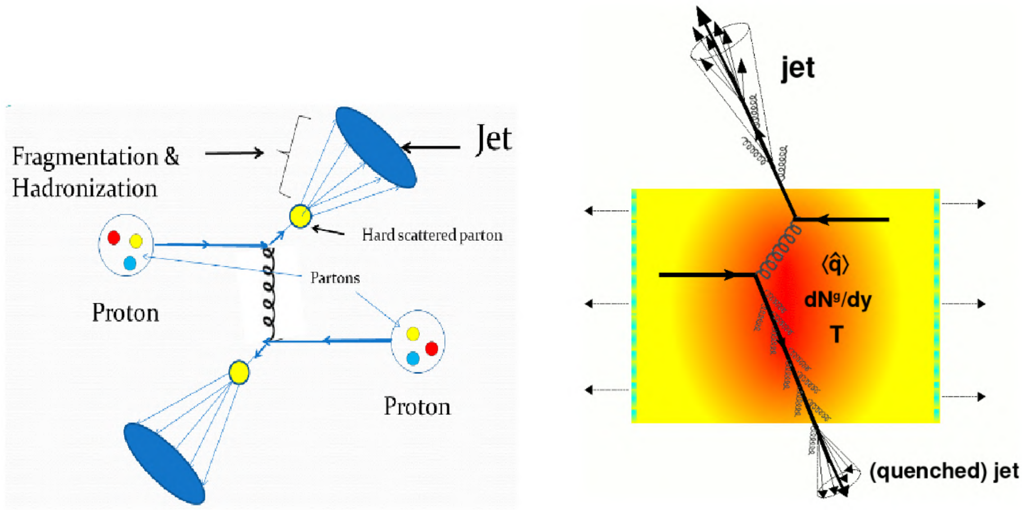

FIGURE 1.29: Illustrations of: jet production in pp collision (left) and jet quenching in heavy-ion collision (right).

gluon radiation when travelling through the QGP. The order of magnitude of the parton energy-loss in QGP would be about $\Delta E \sim 1$ GeV/fm and it is expected to be proportional to the gluon density and also on the path traversed inside the medium. If one takes the thickness of the medium to be 1-3 fm, then ΔE could be expressed as [144, 145]

$$\Delta E \sim \alpha_s \times C_R \, \hat{q}(\rho_g) \times L^2 \tag{1.36}$$

where C_R is the color charge factor, $\hat{q}$ is the transport coefficient which depends on the gluon density ρ_g and L is the thickness of the medium. The energy loss also depends on the flavor of the parton:

- Gluons will exhibit larger energy-loss per unit of length than that of quarks. A relative factor 9/4 due to the color charge, is associated to the *gluonsstrahlung* mechanism from a gluon with respect to that from a quark [146, 147].

- Heavy quarks are expected to lose less energy than light quarks, due to the absence of gluon radiation at forward angles and this phenomenon is known as the $dead - cone\ effect$ [147].

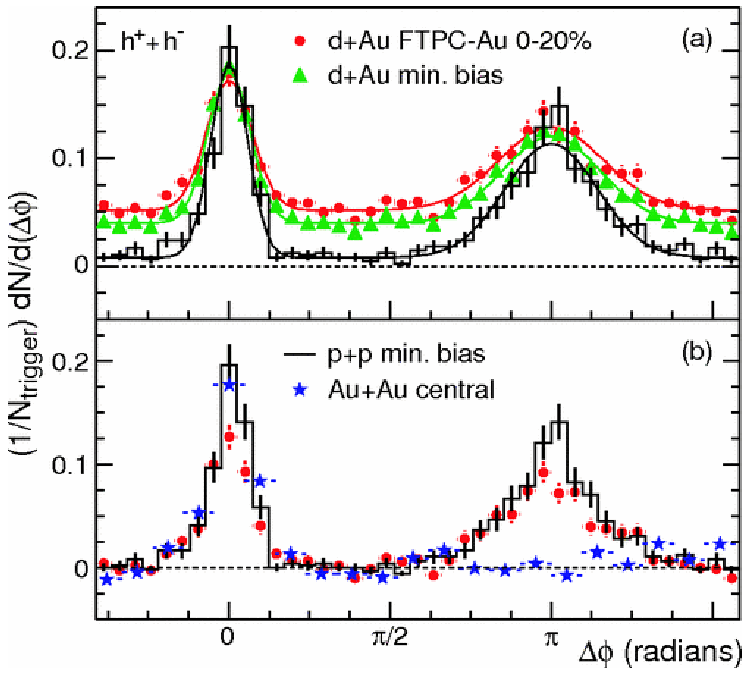

FIGURE 1.30: Quenching of away side jet as seen by the STAR experiment in Au-Au collisions [148]

Figure 1.30 presents jet quenching phenomenon measured by STAR experiment and more on this topic has been described in Chapter 3.

1.5 pp collisions in this scenario

As described in the subsection of pQCD, pp collision provides the testing ground for various pQCD calculations. Especially, it provides validation for the cross-section prediction from pQCD and based on the agreement, the theoretical models are tuned. Moreover, while studying heavy-ion collisions, the pp collisions measurement are taken as the baseline reference to extract various signals of QGP production. The pp collisions are expected to be the elementary collisions in which no medium supposedly can form [149].

Therefore measurements in heavy-ion collisions are compared to pp measurements to find out deviations from the vacuum measurement and thus probing the medium formation.

1.6 Organization of the thesis

This thesis is organized as follows:

Chapter 1 gives the formal introduction of the field. It consists of historical introduction of particle physics, a brief description of QCD, Prediction of QGP by QCD and finally the discovery of it through heavy-ion collisions study.

In Chapter 2, the LHC and the ALICE experiment have been described with brief description of all the detectors and analysis tools and scheme.

Chapter 3 introduces the field of work for this thesis i.e., jet. The evolution of jet starting from a simple pp collision and then the energy loss in dense partonic medium has also been described in this chapter. Different methods of jet reconstruction have been discussed here.

Chapter 4 presents the analysis of ALICE pp data at $\sqrt{s}$ = 2.76 TeV. It describes all the intermediate steps, such as correction of the data for the detector effects, subtraction of the background and evaluation of systematic uncertainties, to reach the final result. Comparison with theoretical models and with measurements at higher energy has also been presented with the final result.

In Chapter 5, measurements of inclusive and intra-jet properties measurement with a model, JEWEL, has been presented. This chapter also introduces the JEWEL.

Chapter 6 is the summary of this thesis.

There are three appendices in this thesis. Appendix A presents quality assurance study of PMD data to clean up the data and normalize it in order to provide it to the analyzer. All the techniques undertaken regarding the QA study with brief description of PMD itself has been presented here. This task was assigned to me as the thesis service work for ALICE.

Appendix B describes general purpose Monte Carlo event generators. It describes few features of the event generators used in the thesis work: PYTHIA, HERWIG and PHOJET.

Appendix C shows some photographs regarding the dismantling of PMD from ALICE in December 2018.

Bibliography

[1] J.J. Thomson, Philosophical Magazine, 44, 293 (1897)

[2] P. Dirac, Proc. Roy. Soc. Lond. A 117, 610 (1928)

[3] C. Anderson, Phys. Rev. 43, 491 (1933)

[4] J. Chadwick, Nature 129, 312 (1932)

[5] S. Neddermeyer and C. Anderson, Phys. Rev. 51, 884 (1937)

[6] H. Yukawa, I. Proc. Phys. Math. Soc. Jap. 17, 48 (1935)

[7] C. Lattes, G. Occhialini and C. Powell, Nature 160, 453 (1947)

[8] C. Lattes, G. Occhialini and C. Powell, Nature 160, 486 (1947)

[9] T. Lee and C. Yang, Phys. Rev. 119, 1410 (1960)

[10] R. Cahn and G. Goldhaber, The Experimental Foundations of Particle Physics (2nd edn.), Cambridge University Press (2009)

[11] V. Barnes et al., Phys. Rev. Lett. 12, 204 (1964)

[12] M. Gell-Mann, Phys. Lett. 8, 214 (1964)

[13] G. Zweig, Technical report, CERN-TH-401 (1964)

[14] G. Zweig, Technical report, CERN-TH-412 (1964)

[15] M. Gell-Mann, Proceedings of "Workshop on QCD—20 Years Later", Vol. C920609 (1992)

[16] O. Greenberg, Phys. Rev. Lett. 13, 598 (1964)

[17] J. Rafelski, Melting Hadrons Boiling Quarks, DOI 10.1007/978-3-319-17545-4 (2016)

[18] E. Bloom et al., Phys. Rev. Lett. 23, 930 (1969).

[19] M. Breidenbach et al., Phys. Rev. Lett. 23, 935 (1969)

[20] J. Bjorken, Phys. Rev. 179, 1547 (1969)

[21] H. Fritzsch and M. Gell-Mann, Proc. XVI Int. Conf. on High Energy Physics, Chicago (1972)

[22] M. Gell-Mann, Phys. Rev. 125, 1067 (1962)

[23] H. Fritzsch, M. Gell-Mann and H. Leutwyler, Phys. Lett. B 47 365 (1973)

[24] J. Resner, "New Physics", American Association of Physics Teachers, New York (1981); SLAC Collaboration, "Beam Line", Volume 7, No. 11 (1976); Articles in Scientific Americans by S. Drell (June 1975) and by S. Glashow (October 1975)

[25] G. Aad et al., ATLAS Collaboration, Phys. Lett. B 716, 1-29 (2012)

[26] W. Adam et al., CMS Collaboration, Phys. Lett. B 716, 30-61 (2012)

[27] S. Weinberg, Eur. Phys. J. C 34, 5 (2004)

[28] CERN Short note on the Standard Model, https://home.cern/science/physics/standard-model

[29] The physics Hypertextbook, https://physics.info/standard/

[30] S. Raby, R. Slansky and G. West, Particle physics and the standard model, Los Alamos Science, Summer/Fall 1984

[31] P. W. Higgs, Phys. Lett. 12, 132 (1964)

[32] F. Englert and R. Brout, Phys. Rev. Lett. 13, 321 (1964)

[33] K. Rabbertz, Jet Physics at the LHC: The Strong Force beyond the TeV Scale, Springer (2017)

[34] D. Binosi and L. Theussl, Comput. Phys. Commun. 161, 76 (2004)

[35] L. Faddeev and V. Popov, Phys. Lett. B 25, 29 (1967)

[36] J. Goldstone, Nuovo Cimento 19, 154 (1961)

[37] J. Goldstone, A. Salam and S. Weinberg, Phys. Rev. 127, 965 (1962).

[38] F. Halzen and A. Martin, Book:"Quarks and leptons: An introductory course in modern particle physics", John Wiley and Sons (1984)

[39] M. Knecht, Proceedings: Ecole Joliot-Curie 1998 (1998)

[40] T. Schaefer, Lectures: "Phases of QCD", arXiv:hep-ph/0509068 (2005)

[41] J. Beringer et al., Phys. Rev. D 86 010001 (2012)

[42] M. Peskin and D. Schroeder, Book: "An Introduction to Quantum Field Theory (Frontiers in Physics)" Westview Press, Boulder, CO (1995)

[43] G. Dissertori, I. Knowles and M. Schmelling, Book: "Quantum Chromodynamics: High Energy Experiments and Theory (2nd edn.)", Oxford University Press (2009)

[44] T. van Ritbergen, J. Vermaseren and S. Larin, Phys. Lett. B 400, 379 (1997)

[45] D. Gross and F. Wilczek, Phys. Rev. Lett. 30, 1343 (1973)

[46] D. Gross and F. Wilczek, Phys. Rev. D 8, 3633 (1973)

[47] D. Gross and F. Wilczek, Phys. Rev. D 9, 980 (1974).

[48] H. Politzer, Phys. Rev. Lett. 30, 1346 (1973)

[49] K. Nakamura et al., J. Phys. G 37. 075021 (2010)

[50] S. Bethke, Eur. Phys. J. C 64, 689 (2009)

[51] J. Beringer et al., Phys. Rev. D 86, 010001 (2012)

[52] J. Collins, Book: "Foundations of Perturbative QCD, Nuclear Physics and Cosmology", Cambridge University Press (2011)

[53] J. Collins, D. Soper and G. Sterman, Book: "Factorization of Hard Processes in QCD" (Volume 5 of Advanced Series on Directions in High Energy Physics), World Scientific Pub. Co. Inc. (1988)

[54] R. Alemany-Fernandez et al., "The Large Hadron Collider: Harvest of Run 1 (1st edn.)" Springer (2015)

[55] J. Andersen et al., "Physics at TeV Colliders: Standard Model Working Group Report", arXiv:1405.1067 (2013)

[56] S. Dittmaier, A. Huss and C. Speckner, JHEP 11, 095 (2012)

[57] R. Hagedorn, Nuovo Cimento Suppl. 3, 147 (1965)

[58] CERN Courier, September2003: Page-30 (2003)

[59] R. Hagedorn, Proceedings: Quark matter 84, Springer-Verlag (1984)

[60] R. Hagedorn and J. Rafelski, Phys. Lett. B 97, 136 (1980)

[61] E. Shuryak, Phys. Lett. B 78, 150 (1978)

[62] E. Shuryak, Phys. Rep. 61, 71 (1980)

[63] K. Huang and S. Weinberg, Phys. Rev. Lett. 25, 895 (1970)

[64] J. Collins and M. Perry, Phys. Rev. Lett. 34, 1353 (1975)

[65] N. Cabibbo and G. Parisi, Phys. Lett. B 59, 67 (1975)

[66] S. Borsanyi et al., JHEP 1011, 077 (2010)

[67] S. Borsanyi, Z. Fodor, C. Hoelbling, S. Katz, S. Krieg and K. Szabo, Phys. Lett. B 730, 99 (2014)

[68] HotQCD Collaboration, Phys. Rev. D 90(9), 094503 (2014)

[69] A. Majumder and B. Müller, Phys. Rev. Lett. 105, 252002 (2010)

[70] A. Bazavov et al., Phys. Rev. Lett. 113(7), 072001 (2014)

[71] F. Brown et al., Phys. Rev. Lett. 65, 2491 (1990)

[72] S. Shapiro and S. Teukolsky, Book: "Black Holes, White Dwarfs, and Neutron Stars: The Physics of Compact Objects" Wiley (1983)

[73] M. Alford, K. Rajagopal and F. Wilczek, Nucl. Phys. B 537, 443 (1999)

[74] K. Rajagopal and F. Wilczek, hep-ph/0011333 (2000)

[75] M. Alford, Ann. Rev. Nucl. Part. Sci. 51, 131 (2001)

[76] T. Schaefer, hep-ph/0304281 (2003)

[77] D. Rischke, Prog. Part. Nucl. Phys. 52, 197 (2004)

[78] D. Hong, Acta Phys. Pol. B 32, 1253 (2001)

[79] F. Karsch, Lecture Notes of Physics, vol. 583 (2002)

[80] J. Blaizot, E. Iancu and A. Rebhan, Phys. Lett. B 470, 181 (1999)

[81] G. Chapline and A. Kerman, "On the possibility of making quark matter in nuclear collisions" MIT Cambridge -CTP-695 (78,REC.APR)10p, http://inspirehep.net/record/134446/files/CTP-695.pdf (1978)

[82] S. Chin, Phys. Lett. B 78, 552 (1978)

[83] S. Chin and A. Kerman, Phys. Rev. Lett. 43, 1292 (1979)

[84] T. Lee and G. Wick, Phys. Rev. 2, 2291 (1974)

[85] F. Becattini et al., Phys. Rev. C 69, 024905 (2004)

[86] E. Andersen et al., Phys. Lett. B 449, 401 (1999)

[87] F. Antinori et al., Eur. Phys. J. C 11, 79 (1999)

[88] J. Letessier and J. Rafelski, Acta Phys. Pol. B 30, 153 (1999)

[89] R. Stock, Phys. Lett. B 456, 277 (1999)

[90] U. Heinz, Nucl. Phys. A 661, 140 (1999)

[91] U. Heinz and M. Jacob, "Evidence for a new state of matter: An assessment of the results fromthe CERN lead beam program", CERN February 2000 press release (2000)

[92] New state of matter created at CERN, https://cds.cern.ch/record/716634?ln=en (2000)

[93] C. Chiu, E. Sudarshan and K. Wang, Phys. Rev. D 12, 902 (1975)

[94] K. Geiger and B. Müller, Nucl. Phys. B 369, 600 (1992)

[95] J. Bjorken, Phys. Rev. D 27, 140 (1983)

[96] BRAHMS Collaboration, Nucl. Phys. A 757 1 (2005)

[97] PHENIX Collaboration, Nucl. Phys. A 757 184 (2005)

[98] PHOBOS Collaboration, Nucl. Phys. A 757 28 (2005)

[99] STAR Collaboration, Nucl. Phys. A 757 102 (2005)

[100] D. Teaney, Phys. Rev. C 68,034913 (2003)

[101] P. Romatschke and U. Romatschke, Phys. Rev. Lett. 99 172301 (2007)

[102] H. Song et al., Phys. Rev. Lett. 106 192301 (2011)

[103] H. Song et al., Phys. Rev. Lett. 109 139904 (2012)

[104] R. Fries, B. Müller, C. Nonaka and S. Bass, Phys. Rev. Lett. 90, 202303 (2003)

[105] R. Fries, B. Müller, C. Nonaka and S. Bass, Phys. Rev. C 68, 044902 (2003)

[106] P. Sorensen, J. Phys. Conf. Ser. 446, 012015 (2013)

[107] N. Sahoo, J. Phys. Conf. Ser. 535, 012007 (2014)

[108] B. Müller, J. Schukraft and B. Wyslouch, Annu. Rev. Nucl. Part. Sci. 62, 361 (2012)

[109] B. Betz and M. Gyulassy, Phys. Rev. C 86, 024903 (2012)

[110] C. Gale, S. Jeon, B. Schenke, P. Tribedy and R. Venugopalan, Phys. Rev. Lett. 110, 012302 (2013)

[111] PHOBOS Collaboration, Phys. Rev. Lett. 012301 (2006)

[112] CDF Collaboration, Phys. Rev. D 41, 2330 (1990)

[113] M. Miller, K. Reygers, S. Sanders and P. Steinberg, Annu. Rev. Nucl. Part. Sci. 57 (1) 205–243 (2007)

[114] B. Schenke, P. Tribedy and R. Venugopalan, Phys. Rev. Lett. 108, 252301 (2012)

[115] J. Moreland, J. Bernhard and S. Bass, Phys. Rev. C 92, 011901 (2015)

[116] B. Schenke, S. Jeon and C. Gale, Phys. Rev. Lett. 106, 042301 (2011)

[117] C. Shen et al., Comp. Phys. Comm. 199, 61–85 (2016)

[118] L. Pang, H. Petersen and X. Wang, Phys. Rev. C 97, 064918 (2018)

[119] Z. Lin, C. Ko, B. Li, B. Zhang and S. Pal, Phys. Rev. C 72, 064901 (2005)

[120] J. Uphoff, O. Fochler, Z. Xu and C. Greiner, Phys. Rev. C 82 044906 (2010)

[121] A. Toia, CERN Courier April issue of 2013

[122] STAR Collaboration, Phys. Rev. C 79, 034909 (2009)

[123] ALICE Collaboration, Quark Matter 2011 proceedings, arXiv:1108.3257 (2011)

[124] STAR Collaboration, Nucl. Phys. A 757, 28 (2005)

[125] ALICE Collaboration, Phys. Lett. B 736, 196-207 (2014)

[126] S. Voloshin and Y. Zhang, Zeit. Phys. C 70, 665 (1996)

[127] ALICE Collaboration, Phys. Lett. B 727, 371-380 (2013)

[128] R. Hagedorn, CERN Rept. 71 (1971)

[129] E. Shuryak, Phys. Lett. B 42, 357 (1972)

[130] J. Rafelski, and M. Danos, Phys. Lett. B 97, 279 (1980)

[131] R. Hagedorn et al., Zeit. Phys. C 27, 541 (1985)

[132] A. Tounsi and K. Redlich, arXiv:0111159 (2001)

[133] NA57 Collaboration, J. Phys. G: Nucl. Part. Phys. 28 1607 (2002)

[134] T. Matsui and H. Satz, Phys. Lett. B 178, 416 (1986)

[135] T. Matsui, Zeit. Phys. C 38, 245 (1988)

[136] M. Gyulassy et al., arXiv:0302077 (2003)

[137] http://ars.els-cdn.com/content/image/1-s2.0-S0146641008001336-gr1.jpg

[138] ALICE Collaboration, Phys. Rev. Lett. 105, 252302 (2010)

[139] ALICE Collaboration, JHEP 06, 190 (2015)

[140] STAR Collaboration, Phys. Rev. C 72, 014904 (2005)

[141] PHENIX Collaboration, Phys. Rev. C 85, 064914 (2012)

[142] J. Beringer et al., Phys. Rev. D 86, 010001 (2012)

[143] H. Stocker, F. Jundt and G. Guillaume, Toute la physique - DUNOD (1999)

[144] R. Baier, Y. Dokshitzer, A. Mueller, S. Peign and D. Schiff, Nucl. Phys. B 483 (1997)

[145] B. Zakharov, JETP Letter 65 (1997)

[146] Y. Dokshitzer, V. Khoze and S. Troyan, Jour. Phys. G 17 1602 (1991)

[147] Y. Dokshitzer and D. Kharzeev, Phys. Lett. B 519, 199 (2001)

[148] STAR Collaboration, Phys. Rev. Lett. 91, 072304 (2003)

[149] G. Roland, PRAMANA journal of physics 84, 5 (2015)

Chapter 2

The LHC and the ALICE experiment

Particle accelerators are the most essential and key tool for nuclear and particle physics experiment. While they are unable to deliver energies as high as that found in cosmic rays, they make particle collisions within a designed framework and in a controlled environment. Particle accelerators are complemented by a well designed detector system to capture all the signals coming out from the experiments to procure physics messages by analysing them. This set up allows for the detailed measurement of fully reconstructed events (collisions) in a controlled environment.

In this chapter, details of the Large Hadron Collider (LHC) have been presented with the description of A Large Ion Collider Experiment (ALICE). Central barrel detectors, the forward detectors, the trigger detectors and the muon spectrometers have been described as a part of the ALICE detector system. A description of the trigger setup for event selection, the data acquisition system, the online and offline computation for data processing and the physics analysis procedure has also been presented along with the physics goal.

2.1 The Large Hadron Collider (LHC)

The Large Hadron Collider (LHC) at CERN, the largest particle accelerator in the world [1, 2], was installed in the 26.7 km tunnel constructed for the CERN Large Electron-Positron (LEP) Collider, in 2001. The LHC is located under the Swiss-French border area, as can be seen in Figure 2.1, at a depth of 50 to 175 m underground. It is a two ring superconducting hadron accelerator operated at ultrahigh vacuum and it can collide particles at a speed close to the speed of light in vacuum. With the current design, LHC can accelerate proton beams with maximum energy of 7 TeV (making top collision energy to be 14 TeV) and with a luminosity of $10^{34} cm^{-2} s^{-1}$. It can also accelerate and collide heavy ion beams (Pb-Pb) at an energy of 2.75 TeV/nucleon (making top collision energy to be 5.5 TeV) with a peak luminosity of $10^{27} cm^{-2} s^{-1}$.

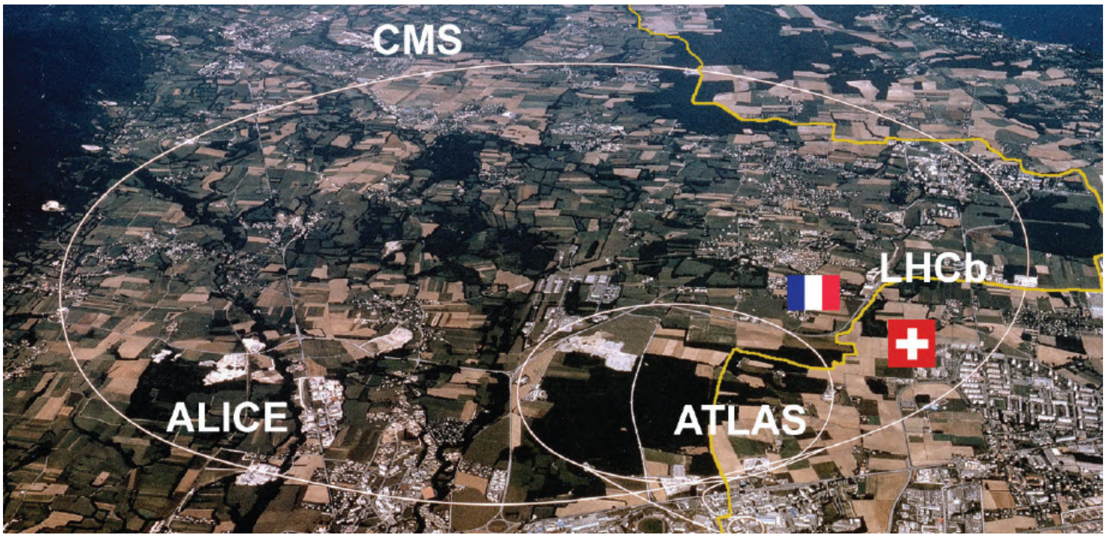

FIGURE 2.1: The aerial view of the LHC accelerator complex.

The injection chain is shown in Figure 2.2. Protons are first extracted from hydrogen gas by removing the electrons and then accelerated in Linear Accelerator 2 (LINAC2) (up to 50 MeV). The proton beam is then injected to the Proton Synchrotron Booster where they achieve acceleration up to 1.4 GeV. Then, the beam is passed on to the Proton Synchrotron (PS) and accelerated up to 25 GeV and then it is fed into the Super Proton Synchrotron (SPS) where it achieves the acceleration of maximum 450 GeV. Finally, the accelerated beam from SPS is injected to the LHC where it attains the maximum beam energy available. Lead beam is obtained from different source point and injected first in the LINAC3 where the beam gets accelerated up to 160 MeV and then to the Low Energy Ion Ring (LEIR). After that point the Pb beam follows the same path as does the proton beam. One important point to mention is that after SPS, the beams are separated and inserted to two parallel transfer lines and then fed to the LHC where one beam circulates clockwise and the other one circulates in anti-clockwise direction.

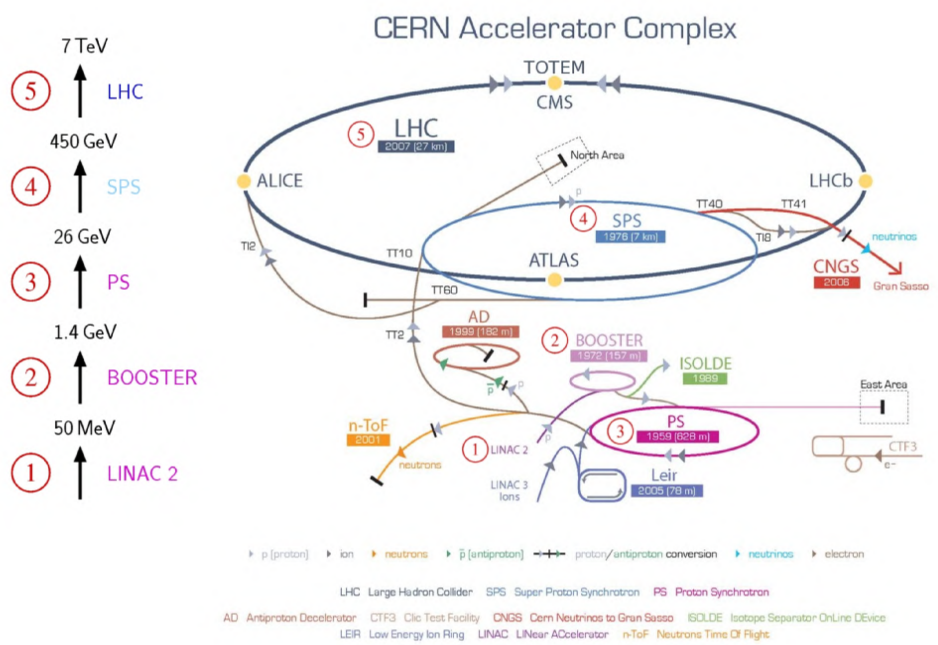

FIGURE 2.2: The schematic diagram of the whole accelerator complex with LHC at CERN.

Figure 2.3 shows the design layout of the LHC. The ring is divided into 8 sectors each of which is approximately 528 m long. Each sector has a straight section in its centre, known as the *pit* or *point*. The two beams enter the LHC through points 2 and 8. The beam intersection happens at four points: 1, 2, 5 and 8 where the four major experiments have been built. Beam collimation systems are placed at point 3 and 7 and these systems clean the beam. The task of the cleaning system is to prevent loss of particles in an uncontrolled manner within the accelerator. The Radio-Frequency (RF) system accelerates the beams and is housed at point 4. Point 6 houses the beam dumping system. Around 5000 superconducting magnets of different types and sizes are used in the LHC.

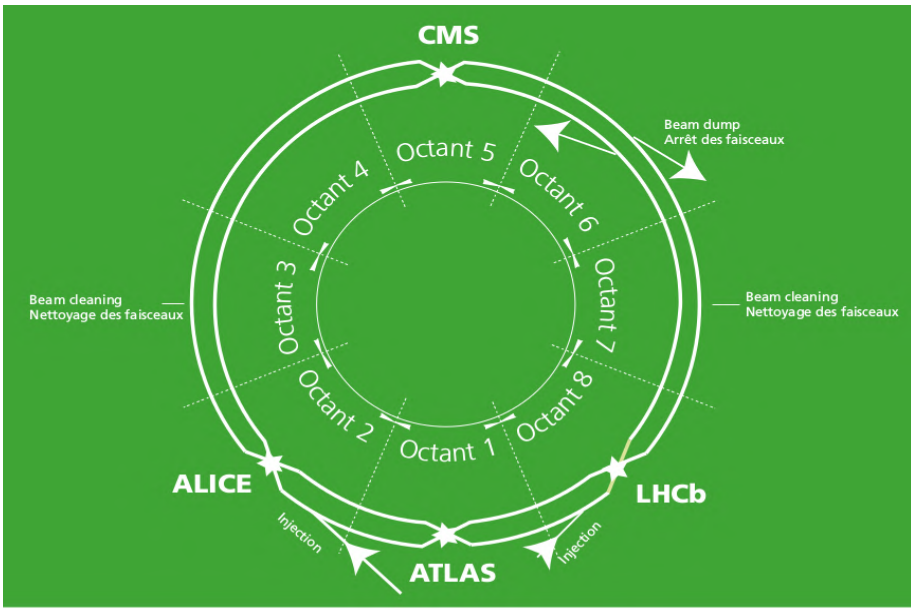

FIGURE 2.3: Schematic diagram of LHC tunnel with the sector divisions and interaction points.

A total of 1232 dipole magnets, each 14.3 m long are used to bend the beams. 392 quadrupole magnets, each 5-7 m long, help to control the transverse spread of the beam and focus the beam. The dipole magnets are also equipped with sextupole, octupole and decapole magnets, which correct for small imperfections in the magnetic field. The maximum attainable energy of the LHC is restricted by the superconducting dipole magnets (strength $\approx$ 8.3T) that bends the beam around the ring. Insertion magnets take over charge once the beams enter the detector points for collisions. Three quadrupoles are used to create a system called an inner triplet. There are eight inner triplets, two of which are located at each of the four large LHC detectors which tighten the beam, making it 12.5 times narrower, – from 0.2 millimetres down to 16 micrometres across.

Beam species	$\sqrt{s_{NN}}$ TeV	L $(cm^{-2}s^{-1})$	N/bunch	β^* (m)	Bunch spacing (ns)
pp	14	10^{34}	1.15×10^{11}	0.55	25
Pb-Pb	5.52	10^{27}	7×10^{7}	0.5	100

TABLE 2.1: LHC design values[3] for pp and Pb-Pb system

Protons are injected in bunches of around 10^{11} protons per bunch making the beam to be approximately $\approx$ 64 μm wide. A maximum of 2808 bunches, separated by typically 25 ns bunch spacing, can circulate simultaneously. The beams circulate with a speed very close to the speed of light in the vacuum and each bunch travels the 26.7 km ring at $\approx$ 11 kHz with a bunch crossing rate up to $\approx$ 31 MHz. Since multiple collisions per bunch crossing (up to $\approx$ 50 in ATLAS and CMS) are possible, this yields a delivered collision rate up to hundreds of MHz which implies a design luminosity of $\mathcal{L} \approx 10^{34} s^{-1} cm^{-2}$. Various design parameters of LHC for both pp and Pb-Pb systems can be found at Table 2.1 Among the four large scale experiments, ALICE is not optimized to handle such high collision rate and for this, LHC does the "leveling" of the luminosity before delivering it to ALICE. The summary of the runs in the LHC with beam type has been tabulated year-wise in Table 2.2

Year	Collision system	$\sqrt{s}$ or $\sqrt{s_{NN}}$ (TeV)
2009	pp	0.9
		2.36
2010	pp	7
	Pb-Pb	2.76
2011	pp	2.76
		7
	Pb-Pb	2.76
2012	pp	8
	p-Pb	5.02
2013	pp	2.76
	p-Pb	5.02
2015	pp	5.02
		13
	Pb-Pb	5.02
2016	pp	13
	p-Pb	8.16
2017	pp	5.02
		13
	Xe-Xe	5.44
2018	pp	14
	Pb-Pb	5.02

TABLE 2.2: Year-wise summary of the LHC runs [4] up to Long Shutdown-2 (2018) with beam type.

2.1.1 Experiments at the LHC

There are a total of 8 experiments (4 large scale and 4 smaller) of which 7 have been recording data and a new one has been approved in 2019 and most likely to record data in 2021 after the Long Shutdown of the LHC is over. These experiments are designed around the interaction regions which use the beam from the LHC. Among the large experiments, there are two multi-purpose detectors, ATLAS and CMS, one specially designed experiment on b-physics and a dedicated heavy-ion experiment, ALICE. At a glance information on the experiments are given below:

2.1.1.1 A Large Ion Collider Experiment (ALICE)

ALICE[6, 11] is built around point 2 and it is a specialized heavy-ion experiment with a goal to study Quark Gluon Plasma (QGP). It will be discussed in detail in the next section.

2.1.1.2 A Toroidal LHC Apparatus for Spectroscopy (ATLAS)

It is a general purpose detector installed at interaction point 1[8] to search for Higgs boson and physics beyond the Standard Model. The particle trajectories are detected in the magnetic field of a solenoid in the vicinity of the interaction point and a toroid further out. Charged particle tracking is achieved by the combination of silicon pixels system and transition radiation tracker. Liquid argon technology was adopted for calorimeters both in the central barrel and the end caps, as well as hadronic calorimeters. The detector system is complemented with extensive muon detection stations.

2.1.1.3 Compact Muon Solenoid (CMS)

CMS is another general purpose detector placed at point 5[9], diametrically opposite to ATLAS with almost similar physics goals of that of ATLAS like search for the Higgs boson, supersymmetric (SUSY) particles, extra dimensions and black holes. It differs from ATLAS in the used detector technologies. The detector is installed within a large super-conducting solenoidal magnet. Charged particle tracking is performed using silicon pixels detectors and for neutral particles, there are electromagnetic and hadronic calorimeters. Muon chambers are embedded in the return yoke of the magnet.

2.1.1.4 Large Hadron Collider beauty (LHC-b)

LHC-b[9] is a dedicated experiment to explore heavy-flavor physics with the objective to search new physics in CP violation and other rare phenomena in the decays of beauty and charmed hadrons. The detector is built at point 8 as a single arm spectrometer to capture the forward and backward production of b and $\bar{b}$. A field of 4 Tm is required for the detectors and is supplied by a warm dipole magnet. Secondary vertices are reconstructed with good precision by a vertex locator. Tracking is done by the combination of silicon microstrip detectors and straw tube detectors.

2.1.1.5 Large Hadron Collider forward (LHC-f)

This detector shares the same interaction point (point 1) with ATLAS and is installed on both sides of point 1[10]. It measures the production cross section and energy spectra at very forward rapidity. To address this, sampling calorimeters have been installed in the Target Neutral Absorbers, where the common beam pipe gets split into two. This experiment gives scientists the privilege to interpret, simulate and calibrate large-scale cosmic-ray experiments.

2.1.1.6 TOTal Elastic and diffractive cross-section Measurement (TOTEM)

This detector is installed around point 5[11] and it shares the same with CMS. It aims at a luminosity independent measurement of the total proton-proton cross section, studies of diffractive events and to focus on physics that is not accessible to the general purpose experiments. The detector system comprises two telescopes for the detection of charged particles with sub-detectors housed in specially designed vacuum chambers called Roman pots.

2.1.1.7 Monopole and Exotics Detector At the LHC (MoEDAL)

This detector is built around point 8[12] and it shares the same interaction point with LHCb. It was installed for the direct search of magnetic monopoles and other highly ionizing massive particles directly. Nuclear Track Detectors (NTDs) are used to serve the purpose.

2.1.1.8 ForwArd Search ExpeRiment (FASER)

It is designed to search for new light and weakly coupled elementary particles and to study the interactions of high-energy neutrinos[13]. It is placed behind 100 meters of rock and concrete from ATLAS for a low background environment required for neutrino physics. The detector system comprises many layers of emulsion films interleaved with tungsten plates as target material, plastic scintillators as charged particle veto, 1.5 meter long empty decay volume and a 2 meter long spectrometer consisting silicon strip detectors to track charged decay products. The detector system is operated in a magnetic field of 0.55 T strength.

2.2 A Large Ion Collider Experiment (ALICE)

As already introduced, ALICE was proposed and designed to study the properties of strongly interacting matter and the QGP. At the same time it can also record pp or p-Pb collision data. The optimization for heavy-ion physics led to design requirements which are different from the other LHC experiments [11]. Central heavy-ion collisions produce very large abundances of charged particles and at the same time there should be a provision to reconstruct all the produced tracks for event-by-event analyses. The detector must determine centrality and event plane to allow global event characterization. Particles are most abundantly produced at the low transverse momenta region and tracking should have very good resolution for the measurement of total particle yields. On the other hand, a good tracking resolution is also required up to very high momenta for the measurement of high p_T probes like jets. In addition, Particle IDentification (PID) is also of utmost importance which enables, for example, study of chemical composition of the produced particles.

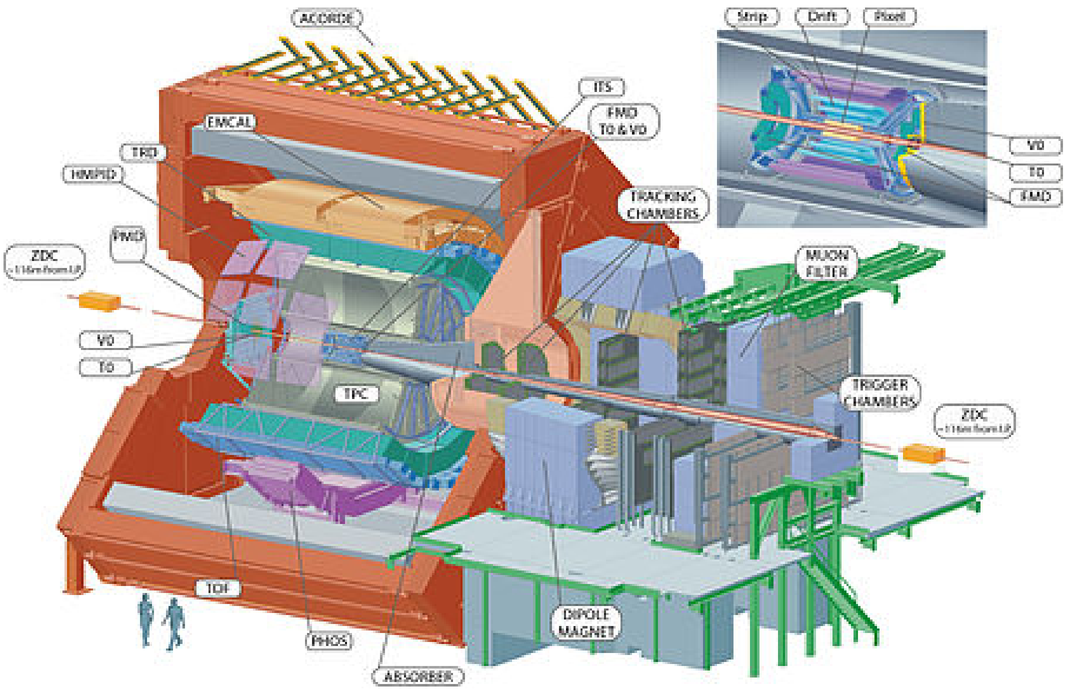

FIGURE 2.4: The schematic diagram of the ALICE detector with its sub-systems.

To meet the requirements, ALICE has an above 10,000-ton detector system consisting 19 sub-detectors which, on the whole, is 26 m long, 16 m high and 16 m wide. Figure 2.4 presents a schematic diagram of the ALICE detector system including the sub-detectors. The detector is designed to measure the particles produced in the collisions which take place at its center, so that the evolution of the system produced during these collisions can be reconstructed and studied. The 19 sub-detectors can broadly be classified into two categories: the central barrel detectors and the forward detectors. The central part of the ALICE detectors, an almost symmetrical central barrel detector system, is installed inside a solenoid magnet that was inherited from the L3 experiment at LEP. It has an internal length of 12.1 m and a radius of 5.75 m and the solenoid produces an axial field of about 0.5 T. The central barrel detector system consists of the Inner Tracking System (ITS) , Time Projection Chamber (TPC), Transition Radiation Detector (TRD), Time Of Flight (TOF) detector, High-Momentum Particle Identification Detector (HMPID), PHOton Spectrometer (PHOS), ElectroMagnetic Calorimeter (EMCal) and ALICE COsmic Ray DEtector (ACORDE). ITS, TPC, TRD and TOF are supported by a stainless steel construction of 7 m length and 8.5 m diameter and is called the space-frame. This structure rests on two 12 m long support rails which are attached to the octagonal frame for the L3 magnet doors. Separate pairs of similar rails support the PHOS and EMCal. HMPID is mounted on a cradle which is attached to the space- frame. All the rails and the space frame have the facility to move the structures for maintenance, service and installation. The muon spectrometer consists of a warm dipole magnet with an integrated horizontal field of 3 Tm, six tracking stations and additional trigger stations. It is installed behind an absorber in the forward direction and the trigger stations sit behind further iron shielding.

In the next sub-section, there is a very brief paragraph on ALICE coordinate system and the following one discusses the detector system designing principle as incorporated in collider experiments. After those, in the following sub-sections, all the sub-detectors has been described. For convention, in ALICE, the side nearer to the ATLAS side is called the A-side and the side in the direction of CMS is called the C-side. For all the forward detectors described here, it has been mentioned whether it sits in the A or C side.

2.2.1 ALICE coordinate system

The ALICE coordinate system, shown in Figure 2.5, follows a right handed orthogonal Cartesian system with origin at the interaction point (IP). Its x and y coordinates are perpendicular to the beam direction such that the positive x and y direction point to the centre and upward of the accelerator respectively. The z axis is along the beam direction with positive z is along the A-side and negative z towords the C-side.

2.2.2 Detector system layout overview

The detector system of modern particle experiments, like ALICE in the LHC, are designed to cover as much solid angle as possible around the interaction point. This particular arrangement is called the hermetic detectors. This is nearly always accomplished with a cylindrical barrel around the IP with end-caps sealing both the ends of the barrel. As introduced in Chapter 1, the hermetic detector system consists of different detector

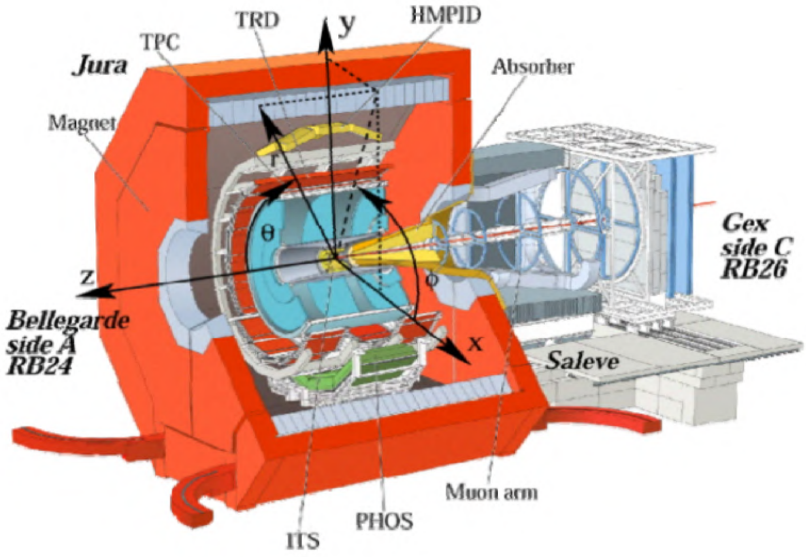

FIGURE 2.5: The coordinate system of the ALICE detector.

technologies and those are built up in concentric layers with each layer having different responsibilities as shown in the Figure 2.6. Starting from the innermost layer, the

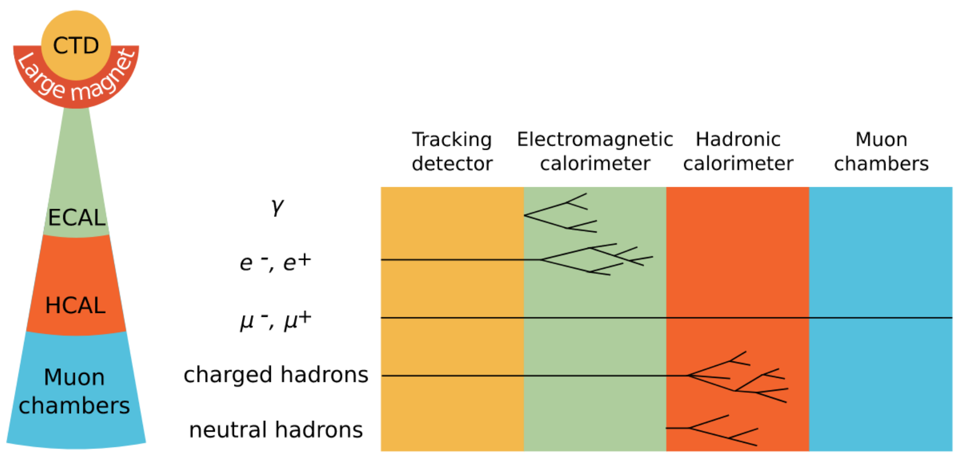

FIGURE 2.6: The hermetic detector system design layout (left) with detection specifications (right).

successive layers in a hermite detector are:

- *Central tracking detector (CTD)*: this is designed to track all the charged particles and allow for complete event reconstruction with vertex determination.

- *Large magnet*: this produces a magnetic field strong enough to curve the tracks of charged particles in the tracking detector, allowing their momentum to be calculated.

- *Electromagnetic Calorimeter (ECAL)*: this layer records the shower energy of electrons and photons.
- *Hadronic Calorimeter (HCAL)*: the hadronic showers deposit their energy in this layer.
- *Muon tracking chamber*: This is the outermost layer of the hermite detectors and this layer is associated with some additional shielding (like concrete) just to ensure that the particles reaching here are only muons.

The components of ALICE hermite detector are described in the following sections.

2.2.3 Central barrel detectors

2.2.3.1 Inner Tracking System (ITS)

The ITS [14] is the first sub-detector around the geometrical or nominal interaction point. It consists of total six layers of cylindrical shaped silicon detectors of which two layers are Silicon Pixel Detector (SPD), two layers are Silicon Drift Detector (SSD) and two layers are Silicon Strip Detector (SSD) starting from the interaction point to outwards respectively.

Layer/Type	r (cm)	$\pm$z (cm)	No. of Modules	Intrinsic resolution (μm)
1/SPD	3.9	14.1	12	100
2/SPD	7.6	14.1	12	100
3/SDD	15.0	22.2	35	25
4/SDD	23.9	29.7	35	25
5/SSD	38.0	43.1	20	830
6/SSD	43.0	48.9	20	830

TABLE 2.3: Design parameters of all the six ITS layers

The geometrical details of the six layers has been given in tabulated form in Table 2.3 and the detector layout can be seen in Figure 2.7.

ITS has the following responsibilities:

- Localize or reconstruct primary vertex with high precision (resolution $< 100\mu m$)
- Locate secondary vertices from weak decays of strange, charm and beauty mesons.
- Help to reconstruct and identify charged particles at low p_T region (momentum below 100 MeV/c)

ITS covers a pseudorapidity range of $|\eta| < 0.9$, however the very first layer has a more extended pseudorapidity coverage ($|\eta| < 1.98$) to provide continuous coverage for the measurement of charged particle multiplicity along with the Forward Multiplicity Detector (FMD). The four inner layers (SPD and SDD) provide a 2D tracking in the highly dense environment (90 tracks/cm^2) of heavy-ion collisions to separate tracks. The outermost two layers (SSD) gives 1D read-out which is sufficient due to lesser track density in there. SDD and SSD have analog read-out which enables them to measure the energy loss (dE/dx) of the charged particles traversing them.

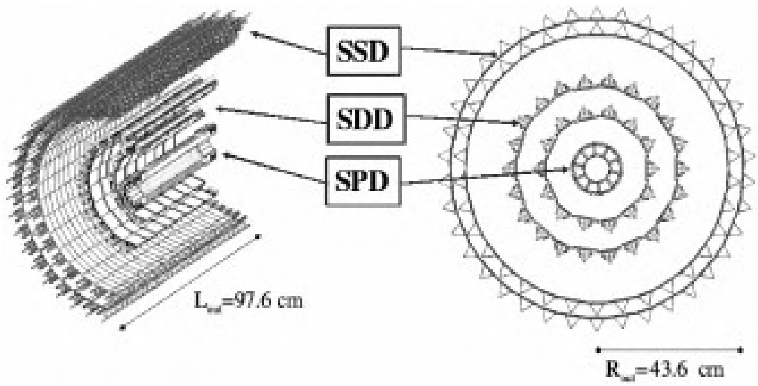

FIGURE 2.7: Layout of the ITS detector.

In the long shutdown number 2 (LS2) in 2018-2020, ITS is supposed to be undergoing major upgradation. The previous 6 layers system will be replaced by a new 7 layer system with a faster readout, more precise resolution and less material. The pixel size will also be reduced from $50\mu m \times 425\mu m$ to $27\mu m \times 29\mu$m and the innermost layer will be moved to more close to the beam line, moving from 3.9 cm to 2.2 cm.

2.2.3.2 Time Projection Chamber (TPC)

The TPC [15] is the largest (it is also world's largest TPC) and the main tracking detector in the central barrel with a cylindrical shape of ≈ 92 m^3 volume covering a distance from the beam pipe from r = 85 cm to r = 250 cm within the pseudorapidity range of $|\eta| < 0.9$. It is 500 cm in length along the beam direction and it can reconstruct tracks with full radial length within $|\eta| < 0.9$ and with 1/3 radial length (with reduced or no matching with the other detectors) within $|\eta| < 1.5$. TPC has full azimuthal coverage and a large transverse momentum range of 0.1 GeV/c $< p_T <$ 100 GeV/c with good momentum resolution (less than 2%). A schematic view of TPC can be found at Figure 2.8 and the detector layout has been shown in Figure 2.9.

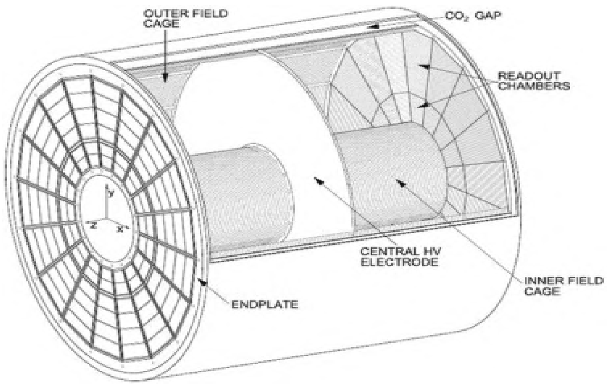

FIGURE 2.8: Schematic view of the TPC.

TPC is a gaseous detector and a gas mixture of Ne/CO_2/N_2 (90%/10%/5%) acts as the active medium in the two cylindrical shaped volumes separated by a cathode. The readouts at the end plates of the cylinder consist of multi-wire proportional chambers and are divided into 72 sectors (18 inner/outer on each end cap) with about 560,000 readout pads. A central high voltage (100 kV) electrode creates a highly uniform electrostatic field with a gradient of about 400 V/cm which results in a maximum drift time of about 90 μs. When a charged particle traverses the TPC, it ionizes the TPC gas and the resulting electrons are drifted by an electric field to the readout endcaps. The multi-wire proportional chambers provide the necessary signal amplification (known as the gas amplification) through the avalanche effect in the vicinity of the anode wires strung in the read-out.

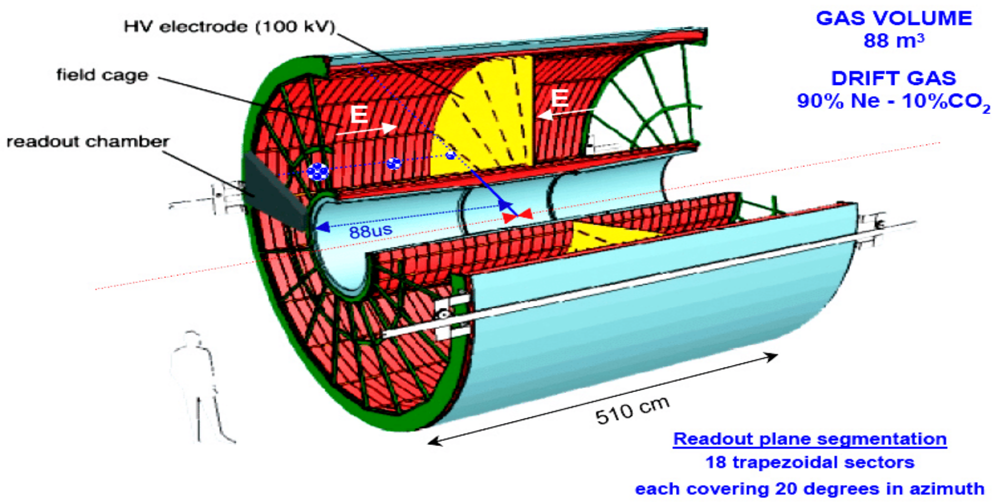

FIGURE 2.9: Layout of the ALICE TPC showing the central electrode, the field cage and the end plates supporting the readout chambers.

The trajectory of a track can be constructed with a maximum of 159 space points in the TPC. The x and y coordinates of the tracks are provided by the drift electrons induced signal on the 2D readout pads. The z coordinate of the tracks is provided by the time taken by the drifted electrons to reach the endcaps. TPC uses the Kalman filter based "inward-outward-inward" iterative approach for track reconstruction. It has a decent tracking efficiency of 80%-90% above $p_T \approx 5$ GeV/c and it drops drastically below that. Being a gaseous detector TPC provides the energy loss, dE/dx, information using a truncated mean of the distribution of cluster energies of the track and thus can perform PID of the tracks. The specific energy loss described by the Bethe-Bloch formula is parameterized by a function originally proposed by the ALEPH Collaboration [18]:

$$f(\beta\gamma) = \frac{P_1}{\beta^{P_4}}(P_2 - \beta^{P_4} - ln(P_3 + \frac{1}{(\beta\gamma)^{P_5}})) \tag{2.1}$$

where β is the particle velocity, γ the relativistic factor and P_{1-5} are fit parameters. Figure 2.10 shows the energy loss in the TPC as a function of momentum p (GeV/c) for Pb-Pb collisions at $\sqrt{s_{NN}} = 2.76$ TeV, p-Pb collisions $\sqrt{s_{NN}} = 5.02$ TeV and pp collisions at $\sqrt{s_{NN}} = 7$ TeV. The background is larger in Pb-Pb collisions than p-Pb collisions which shows much cleaner distribution. Low momentum particles (< 1 GeV/c) are identified on a track by track basis whereas for higher momenta particles, a statistical nσ approach is used. nσ cut is defined in terms of resolution as:

$$n\sigma_{TPC} = \frac{dE/dx_{measured} - dE/dx_{expected}}{\sigma_{TPC}} \tag{2.2}$$

where dE/dx$_{measured}$ is the energy loss of the tracks measured in TPC, dE/dx expected is the expected energy loss of the tracks using a parameterization of modified Bethe-Bloch function and σ_{TPC} is the resolution of the TPC. The separation of pions from electrons in TPC is up to several GeV/c and the identification of pions from kaons and protons are also up to several GeV/c as well, as shown in Figure 2.10.

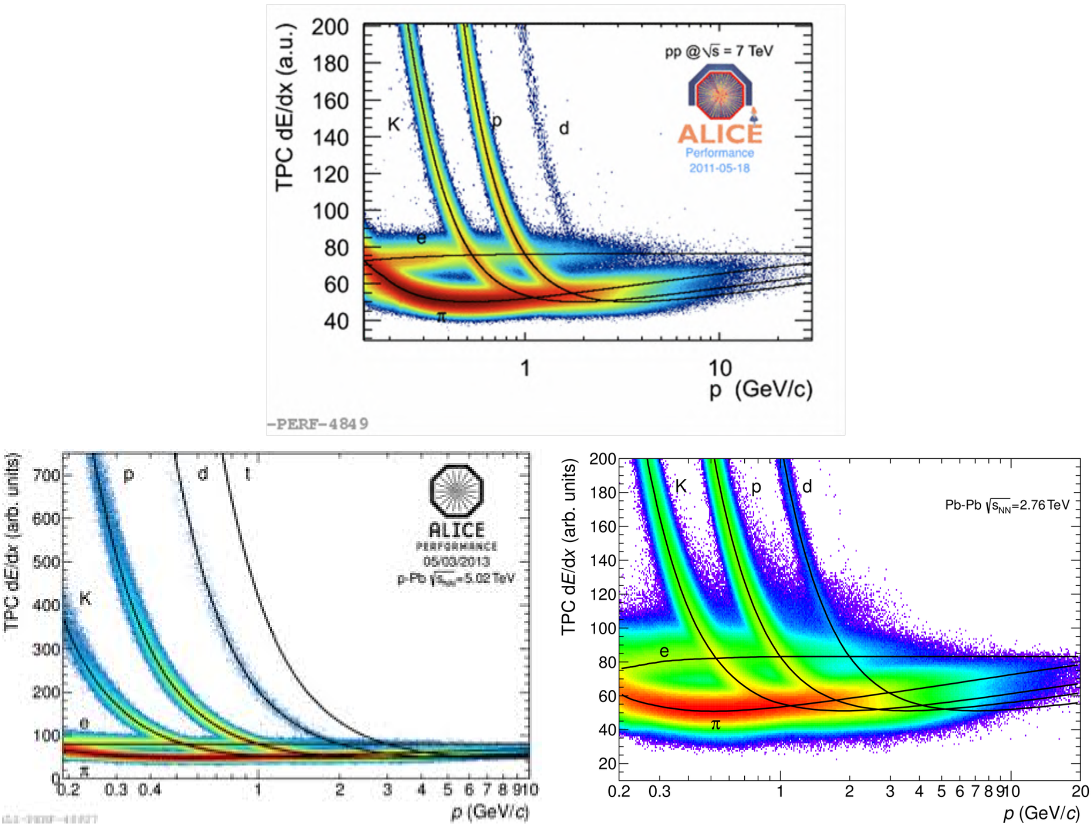

FIGURE 2.10: Energy loss in the TPC (dE/dx) versus momentum p (GeV/c) with Bethe-Bloch predictions (black lines) for different particles in pp collisions [16] (top), p-Pb collisions (bottom left) and in Pb-Pb collisions [17] (bottom right).

In high rate gas TPCs, the tracking and PID performance get distorted by the effect of ion back-flow (IBF). This affects the drift field from the gas amplification region to the drift volume (from the same E-field that drifts ionized electrons to the readout). A structure known as the gating grid is installed to minimize IBF. Gating grid allows smooth passing of electrons through the gas amplification region in "open" configuration. When the gating grid is closed, the ions get collected before they drift back into the active volume of the TPC. The gate remains closed for ≈200 μs per ≈100 μs event drift time due to the slow mobility of ions and this actually limit the readout rate to approximately 3 kHz.

In LS2, the TPC is also supposed to get upgraded. For LHC Run 3, a continuous readout at 50 kHz is required and for this, the multi-wire chambers and the gating grid technology are not suitable at all. The solution is to use multi-layer micro-pattern gas detectors (MPGDs) and gas electron multipliers (GEMs) was finalised from this family of gas detectors. Simulation studies have optimized a gain of 2000 (Ne-CO_2-N_2, 90-10-5), with IBF 2% and energy resolution of 14% or better, with acceptable correction of TPC space charge distortions in regards to TPC track finding, PID capability and momentum resolution. A stack of 4 GEM layers has been considered as the suitable detecting elements and the entire readout of the TPC is going to be replaced by this configuration.

2.2.3.3 Transition Radiation Detector (TRD)

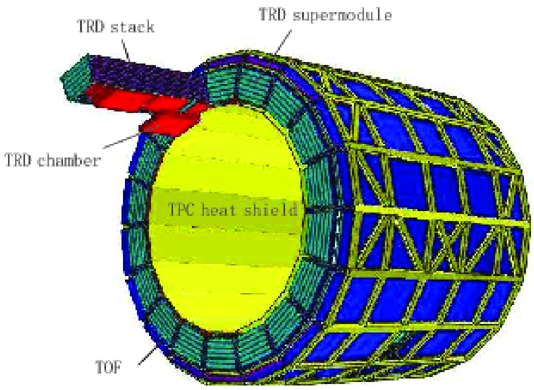

FIGURE 2.11: Layout of the ALICE TRD has been shown here with one displaced chamber for clarity. On top of the TRD, the TOF system can be seen and inside TRD, the heat shield of TPC is visible.

The TRD [19] provides the identification of electrons above 1 GeV/c using EM radiation from a particle passing through an inhomogeneous medium (transition radiation) in conjunction with the TPC. The measurements of electrons in heavy-ion collisions gives access to the di-lepton continuum, light and heavy vector meson resonances as well as hadrons with open charm and beauty in semi-electronic decays. As pions are the most abundant particles, the clean identification of electrons, in the background of pions, is a crucial ingredient for a higher significance measurement.

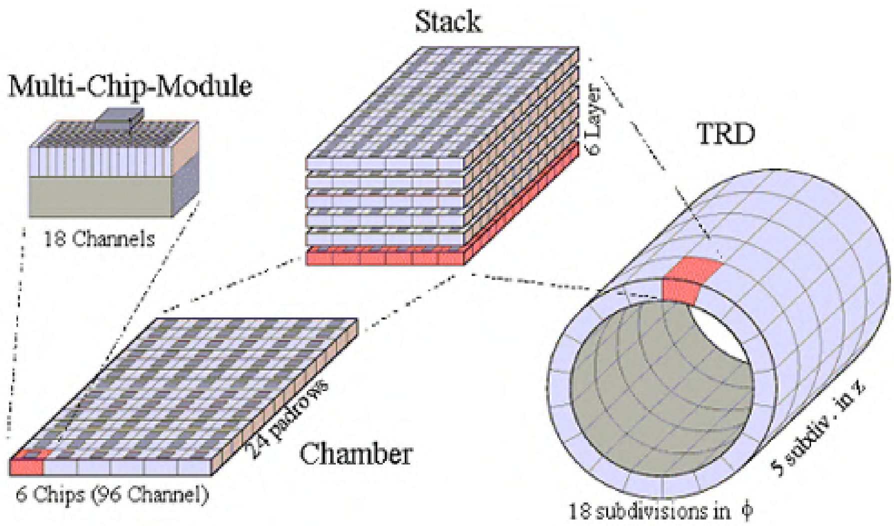

FIGURE 2.12: Cross-sectional view of TRD.

Below 1 GeV/c, electrons can be identified via specific energy loss measurement provided by the TPC. Above 1 GeV/c, transition radiation passing a radiator can be exploited in concert with the specific energy loss in a suitable gas mixture to obtain necessary pion rejection capability and also the absorption of the radiation generated by electrons at the beginning of the drift section corresponding to the large drift time helps the process. TRD layout and cross-sectional view have been shown in Figure 2.11 and Figure 2.12 respectively.

The TRD is installed at radii of 2.9 m to 3.68 m with the pseudorapidity coverage of $|\eta| < 0.84$. It consists of 540 individual read-out detector modules divided into a total of 18 supermodules, each of them contains 30 modules. These modules are arranged in 5 stacks along the z direction and six layers in radius. Each module consists of a 48 mm thick radiator, a 30 mm thick drift section and a 7 mm thick multi-wire

Parameter	Value
Gas	Xe (85%)/CO_2(15%)
Drift velocity	1.5 cm/μs
Gas gain	$\sim$ 4000
Pre-Amplifier Shaper (PASA) gain	12 mV/fC
ADC depth	10 bit
Sampling frequency	10 MHz
Total number of pads	1.15×10^6
Total number of Multi-Chip Module (MCMs)	6.9×10^5
Material budget	$\sim 25\% X_0$

TABLE 2.4: Overview of TRD parameters

proportional chamber section with pad readout. The active gas medium used here is the combination of Xe/CO_2 (85:15). Particles exceeding the threshold for TR production ($\gamma \sim 1000$), produce about 1.45 additional X-ray photons in the energy range of 1 to 30 keV. X-rays in this energy regime are efficiently converted by the high-Z counting gas with the largest conversion probability at the very beginning of the drift region. All the primary electrons and the converted electrons drift towards the anode wires. In the vicinity of the anode wire, the gas amplification is done and the signal is induced on the readout pads. The readout electronics of TRD consists of 1.18 million channels. The signals of a typical track are shown in for a particle of momentum 2 GeV/c. The design parameters of TRD are tabulated in Table 2.4.

2.2.3.4 Time-Of-Flight (TOF)

ALICE TOF [20] detector is designed to identify particles produced in high energy collisions from 1 GeV/c (beyond the TPC limit) to a few GeV/c. It is located at 3.7 m from the beam axis. The TOF consists of a large cylindrical array ($\sim$ 170 m^2) of Multi-gap Resistive Plate Chamber (MRPC) strips operated in a $C_2H_2F_4$ (90%), C_4H_{10} (5%), SF_6 (5%) gas in the central pseudorapidity region ($-0.9 < \eta < 0.9$). A layout of the detector can be seen at Figure 2.13.

TOF consists of a 10 gap double-stack MRPC strip of 122 cm long and 13 cm width, with an active area of 120×7.4 cm^2 subdivided into two rows of 48 pads. It has

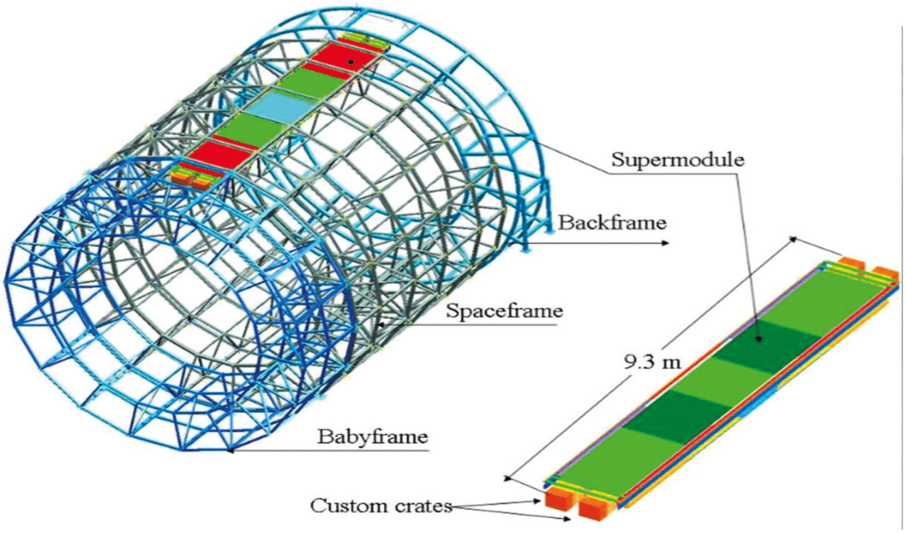

FIGURE 2.13: Layout of the ALICE TOF detector.

90 modules each of which is made of a group of MRPC strips (15 in the central, 19 in the intermediate and external modules) closed inside a box that seals the gas volume and supports the external front -end electronics. The detector covers a cylindrical surface and the modules are arranged in 18 sectors in ϕ and in 5 segments in the z-direction. The length of the central module is 117 cm, the intermediate ones 137 cm and the external ones are of 177 cm. The active region of the TOF barrel is 741 cm long. The chambers have high and uniform electric field over the full sensitive gaseous volume the detector and it has about 160,000 channels for signal readout.

The working principle of TOF detector is based on the measurement of mass of the particle from its flight time using the following equation:

$$m^2 = p^2(\frac{t^2}{L^2} - 1) \tag{2.3}$$

where m, p, t and L are the mass of the particle, the momentum, the time of flight and the track length respectively. ITS and TPC provide momentum information. The flight time, t, is t_{hit}-t_0 where the hit time (t_{hit}) is the time measured by TOF and t_0 is the time of interaction, measured by ALICE T0 detector or TOF itself. L is the particle track length ($\sim$ 3.7 m). For two particles of unequal mass m_1 and m_2 having the same momentum p and the same track length L, the time-of-flight difference can be measured

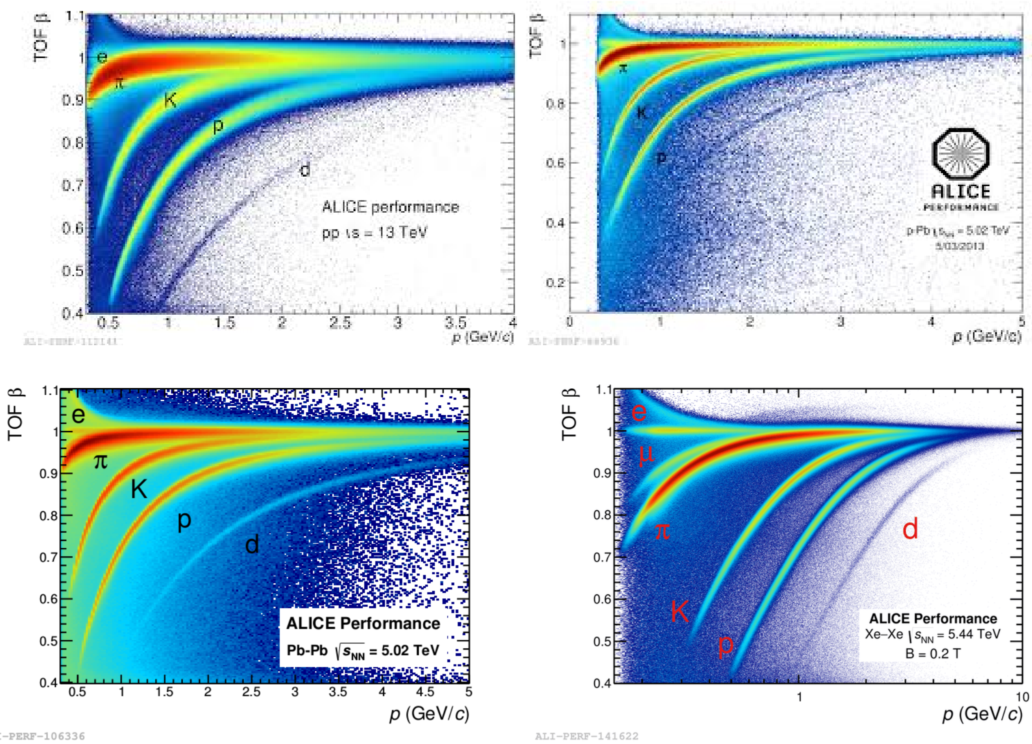

FIGURE 2.14: Energy loss in the TOF (dE/dx) versus momentum p (GeV/c) for different particles in pp collisions (top left), p-Pb collisions (top right), Pb-Pb collisions (bottom left) and in Xe-Xe collisions [21].

as:

$$t_1 - t_2 = \frac{L}{2}(\frac{m^2{}_1 - m^2{}_2}{p^2}) \tag{2.4}$$

The time-of-flight difference is related to the standard deviation of the time difference of the two particles. The nσ cut is applied for this:

$$n\sigma_{TOF} = \frac{t_1 - t_2}{\delta t} \tag{2.5}$$

where δt is the time resolution. With a global TOF time resolution of 80 ps, it provides a π/K and K/p separation better than 3σ up to a particle momentum p $\simeq$ 2.5 GeV/c and p $\simeq$ 4 GeV/c respectively. Figure 2.14 presents particle identification performance of TOF.

2.2.3.5 High-Momentum Particle Identification Detector (HMPID)

HMPID [22] is based on the proximity-focusing Ring Imaging CHerenkov (RICH) counters and it provides PID beyond the momentum interval attainable through energy-loss mechanism (in ITS, TPC and TOF). The working principle of the HMPID has been portrayed in Figure 2.15. It is optimised for a track-by-track identification for π/K and K/p up to 3 GeV/c and 5 GeV/c respectively. Particle identification performance of this detector can be seen in Figure 2.16.

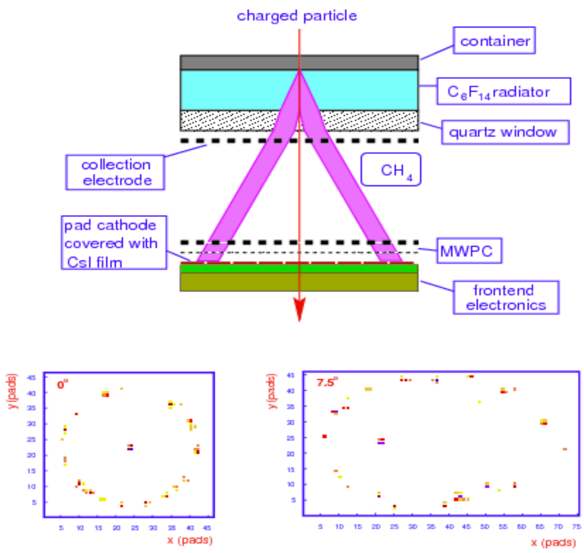

FIGURE 2.15: The working principle of the ALICE HMPID detector with the pad occupancy.

HMPID consists of seven modules of about 1.5 × 1.5 m^2 each, mounted in an independent support cradle which in turn is fixed to the space frame at two o'clock position. The momentum range defining radiator of HMPID is a 15 mm thick layer of low chromacity C_6F_{14} (perfluorohexane) liquid with refractive index n = 1.2989 at λ = 175 nm corresponding to β_{min} = 0.77. A multi-wire proportional chamber (MWPC) detects the cherenkov photons emitted while a fast charged particle traverses the thick radiator by using the novel technology of a thin layer of CsI deposited on the cathode pad of the MWPC, converting it into a photon counter. HMPID actually represents the largest scale application of this technique.

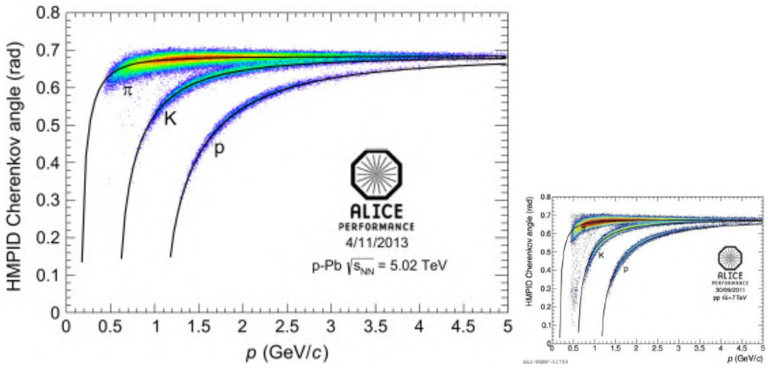

FIGURE 2.16: PID performance by HMPID in pp collisions (left) and in p-Pb collisions (right) [23].

2.2.3.6 The PHOton Spectrometer (PHOS)

PHOS [24] is a high resolution electromagnetic calorimeter made of lead tungstate crystals ($PbWO_4$) with a Charge Particle Veto (CPV) detector, covering a limited acceptance of $|\eta| < 0.12$ at central rapidity and 100^o in azimuth. It is located inside of the solenoid magnet at 460 cm from the interaction point and can be seen in Figure 2.17. The basic unit of the detector is a "crystal" of $22 \times 22 \times 180 mm^3$ dimension corresponding to 20 X_0 radiation lengths on which the Avalanche Photodiodes (APD) read out is directly glued. PHOS consists of 3 super modules (SMs) and 1 half SM. Each SM contains 56x64 crystals and in total, PHOS has 12,544 crystals.

The primary aim of PHOS is to measure and identify photon and neutral meson coming out from the produced hot QCD matter. It has been designed to detect photons produced over a wide energy range up to 100 GeV and reconstruct neutral mesons decaying to photons with very high energy and position resolutions. When the high energy photons or electrons cross the detector medium, they produce electromagnetic shower (via pair production and bremsstrahlung) which in turn produce light to be detected by the attached Avalanche Photo Diodes (APD) attached to it. However, the lead tungstate is so dense that it stops most of the incoming photons. In addition, the light yield in the crystals have a strong temperature depend. Therefore, in order to achieve a very good

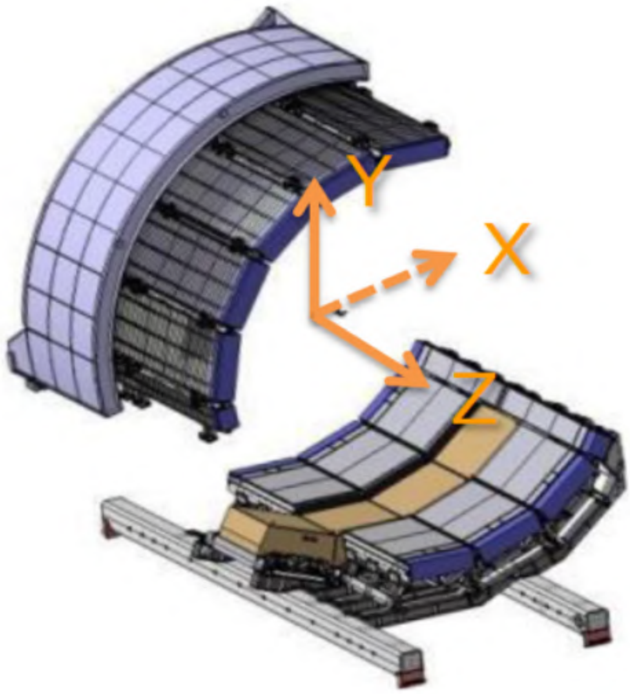

FIGURE 2.17: Three calorimeters installed in ALICE at Run2 period: EMCal (upper side), PHOS (bottom, drawn in orange) and DCal (placed on both side of PHOS in z-direction).

energy resolution, PHOS is operated under a temperature of -25^{o}C, where the noise is minimised.

2.2.3.7 Electromagnetic Calorimeters (EMCAL and DCAL (Di-Jet Calorimeter))

The EMCAL [25] and DCAL [26] are lead-scintillator sampling calorimeters with large acceptance, comprising 12,288 and 5,376 individual towers respectively. They are located at 45 cm from the beam line and inside the ALICE solenoid magnet occupying a cylindrical volume of approximately 110 cm deep in the radial direction. EMCAL and DCAL consist of module which is a sandwich of 77 plastic scintillator layers and 76 lead foils corresponding to 20.1 X_0 radiation lengths. Each module comprises 2 $\times$ 2 independent detection channels (towers). These calorimeters cover a pseudorapidity range $|\eta| < 0.7$ and $\Delta\phi = 107^{o}$. Each SM for EMCAL and DCAL has been arranged in the form of continuous arch, spanning 20^{o} in azimuth. There are two types of SMs in both the calorimeters, full size and one-third size. For EMCAL, each full size SM contains 24×12 modules and for DCAL it contains 16×12 modules while the one-third size SM for both the calorimeters comprise of 24×4 modules. There are a total of 10 full size and 2 one-third SM for EMCAL, whereas DCAL numbers 6 full size and 2 one-third SMs. All the parameters for the electromagnetic calorimeters (including PHOS) in ALICE has been tabulated in Table 2.5

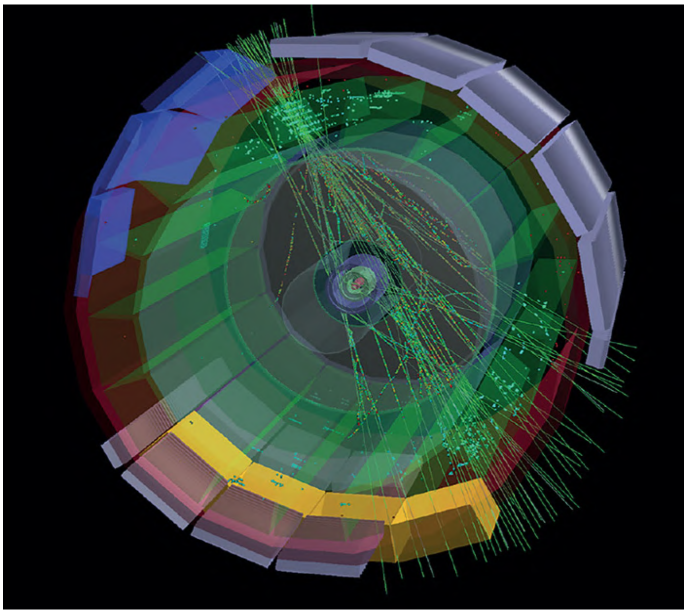

FIGURE 2.18: All the 3 calorimeters in ALICE with real-time events. In the top side there is EMCal, in the bottom PHOS is shown in orange and on both side of the PHOS, there is DCal.

A particle while crossing the module, interacts with the lead and induces electromagnetic cascade and make it scintillate. APD convert the light which is collected and guided by the double-clad wavelength-shifting (WLS) fibres, into an electrical signal. EMCAL and DCAL focus on jet physics for the improvement of jet energy resolution for QGP tomographic study. They complement the charged jet measurement by supplying the neutral particle information. Also because of the back-to-back layout in the azimuth, EMCAL and DCAL makes high precision hadron-jet and jet-jet correlation studies possible due to their agreement with the di-jet topology. The caloriemeters with real-time events display can be found at Figure2.18.

Parameter	PHOS	EMCAL	DCAL
Total weight	12.5 t	∼82 t	∼36 t
Number of SMs	3 SMs 1 half SM	10 SMs 2 one-third SMs	6 SMs 2 one-third SMs
Coverage	$250^o < \phi < 320^o$ $\|\eta\| < 0.13$	$80^o < \phi < 187^o$ $\|\eta\| < 0.7$	$260^o < \phi < 327^o$ $\|\eta\| < 0.7$
Tower size $\delta\eta \times \delta\phi$	$\sim 22 \times 22 \times 180mm^3$ 0.004 × 0.004	$\sim 60 \times 60 \times 246mm^3$ 0.0143 × 0.0143	$\sim 60 \times 60 \times 246mm^3$ 0.0143 × 0.0143
Effective Rad. Length X_0	20	20.1	20.1
Effective density	8.28 g/cm^3	5.68 g/cm^3	5.68 g/cm^3
Energy resolution	$3.3\%/\sqrt{E}\oplus1.1\%$	$7\%/\sqrt{E}\oplus1.5\%$	$7\%/\sqrt{E}\oplus1.5\%$

TABLE 2.5: Specifications of ALICE electromagnetic calorimeter.

2.2.3.8 ALICE COsmic Ray DEtector (ACORDE)

The ACORDE provides a fast (level-0) trigger signal for the commissioning, calibration and alignment procedures of some of the ALICE tracking detectors. As an independent cosmic ray detector, it also detects single atmospheric muons and multi-muons (so-called muon bundles) in combination with the TPC, TRD and TOF which allows us to study high-energy cosmic rays in the energy region of knee in the cosmic ray spectrum ($\tilde{}$few PeV).

The detector is located at the radial distance of 8.5 m from the beam line and covers a pseudorapidity range $|\eta| < 1.3$. It is an array of plastic scintillator counters placed on the upper surface of the L3 magnet. The detector consists of 60 modules and a single ACORDE module contains two scintillator counters each with 190x20 cm^2 effective area, placed on top of each other and read out in coincidence. The detector layout can be seen in Figure 2.19.

2.2.4 Muon Spectrometer (Muon Chamber (MCH) and Muon Trigger (MTR)

The muon spectrometer [28] in the forward region of ALICE features a very thick and complex front absorber and an additional muon filter consisting of an iron wall 1.2 m thick

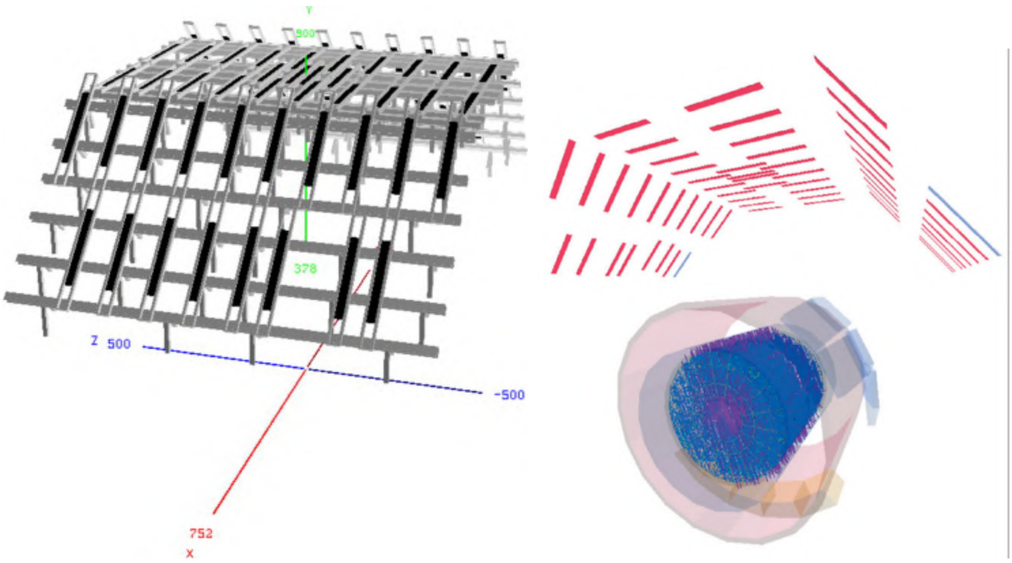

FIGURE 2.19: ALICE cosmic ray detector layout.

as shown in Figure 2.20. It covers the pseudorapidity interval $2.5 \leq \eta \leq 4$. The Muon spectrometer provides the measurement of the complete spectrum of heavy quarkonia ($J/\psi, \Psi', \Upsilon, \Upsilon', \Upsilon''$) via their decay in the $\mu^+\mu^-$ channel. The invariant mass resolution is of the order of 70 MeV in the charmonium (J/ψ and Ψ') region and about 100 MeV close to the bottomonium (Υ, Υ' and Υ'') region. The spatial resolution is better than 1 cm and the time resolution is 2 ns and these values are good enough to separate out all the five resonance states.

Muons with momenta below a few hundred GeV/c do not suffer from radiative energy losses and consequently do not produce electromagnetic showers. Moreover, because they are leptons, they are not subject to strong interactions with the nuclei of the material they traverse. All charged particles other than muons are completely stopped, producing electromagnetic (and hadronic) showers while passing through the absorber. Muon candidates selected from tracks penetrating these absorbers are measured precisely in a dedicated set of tracking detectors. The whole spectrometer consists of the mentioned absorber, high granularity tracking system of 10 detection planes, a large dipole magnet, a passive muon filter wall, four planes of trigger chambers and an inner beam shield to protect the chamber from primary and secondary particles produced at large rapidity. 10 cathode pads (multi-wire proportional chambers with segmented cathode plane using Ar-CO_2 gas mixed as 80:20 ratio) arranged in 5 stations with 2 chambers for

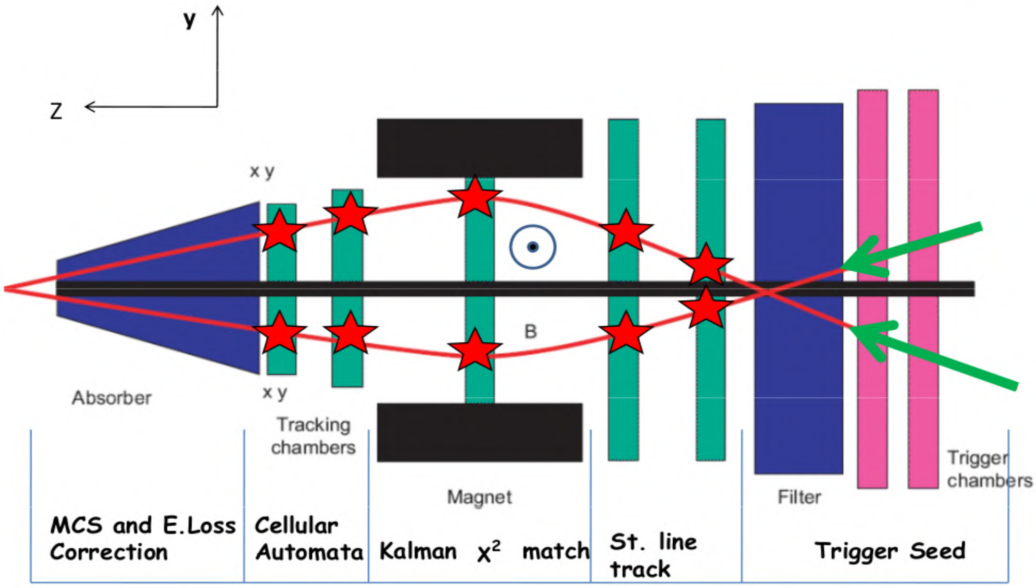

FIGURE 2.20: Layout of the Muon spectrometer.

each station make the tracking system. 1 million channels for the full set up of chambers, limit the occupancy within 5%. The trigger system selects heavy quark resonance decays on the basis of the p_T of the two individual muons. Four planes of Resistive Plate Chambers (RPCs) operated in a gas mixture of Ar, CH_2F_4, C_4H_{10} and SF_6 arranged in 2 stations and positioned behind a passive muon filter to provide the transverse momentum of each muon. For data recording, there are front end MANU board consisting of 4 MANAS chips each (pre-amplifier and shaper chip), several ADC's and the controller chip (Muon Arm Readout Controller). The data flow is gathered with the help of 100 front-end CROCUS board placed in 20 crates.

2.2.5 Forward detectors

2.2.5.1 ALICE Diffractive detector (AD0)

The ALICE Diffractive detector [29] has been installed in RUN-II operations of ALICE to overcome the limitation, on the selection of the diffractive events, by the means of rapidity gap. AD0 extends the detection capacity of the diffractive events in the ALICE in pp and Pb-Pb collisions by adding four planes of particle counters at very small angles with respect to the beam direction. The inclusion of AD0 as the diffractive physics trigger has contributed to the large number of recorded data as the 25% of the results of the collision events are diffractive in nature.

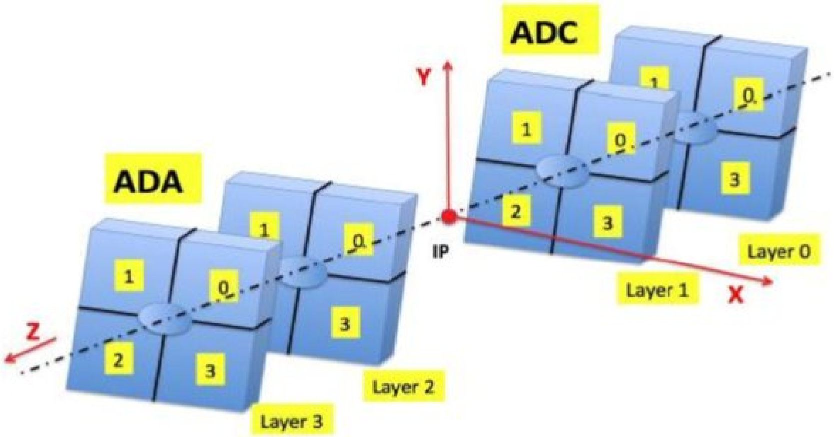

FIGURE 2.21: Schematic diagram of the AD0 detector.

AD0 consists of two sub-detectors, ADA and ADC, on both sides of the IP as shown in Figure 2.21. Each of the sub-detectors have two layers and each layer contains four scintillator modules arranged around the LHC beam-line. One module is made up of tile of plastic scintillator of dimension 216 mm $\times$ 181 mm $\times$ 25 mm, coupled to a pair of WLS bars. The light collected by the WLS bars is transmitted to the PMT.

2.2.5.2 Zero Degree Calorimeter (ZDC)

The ZDC [30] is calorimeter which detects the energy of the spectator nucleons in order to determine the overlap region of the two colliding nuclei and thus provides the centrality trigger. In addition, the ZDC, being a position-sensitive detector, can give an estimate of the reaction plane in nuclear collisions. The centrality information provided by ZDC is also used for triggering at Level 1.

In ALICE, two identical sets of hadronic ZDCs are located at 116 m away from the interaction point on both sides, exactly along the beam line. It is composed of total four calorimeters, of which two are to detect neutrons (ZN) placed between the beam pipes at 0^o relative to the LHC axis and two to detect protons (ZP) placed

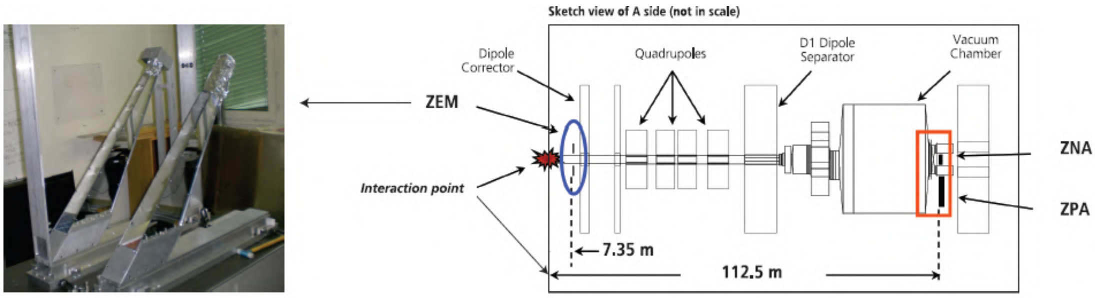

FIGURE 2.22: Schematic diagram of the ZDC detector.

externally to the outgoing beam pipe on the side where positive particles are deflective. The layout of the ZDC is shown in Figure 2.22. The measurement is complemented by an electromagnetic calorimeter (ZEM) located at z = 7.25 m covering a pseudorapidity range $4.8 < \eta < 5.7$ and it measures the total forward energy. The ZDCs are the "spaghetti calorimeters", made by the stack of heavy metal plates grooved to allocate a matrix of quartz fibres. The metal plates contain a tungsten alloy for neutrons and uses brass for protons. These metal plates act as the passive material while the quartz fibres act as the active material. High energy protons and neutrons while passing through the passive material, produce shower and these shower particles in turn produce light by the means of Cherenkov effects while passing through the fibres. The light is converted into electrical signal by the photo-multiplier attached at the end of the fibre. The amplitude of the electrical signal is proportional to the energy of the incoming protons and neutrons allowing to measure the energy carried away by the spectator nucleons and therefore, indirectly the size of the overlap region of the two colliding nuclei.

2.2.5.3 Photon Multiplicity Detector (PMD)

The ALICE PMD [31] is a pre shower detector which measures multiplicity and spatial distributions of photons in the forward rapidity region ($2.3 < \eta < 3.9$) with full azimuthal coverage. It consists of gaseous proportional counters, made of two identical planes with a lead converter of thickness $3X_o$ sandwiched between them. The photons, while passing through the lead plate produce a shower of positrons and electrons by the combined effect of two processes, pair production and bremsstrahlung and these charged particles are detected in the granular gaseous detector producing electrical signal and the front-end electronics read them. In Appendix A, PMD has been discussed in detail.

2.2.5.4 Forward Multiplicity Detector (FMD)

The FMD [32] extends the coverage for multiplicity of charged particles into the forward regions giving ALICE the widest coverage of the four LHC experiments for these measurements. It provides the measurement of charged particle multiplicity in the pseudorapidity range $-3.4 < \eta < -1.7$ and $1.7 < \eta < 5$ in full azimuthal angle. FMD helps to study in the area of event-by-event multiplicity fluctuations, reaction plane determination and elliptic flow measurement. In conjunction with PMD, FMD can also be used to study the correlation between photons and charged particles in forward rapidity.

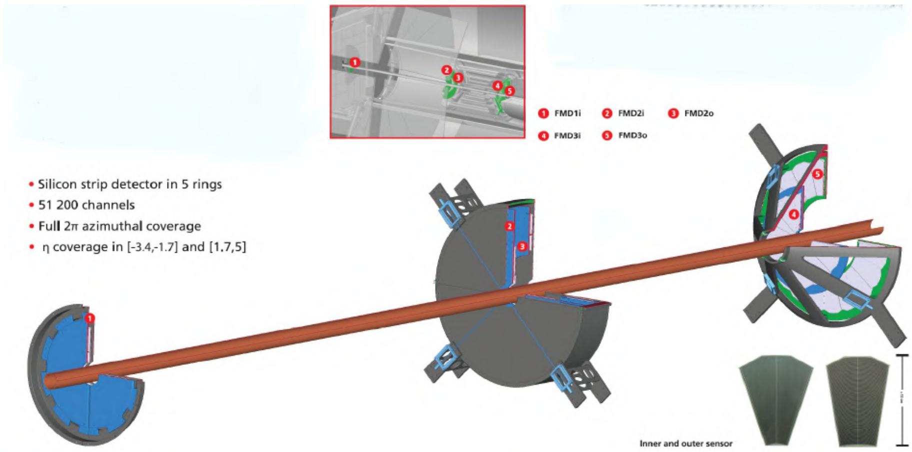

FIGURE 2.23: The ALICE Forward Multiplicity Detector layout.

FMD is made of 5 silicon discs, each having 10,240 individual detector channels to detect the charged particles emitted at small angles relative to the beam. The locations of the FMD rings and the basic layout is shown in Figure 2.23. The discs are basically of two types: the inner type consists of 10 wafers subdivided into 20 sectors with 1024 channels each and the outer type is subdivided into 40 sectors each with 512 strips. The silicon wafers are 300 μm thick and are manufactured out of Si discs of 6 μm diameter. The FMD consists of three groups of detectors called FMD1, FMD2 and FMD3. FMD1 consists of a ring of inner type Si sensors and placed opposite to the muon spectrometer. Each of FMD2 and FMD3 consists of a ring of inner type Si sensors and a ring of outer type Si sensors and they are located on either side of the IP.

2.2.5.5 V0 detector

The V0 [32] detector is a forward detector consisting of two arrays of 32 scintillating counters in 4 rings, called V0A and V0C, which sits on each side of the IP as shown in Figure 2.24. The V0A is located 330 cm away from the primary vertex covering the pseudorapidity range $2.8 < \eta < 5.1$ while the V0C is mounted at 90 cm in the opposite direction in the pseudorapidity region $-3.7 < \eta < -1.7$. Each of these rings are divided into 8 sectors (45^o) in azimuth and covers pseudorapidity unit of 0.5 and 0.6. V0 detector is designed to provide:

- Minimum bias trigger for central detectors
- Discrimination of beam-gas interactions by correlating V0A and V0C
- Luminosity information
- Estimation of collision centrality and event plane by V0A and V0C amplitudes
- Measurement of the charged particle multiplicity density

V0 is made by plastic scintillator BC404 (2.5 and 2.0 cm thickness for V0A and V0C respectively). The scintillating light is collected by photo-multipliers (PMT) through Wave Length Shifting (WLS) fibres of 1 mm in diameter.

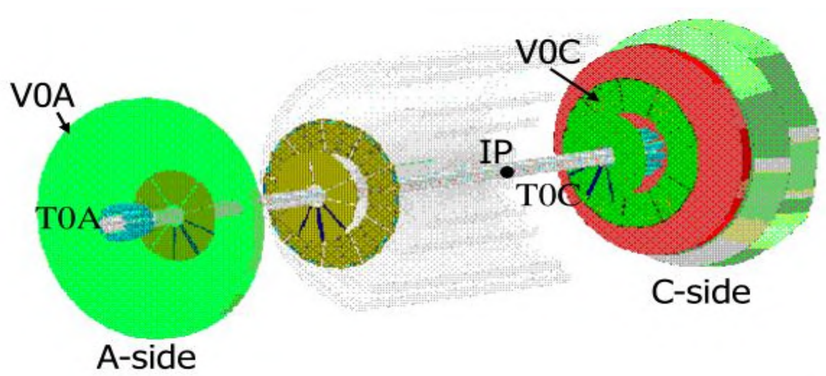

FIGURE 2.24: The layout and positions of T0 and V0 detectors..

2.2.5.6 T0 detector

The T0 [32] detectors are a pair of Cherenkov counters, T0A and T0C, surrounding the beam pipe at 4.61 < η < 4.92 and -3.28 < η < -2.97 respectively, to measure the initial time of the collision event with a good resolution of about $\approx$ 50 ps and to provide vertex and centrality information. T0 is the fast timing and trigger detectors in ALICE. It delivers an early (prior to L0 trigger) wake-up to the TRD and gives a precise start signal for TOF. It can also measure the vertex position with a precision of $\pm$1.5 cm, for each interaction and generates L0 trigger when the trigger is within the reset values allowing a discrimination against the Beam-Gas interactions.

The T0A is located at 375 cm from the IP while T0C is at 72.7 cm from the IP. Both T0A and T0C are segmented into 12 individual counters. The T0 signal is generated online by a mean timer. The position of the T0 signal on the time axis is equal to (T0C + T0A)/2 + T_{delay}, where T_{delay} is the fixed delay of the analog mean timer. The position of vertex is measured as (T0A-T0C) and this value is sent to a digital discriminator with preset upper and lower limits thus providing the $T0_{vertex}$ trigger signal.

2.2.6 ALICE data taking: Online

ALICE data recording is based on some systems involving detector activities and some logic conditions. The activities can be broadly categorised into four online activity domains:

- Detector Control System (DCS)
- Trigger (TRG)
- Data Acquisition (DAQ)
- High Level Trigger (HLT)

The Experiment Control System (ECS) sits on the top of the hierarchy tree of the online systems as shown in Figure 2.25. ECS coordinates the operations controlled by the online systems [11, 33]. It permits independent, concurrent activities on part of the experiment by different operators and coordinates the functions of the all the online systems for all the detectors. The components of the ECS receive status information from the online systems and send commands to them through interfaces based on Finite State Machines (FSM).

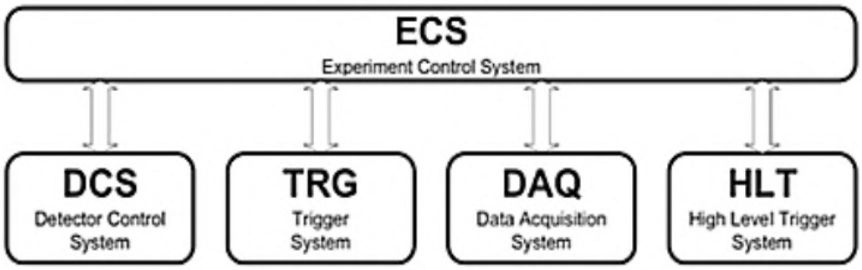

FIGURE 2.25: The online control system in ALICE.

2.2.6.1 Detector Control System (DCS)

The DCS [34] is the online module which controls all the detector services like the cooling system, the ventilation system, the magnetic fields, high and low voltage power supplies, monitoring of the Front-End Electronics etc. The interface provides remote control and monitoring for all the detectors, for the smooth execution of the experiment from the ALICE Run Control (ARC) room at the LHC point 2.

2.2.6.2 Trigger system (TRG)

The interaction rate at the LHC luminosity is much higher than the possible data acquisition rate and for this a trigger system was needed to make a decision whether an event needs to be recorded [35]. The trigger system consists of two basic parts: Central Trigger Processor (CTP) and Local Trigger Unit (LTU). With each positive decision, trigger signals are sent to all the detectors in order to make them synchronized and ready for data recording. The CTP is the decision making unit and the LTUs are the interface between the CTP and the readout detectors. The ALICE trigger system has 3 levels: L0, L1 and L2 with latencies 1.2 μs, 6.5 μs and 88 μs respectively.

- The trigger signal of the lowest level (level 0, L0) reaches the detectors after a delay of only 1.2 μs and can provide simple information as whether there was a collision or what its multiplicity is. The L0 trigger inputs (L0b, b for "before the CTP") are the first to arrive to the CTP. They are sent by detectors such as V0, T0, SPD, EMCAL, PHOS and MTR. The CTP sends a L0 trigger signal (L0a, a for "after the CTP") to the corresponding read-out detectors in the trigger cluster.

- The L1 trigger inputs are sent to the CTP by detectors such as the TRD, ZDC and EMCAL after the online calculation of some characteristic of an event. The CTP makes a decision and sends a L1 trigger signal, which arrives to the read-out detectors with 6.5 μs delay. If the L1 trigger signal does not arrive on time to the read-out detectors they ignore the event.

- The subsequent trigger level L2 waits for the end of the so-called "past future protection interval" to reject pile-up events. The length of this interval is essentially defined by the TPC readout time ($\sim$100 μs). At nominal LHC luminosities a pile-up of events is frequent. The L2 trigger logic has to take care of that its degree is still tolerable and the event has not been spoiled. The L2 delay time can also be used to apply more complex trigger algorithms.

The output from the CTP go to the 24 LTUs for each detector and then to the front-end electronics of the respective detectors via LVDS cables and optical fibres.

CTP can form up to 50 independent trigger classes combining 24 L0 inputs, 24 L1 inputs and 12 L2 inputs [36]. Information from the V0 detector and SPD detector are combined to form the $Minimum - Bias$ triggers which is designed to trigger on all the inelastic interactions; the following table shows some trigger combinations. The signal names, V0or means a hit in the appropriate time window on either side of the V0 and BEAMGASor, BEAMGASc are to signals in the time windows for beam gas on either side (suffix 'or') or coming from C-side (suffix 'c') [11]. Various triggers conditions have been summarized in Table 2.6.

Number	Description	Conditions
1	MB1	V0or $\bigoplus$ PIXELor $\bigodot$ BEA$\bar{M}$GASor
2	MB2	V0or $\bigodot$ PIXELor $\bigodot$ BEA$\bar{M}$GASor
3	MB3	V0and $\bigodot$ PIXELor $\bigodot$ BEA$\bar{M}$GASor
4	BG	BEAMGASor
5	BGDM	BEAMGASc

TABLE 2.6: The list of trigger classes with trigger conditions. The symbols $\bigoplus$ and $\bigodot$ indicate OR and AND operations respectively.

2.2.6.3 Data AcQuisition (DAQ) System

The ALICE DAQ [37] handles the data flow from the sub-detector electronics to the permanent storage. The DAQ is designed to process a data rate of up to 1.25 GB/s in heavy-ion collisions. The trigger and DAQ systems work in sync to balance the capacity to record the collisions which generate large events with ability to acquire the largest possible fraction of rare events and finally to archive the data to permanent data storage. The event building mechanism consists of two steps: the sub-detectors send the data through the Detector Data Links (DDLs) to the Local Data Concentrators (LDCs) and the LDCs, after organising the data into sub-events, pass it to the Global Data Collectors (GDCs). The GDCs archive the data over the storage network as data files of a fixed size to the Transient Data Storage (TDS). During a run period, each GDC produces a sequence of such files and registers them in the ALICE Grid software (AliEn). The data files are then read by the TDS movers (TDSM) over the storage network and exported to the computing centre where they are recorded to the Permanent Data Storage (PDS). Schematic diagram of the DAQ system has been shown in Figure 2.26.

The DATA Acquisition and Test Environment (DATE)

The DATE [37, 38] controls and synchronizes the processes running in the LDCs and the GDCs and can run on an LDC, GDC or any other computer. It is basically a distributed and process oriented software framework. It is based on standard Unix system to process synchronization and data transmission and uses MySQL for the system configuration.

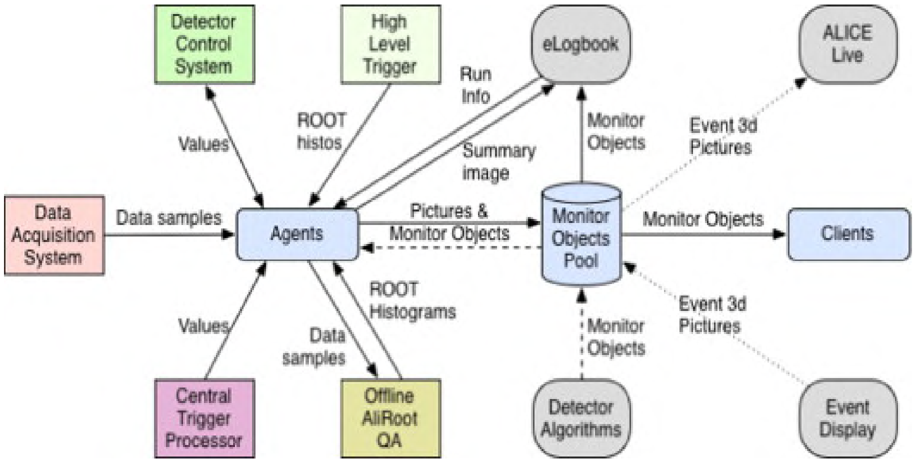

FIGURE 2.26: The DAQ system of ALICE.

The DAQ framework for the Monitoring Of Online Data (MOOD)

MOOD [39, 40] is a data visualization and data quality monitoring tool for the data recorded by the ALICE detectors. It has an interface with the DATE and a detector-specific part that can be customized to detector specific requirements. MOOD can handle on-line and off-line data streams, available on the LDCs and on the GDCs. The system is compatible with the ALICE common event data format and is integrated with ROOT-AliROOT environment.

The DAQ framework for the Automatic MOnitoRing Environment (AMORE)

AMORE [41] is the automated data quality monitoring system which continuously checks a set of physics plots filled by the detectors against the reference ones. It has three components: the client part that collects the data, the server part that accumulates the plots and archives them, and the display which gives an interactive distributed access to the plots archives. The system raises alarms as soon as the generated plots do not conform anymore to the expected reference and these alarms are displayed on the operator screens with automatic recovery actions.

2.2.6.4 High Level Trigger (HLT)

The main purpose of the HLT [42] is to reduce the data volume by well over one order of magnitude in order to fit the available storage bandwidth while retaining the physics information. In order to meet the high computing demands, the HLT consists of a PC farm of up to 1000 multi-processor computers. The raw data of all ALICE detectors are received by HLT via 454 Detector Data Links (DDLs) at layer 1. The first processing layer performs basic calibration and extracts hits and clusters (layer 2). This is done in part with hardware co-processors and therefore simultaneously with the receiving of the data. The third layer reconstructs the event for each detector individually. Layer 4 combines the processed and calibrated information of all detectors and reconstructs the whole event. Using the reconstructed physics observables, layer 5 performs the selection of events or Regions-of-Interest (RoI), based on run specific physics selection criteria. The selected data is further subjected to complex data compression algorithms to reduce the data rate from 25GB/s to 1.25GB/s and stored to PDS.

2.2.7 ALICE data analysis and computing: Offline

The ALICE offline computing project focuses on the development and smooth operation of the data processing framework which handles simulation, reconstruction, calibration, alignment, visualization and physics analyses. During active run, the amount of data produced by the LHC comes in trillion bytes and this is beyond the capability of a single computing centre to handle those. For this, the job data processing is distributed over several computing centres worldwide [11]. The ALICE-Grid [43] provides the necessary automated system for data reconstruction and analysis. The Grid-Middleware connects the distributed resources and makes it an integrated one. ALICE has developed an environment (AliEn [44]) which provides the user interface with the Grid.

The distributed computing infrastructure serving the LHC experimental program is coordinated by the Worldwide LHC Computing Grid (WLCG). The WLCG is highly hierarchical by nature. All real data originate from CERN, at a very large computing centre called $Tier-0$. Large regional computing centres, called Tier-1, share with CERN the role of a safe storage of the data. Smaller centres, called Tier-2 (e.g., VECC, Kolkata), are logically clustered around the Tier-1 centres. The main difference between the two is the availability of high reliability mass-storage media at Tier-1. The major role of Tier-2 centres is simulation and end-user analysis. Smaller centre, corresponding to departmental computing centre and sometimes called Tier-3's, contribute to the computing resources but there is no definite role or definition for them.

The reconstruction of ALICE events, simulation are performed by the ALICE offline framework called AliRoot [45] which is based on the object oriented programming language C++ which in turn is based on the ROOT [46] platform. AliRoot package was developed for event generation, detector simulation, event reconstruction and physics analysis. It is also incorporated with advanced statistical analysis tool like histogram filling, random number generation, fitting and many more. ALICE also gives access to its users to a system called CERN Analysis Facility (CAF) which enables the use of parallel computing cluster to perform different analysis.

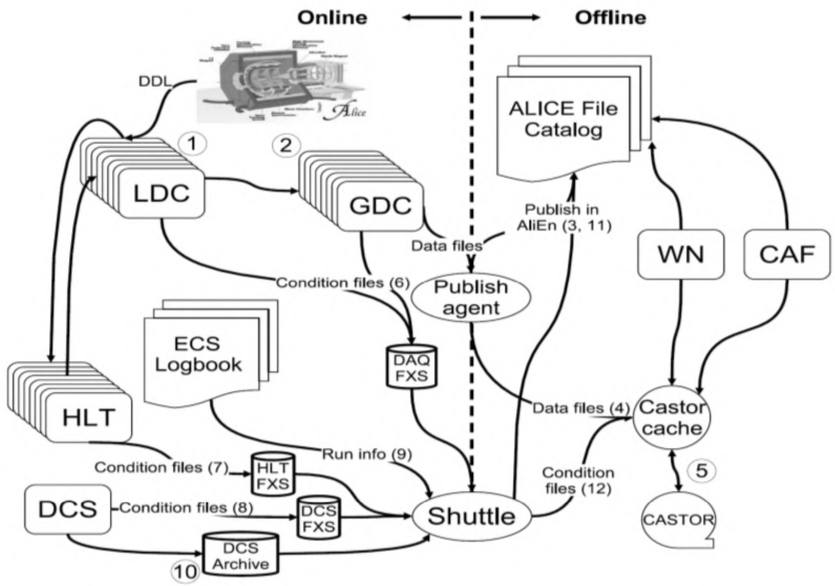

FIGURE 2.27: Global view of the data flow in ALICE.

2.2.7.1 Raw data flow

The raw data recorded by the detectors are first processed before being made available in the form of reconstructed events. The strategy for data processing varies according to the type of collisions. In pp collisions, the data taken by the detectors are written by the DAQ on a disc buffer at the Tier-0 (at CERN) computing centre with another copy of this raw data being written on the CASTOR tapes exported to the Tier-1 centres. In Tier-1 facilities the second distributed copy goes through successive reconstruction passes to be processed there. At the Tier-0, raw data undergoes the very first processing (reconstruction, processing of alignment and calibration constants and the scheduled analysis) and then the selected data follows "fast processing" on the CERN Analysis Facility (CAF). During the heavy-ion runs, the processing of raw data is done in the following steps

- Registration of raw data in CASTOR
- Partial export to Tier-1 centres for remote users
- Partial first pass processing at the Tier-0 centre to provide rapid feedback on the offline chain
- Fast processing and analysis on CAF

High precision alignment and calibration of the data are done during the first pass reconstruction and the first set of Event Summary Data (ESD) and Analysis Object Data (AOD) are produced. The feedback derived from the first pass, including analysis, is used to tune the code for the second pass of reconstruction and shared by the Tier-1 centres. Subsequent data reduction, analysis and Monte Carlo production is a collective operation where all Tiers participate, with Tier-2 being particularly active for simulation and end-user analysis. Figure 2.27 presents data flow shematics in ALICE.

2.2.7.2 AliEn framework

The Grid facility is developed for unification of resources of distributed computing centres, computing power and storage to users all over the world. It is built on Open Source components and uses a set of middleware tools, protocols and services that implement a Grid infrastructure. The Grid gives the advantage of analyzing a large set of data by splittings one analysis job into many clone sub-jobs running in parallel on different computing nodes. The ALICE VO (Virtual Organisation) is made of more than 80 sites distributed worldwide (in more than 20 countries) and Figure 2.28 presents the European sites. The users interact with the Grid through the AliEn web services by the exchange of Simple Object Access Protocols (SOAP) messages and they constantly exchange messages between themselves behaving like a true web of collaborating services.

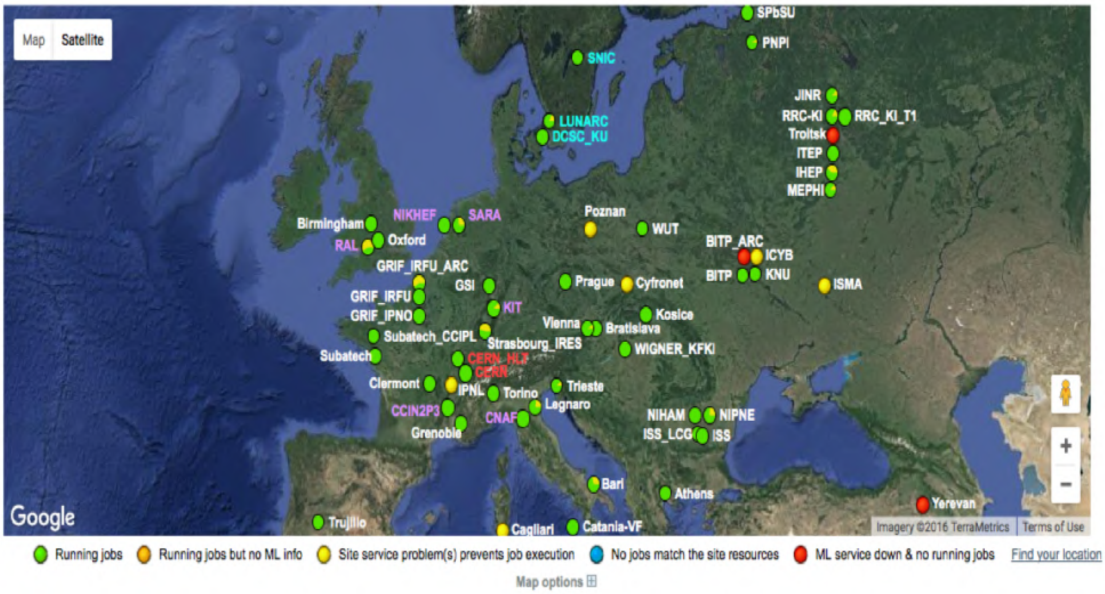

FIGURE 2.28: A snapshot of the ALICE V0 sites in Europe. A green circle indicates that jobs are running on the site while red and yellow circles indicate sites that are facing trouble.

2.2.7.3 The AliRoot platform

As already introduced, AliRoot [45] is the offline framework developed by ALICE for simulation, alignment, calibration, reconstruction, visualization, quality assurance and analysis of experimental and simulated data. This ALICE specific framework has been built on the general purpose backbone of ROOT[46]. The schematic diagrams of the AliRoot framework have been shown in Figure 2.29. The codes are written mostly in C++ with some parts written in FORTRAN that are wrapped inside C++ codes. The whole framework works as follows:

- **Event generation:** Event simulation is performed through events generators like

PYTHIA [47, 48], HIJING [49], PHOJET [20, 21], DPMJET [52] etc. with AliRoot interface. It produces the "Kinematics Tree" containing the full information on the generated particles (type, momentum, charge, production process, originating particle and decay products).

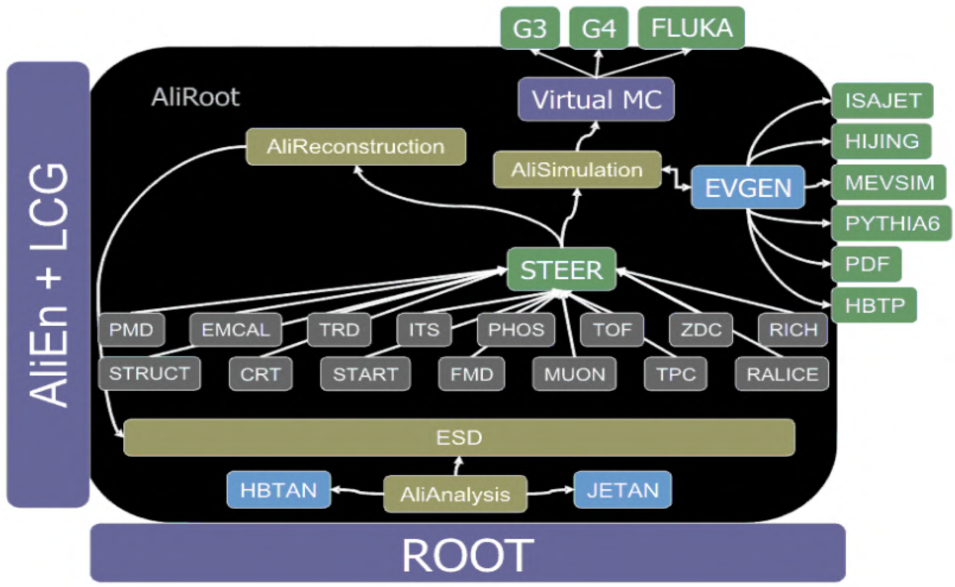

FIGURE 2.29: Schematic diagram of the AliRoot framework.

- **Particle transport:** In order to transport the produced particles through realistic detector geometry, AliRoot is incorporated with Monte Carlo packages like GEANT3 [18], GEANT4 [54] and FLUKA [55]. They help to fetch realistic detector response as the experiment itself.

Alignment framework

The AliRoot-framework is also equipped with the tools to take care of the misalignment in positioning the part of detectors, known as the alignable volumes, from their ideal positions. During the start of the simulation, the ideal geometry is generated by the compiled code or read from the Offline Conditions Data Base (OCDB) where it was saved in previous run. The objects marked as alignable, receive modifications by the geometrical modeller, even if they were obtained by replication and particles are transported through the modified geometry. This alignment procedure is tested by repeating it during the reconstruction of the data. During the real data reconstruction, best alignment objects are loaded from the OCDB. These are the alignment objects produced from the survey data which are stored in the Grid. Alignment objects are stored in the OCDB and accessed via meta-data.

Calibration framework

All the cells or units of a single sub-detector can show different gains and for this, calibration of each detector is needed before recording the data. For first reconstruction pass, initial calibration constants come from the detector properties as measured during construction or taken from the online algorithms running during data taking and the calibration constants are finally stored in the OCDB. These calibration files get updated in every reconstruction pass.

The information of the produced particles are digitized after their transportation through the detector simulation and those are stored as specific hardware format of the detector. The next step in the chain is the reconstruction of the real events as well as that of the simulated events. The reconstruction for real and simulated data follows the same procedure and includes the inputs from ITS, TPC, TRD, TOF and HMPID. Figure 2.30 shows schematic diagram of the reconstruction framework.

- **Cluster finding:** Particles that interact with the detector usually leave a signal in several adjacent detecting elements or in several time bins of the detector. In this step, all these signals are combined to form clusters. Basically, a cluster is a set of digits adjacent in space and time, presumably generated by same particle.

- **Primary vertex reconstruction:** Primary vertex reconstruction is done in two steps. First, primary vertex is estimated by SPD prior to tracking. Second iteration of 3D vertex determination is performed using already reconstructed tracks. Approximation of z-coordinate of primary vertex in SPD is obtained from the distribution of reconstructed space-points in first pixel layer, using a threshold cut on the position along beam axis. Transverse plane coordinate is determined similarly from x and y distribution of these points. Then linear approximations of tracks are done using points in first and second layer of ITS omitting correlations between points whose $\Delta\varphi > 0.1^o$.

Tracks reconstructed in TPC and ITS are approximated as straight lines at the point of closest approach to nominal primary vertex. All tracks pairs are used to determine the set of centres of closest approach for each track pair. Primary vertex is calculated as an average of these centres, and gives improved estimate on vertex position. Vertex position is determined by minimizing track distances of closest approach to this vertex,

$$\chi^2(\overrightarrow{r_v}) = \sum_i (\overrightarrow{r_v} - \overrightarrow{r_i})^T V_i^{-1} (\overrightarrow{r_v} - \overrightarrow{r_i}) \tag{2.6}$$

where $\overrightarrow{r_v}$ is position of vertex, $\overrightarrow{r_i}$ is point of closest approach of track i to vertex, V is co-variance matrix for point $\overrightarrow{r_i}$. Tracks giving contribution larger than χ^2_{max} are excluded from primary vertex determination and considered for determination of secondary vertices, kinks or decaying neutral particles.

- **Track reconstruction:** Track parameters are determined locally using Kalman filter [56–58], which is advantageous in fitting and track recognition. Additionally, it has greater possibility to reject incorrect space-points on-fly, and can handle multiple scatterings and energy loss. Furthermore, it can be used to easily extrapolate tracks from one detector to another.

  Clusters are found in all detectors. Starting from TPC, reconstruction proceeds from the outer to inner radius due to the minimal density of reconstructed clusters. Reconstruction of each track starts at a seed. Going from outer to inner radii, clusters are associated to existing seeds, or track candidates, refitting track parameters. When inner TPC is reached ITS clusters are processed in the same way, elongating tracks to primary vertex and improving track parameters.

  Afterwards, stand-alone ITS tracking is done on clusters not associated to any track. This may recover tracks not found in TPC. Subsequently, tracking is resumed starting from the primary vertex proceeding to outer TPC radii and extrapolating tracks to TRD, TOF, HMPID. TRD clusters are also taken into consideration

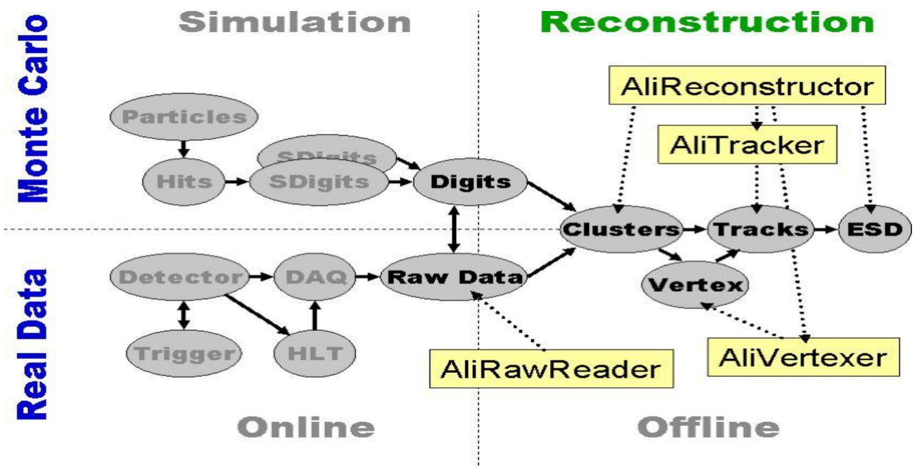

FIGURE 2.30: The schematic diagram of the ALICE reconstruction framework..

to improve the resolution of the tracks and to help with particle identification. Similarly, TOF and HMPID are used to determine particle type.

- **Secondary vertex reconstruction:** In order to reconstruct the decay daughter particles, tracks are combined to find the secondary vertices. Opposite-sign tracks that originate sufficiently far away from the primary vertex are combined. If distance of closest approach (DCA) is below some predetermined value and the topology of the two tracks is consistent with a decay, the pair is accepted as a candidate for a secondary decay vertex. Different topological cuts are imposed at different physics analysis level.

The data after passing through the reconstruction is called the Event Summary Data (ESD). It contains the full information of a track (particle) like the vertex, PID related information, positions of secondary vertex, parameters of particles reconstructed in the calorimeter and integrated signals of some sub-detectors. Due to the full event information, ESD consumes huge size and it is reduced down to relatively smaller analysis friendly format known as Analysis Object Data (AOD). AOD can also be enriched with additional information for different physics studies if necessary. The entire analysis activities are categorized into two parts: scheduled and end-user analysis. The analysis framework is developed which can be used for both the categories. The analysis framework permits the splittings of each analysis into a tree of dependent tasks. Each task is data oriented, it registers the required input data and publishes the output. The framework is used extensively for obtaining the results presented in this thesis.

2.2.7.4 CERN Analysis Facility (CAF)

The CERN Analysis Facility provides interactive and prompt analysis of pp data, pilot analysis of the Pb-Pb data, fast event reconstruction, calibration and alignment. CAF gives access to a part of the Grid data recorded by the experiment and some simulated data. The users can access the data and perform their analysis and tests using a parallel computing facility which is based on ROOT framework and known as Parallel ROOT Facility (PROOF) [59]. CAF is a very useful facility for quick checks on the experimental data, generating reliable parameters needed during the reconstruction such as calibration constants etc before the second reconstruction pass.

Bibliography

[1] T.S. Pettersson (ed.), P. Lefevre (ed.), The Large Hadron Collider : conceptual design, CERN-AC-95-05 LHC (1995)

[2] LHC Design Report Volume I+II+III, CERN-2004-003-V-1, CERN-2004-003-V-2, CERN-2004-003-V-3 (2004), http://ab-div.web.cern.ch/ab-div/Publications/LHC-DesignReport.html

[3] L. Evans and P. Bryant. LHC Machine. JINST , 3:S08001 (2008)

[4] LHC statistics. https://lhc-statistics.web.cern.ch/LHC-Statistics

[5] ALICE Collaboration, The ALICE experiment at the CERN LHC, JINST 3:S08002 (2008)

[6] ALICE Collaboration, URL http://alice-collaboration.web.cern.ch

[7] ATLAS Collaboration, ATLAS Technical Proposal, CERN/LHCC 94-43 (1994)

[8] CMS Collaboration, The Compact Muon Solenoid Technical Proposal, CERN/LHCC 94-38 (1994)

[9] LHCb Collaboration, LHCb Technical Proposal, CERN/LHCC 98-4 (1998)

[10] LHCf Collaboration, Technical Proposal for the CERN LHCf Experiment, CERN/LHCC 2005-032 (2005)

[11] TOTEM Collaboration, TOTEM Technical Proposal, CERN/LHCC 99-7 (1999)

[12] MoEDAL Collaboration, Technical Design Report of the Moedal Experiment, CERN-LHCC-2009-006; MOEDAL-TDR-001(2009)

[13] J.L. Feng, I. Galon, F. Kling, and S. Trojanowski, PRD97, 035001 (2018)

[14] ALICE Collaboration, ALICE Inner Tracking System (ITS): Technical Design Report, CERN-LHCC-99-012 (1999), http://edms.cern.ch/file/398932/1

[15] ALICE Collaboration, ALICE time projection chamber: Technical Design Report, CERN-LHCC-2000-001 (2000), http://cdsweb.cern.ch/record/451098

[16] ALICE Collaboration, EPJ Web of Conference 70, 00029 (2014)

[17] ALICE Collaboration, Int. J. Mod. Phys. A29, 1430044 (2014)

[18] W. Blum, W. Riegler, and L. Rolandi, Springer-Verlag, 2nd edition (2008)

[19] ALICE Collaboration, Technical Design Report of the Transition Radiation Detector, CERN/LHCC 2001-021 (2001) http://cdsweb.cern.ch/record/519145

[20] ALICE Collaboration, Technical Design Report of the Time of Flight System, CERN/LHCC 2000-012 (2000) http://cdsweb.cern.ch/record/430132; ALICE Time-Of Flight system (TOF): addendum to the technical design report, CERN-LHCC-2002-016 (2002) http://cdsweb.cern.ch/record/545834

[21] ALICE Collaboration, Nuclear Instruments and Methods in Physics Research A706, 29-32 (2013)

[22] ALICE Collaboration, Technical Design Report of the High Momentum Particle Identification Detector, CERN/LHCC 98-19 (1998) http://cdsweb.cern.ch/record/381431

[23] ALICE Collaboration, Nucl. Inst. Meth. Phys. Res. A 766 19-21 (2014)

[24] ALICE Collaboration, Technical Design Report of the Photon Spectrometer, CERN/LHCC 99-4 (1999) http://cdsweb.cern.ch/record/381432

[25] ALICE Collaboration, The Electromagnetic Calorimeter Addendum to the Technical Proposal, CERN-LHCC-2006-014 (2006) http://cdsweb.cern.ch/record/932676

[26] ALICE Collaboration, ALICE DCal: An Addendum to the EMCal Technical Design Report Di-Jet and Hadron-Jet correlation measurements in ALICE, CERN-LHCC-2010-011 ; ALICE-TDR-14-add-1 https://cds.cern.ch/record/1272952

[27] A. Fernndez et al., Cosmic ray physics with the ALICE detectors, Czech. J. Phys. 55 B801 (2005); A. Fernndez et al., ACORDE a cosmic ray detector for ALICE, Nucl. Instrum. Meth. A 572 102 (2007)

[28] ALICE Collaboration, ALICE dimuon forward spectrometer: Technical Design Report, CERN-LHCC-99-022 (1999) http://cdsweb.cern.ch/record/401974; ALICE dimuon forward spectrometer: addendum to the Technical Design Report, CERN-LHCC-2000-046 (2000) http://cdsweb.cern.ch/record/494265

[29] J.C. Cabanillas et al., J. Phys.: Conf. Ser.761 012025 (2016)

[30] ALICE Collaboration, ALICE Zero-Degree Calorimeter (ZDC): Technical Design Report, CERN-LHCC-99-005 (1999) http://cdsweb.cern.ch/record/381433

[31] ALICE Collaboration, ALICE Photon Multiplicity Detector (PMD): Technical Design Report, CERN-LHCC-99-032 (1999) http://cdsweb.cern.ch/record/451099 ALICE Photon Multiplicity Detector (PMD): addendum to the technical design report, CERN-LHCC-2003-038 (2003) http://cdsweb.cern.ch/record/642177

[32] ALICE Collaboration, ALICE forward detectors: FMD, TO and VO: Technical Design Report, CERN-LHCC-2004-025 (2004) http://cdsweb.cern.ch/record/781854

[33] THE ALICE EXPERIMENT CONTROL SYSTEM, F. Carena et. al, CERN, Geneva, Switzerland

[34] P.Chochula et al., 9th Workshop on Electronics for LHC Experiments, pp.316-320 (2003)

[35] ALICE trigger system for newcomers, ALICE twiki: http://www.ep.ph.bham.ac.uk/twiki/bin/view/ALICE/AliceTriggerIntroduction.

[36] ALICE Collaboration, ALICE Technical Design Report of the Trigger, Data Acquisition, High-Level Trigger, Control System, CERN/LHCC 2003/062 (2004) https://edms.cern.ch/document/456354/2

[37] F. Bergsma et al., CERN ALICE DAQ Group, ALICE DAQ and ECS users guide, ALICE Internal Note ALICE-INT-2005-015 (2005) http://cdsweb.cern.ch/record/960457.

[38] J. P. Baud et al., ALICE data challenge III, ALICE Internal Note ALICE-INT-2001-36 (2001) https://edms.cern.ch/document/336659/1

[39] O. Cobanoglu, et al., Development of an on-Line data quality monitor for the relativistic heavy-ion experiment ALICE, Proceedings of the IEEE RT2005, Real Time Systems conference, Stockholm Sweden (2005) http://dx.doi.org/10.1109/RTC.2005.1547409

[40] O. Cobanoglu, et al., The ALICE-LHC online data quality monitoring framework: present and future, Proceedings of the IEEE RT2007, Real Time Systems conference, Fermilab, Batavia Illinois U.S.A. (2007)

[41] F. Roukoutakis et al., The ALICE-LHC online data quality monitoring framework, Proceedings of the Computing in High Energy Physics (CHEP2007), Victoria BC Canada (2007) http://cdsweb.cern.ch/record/1066450

[42] A. Vestbo et al., The ALICE high level trigger, J. Phys. G30, s1097 (2004)

[43] ALICE Environment for Grid, http://alien2.cern.ch/

[44] AliEn: ALICE Environment Grid Framework, http://alien.web.cern.ch/

[45] The ALICE experiment Offline project, http://alice-offline.web.cern.ch/

[46] An object-oriented data analysis framework, http://root.cern.ch

[47] PYTHIA 6.4, Physics and Manual, hep-ph/0603175, FERMILAB-PUB-06-052-CD-T (2006)

[48] T. Sjostrand, Comput. Phys. Commun. 82, 74 (1994)

[49] M. Gyulassy, X. -N. Wang, Phys. Rev. C80, 024906 (2009)

[50] R. Engel, Z. Phys. C 66, 203 (1995)

[51] R. Engel, J. Ranft, S. Roesler, Phys. Rev. D 52, 1459 (1995)

[52] J. Ranft: New features in DPMJET version II.5, Siegen preprint (1999)

[53] R. Brun, F. Bruyant, M. Maire, A. C. McPherson and P. Zanarini, GEANT3 user guide, CERN data handling division DD/EE/84-1 (1985),

http://wwwinfo.cern.ch/asdoc/geantold/GEANTMAIN.html; M. Goossens et. al., GEANT detector description and simulation tool, CERN program library long write-up W5013 (1994) http://cdsweb.cern.ch/record/1073159

[54] S. Agostinelli et al., Geant4, a simulation toolkit, Nucl. Instrum. Meth. A506, 250 (2003), CERN-IT-2002-003, http://cdsweb.cern.ch/record/602040; http://wwwinfo.cern.ch/asd/geant4/geant4.html

[55] A. Fasso et al., FLUKA: present status and future developments, Proceedings of the IV International Conference on Calorimeters and their Applications, World Scientific, Singapore (1994)

[56] P. Billoir, Nucl. Instrum. Meth. A 225, 352 (1984)

[57] P. Billoir, Nucl. Instrum. Meth. A241, 115 (1985)

[58] P. Billoir, Comput. Phys. Commun. 57, 390 (1989)

[59] M. Ballintijn, R. Brun, F. Rademakers and G. Roland, Distributed parallel analysis framework with PROOF, http://root.cern.ch/twiki/bin/view/ROOT/PROOF

Chapter 3

Introduction to Jets

The hot and dense medium (QGP) produced in the heavy-ion collisions has a lifetime too short to test the produced system using external probes. Thus, the characterization of the properties of the produced system must proceed by studying the particles that have been produced during the lifetime of the collisions or by their decay products. At the LHC, partonic interactions at perturbatively large momentum transfer is abundant and the remnants of high energy partons have become experimentally accessible. This gives access to a qualitatively novel class of auto-generated hard probes for the produced matter. Jet is the foremost member of the hard probe class.

Hard processes are hadronic processes involving large momentum transfer. Their medium-dependence must be established on top of a reliable baseline. The obvious baseline is the same hard process, measured in the absence of a medium, that is, in elementary hadronic interactions such as proton-proton collisions. Though probing the produced medium in relativistic heavy-ion collisions is the centre of attraction in jet study, one of the primary utilisation of jets is also to validate the pQCD predictions via elementary hadronic collisions. By comparing 3-jet (NLO) to a 2-jet (LO) event, we can even determine the value of the strong coupling constant, α_s, by taking the ratio of abundances of NLO process to LO which is proportional to the value of the coupling constant. Jets provide a link between the observed colorless stable particles and the underlying physics at the partonic level. It gives the clue about the direction and magnitude of the momentum carried by the originating parton. Information on the fragmentation of the jet initiating parton enable us to study the collimation and even help to determine the flavor of the parton itself. Recent interests in jet sub-structure study at current LHC energies have opened a new window in the search of rare particles like the Higgs Boson and SUSY particles due to the abundance of the respective particles at the expected mass regions in the background dominated yields.

In this chapter, a few of the most important aspects regarding jet (and relevant to this thesis), for example, evolution of jet in vacuum, fragmentation, jet clustering algorithm and jet reconstruction and jet-medium interactions have been discussed.

3.1 Evolution of jet (in vacuum)

The partons produced in high-Q^2 interactions are the seeds of final state parton showers. They are highly virtual and branch in the vacuum under the QCD time evolution into multi-parton final states which in turn hadronize and produce the final state hadrons. As a consequence, the nature of the projectile changes as a function of the time passed since production. What matters is not only whether the projectile interacts with a target, but also when.

There are many hard processes that are not perturbatively calculable but process-independent like the large distance physics of hadrons and also the processes those are perturbatively calculable but process dependent like the very short distance physics of partons. The factorization theorem enables us to factorize these processes and study the intermediate steps. For single-inclusive hadron spectra in proton-proton collisions, for instance, this factorization takes the schematic form:

$$\begin{aligned} E\frac{d^3\sigma}{d\overrightarrow{p}} = \sum_{abcd}\int dx_a dx_b dz_c f_{a/p}\left(x_a,\mu_F^2\right) f_{b/p}\left(x_b,\mu_F^2\right)\otimes \\ \left.\frac{d\sigma}{dt}\right|_{a+b\to c+d}\left(x_a,x_b,\alpha_S\left(Q^2,\mu_R^2\right),\frac{Q^2}{\mu_R^2},\frac{Q^2}{\mu_F^2}\right)\otimes \\ F_{h/c}\left(z_c,\mu_F^2\right) \end{aligned} \tag{3.1}$$

Here, $\otimes$ denotes convolutions. All the terms have been described sequentially in the next subsections. It has always been a study of great interest to know the whole process of parton evolution in experiment, starting from the hard scattering to jet reconstruction from the final state hadrons. If we keep in mind Figure 3.1 and try to understand it in terms of the factorization equation, we would be able to understand the evolution process as has been done in the following sub-sections. At a glance, the part marked as (1) is the hard scattering part, (2) represent hadronisation part, in stage (3) non-perturbative aspects of QCD gets incorporated, at (4) unstable particles decay, (5) represents effects of detector reconstruction and (6) is where jet is reconstructed using a jet clustering algorithm.

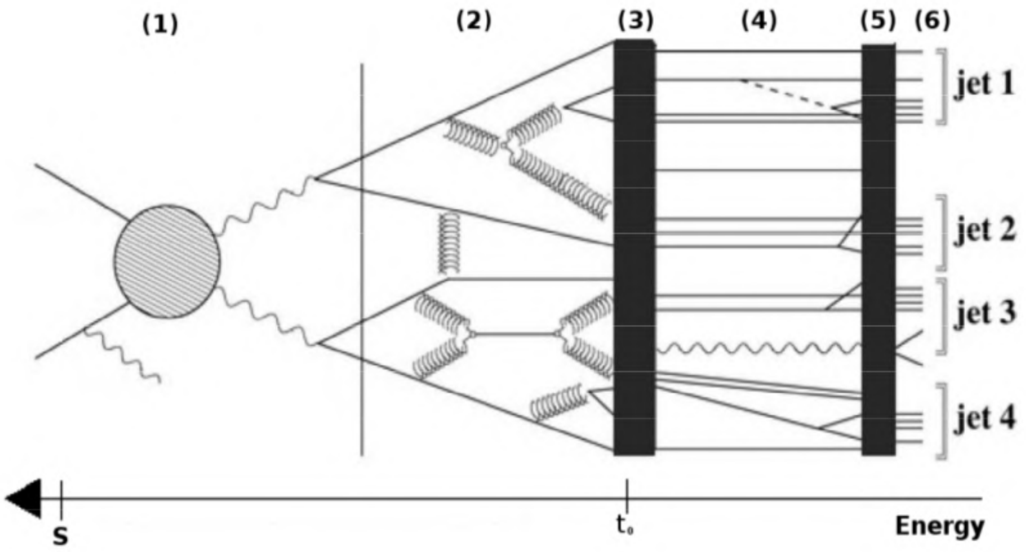

FIGURE 3.1: Schematic diagram of parton evolution. Energy axis at the bottom represents the decreasing energy with time starting from the scattering. This diagram represents a four jet events. This figure is reproduced from [1]

3.1.1 Initial conditions

The primary criteria of calculating the cross section of any process is to have the information about the colliding particles. In case of hadronic collisions, hadrons being a composite particle, many underlying processes are incorporated. In relativistic particle collision, the longitudinal motion of the constituent partons plays a pivotal role and for this physicists use a term called the parton distribution function [3] (PDF) to describe the colliding particles. PDF is in general a probability function and it satisfies the following relation:

$$\int_0^1 dx_i f_{i/Y}(x_i, \mu_F^2) = 1 \tag{3.2}$$

where $f_{i/Y}(x_i, \mu_F^2)$ is the PDF, x is the momentum fraction of parton type i of hadron Y and μ_F is the factorization scale. These PDFs come from the analysis of Deep Inelastic Scatterings [4] (DIS) where lepton-hadron collisions are studied, for example H1 [5–7], ZEUS [2] at HERA, complemented by the theoretical works.

Before the hard scatterings, the radiations (mainly gluonic) from the interacting partons are called the Initial State Radiation [9] (ISR) and this can contribute to the modification of energies of the scattered partons and the processes resulting in the outgoing particles. This becomes more important with increasing collision energy.

3.1.2 Hard scattering and final state conditions

Hard processes are hadronic processes involving a large momentum transfer. In colliding beam experiment, the detectors focus on the physics in transverse direction to the beam where the scattered particles have high momenta. There are plenty of processes which are responsible for jet production and these can be calculated with perturbative QCD. The leading order (LO) processes relevant for jet productions have been shown in Figure 3.2.

The cross-sections of these hard processes ($a + b \to c + d$) can be expressed in simple

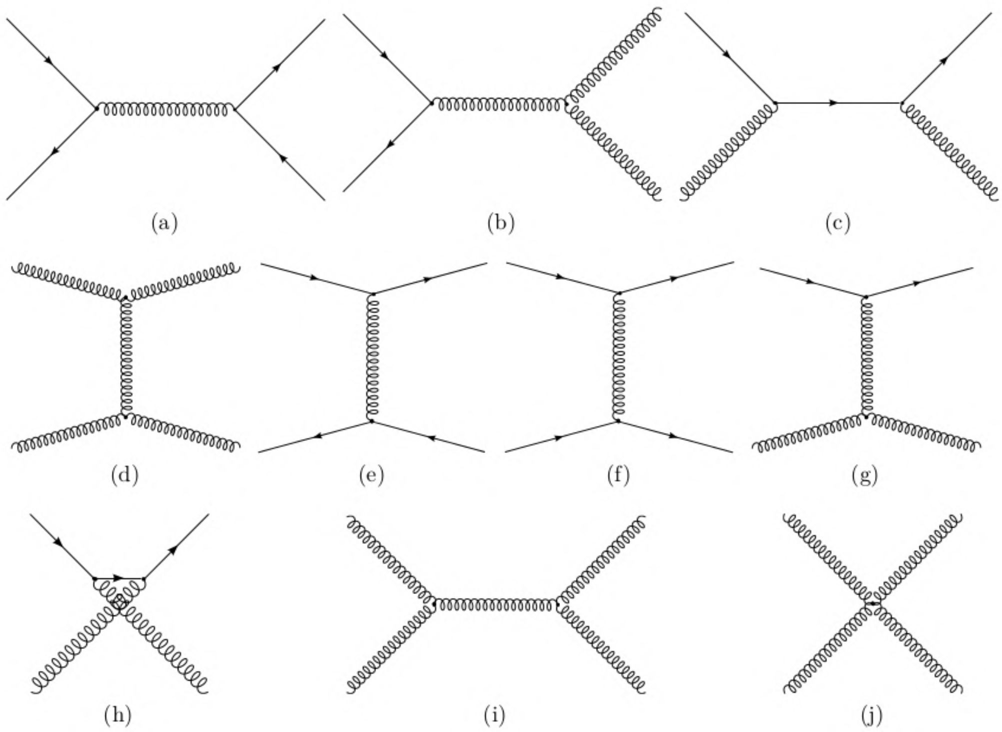

FIGURE 3.2: Leading order hard scatterings: the most dominant process is gluon-gluon scattering (gg→gg) represented by (d), (i) and (j). Rests are quark-gluon scattering, quark-quark scattering and quark-antiquark annihilation.

form as below:

$$\left.\frac{d\sigma}{dt}\right|_{a+b\to c+d} = \frac{1}{16\pi\hat{s}^2}|M| \tag{3.3}$$

where, all the variables are in the centre of mass frame, $\hat{s}$ is the Mandelstam variable and M is the scattering amplitude. M is different for different processes. The Mandelstam variables - s, t and u are defined as follows and can be depicted as in 3.3:

$$\begin{aligned} s = (p_1 + p_2)^2 &= (p_3 + p_4)^2 \\ t = (p_1 - p_3)^2 &= (p_4 - p_2)^2 \\ u = (p_1 - p_4)^2 &= (p_3 - p_2)^2 \end{aligned} \tag{3.4}$$

where p_1 and p_2 are the four momenta of the incoming particles and p_3, p_4 are that of the outgoing particles.

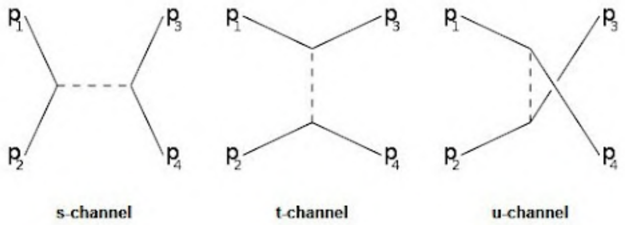

FIGURE 3.3: The s, t and u channel of Mandelstam variables.

The hard cross-sections depend in general on the partonic center of mass energy, the momentum transfer Q, the re-normalization scale μ_R, and possibly the masses of the partons involved in the process. This partonic cross section is calculable perturbatively as a power series in the strong coupling constant α_s up to a remainder term, which is suppressed by a power of Q. The controlled computability of hadronic cross sections rests on the scale dependence of the functions. This scale dependence is governed by QCD evolution equations. Physically, it emerges from the fact that the amount of parton branching, which needs to be included in the incoming parton distributions or outgoing fragmentation functions, depends on the scale, at which the hard process is interfaced with these functions.

As shown in the Figure 3.1, scattered partons may produce Final State Radiation (FSR) similar to ISR and it can change the topology of scattering which in turn can affect non-perturbative fragmentation process. Though here only LO calculations and diagrams are shown, it is also worth mentioning that the parton-parton cross-section can be expanded in orders of α_s, which becomes very small for large Q^2. A 2-to-2 process is the leading order (LO, α_s^2) one and 2-to-3 process represents next to leading order (NLO, α_s^3). Figure 3.4 shows Feynman diagrams for LO and NLO processes. An NLO process is more complicated than an LO process for having 2 or 3 partons in the final state with infra-red (IR) and ultra-violet (UV) divergences (discussed in the jet reconstruction sub-section). The processes with 2 partons in the final state with one internal loop introduces what is known as the UV divergence. The processes with three final state partons diverge if two of the final state partons become collinear or one of them is a soft one. This type of divergences are called the IR divergences.

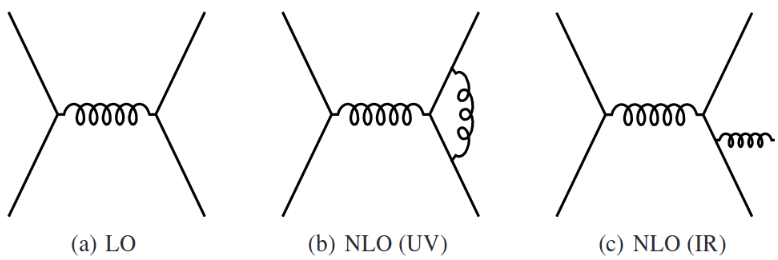

FIGURE 3.4: Feynman diagrams for LO and NLO processes. (a) represent 2-to-2 LO, (b) is the 2-to-2 process with an internal loop (UV) NLO and (c) stands for 2-to-3 NLO (IR) process. Figure taken from [10]

3.1.3 Fragmentation and Hadronization

For a jet definition which can be compared to data, one needs to understand how the partons fragment, and one requires an operational procedure which relates hadronic fragments to jets. In mathematical form, the fragmentation is described by a probability function, called the fragmentation function and takes the following form as in equation (3.1):

$$F_{h/c}(z_c, \mu_F^2) \tag{3.5}$$

It describes the probability of production of a hadron, h, with a momentum fraction z_c from the parent parton c.

A parton emerging from a hard interaction with a high p_T carries an initial virtuality Q. For high p_T , this virtuality is perturbatively large. According to Heisenberg's uncertainty relation, the parton will degrade its virtuality (i.e. will start evolving closer to on-shell conditions) on a time scale $1/Q$ in its rest frame. This degradation of virtuality is achieved by multiple parton branching and this is at the basis of the final state parton shower. This usually involves radiation of gluons or creation of quark-antiquark pairs from the hard scattered parton and these splittings can also be calculated using DGLAP [11, 12] splitting functions as follows:

$$
\begin{aligned}
P_{q\to qg} &= C_F\left(\frac{1+z^2}{1-z}\right),\\
P_{g\to q\bar{q}} &= T_R\left(z^2+(1-z)^2\right),\\
P_{g\to gg} &= C_A\left(\frac{z}{1-z}+\frac{1-z}{z}+z(1-z)\right),
\end{aligned}
\tag{3.6}
$$

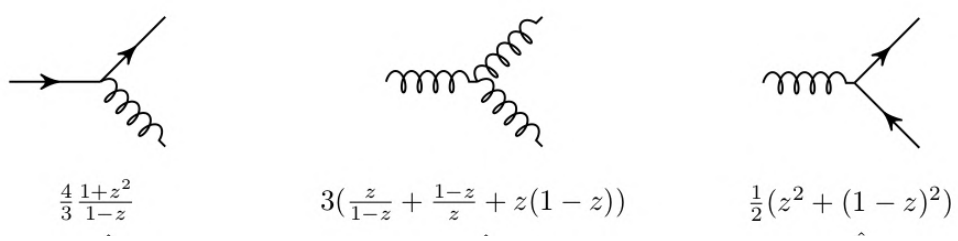

FIGURE 3.5: Schematic diagrams of few splitting functions. Figure taken from [13]

Here C_F, C_A and T_R are the Casimir factor (also called the color factors: for quark it is $\frac{4}{3}$ and for gluon it is 3). z is the fraction of momenta split carried by the splitted partons and it has two extremum: $z = 0$ represents the case where no splitting has occurred and $z = 1$ is the case when all the momentum is transferred and they continue in the direction of originating parton. In Figure3.5 few diagrams for the splitting functions can be seen (z in the first diagram is the fraction of momenta carried by the quark and so on). As described earlier, the splittings continues until a certain hadronisation scale is reached by successive parton energy loss. This process continues until the virtual masses squared of the partons are of the order of the infrared cut-off scale, t_0, taken to be of the order of 1 GeV^2. After this, the low-momentum-transfer, long-distance regime is entered presumably on a scale set by the QCD scale Λ ~250 MeV (Λ_{QCD} is the momentum scale at which α_s diverges), in which non-perturbative effects become important. At this point the partons hadronize and produce final state hadrons.

The Monte Carlo models, that describe the parton evolution and jet production, usually implement fragmentation and hadronization sequentially and treat them independently. They rely on some conditions imposed by the equations described above with some input parameters. For example, these equations hold as long as the virtualities of the outgoing partons are significantly smaller than the virtuality of the incident parton:

$$p_b^2, p_c^2 << p_a^2 = t \tag{3.7}$$

where subscripts b and c stand for the outgoing two partons and a represents the initial parton. Whereas t is the scale of the interaction, often set, as above, to the momentum squared of the original parton. The shower cut-off scale t_0 in principle is not correlated with the hadronization process and used as a parameter in the models. But it has been seen that when t_0 is increased, the parton showering gets terminated earlier. This leaves with fewer partons to hadronize but with higher virtualities than usual. This results in abundant production of hadrons. The changes in the shower and its impact on the hadronization due to changes in t_0 should not affect the model and for this t_0 is tuned in such a way that it agrees with the experimental observation of the final number of hadrons. The general favoured value for t_0 stand as few times Λ^2_{QCD}.

There are plenty of models developed by the theoreticians to explain the hadronization process. They can be divided into two broad categories: generalistic approach and specialized approach. Few of the generalistic approaches are briefly described below:

- **Local parton-hadron duality [14]:** This approach is based on the observation, that hadronization being long-distance process, involves low momentum transfer. Hence the assumption here is that the flow of energy-momentum and flavor quantum numbers at hadron level should follow those at parton level. Thus, for example, the flavor of the quark initiated jet should be present in a hadron near the jet axis. There are results on inclusive spectra and multiplicities in support of this hypothesis.

- **Universal low-scale α_s [15–17]:** As perturbation theory is satisfactorily valid at low scales, Q$\sim$1 GeV, the coupling constant $\alpha_S(Q^2)$ can be described non-perturbatively for all Qs. This approach enables us to evaluate the Feynman diagrams non-perturbatively. It gives a good description of heavy quark spectra and event shapes.

- **Longitudinal phase-space model [18]:** This model is also called the tube model where a color connected pair of partons is termed as a tube. Here a parton produces a jet of light hadrons which occupies a tube in rapidity-momentum $(y - p_T)$ space, both measured with respect to the direction of the initial parton. This approach gives a prediction about the hadronization effects to scale with energy as $1/Q$.

The above simple models successfully describe many of the gross features of the hadronization process. In order to make more detailed predictions, we need a specific model for the mechanism of hadronization. Three of the most popular specific models have been described below:

- **Cluster Model [19–23]:** In this class of model, color-singlet clusters of partons form after the perturbative phase of jet development and then decay into the observed hadrons. The parton showering process has an important property called the *preconfinement* [24, 25] of color and it states that the mass of the pairs of color-connected neighbouring partons have an asymptotic distribution which falls rapidly for higher masses. The model starts by the non-perturbative splitting of gluons into $q\bar{q}$ (g$\rightarrow q\bar{q}$). Due to color singlet $q\bar{q}$ combination, it has lower mass as prescribed by the preconfinement. These color singlet combinations form clusters which mostly undergo simple isotropic decay into pairs of hadrons, chosen according to the density of states with appropriate quantum numbers [20]. The precise form of the spectrum produced by this model is determined by the QCD scale Λ, the parton shower cut-off t_0 and to a lesser extent the gluon-splitting mechanism. Typical cluster masses from this model is normally two to three times t_0.

- **Lund String Model [26–30]:** This model is based on the dynamics of relativistic strings, representing the color flux stretched between the parting $q\bar{q}$ pair. Instead of fragmentation, the parting parton pair lose energy in the color confinement potential produced by the strings. The string produces a linear confinement potential and follows an area law for matrix elements:

$$|M(q\bar{q} \rightarrow h_1...h_n)|^2 \propto e^{-bA} \tag{3.8}$$

  where A is the area swept out in space-time and Figure 3.6 presents such an active area.

  The string has uniform energy per unit length and when it breaks, it produces hadrons via pair production as shown in Figure 3.7. The string may break up

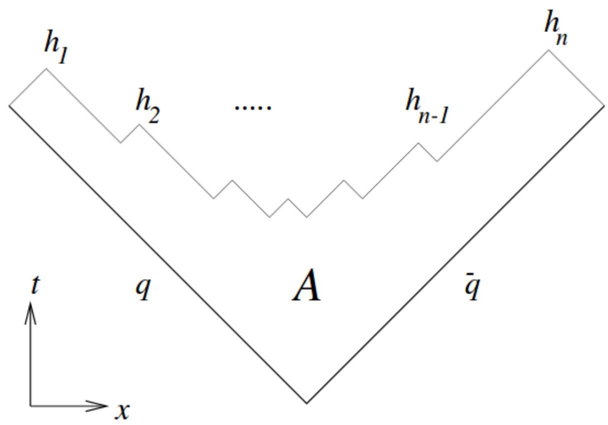

FIGURE 3.6: The active area in space-time in the string model. Figure taken from [31]

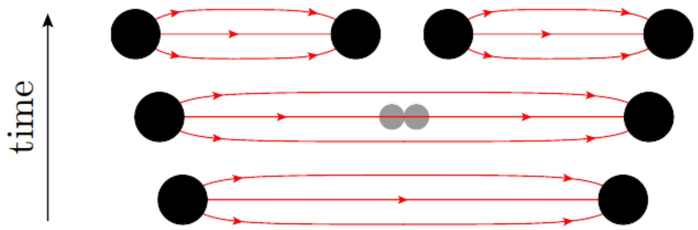

FIGURE 3.7: Illustration of string breaking into pair of partons. Figure taken from [32]

starting at either the quark or the antiquark end, or both simultaneously (the breaking points have space like separations, so their temporal sequence is frame dependent), and it proceeds iteratively by $q\bar{q}$ pair creation, as in independent fragmentation (discussed later). Meson production follows the idea that mesons are short pieces of string between two quark-antiquark endpoints. On the other hand, baryon production is harder to generalize. It can be looked upon as if quark was represented as an anti-diquark or baryon appears from successive productions of several quark-antiquark pairs. The model has extra parameters for the transverse momentum distribution and heavy particle suppression. Figure 3.8 presents decay of a photon into a $q\bar{q}$ in string and cluster model scenario.

- **The UCLA model [33–35]:** This model is a variant of the string model which uses the space-time area law to determine the relative rates of production of different hadron species by assuming the mass-squared of a hadron being proportional to its space-time area. This results in heavy particle suppression without extra parameters.

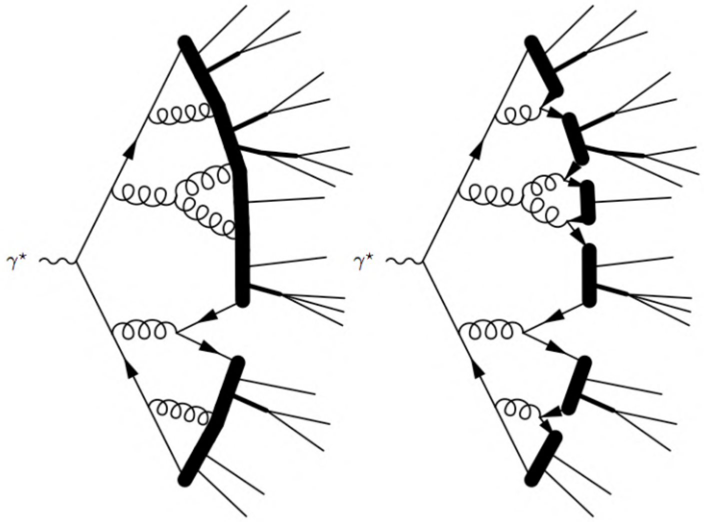

FIGURE 3.8: Schematic diagram of a photon decaying into a $q\bar{q}$ pair in two scenario: left represents string model and right one represents cluster model. This figure is reproduced from [2].

- **Independent Fragmentation model [36–38]:** First idea on this model was given by Field and Feynman in e^+e^- system [39, 40]. This is an iterative model and it treats individual parton fragmentation independently. If the fragmenting parton is a quark, it is combined with an antiquark from a $q\bar{q}$ pair created out of the vacuum to produce meson with energy fractions. The leftover quark, with the rest of the energy fraction, is fragmented in the same way, and so on until the leftover energy falls below some cutoff. When the fragmenting parton is a gluon, it first splits into a quark-antiquark pair. Then all the gluon's momenta is either assigned to one or the other (z = 0 or 1) with equal probability, so that the gluon behaves as a quark of random flavor, similar to the $g \to q\bar{q}$ splitting functions.

More about hadronization schemes and models can be found in [42].

3.1.4 Decay of primary particles

After the hadronization procedure terminates, decay of the unstable particles, such as top quark or $W^{\pm}$, Z bosons or $\pi^0 \to \gamma\gamma$, takes place. These decays are not only indistinguishable from primary particles originating in collisions, they occur very near to the interaction point as well.

3.1.5 Detector effects

The detectors used in the experiments, record data by the principle of interaction of the produced particles with the active detector medium by transferring part or full energy into the medium. While doing so, due to finite detector mechanics, the data recorded by the detectors are induced with some effects from the detector part. The most dominant two effects are limited detector tracking efficiency and finite detector resolution. The most prominent effects are described below:

- **Finite detector efficiency:** Due to finite tracking efficiency, real detectors often can not track all the final state particles. Total detector efficiency is the combination of the geometric efficiency given by the fraction of the particles hitting the detector and the intrinsic efficiency given by the fraction of particles going through the detector with respect to all the hitting particles.This efficiency is also particle species dependent. For example, detection of heavy resonance or muons, need special detector arrangement due to very small cross-sections. The reference detector efficiency is obtained from the parameterization of Monte-Carlo simulations.

- **Finite track p_T resolution of detector:** The transfer process of the radiation energy is random in nature and is based on excitation or ionisation to the detector. The charged particles are detected mainly by using the Bethe-Bloch formula [41] and the neutral particles are detected by using calorimetric principles. However the number of collisions of the incident particles in the detector medium is given by the mean free path of them in given medium and therefore it is subjected to fluctuations. This results in smearing of the reconstructed momentum and hence affects the momentum resolution.

- **Pile up:** This is a particular case of ambiguity which arises generally in the search of extremely rare processes (like the search for Higgs boson or very high p_T jet production) that demand correspondingly high instantaneous luminosities to be provided by a collider. These luminosity values can only be delivered by piling up multiple proton-proton collisions per bunch crossing. Additionally, the finite integration time of detector components in comparison to bunch separation (e.g.: 25 ns in the LHC) leads to cross-talk from adjacent colliding bunches. As a result, each event is interspersed with energy depositions from such pile up (PU) collisions.

In addition there are always some constraints on the design or mechanics due to which not all the detector sub-systems in a complex experiment are fully operational and these put some limitations on the covered range of p_T, η or ϕ or/and even on the type of particles (only charged or all). For example, before Run-II, there were no calorimeter installed in ALICE and there was no scope for full reconstructed jet analysis due to no information on the neutral particles.

3.1.6 Additional processes

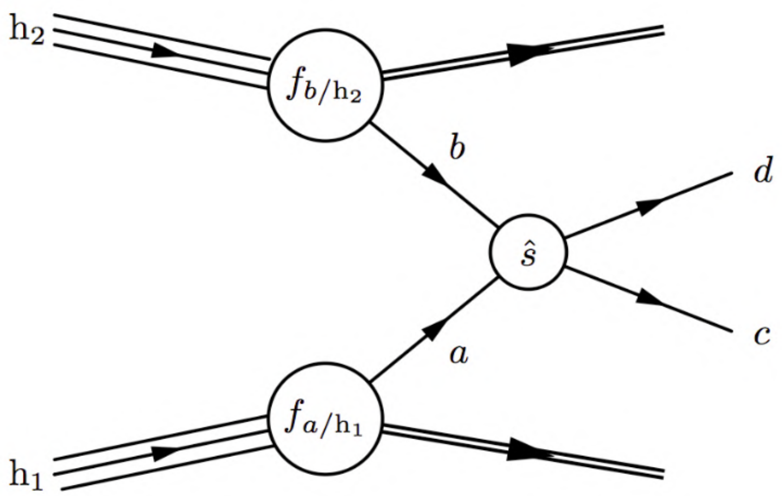

FIGURE 3.9: Schematic diagram of a hard collision between two hadrons, h_1 and h_2, each having three partons. One parton from each of the hadrons (a and b) participate in the hard interaction.

In hadronic collisions, only one constituent parton from each of the participating hadrons experiences hard scattering per event as can be seen in Figure 3.9. The fractional momentum carried by the partons are given by the respective PDFs. The colliding hadrons with the remaining partons are called the beam-beam remnants (BBR). The BBR contribute to soft hadrons from the fragmentation of spectator partons that do not exchange any appreciable transverse momentum in the collision. With this, as already introduced, there are possible radiated gluons known as the ISR which in turn can fragment and produce hadrons. There are hadronic contributions from FSR (Figure 3.10) too. Due to the composite nature of the hadron itself, there are Multi-Parton Interactions (MPI) which are not a part of hard scattering but can produce final state hadrons. So, the resulting event contains final state particles from the two outgoing hard scattered partons, from the beam-beam remnants, from the ISR and FSR and from multi-parton interactions. Except the two hard scattered outgoing partons leading to jets, everything else in an event is termed as the Underlying Event (UE) [43]. UE is an integral part of relativistic hadronic or heavy-ion collisions as depicted in Figure 3.10.

Underlying event in jet study was first described and measured by the CDF Collabora-

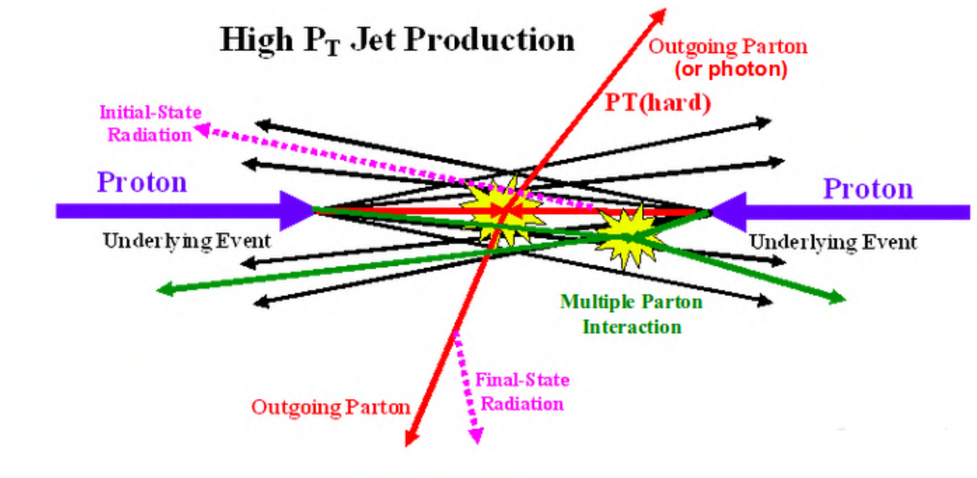

FIGURE 3.10: Schematic diagram of a proton-proton collision with Underlying Event.

tion. UE is treated as the background to the jet as one can not distinguish the final state hadrons coming from hard and soft interactions, while constructing jets. The topological structure of hadron-hadron collisions is used to study the underlying event. The two large transverse momentum jets are roughly back to back in azimuth. The direction of the leading jet (CDF originally did the charged jet reconstruction) in each event is taken as a reference to define three regions in the ϕ space: Near side or Toward region which contains the leading jet, Away region containing the jet in the opposite side and two

Transverse regions which are perpendicular to the 2-to-2 hard scattering plane as shown in Figure 3.11. The Transverse regions are the most sensitive to the UE as those have the least influence from the jet. UE is treated as uniformly distributed over the phase space and stand as the unavoidable background to the jet observables. Thus for making a precise measurements, it is very important to accurately measure it and subtract it (on event-by-event basis) from the actual observables.

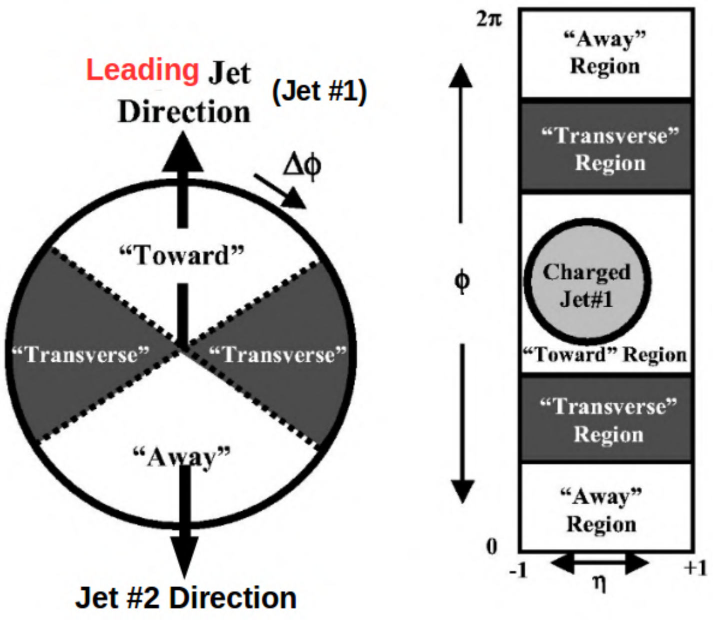

FIGURE 3.11: Illustration of the division of the $\eta - \phi$ phase space for the measurement of UE. The Toward region is defined by $\Delta\phi < 60^0$ and η <1, while the Away region is located at $\Delta\phi < 120^0$ and η <1. The Transverse region is defined by $60^0 < \Delta\phi < 120^0$ and $\eta < 1$. Each region has an area in $\eta - \phi$ space of $4\pi/3$.

3.1.7 Jet reconstruction

This is the final and most important part of any high energy hadronic or heavy-ion collisions studying jet. The signature of a relativistic hadronic interaction in the detector is a large number of tracks due to the virtue of fragmentation and hadronization processes, seemingly close together in (real or phase) space. Due to the higher probability of emitting partons with small angles with respect to the initial parton, most of the final hadrons will be concentrated in a direction close to that of the initial parton. This concentrated shower of observed particles is what is referred to as a jet. This is represented by part 6 of Figure 3.1.

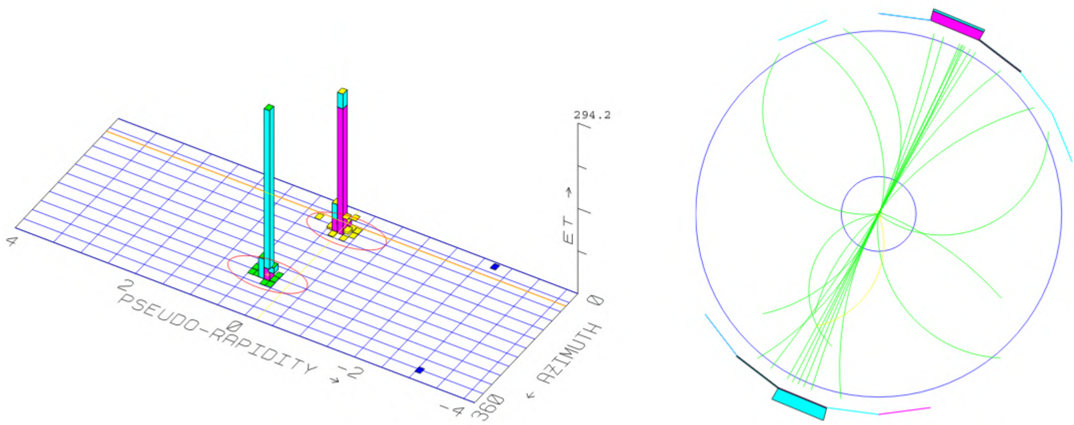

(a) Calorimeter (b) Tracking chamber

FIGURE 3.12: An example of jet event in the CDF (a) calorimeter and (b) central tracking chamber. This figure taken from [44].

In the event display of any collider experiment, jet could be seen with clear structure (Figure 3.12) but the definition of jet is not that straightforward. There are plenty of underlying additional effects in an event with jet as has been described in the previous sections. Jet reconstruction can also get troublesome for the detector induced effects. Because of the possibility of having gluon-mediated interactions, which by far dominate the interaction cross section, there is a possibility of having many jets in the event. This can lead to the shower of particles from one parton overlapping with those from another. All of these effects result in a large number of tracks as well as calorimeter energy deposits which must be disentangled into objects such as jets or isolated particles. This disentanglement is done by using jet clustering algorithms. Moreover, to place the experimental results at the same ground as the theoretical calculation, the algorithms must be same in both cases. In this sub-section, the procedure of jet reconstruction has been described.

3.1.7.1 Jet Definition

There is no single optimal way of defining a jet. In 1990, an accord, called the Snowmass Accord [45], was set out by the then influential physicists to put some conditions on the procedures of defining a jet. This accord have been treated as the reference in the field of developing algorithms to reconstruct jet. Jet reconstruction algorithms in general combine the calorimetry and tracking information to define jets. To reconstruct a jet, parameter like the spatial area resolution (R) in $\eta - \phi$ space is also needed to specify the area in which the particles are to be clustered as a jet. One more important aspect is the recombination scheme by which the algorithm actually combines the nearby tracks into a specific jet. Together, the jet clustering algorithm with the parameter and the recombination scheme is what is referred to as the "Jet definition."

$$Jet\ Definition = Algorithm(procedure, R) + Recombination\ Scheme \tag{3.9}$$

3.1.7.2 Algorithms

The jet stands as a proxy to the hard scattered initial parton and the jet clustering algorithm allows to associate the final state hadrons to the parton. This correspondence is referred to as the Local Parton-Hadron Duality (LPHD). If LPHD is satisfied, the study of jets might be regarded as a tool for mapping the observed long distance hadronic final states onto underlying short distance partonic states. Jet finding algorithms define a functional mapping:

$$Particles \xrightarrow{\text{jet clustering algorithm}} Jet \tag{3.10}$$

After the Snowmass Accord, next big event in this topic was the RUN-II jet discussion of Tevatron in 2000 [46]. All the modern jet reconstruction algorithms are based on the few points raised there, some of which are mentioned below:

- *Fully specified:* The algorithm must be fully specified in terms of clustering, energy and angle definition, and all details of jet splitting and merging.
- *Theoretically well behaved:* The algorithm must be infrared and collinear safe with no ad-hoc clustering parameters.
- *Detector independent:* The algorithm should not depend on the mechanical and geometrical description of the detector.

- *Order independent:* The same algorithm must be applicable at the partonic, particle and detector levels.

Before going to the description of specific algorithms, following few points would try to give the reader some idea on the most faced problems while developing an algorithm and the necessary kinematic and parameter details that are needed while reconstructing a jet with the help of an algorithm. Figure 3.13 shows different level of a jet reconstruction.

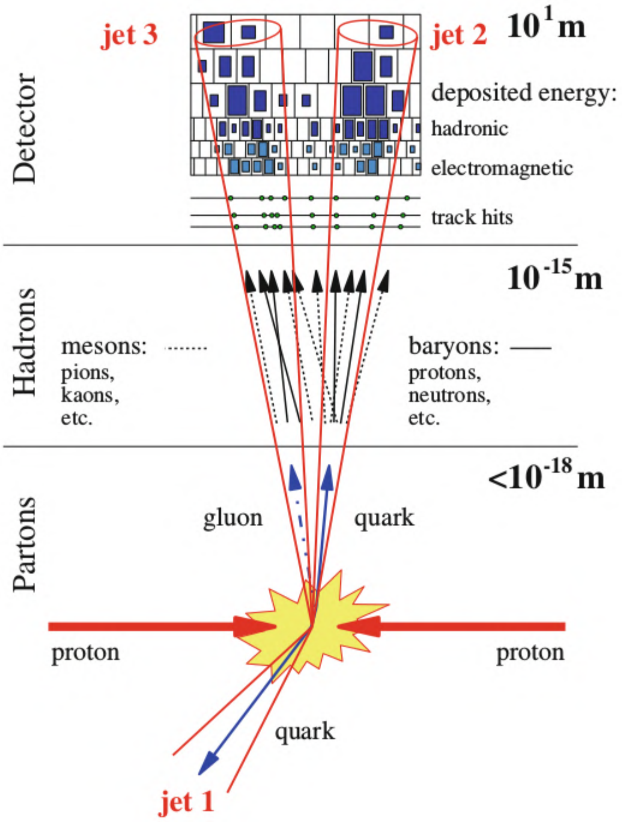

FIGURE 3.13: An algorithm should be order independent i.e., the same algorithm must work with the same accuracy at partonic, particle and detector level. This illustration shows different level of a jet reconstruction.

Infra-Red and Collinear (IR-C) safety

A hard parton undergoes many collinear splittings as part of the fragmentation process. There are also contributions from soft radiation both through the perturbative and non-perturbative processes. The decay of high energy hadrons also contribute to the collinear splittings. Collinear splittings and soft emissions effectively occur randomly

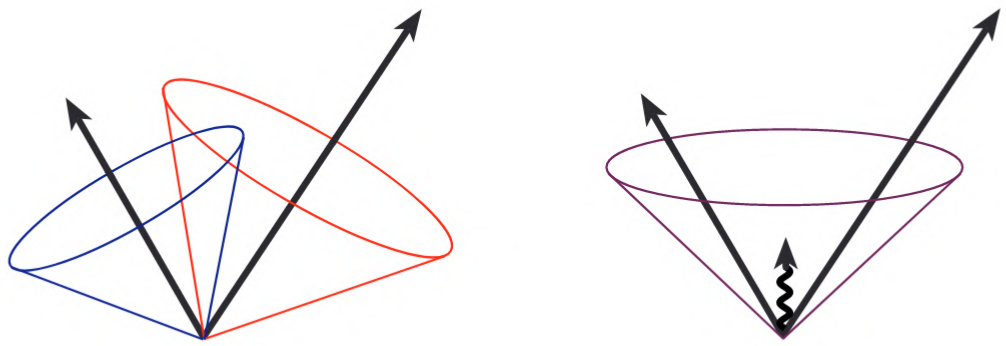

FIGURE 3.14: Illustration of infrared sensitivity in jet clustering. The presence of soft radiation between two jets may cause a merging of the jets that would not occur in the absence of the soft radiation.

and even their average properties are hard to predict because of the way they involve non-perturbative effects. The splitting of a hard particle, while using a collinear unsafe algorithm, will result in the alteration of the number and contents of the jets. A similar problem arises when a soft gluon is added to the system while an infra-red unsafe algorithm is in use. The problems has been shown schematically in Figre 3.14 and Figure 3.15. An IRC unsafe algorithm affects the perturbative QCD calculations. The motivation for constructing jets is precisely that one wants to establish a way of viewing events that is insensitive to all these effects.

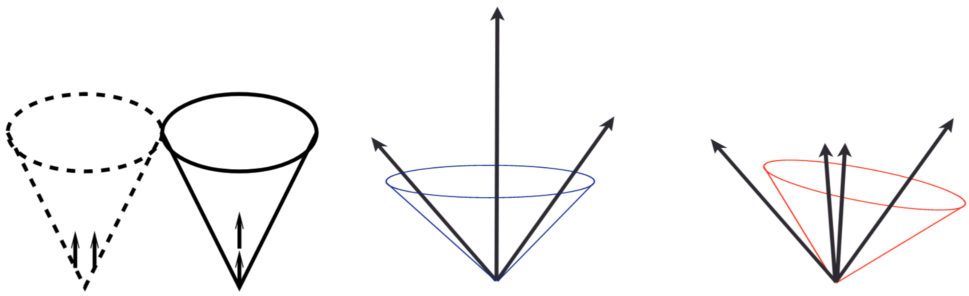

FIGURE 3.15: Illustration of collinear sensitivity in jet clustering. The top case shows an example, where a jet is not being defined due to splitted energy (left) and when the splitted energy is narrower a jet could be defined (right). Another collinear problem is shown in the bottom case where collinear splitting compels the algorithm to change the jet direction and energy and make a new jet.

Jet Kinematics

As described in sub-section 3.1.6, the fraction of the hadronic momentum carried by the constituent partons is not known and it is even different in different events. This changes the frame of reference from the centre-of-mass frame for the colliding partons, which in turn randomly boosts the centre-of-mass frame of the partons along the direction of the colliding hadrons. Therefore, to describe a jet more conveniently, one needs longitudinal boost-invariant variables as described below:

$$\begin{aligned}
&\text{mass} && m = \sqrt{E^2 - p_x^2 - p_y^2 - p_z^2} \\
&\text{transverse momentum} && p_T = \sqrt{p_x^2 + p_y^2} \\
&\text{azimuthal angle} && \phi = \arctan(p_y/p_x) \\
&\text{rapidity} && y = \text{arctanh}(p_z/E) = \frac{1}{2}ln\left(\frac{E+p_z}{E-p_z}\right)
\end{aligned}$$

At the high energy limit ($p >> m$), the most convenient variables are: azimuthal angle (ϕ), transverse energy ($E_T \simeq p_T$) and pseudorapidity ($\eta = -ln[tan\frac{\theta}{2}]$), where polar angle $\theta = arctan(p_T/p_z)$.

Jet Resolution parameter

The jet resolution parameter (R) represents the area in the $\eta - \phi$ space within which the algorithm should perform the jet reconstruction. It is also referred to as the radius of the jet and is expressed as:

$$R = \sqrt{(\eta_2 - \eta_1)^2 + (\phi_2 - \phi_1)^2} = \sqrt{(\Delta\eta)^2 + (\Delta\phi)^2}$$

The jet radius is given as an input to the algorithm with other specific instructions like the minimum p_T of the tracks to be grouped, the range of the p_T of the reconstructed jet and whether to reconstruct jet from only the charged particle information or to also include neutral particle information. The jet size and area determine the susceptibility of a jet to soft radiation. A larger jet radius is important as it allows the jet to capture enough of the hadronized particles for the accurate calculation of the jet's mass and energy. However, a smaller jet radius is useful in reducing the amount of the underlying event (UE) and pile-up (PU) captured with the jet, preventing the overestimation of the jet's mass and energy. Things get even more messy in heavy-ion collisions due to the dominance of the large background. For this the optimization of the jet radius is important for different type of collisions. Figure 3.16 presents a comparative 1D event reconstruction with two different jet Radius parameter.

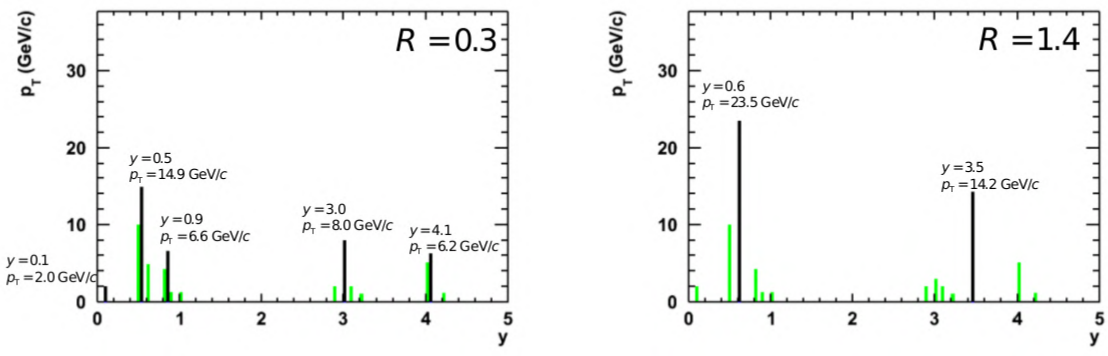

FIGURE 3.16: Plots showing 1D event reconstruction with two different jet resolution parameter: $R = 0.3$ (left) adn $R = 1.4$ (right). With smaller R, number of jets are increased while the reconstructed momenta is smaller [47].

Jet Area

In order to make the measurements more precise and accurate, it has been a topic of importance to study the modification of jet kinematics by non-perturbative effects associated with the proton beams. These effects in general, can be put into two groups: UE and PU. The UE and PU can affect a jet in two ways. Firstly, if particles from the UE and PU get clustered into the jet, the transverse momentum of the jet increases. Secondly, the presence of the UE/PU particles can modify the way in which the particles, from the hard scattering, get clustered into jets. It is even possible to produce complete jets made up of PU energy, as illustrated in Figure 3.17, at low p_T. The charged particles from PU contributions, which appear as the reconstructed tracks but are not a part of the primary vertex of the event, are possible to identify event-by-event. No jet algorithm exists that is insensitive to PU. Instead, PU particles and energy are collected roughly as proportional to the squared jet radius R^2 in a similar fashion as for the UE.

To study these effects and to disentangle them from the original jet, the concept of jet area was introduced. It has been seen that the contributions from UE and PU are uniformly distributed in $\eta - \phi$ space, especially after averaging over a large number of events. So, a good measure of the susceptibility of the jet towards contamination by the UE and PU, could be given by the extent of the region (in the $\eta - \phi$) over which it is liable to capture UE and PU particles, i.e. the "catchment area" of jet. Jet area, as shown in Figure 3.18, can be defined in two ways:

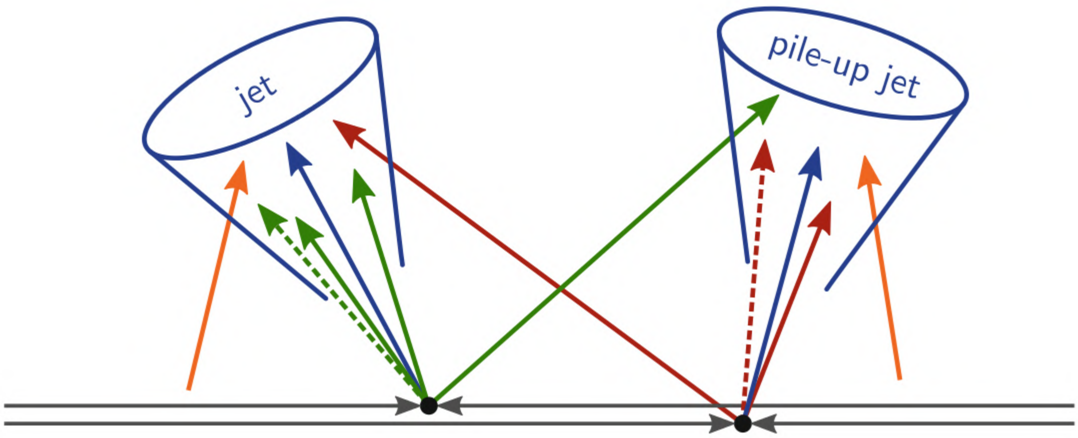

FIGURE 3.17: Illustration showing the co-existence of pile up collision with the primary hard scattering which leads to the additional particle production and energy deposition in the same event. Illustration taken from [48].

- *Passive area:* It involves scanning a single infinitely soft particle (called "ghost") over the $\eta - \phi$ cylinder and determining the region over which it is clustered within a given jet. It can be understood as a measure of the susceptibility of the jet to contamination from an UE with point-like structure.

- *Active area:* It involves adding a dense coverage of infinitely soft "ghosts" and counting how many are clustered inside a given jet. It can be understood as a measure of the susceptibility of the jet to contamination from the UE with uniform, diffused structure.

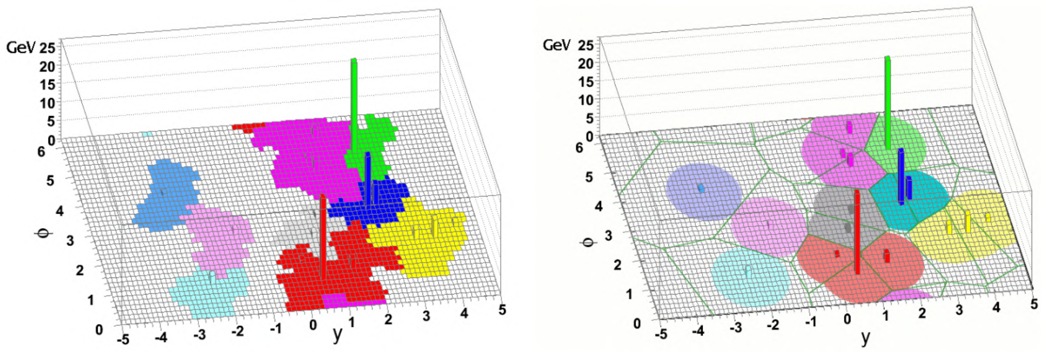

FIGURE 3.18: Active area (left) and passive area (right) determination of a jet algorithm. The shaded regions in both the plots stand for the respective jet areas.

Back-reaction

The presence of UE and PU can have the potential of not only affecting the jet but also the clustering itself. When a jet is placed in a soft background of finite p_T (UE and PU in general sense), the behaviour of the clustering is altered with respect to the original particles by the background by the addition of the soft particle to the jet. This way the jet ends up with either lesser or more particle by the virtue of the effect of the UE and PU on the jet structure. This particular case is known as the back reaction and it can be dealt with analytically.

There are two main classes of jet algorithms in use. The first type is the "Cone" algorithms which uses partitional approach for clustering relying on the idea that QCD showering and hadronisation leaves the bulk features of an event's energy flow unchanged. This category of algorithms are based on defining a cone and the energy flow into the cone and often referred to as the "top-down" approach. The most popular algorithms, of this class, are: iterative cone with progressive removal (IC-PR), the iterative cone with split-merge procedure (IC-SM) and the seedless infra-red safecone (SIScone). Other type is the sequential recombination algorithms class which utilise hierarchical clustering and iterative procedures that try to reverse the pattern of multi-gluon emission. These algorithms define a distance between the particles and recombine the closest pair on an iterative way. This class of algorithms are related to the divergent structure of the QCD matrix elements and referred to as the "bottom-up" approach. The well known algorithms, of this class, are: the K_t, Anti-K_t and Cambridge/Aachen algorithm.

Cone based algorithms

Cone based algorithms cluster the particles based on the $(\eta-\phi)$ space following a conical shape and end up with jet with rigid circular boundary. This class of algorithms are easy to implement and they were favoured in the past. But they are generally IRC unsafe, except SIScone.

IC-PR algorithm [49]:

The CMS iterative cone and Pythia cone are examples of IC-PR category. This algorithm works as follows:

- A list of all the particles is made
- The hardest particle is identified and a seed is made out of it.

- A cone with radius R (input) around this seed is designed and a trial jet axis is constructed by summing up the four- momenta of the particles within this cone.
- If the seed axis coincide with the trial axis, the jet cone is labelled as stable and the particles inside the cone is removed from the list of all the particles.
- The next hardest seed is identified and the above procedures are repeated.
- If the trial axis does not coincide with the seed axis, the trial axis is labelled as the new seed axis and the process is repeated until the axes converge.
- The entire cycle is repeated until the seed falls below an energy threshold, E_{cut}.

IC-SM algorithm [46]:

JetClu, midpoint cone and the ATLAS cone are the example of this category. Its method of clustering is as follows:

- A list of all the particles is made.
- All the particles with E above the E_{cut} are made as seeds.
- All the stable cones associated with the seeds following the method of IC-PR are constructed and labelled as protojets.
- The protojets with $p_T < p_{T,cut}$ are removed to reject the pile-up.
- The hardest protojet, say i, is identified using the scalar sum of the constituent particles' p_T.
- The next hardest protojet, j, which shares particles with i, is identified.
- If no j is found, i is labelled as the final jet and is removed from the protojet list.
- If j exists and $p_{T,shared} < f \times p_{T,j}$, then the particles are shared to the axis they are closer and the momenta of the protojet is recalculated (where f is the merging parameter with 0.5< f <0.75, a measure of the resolution).
- If the condition of the previous step is not satisfied, protojets i and j are merged into one and removed from the list of protojets.

- If the last two steps produce another protojet matching one already found, both are made as two distinct protojets
- Processes are repeated until there is no protojet left.

Except the first three steps, the rest of the algorithm is called the split-merge (SM) procedure.

SIScone algorithm [50]:

This is the only IRC safe cone based algorithm. It has the advantage of good resolution with better control over UE and PU due to it's relatively smaller area of clustering. It finds a jet following the steps described below:

- For a particle i, another particle j is found within $2R$ from i.
- If there is no j, then i is added to the list of protojets.
- If a j exists, then two cone is drawn for i and j in which they lay on the circumferences respectively and the momenta is computed for the two cones.
- For each cone, all four permutations, of the two edge points being contained in or out of the circle, are considered. These four circles are labelled as current cones.
- For each current cone previously not found, a check is done to find whether the particles at the edge of this cone are positionally at the same place as when the cone is defined by the momenta of the particle. If not, the current cone is labelled unstable. If yes, then the cone is labelled as stable cone and added to list of protojet.
- Split-Merge procedure is run over the protojets.

An undesired feature related to the search for stable cones in some cone-type algorithms give rise to the so-called *dark jets*, i.e., measured energy depositions that are not reconstructed as jets [51]. Sequential recombination algorithms are free from such occurrence.

Sequential clustering algorithm

All the algorithms that belong to this class have a very similar method and they group the particles based on the momentum space. They assume that the particles within a jet have small p_T difference and thus result in jets with fluctuating areas in the $(\eta - \phi)$ space. Currently this is the most favoured class of algorithms as they are IRC safe and with the introduction of the FastJet [13] package, all the algorithms have become faster in terms of computation time.

This type of algorithms combine the particles based on the mapping of closest distance as per the flowchart presented in Figure 3.19. First they compute two distances as follows:

$$\begin{aligned} d_{ij} &= min\left(p_{ti}^{2k}, p_{tj}^{2k}\right)\frac{\Delta R_{ij}^2}{R^2}, \text{ where } \Delta R_{ij}^2 = (\Delta\eta)^2 + (\Delta\phi)^2 \\ d_{iB} &= p_{ti}^{2k} \end{aligned} \tag{3.11}$$

Here k is an exponent which takes different value for different algorithms of this class and d_{iB} is the distance of the particle i from the beam axis. They use these two distances in the following way to find a jet:

- A list of all the particles to be clustered is made.
- The minimum of the entire set $\{d_{ij}, d_{iB}\}$ is computed.
- If d_{ij} is the minimum then i and j are combined into one particle by adding the four-vectors and both of them are removed from the list of particles.
- If d_{iB} is the minimum, then i is labelled as a final jet and removed from the list.
- This process is repeated until either all particles are part of a jet with $\Delta R_{ij} > R$ (inclusive clustering) or until a desired amount of jets have been found (exclusive clustering).

K_t algorithm [53]:

When the exponent 'k' in equation 3.11, takes the value 1, the equation reduces to:

$$\begin{aligned} d_{ij} &= min\left(p_{ti}^2, p_{tj}^2\right)\frac{\Delta R_{ij}^2}{R^2} \\ d_{iB} &= p_{ti}^2 \end{aligned} \tag{3.12}$$

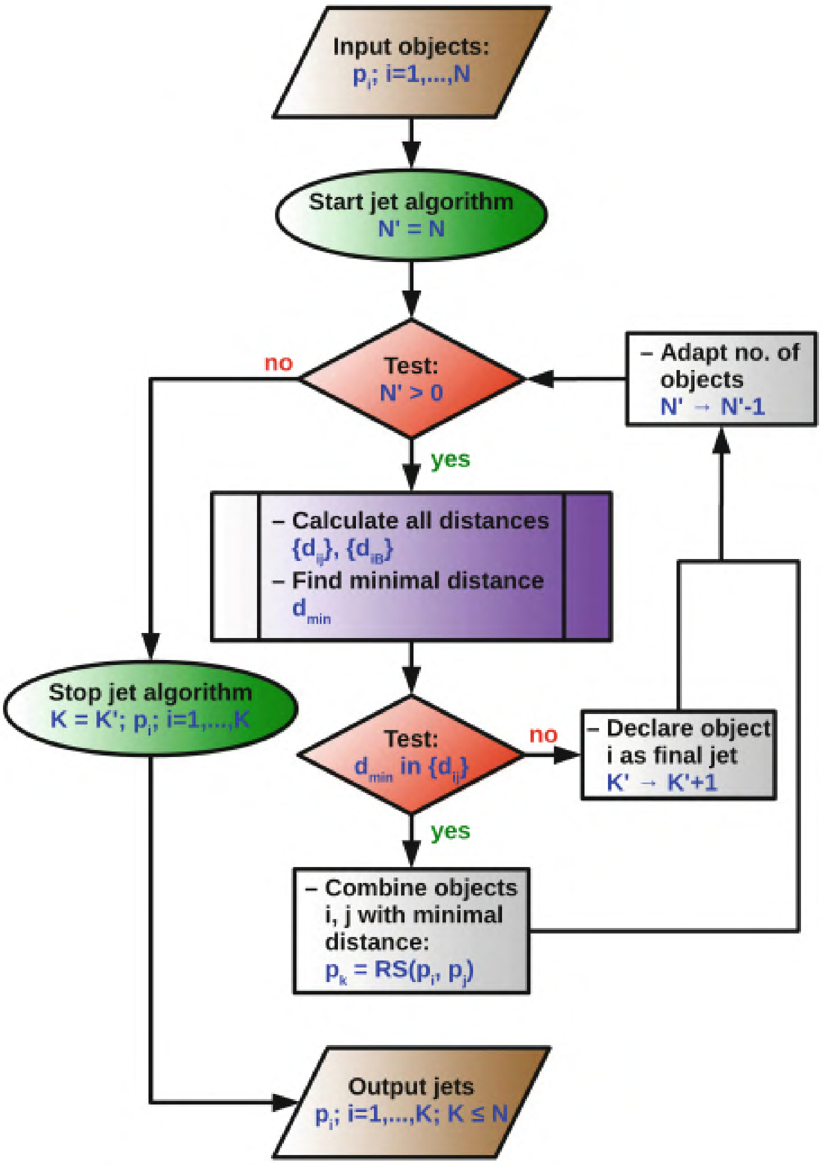

FIGURE 3.19: Flowchart of a sequential recombination jet clustering algorithm.

From equation 3.12, it is clear that the low p_T particles are favoured in this case. This is the procedure that the K_t algorithm follows and it merges the soft particles where the fluctuation is the most. For this reason, this algorithm is preferred in the case of UE and subjet measurement.

Anti-K_t algorithm [54]:

When the exponent 'k' in equation 3.11, takes the value -1, the equation reduces to:

$$\begin{aligned} d_{ij} &= min\left(\frac{1}{p_{ti}^2}, \frac{1}{p_{tj}^2}\right)\frac{\Delta R_{ij}^2}{R^2} \\ d_{iB} &= \frac{1}{p_{ti}^2} \end{aligned} \tag{3.13}$$

This is the case of Anti-k_t algorithm which used to merge the hard particles first. This algorithm gives best result in resolving jets and very less susceptible to UE or jet sub-structure. This is the most favorite algorithm for jet studies of the collider experimental physicists.

Cambridge/Aachen algorithm [55]:

When the exponent 'k' in equation 3.11, takes the value 0, the algorithm is set for the C/A one and the equations reduced to:

$$\begin{aligned} d_{ij} &= \frac{\Delta R_{ij}^2}{R^2} \\ d_{iB} &= 1 \end{aligned} \tag{3.14}$$

From the above equations it is clear that the C/A algorithm is not p_T dependent and somewhat susceptible to UE. This algorithm is best suited for jet substructure study, but it is little bit complicated than the K_t one.

The FastJet jet clustering program presents currently the faster and optimized sequential algorithms for the jet reconstruction and is widely used one in the collider experiments. A comparison of the performances of cone based and sequential recombination algorithm has been presented in Figure 3.20.

3.1.7.3 Recombination scheme

The last piece in the picture of a jet definition is a suitable scheme by which the tracks or calorimeter towers are combined or merged, called the Recombination Scheme. This

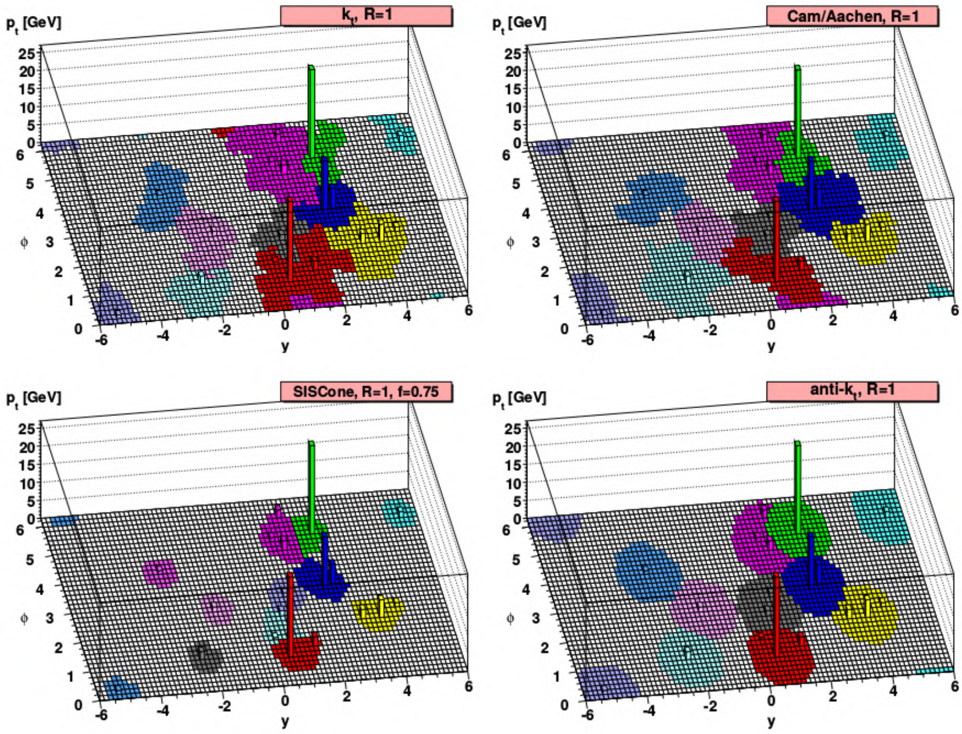

FIGURE 3.20: Jet areas measured by the SIScone and the three widely used recombination algorithm: K_t, Anti-K_t and C/A with the same dataset and input parameters. Figure taken from [56]

.

particular concept is necessary for the successive recombination jet clustering algorithm. In the Snowmass accord, originally proposed scheme was the E_T scheme where the energy and direction of the jet is computed according to the following relations:

$$\begin{aligned} E_{T,jet} &= \sum_i E_{T_i} \\ \eta_{jet} &= \frac{1}{E_{T,jet}} \sum_i E_{T_i} \eta_i \\ \phi_{jet} &= \frac{1}{E_{T,jet}} \sum_i E_{T_i} \phi_i \end{aligned} \tag{3.15}$$

where the sum runs over the particles contained in the jet, and the jet is taken to be massless. This procedure has the drawback that it is not invariant under longitudinal boosts if the component particles are massive.

Most of the current algorithms use the energy scheme (E) where the four momenta of the particles is summed to include in the jet. This scheme takes more computing time as there is also a loop over the associated particles. Practically E_T and E scheme has negligible difference.

There is another scheme called the p_T scheme where the transverse momenta of the tracks are summed and weighted sum of azimuthal angle and pseudorapidity are used for the construction of jet using the following relations:

$$\begin{aligned} p_{T,jet} &= \sum_i p_{T_i} \\ \eta_{jet} &= \frac{1}{p_{T,jet}} \sum_i p_{T_i} \eta_i \\ \phi_{jet} &= \frac{1}{p_{T,jet}} \sum_i p_{T_i} \phi_i \end{aligned} \tag{3.16}$$

There exists a different scheme called the boost invariant one, which takes the particle massless and combines them to produce a jet. All these schemes have different variants depending upon there weighting and summing conventions.

3.2 Parton (jet)-medium interaction

There are two types of medium effects that can be induced in the partons: cold nuclear matter effects and hot nuclear matter effects (QGP). The study on the cold nuclear matter effects is generally conducted by using proton-nucleus events. Such studies has uncovered observation like the softening of the hadron spectra at low p_T and corresponding hardening at intermediate p_T (3< p_T <6 GeV/c) while compared to scaled pp measurement, known as the Cronin effect [57]. But here in this section, only the description of parton interactions with the hot and dense QGP medium will be discussed, which falls in line with the scope of this thesis.

In the case of elementary hadron collisions, for example pp collisions, where no medium is expected to be produced, the hard scattered parton fragments in vacuum and produces final state hadrons. But in the case of relativistic heavy-ion collisions, as described in Chapter 1, the hot-dense QGP medium consisting freely moving partons is produced. Feynman diagrams for the two processes can be found in Figure 3.21.

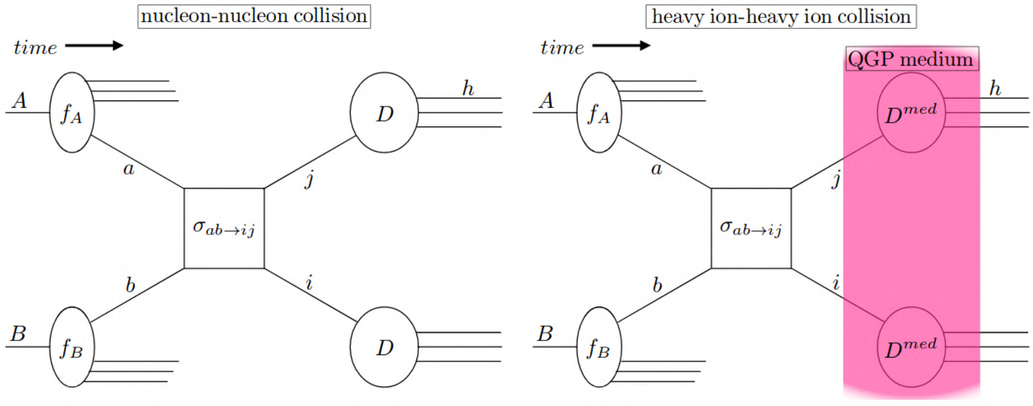

FIGURE 3.21: Feynman diagrams for hard processes in nucleon-nucleon collision (left) and in heavy ion-heavy ion collision (right). Figure taken from [59].

This medium has been described in different ways by many scientists over the years. To name a few, Fermi gave a purely statistical model of a dense volume breaking up into hadrons, Landau presented a model with hydro-dynamical treatment. Bjorken extended this approach by introducing time evolution of the medium with the help of some assumptions [58]. The evolution of jet and the medium takes longer time whereas the time scale of a hard scattering is very short. A hard scattered parton propagating through the QGP medium can scatter elastically by the partons present in the plasma and therefore suffers differential energy loss. This collisional energy loss was estimated to be:

$$\frac{dE}{dx} = \alpha_S^2\sqrt{\epsilon}, \quad \text{where } \epsilon \text{ is the energy density of ideal QGP} \tag{3.17}$$

Bjorken found that energy loss to be very low and in the order of $\simeq 0.1$ GeV/fm [60]. QCD gluon bremsstrahlung (analogue of QED bremsstrahlung) found to be another important source of energy loss [61] and was studied in details by Landau, Pomeranschuk and Migdal and their theory is called the LPM effect [62–64]. The radiative energy loss is considerably larger than the collisional loss and also due to the presence of coherence effect, this process is much more complicated than the elastic scatterings. Figure 3.22 presents a schematic illustration of medium induced gluon radiation process. The high energy jets are quenched or even go extinct due to the combined effect of multiple inelastic scattering and induced gluon radiation.

There exist a few energy loss calculations incorporated in some models and couple of them are listed below with very brief description:

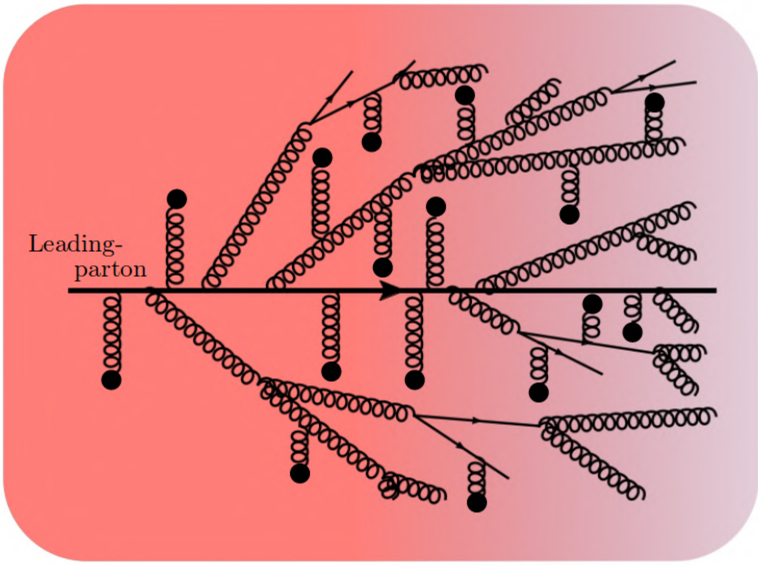

FIGURE 3.22: Schematic illustration showing medium induced gluon radiation during the propagation of the parton through the medium. Figure taken from [59].

- **BDMPS-Z [65–68]:** This model was proposed by Baier, Dokshitzer, Mueller, Peigné, Schiff and Zakharov. They have described the medium as a collection of scattering centres [69]. Collisional energy loss are depicted by the inclusion of recoils. The energy loss prediction for this model is expressed by the quadratic dependence on the in-medium path length ($\propto L^2$) with the assumptions: each scattering centre can scatter once, the mean free path (λ) is larger than the Debye screening length and energy of the radiated gluon is much smaller than the propagating hard scattered parton. The gluon spectrum obtained from this model shows the characteristic LPM suppression. Few key points of this model are described later in this section.

- **GLV [70, 71]:** This model given by Gyulassy, Levai and Vitev is based on the description of a reaction operator which gives the scattering off the scattering centres. The complete energy loss is described by the expansion in the number of scatterings in the medium, given by $n = \frac{L}{\lambda}$. One contribution is induced from $(n-1)$ terms by means of the reaction operator and here also the L^2 dependence is seen.

- **ASW [72]:** C. Salgado and Wiedemann conceptualised this model by using path integral formalism. It considers the incoming parton as a superposition of Fock states, which decohere while interacting with the medium and produce real particles. In the respective limits, it reproduces the results of multiple soft scatterings and single hard scattering.

- **AMY [73]:** The Arnold, Moore and Yaffe model is based on pQCD using hard thermal loop improvements. It describes the propagation of the parton through a thermal medium having temperature larger than the critical temperature.
- **AdS/CFT:** The energy loss in this model is based on the dual formalism [74] of Conformal Field Theories (CFT) and super-gravities in Anti-de-Sitter (AdS) [75] spaces to map the strong coupling scenario.

3.2.1 Medium-induced radiative energy loss

The hard scattered parton with energy E, radiates a gluon with energy ω both of which traverse a finite distance L in the medium. The split gluon subsequently suffers multiple collisions in its path with a mean free path λ, which is inversely proportional to the medium density. The number of collisions with momentum transfer q_T^2 that the emitted gluon suffers until it decoheres, is proportional to L and this makes the average partonic energy loss to be proportional to L^2. In the limit $E \rightarrow \infty$, the average energy loss by gluon radiation with an energy spectrum $\omega \frac{dI}{d\omega}$ is expressed in terms of the characteristic gluon energy, ω_c as:

$$\Delta E = \int_c^{\omega} \frac{\omega dI}{d\omega} d\omega \simeq \alpha_S \omega_c \text{ where, } \omega_c = \frac{1}{2}\hat{q}L^2 \tag{3.18}$$

which depends on the in medium path length and the transport coefficient $\hat{q}$ generally given by:

$$\hat{q} \simeq \rho \int q_{\perp}^2 \frac{d\sigma}{d^2 q_{\perp}} d^2 q_{\perp} \tag{3.19}$$

where ρ is the density of the medium (in the model, number of scattering centres), $q_{\perp}$ is the transverse momentum of the emitted gluon and σ is the cross-section of radiated gluon-medium interaction. For information, typically the transport coefficients for cold

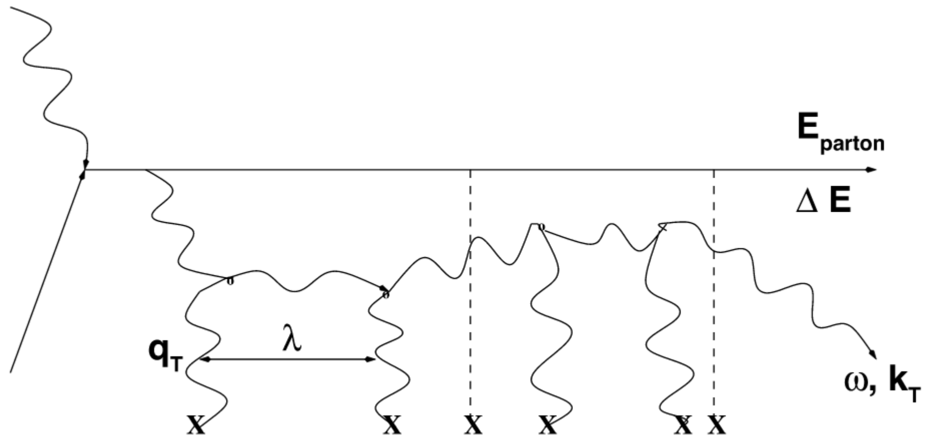

FIGURE 3.23: Schematic illustration of typical gluon radiation. Figure taken from [76]

and hot nuclear matter are estimated as [65, 67]:

$$\hat{q}_{cold} \simeq 8\rho_0 \quad and \;\; \hat{q}_{hot} \simeq 20\hat{q}_{cold}, \quad \text{where } \rho_0 \text{ is the nuclear density} \tag{3.20}$$

There are a few semi-quantitative arguments in view of the above relations, pointed out below:

- The number of coherent scattering centers, which act as a single source of gluon radiation: $N_{coh} \simeq t_{coh}/\lambda \simeq \sqrt{\omega/\mu^2\lambda} >> 1$
- Formation (coherence) time: $t_{coh} \simeq \omega/k_\perp^2 \simeq \sqrt{\omega/\hat{q}}$
- The average transverse momentum gain of the emitted gluon (random walk of gluon, referring to Figure 3.23) $k_\perp \simeq N_{coh}\mu^2$
- The momentum broadening of the gluon due to multiple scatterings is related to the transport coefficient: $\langle q_\perp^2 \rangle = \hat{q}L$ such that the differential energy loss is given by [77]:
$$-\frac{dE}{dz} \simeq \alpha_S < q_\perp^2 > \tag{3.21}$$
- The saturation scale [78], Q_s, of the gluon-nucleus (radius R_A) collision is related with the transport coefficient as [79]: $Q_s^2 = 2R_A\,\hat{q}$.

Other than these medium interactions, jet studies in heavy-ion collisions also get affected by the collective feature of the produced medium. The collective behaviour is manifested as radial flow and elliptic flow [80]. Elliptic flow originates from the spatial asymmetry in the non-central collisions and causes different pressure gradients in different directions which in turn affects in the azimuthal asymmetry in the final state hadrons.

3.3 Theoretical uncertainties

There are plenty of assumptions and approximations which help to arrive at a prediction comparable to experimental data and due to this a thorough assessment of the associated uncertainties is a must. Few of the most common theoretical uncertainties in jet physics are listed here:

- *Scale uncertainty:* This arises due to the truncation of the perturbative expansion of α_s. All the fixed order calculations suffer from the fact and the missing higher orders somehow need to be accounted for in an uncertainty.
- *PDF uncertainty:* This arises due to our limited knowledge on the structure of the hadrons. There exist a number of models which follow different descriptions of the internal distribution of the hadrons and this induces an uncertainty.
- α_s *uncertainty:* The limited knowledge of the strong coupling constant is the reason behind this uncertainty. This particular uncertainty is sometimes coupled with the PDF uncertainty.
- *Non-perturbative uncertainty:* Since fixed-order predictions as used in fits of SM parameters are at parton-level only, corrections for non-perturbative effects must be applied. This implies model assumptions and parameter tuning and hence induces a corresponding uncertainty.

Depending on the observable under study and the employed theoretical tools and techniques or limited statistical precision in numerical approximations may give rise to further uncertainties. A good description can be found here [81].

Bibliography

[1] Alison Lister, Thesis: "Measurement of b quark Jet Shapes at CDF" (2006)

[2] G. Dissertori, I. Knowles and M. Schmelling, Quantum Chromodynamics: High Energy Experiments and Theory, Oxford Science Publications (2003)

[3] S. Dulat et. al., arxiv:1506.07443v3 (2015)

[4] J. Blumlein, Prog. Part. Nucl. Phys. 69, 28-84 (2013)

[5] B. Andrieu et. al., H1 Calorimeter Group Collaboration, Nucl. Inst. Meth. A 336, 460 (1993)

[6] I. Abt et. al., H1 Collaboration, Nucl. Inst. Meth. A386, 310 (1997)

[7] R. Appuhn et. al., H1 SPACAL Group Collaboration, Nucl. Inst. Meth. A 386, 397 (1997)

[8] U. Holm (ed.), ZEUS Collaboration, The ZEUS Detector. Status Report, DESY (1993) doi:10.3204/PUBDB-2017-12635 http://www-zeus.desy.de/bluebook/bluebook.html

[9] F. Berends and R. Kleiss, Nucl. Phys. B 178 141-150 (1981)

[10] C. Loizides, Thesis: Jet physics in ALICE (2005)

[11] G. Altarelli and G. Parisi, Nucl. Phys. B 126 298 (1977)

[12] Y Dokshitzer, Sov.Phys. JETP 46 641 (1977)

[13] J. Klein, Thesis: Jet Physics with A Large Ion Collider Experiment at the Large Hadron Collider (2014)

[14] Y. Azimov, Y. Dokshitzer, V. Khoze and S. Troian, Z. Phys. C27, 65 (1985)

[15] Y. Dokshitzer and B. Webber, Phys. Lett. B 352, 451 (1995)

[16] Y. Dokshitzer, V. Khoze and S. Troian, Phys. Rev. D 53, 89 (1996)

[17] Y. Dokshitzer, G. Marchesini and B. Webber, Nucl. Phys. B 469, 93 (1996)

[18] R. Feynman, 'Photon Hadron Interactions', W.A. Benjamin, New York (1972)

[19] G. Marchesini and B. Webber, Nucl. Phys. B 238, 1 (1984)

[20] B. Webber, Nucl. Phys. B238, 492 (1984)

[21] G. Marchesini and B. Webber, Nucl. Phys. B 310, 461 (1988)

[22] G. Marchesini, B. Webber, G. Abbiendi, I. Knowles, M. Seymour and L. Stanco, Comput. Phys. Commun. 67, 465 (1992)

[23] G. Marchesini, B. Webber, G. Abbiendi, I. Knowles, M. Seymour and L. Stanco, hep-ph/9607393

[24] D. Amati and G. Veneziano, Phys. Lett. B 83, 87 (1979)

[25] G. Marchesini, L. Trentadue and G. Veneziano, Nucl. Phys. B 181, 335 (1981)

[26] B. Andersson, G. Gustafson, G. Ingelman and T. Sjöstrand, Phys. Rept. 97, 31 (1983)

[27] T. Sjöstrand, Comput. Phys. Commun. 39, 347 (1986)

[28] T. Sjöstrand and M. Bengtsson, Comput. Phys. Commun. 43, 367 (1987)

[29] T. Sjöstrand, Comput. Phys. Commun. 82, 74 (1994)

[30] T. Sjöstrand, CERN-TH-7112-93, hep-ph/9508391

[31] B. Webber XIX International Symposium on Lepton and Photon Interactions at High Energies, Stanford University, http://arXiv.org/abs/hep-ph/9912292v1 (1999)

[32] PDG group, http://pdg.lbl.gov/2019/reviews/rpp2018-rev-mc-event-gen.pdf

[33] C. Buchanan and S. Chun, Phys. Rev. Lett. 59, 1997 (1987)

[34] S. Chun and C. Buchanan, Phys. Lett. B 308, 153 (1993)

[35] S. Chun and C. Buchanan, Phys. Rept. 292, 239 (1998)

[36] P. Hoyer et. al., Nucl. Phys. B 161, 349 (1979)

[37] A. Ali et al., Phys. Lett. B 93, 155 (1980)

[38] A. Ali et al., Nucl. Phys. B 168, 409 (1980)

[39] R. Field and R. Feynman, Phys. Rev. D 15, 2590 (1977)

[40] R. Field and R. Feynman, Nucl. Phys. B 138, 1 (1978)

[41] C. Amsler et. al., Particle Data Group, Phys. Lett. B 667, 1-6 (2008)

[42] G. Dissertori, I. Knowles, and M. Schmelling, Quantum Chromodynamics: High Energy Experiments and Theory. International Series of Monographs on Physics, OUP Oxford (2009)

[43] R. Field for the CDF Collaboration, C010630:P501, arXiv:hep-ph/0201192 (2001)

[44] T. Affolder, CDF Collaboration, Phys. Rev. D 64, 032001 (2001)

[45] J. Huth et. al., FNAL-C-90-249-E (1990)

[46] G. Blazey et. al., “Run II jet physics,” hep-ex/0005012 (2000)

[47] G. Salam, Eur. Phys. Jour. C 67, 637-686 (2010)

[48] J. Berger, Thesis: Search for the Higgs Boson Produced via Vector-Boson Fusion in the Decay Channel $H \rightarrow \tau\tau$ (2014)

[49] G. Arnison et. al., UA1 Collaboration, Phys. Lett. B 132, 21 (1983)

[50] G. Salam and G. Soyez, JHEP 0705, 086 (2007)

[51] S. Ellis, J. Huston and M. Tönnesmann, eConf C010630 513, arXiv:0111434 (2001)

[52] M. Cacciari and G. P. Salam, Phys. Lett. B 641, 57 (2006)

[53] S. Catani, Y. Dokshitzer, M. Seymour, and B. Webber, Nucl. Phys. B406, 187224 (1993)

[54] M. Cacciari, G. Salam, and G. Soyez. JHEP 0804, 063 (2008)

[55] CMS collaboration, CMS PAS JME-09-001 (2009)

[56] G. Salam, arxiv:0906.1833 (2010)

[57] J. Cronin, Phys. Rev. D 11, 3105 (1975)

[58] J. Bjorken, FERMILAB-PUB-82-059-THY (1982)

[59] Y. Tachibana, Thesis: Hydrodynamic response to jetpropagation in quark-gluon plasma (2014)

[60] M. Thoma, Applications of high temperature field theory to heavy-ion collisions. In R.C. Hwa, editor, Quark-Gluon Plasma 2, page 51. World Scientific, Singapore, ISBN 981-02-2399-4 (1995)

[61] M. Gyulassy and X. Wang, Nucl. Phys., B 420:583–614 (1994)

[62] L. Landau and I. Pomeranchuk, Dokl. Akad. Nauk Ser. Fiz. 92:535–536 (1953)

[63] L. Landau and I. Pomeranchuk, Dokl. Akad. Nauk Ser. Fiz. 92:735–738 (1953)

[64] A. Migdal, Phys.Rev., 103:1811–1820 (1956)

[65] R. Baier, Y. Dokshitzer, A. Mueller, Nucl. Phys. B 483(1-2):291–320 (1997)

[66] B. Zakharov, JETP Lett., 63:952–957 (1996)

[67] R. Baier, Y. Dokshitzer, A. Mueller, Nucl. Phys. B 484(1-2):265–282 (1997)

[68] R. Baier, Y. Dokshitzer, A. Mueller, Nucl. Phys. B 531(1-3):403–425 (1998)

[69] M. Gyulassy and X. Wang, Nucl. Phys. B 420:583–614 (1994)

[70] M. Gyulassy, P. Levai, and I. Vitev, Nucl. Phys. B 571(1-2):197–233 (2000)

[71] M. Gyulassy, P. Levai, and I. Vitev, Nucl. Phys. B 594(1-2):371–419 (2001)

[72] C. Salgado and U. Wiedemann, Phys. Rev. D 68:014008 (2003)

[73] P. Arnold, G. Moore and L. Yaffe, JHEP 2001(11):57 (2001)

[74] J. Casalderrey-Solana, H. Liu, D. Mateos, Gauge/String Duality, Hot QCD and Heavy Ion Collisions, pre-print (2011)

[75] J. Maldacena, Adv. Theor. Math. Phys. 2:231–252 (1998)

[76] R. Baier, Nucl. Phys. A715:209–218 (2003)

[77] R. Baier, Y. Dokshitzer, A. Mueller, S. Peign and D. Schiff, Nucl. Phys. B 483 291; ibidem B 484 265 (1997)

[78] Y. Kovchegov and A. Mueller, Nucl. Phys. B 529 451 (1998)

[79] A. Mueller, Nucl. Phys. B 558 285 (1999)

[80] C. Shen, U. Heinz, P. Huovinen and H. Song, Phys. Rev. C 84, 044903 (2011)

[81] R. Barlow and others, Book: Data Analysis in High Energy Physics (1st edn.) (2013)

Chapter 4

Jet properties study in pp events with ALICE

In this chapter the analysis of data from pp collisions at $\sqrt{s} = 2.76$ TeV recorded by the ALICE detector system has been described in details. This is a charged jet analysis with leading jet, i.e., jets are reconstructed taking into account only the charged particle information and also taking the highest p_T jet of the event into consideration. Properties of the leading charged jets have been studied by defining various differential jet shape observables. Starting from the raw data, it takes many subsequent steps to obtain the final results and draw physics messages. This chapter deals with all these intermediate details in terms of obtaining the physics observables from the raw data, correction of the raw data, subtraction of the background from the observables, study of systematic uncertainties to quantify the measurement precision and comparison of the results to the predictions from models based on theoretical inputs.

4.1 Prelude

The internal structure of jets is dominated by the emitted multiple gluons from the hard scattered initial parton. The jet structure is also sensitive to the parton flavor and is modified by the contributions from ISR and BBR. These are all part of the fragmentation process and involve higher order QCD processes which are usually difficult to calculate. Various Monte Carlo models try to reproduce this fragmentation pattern by using some theoretical assumptions. These models are periodically tuned to achieve the result exactly comparable to the experimental ones. A good understanding of the hadronization process is also needed to compare the simulated results at the partonic level with the ones observed at the detector level. In the study of the internal structure of jets, jet shape observables provide a stringent test of QCD predictions and validate the existing models for parton fragmentation in hadronic collisions.

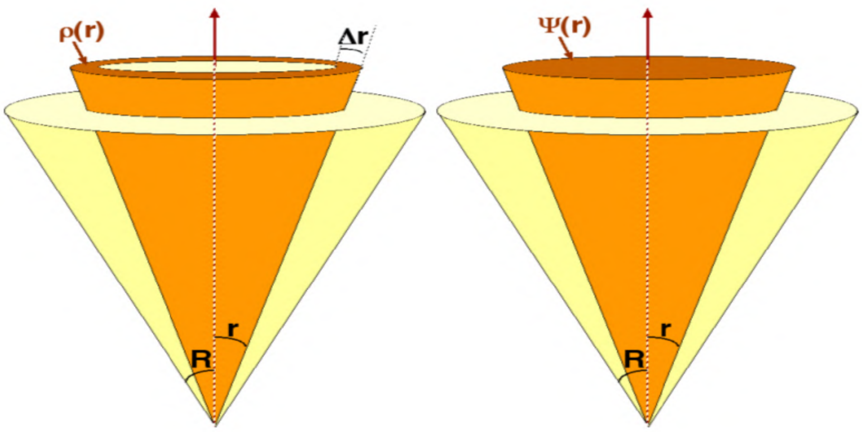

FIGURE 4.1: Schematic illustrations showing differential (left) and integrated (right) jet shape measurements. Figure taken from [1]

Before we move into measurements of jet shape, we need to have some basic idea about the jet shape observables. Jet shapes look at the fractional p_T distribution inside the jet cone as a function of distance from the jet axis. Jet shape observables could be defined in two broad categories: differential form and integral form. Differential jet shape, $\rho(r)$, computes the change in p_T with increasing distance from the jet axis (at a distance r and within the annular disc of width Δr, $r = \sqrt{(\Delta\eta)^2 + (\Delta\phi)^2}$), whereas integrated jet shape, $\psi(r)$, gives the fractional jet p_T inside a cone (of radius r) around the jet axis, as shown in Figure 4.1. The first generation of jet shape observables were expressed as follows (first by the ZEUS [2] and then CDF [3] collaboration):

$$\rho(r) \;=\; \frac{1}{N_{jets}} \sum_{jets} \frac{p_T^{jet}\left(r - \frac{\Delta r}{2}, r + \frac{\Delta r}{2}\right)}{p_T^{jet}(0, R)} \quad \text{for } \; 0 \leq r \leq R \tag{4.1}$$

where N_{jets} is the total number of jets. The differential shape is defined as,

$$\psi(r) \;=\; \frac{1}{N_{jets}} \sum_{jets} \frac{p_T^{jet}(0, r)}{p_T^{jet}(0, R)} \quad \text{for } \; 0 \leq r \leq R \tag{4.2}$$

Since then the observation of jet properties via the jet shape observables have been the basic measurements in jet studies and plenty of new jet shape observables have been constructed over the years. Jet properties have been measured using these observables by different collaborations by using different colliding systems at different energies and some of them can be found in: CDF[4–6], D0[7], ATLAS[8], CMS[9, 10], ALICE[11].

In this chapter, the details of the jet properties study using the jet shape observables like the mean charged particle multiplicity in the leading jets, leading charged jet size and the radial distribution of jet momentum have been discussed.

4.2 Observables

Following are the descriptions of the observables undertaken in this analysis:

4.2.1 Charged particle multiplicity in leading jets, N_{ch}

Charged particle multiplicity in leading jets, N_{ch}, is defined as the number of charged particles that falls within the leading jet cone. In this analysis the average distribution of this multiplicity, $\langle N_{ch} \rangle$, is reported which is computed in bins of jet p_T starting from 10 GeV/c to 70 GeV/c. The mean is computed following the relation stated below :

$$\langle N_{ch} \rangle (p_T) = \frac{\sum_{i=1}^{N_{jets}} N_{ch}}{N_{jets}} \tag{4.3}$$

where the sum runs for jets within a jet p_T bin and N_{jets} is the total number of jets within that bin.

4.2.2 Charged jet size, R_{80}

The size of the leading charged jet, R_{80}, is defined as the radius of the jet cone in the $\Delta\eta - \Delta\phi$ space that confines 80% of the total jet p_T found in the jet cone. The mean distribution of this, $\langle R_{80} \rangle$, is computed as a function of jet p_T.

4.2.3 Radial transverse momentum density of charged jet, p_T^{sum}

The transverse profile of the jet energy (momentum), p_T^{sum} gives the idea of the p_T composition of constituent particles around the jet axis. The radial distribution of transverse momentum density, dp_T^{sum}/dr, within a leading charged jet is measured as a function of the distance r radially outword from the jet axis. The momentum density is calculated constructing concentric annular regions of width Δr as shown in Figure 4.2, at radius r jet by jet taking only the scalar sum of the transverse momentum, p_T^{sum}, of all the charged particles that falls within the annular regions. Then the mean value of the momentum density, $\langle p_T^{sum}/dr \rangle$, is calculated in different jet p_T bins and as a function of r following the equation:

$$\langle \frac{dp_T^{sum}}{dr} \rangle (r) = \frac{1}{\Delta r} \frac{1}{N_{jets}} \sum_{i=1}^{N_{jets}} p_T^i \, (r - \Delta r/2, r + \Delta r/2) \tag{4.4}$$

where $p_T^i(r - \Delta r/2,\ r + \Delta r/2)$ denotes the scalar sum of the p_T of all tracks inside the annular ring with radius between $r - \Delta r/2$ and $r + \Delta r/2$. In this analysis, this measurements have been done in four jet p_T bins: 20< p_T^{jet} <30 GeV/c, 30< p_T^{jet} <40 GeV/c, 40< p_T^{jet} <60 GeV/c and 60< p_T^{jet} <80 GeV/c.

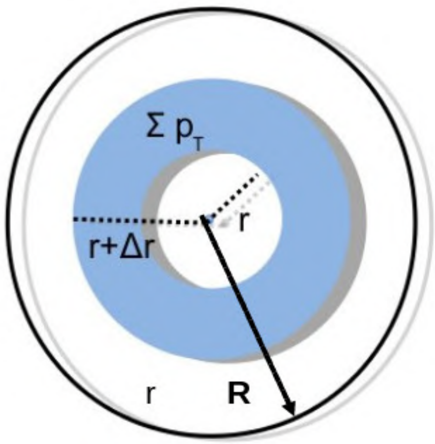

FIGURE 4.2: Radial transverse momentum distribution about jet axis in leading jet. Scalar p_T^{sum} is obtained for each annular regions as a function of distance r in different jet p_T bins.

4.3 Analysis overview

The observables are first measured with the raw ALICE data collected in the year 2011 (technically known as LHC11a in ALICE) in pp collisions at $\sqrt{s}$ = 2.76 TeV. The values are then corrected by following a correction method known as the bin-by-bin correction procedure. The background i.e., the UE (described in Chapter 3) is subtracted from each observable. At the end the systematic uncertainties introduced in the measurement are estimated to obtain the final results. These results at the detector level are then compared to the ones obtained from various Monte Carlo models to check the agreement with theoretical predictions. The analysis flow chart has been depicted in Figure 4.3.

Some of the details related to this analysis are given below:

- *Data:* pp 2.76 TeV minimum bias events. Events are accepted if there are at least two tracks contributing to the primary vertex. A total of 44 million minimum bias events were selected after applying various event selection cuts as shown in Figure 4.4.

- *Vertex:* -10 $< V_z <$ 10 cm, only the events recorded within ±10 cm along the beam axis from the nominal interaction point are considered. Figure 4.5 shows the vertex z distribution where '0' denotes the nominal or geometrical interaction

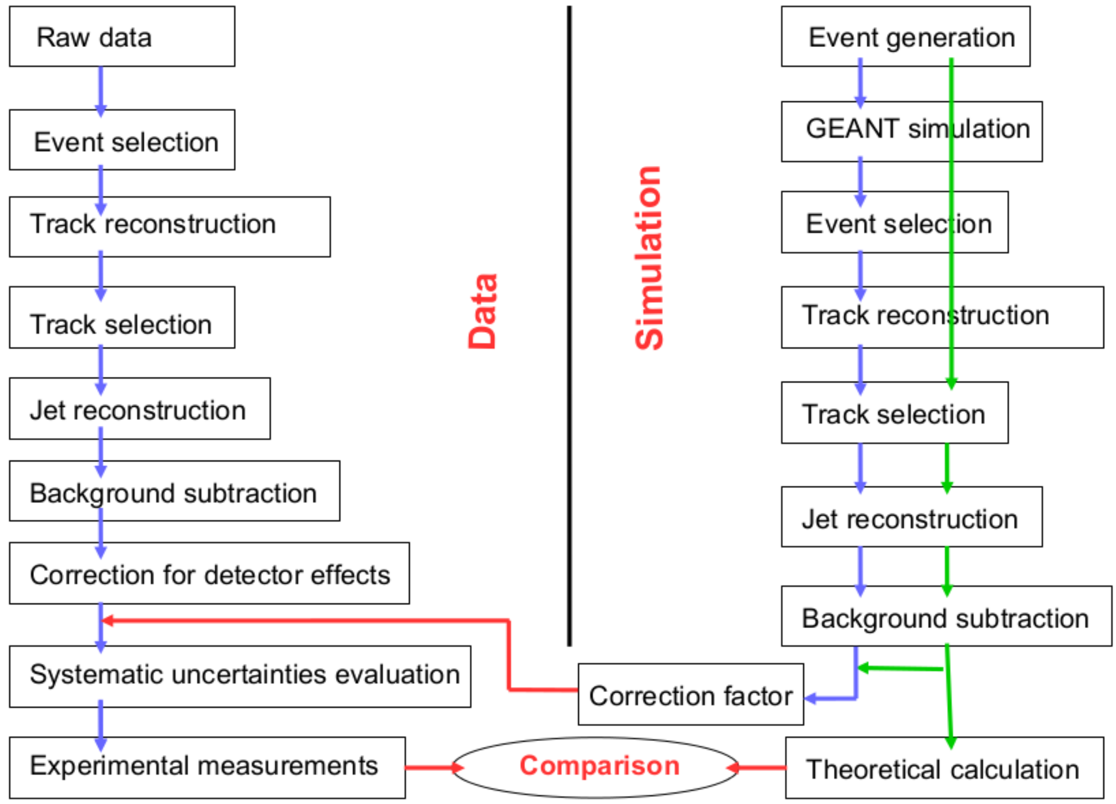

FIGURE 4.3: The analysis flow chart.

point defined by the detector geometry.

- *Tracks:* Tracks are taken if they have $p_T \geq 150$ MeV/c and within $\eta = \pm 0.9$. Charged tracks from ITS and TPC satisfying some technical specification [12] are used to make hybrid tracks and then these tracks are in turn used in the analysis.

- *Jet reconstruction:* Jets are reconstructed using the Anti-K$_t$ clustering algorithm (discussed in the last chapter) for $R = 0.2$, 0.3 and 0.4, taking only charged tracks. Jets are reported for the jet p_T range: 10 GeV/c< p_T^{jet} <70 GeV/c. Jet reconstruction in this analysis is done using FastJet-v2.4.3 [13]. The analysis started with three jet resolution parameters as mentioned but the results presented in this thesis were finalised for only $R = 0.4$ and those are presented in this thesis.

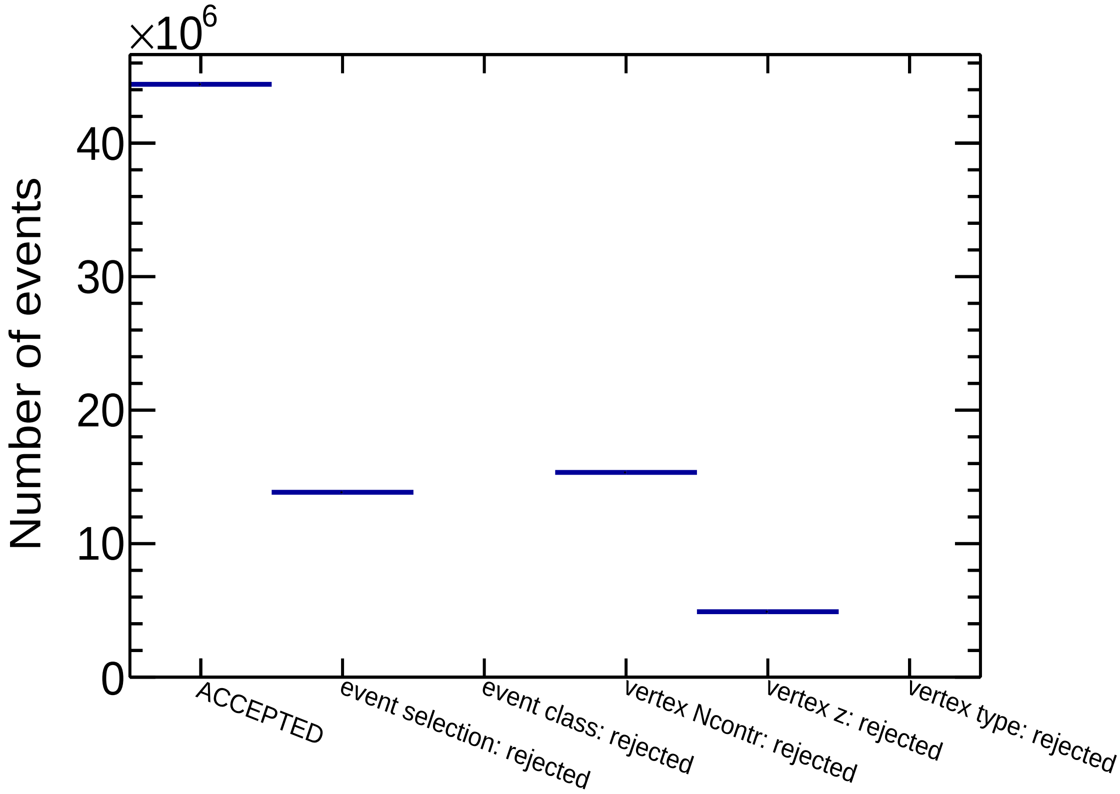

FIGURE 4.4: Event selection cuts.

4.4 Monte Carlo simulation

Monte Carlo simulation have three general utilities: to correct the raw data, to estimate the systematic uncertainties and to compare the experimental results. For this analysis the ALICE official Monte Carlo production (technically specified as LHC11a2a to LHC11a2j) with PYTHIA6.425 [14] tune Perugia0 has been used for the correction of the data. For the systematic uncertainty study and comparison of theoretical predictions, local production with various tunes of PYTHIA6 (Perugia0, Perugia2010, Perugia2011, AMBT1), HERWIG6.510 [17, 18] and PHOJET1.12.3.15 [20] have been used. A very brief discussion on the general purpose MC event generator and introduction to the models used in this analysis has been given in Appendix A.

Monte Carlo productions are produced at two levels: generated or particle level production and reconstructed or detector level production. To obtain the detector level production, the particle level is passed through the full detector simulation provided by

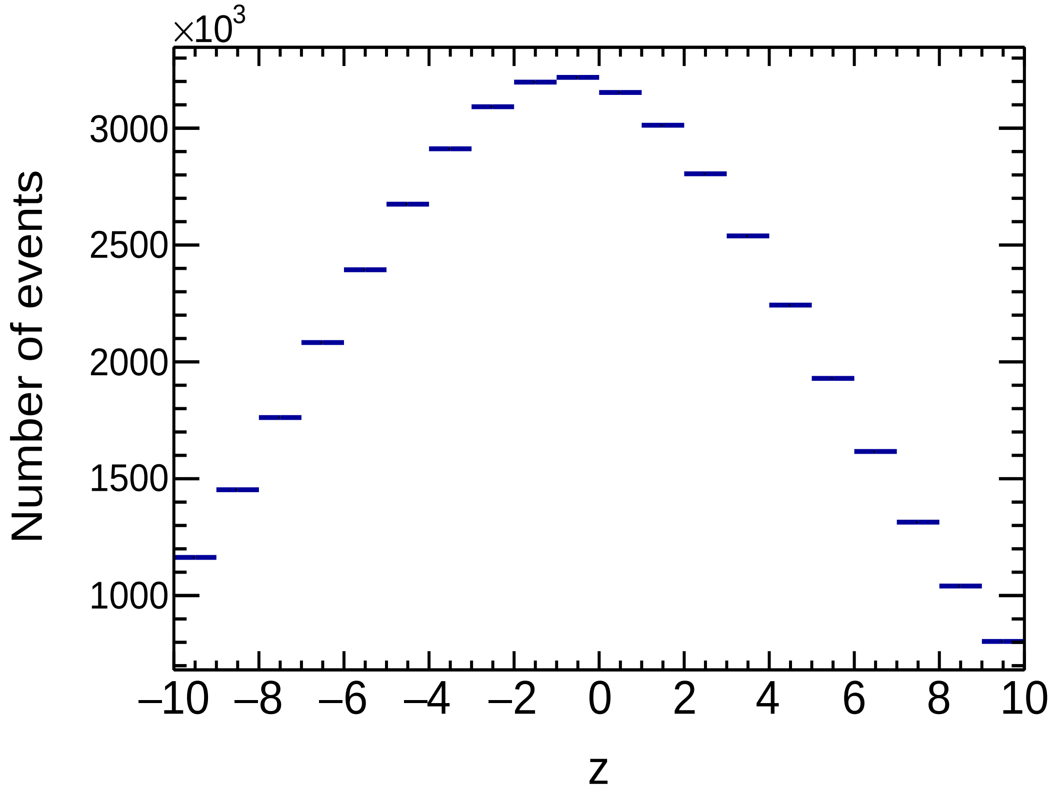

FIGURE 4.5: Vertex z distribution.

GEANT3 [18] package. Particle level observables are equivalent to the original production and treated as the theory predictions and compared to the experimental measurements. Whereas both the detector level and particle level measurements are used to correct the data and will be described in the subsequent section in this chapter.

4.5 Measurements with uncorrected raw data

In this section the measurements of $\langle N_{ch} \rangle$, $\langle R_{80} \rangle$ and $\langle \frac{dp_T^{sum}}{dr} \rangle$ with the raw data for three R: 0.2, 0.4 and 0.6 have been presented and those can be found in Figure 4.7. These measurements stand for the uncorrected case. With these, the UE measurements for $\langle N_{ch} \rangle$ and $\langle \frac{dp_T^{sum}}{dr} \rangle$ are also conducted and presented in Figure 4.6. No UE measurements for $\langle R_{80} \rangle$ is done as there exists no unique way to measure this for this observable. $\langle \frac{dp_T^{sum,UE}}{dr} \rangle$ measurement for only $R = 0.4$ has been shown here for the four selected jet p_T bins.

Also for $R = 0.4$, the raw measurements are compared with the raw measurements at $\sqrt{s} = 7$ TeV for $\langle N_{ch} \rangle$ and $\langle R_{80} \rangle$ distributions as can be seen in Figure 4.8. It is seen that for the entire range of p_T, the $\langle N_{ch} \rangle$ at 7 TeV is slightly higher than that at 2.76 TeV. At raw level, the comparison of UE at 7 TeV and 2.76 TeV uncovers the possible fact that UE is slightly higher for 7 TeV.

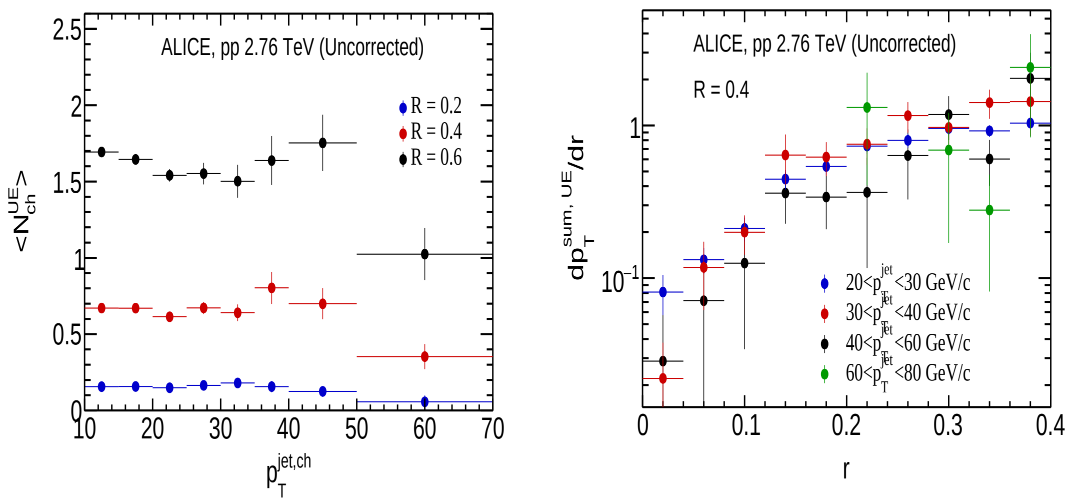

FIGURE 4.6: UE measurements with the raw data for $\langle N_{ch} \rangle$ for three different R: 0.2, 0.4 and 0.6 and $\langle \frac{dp_T^{sum}}{dr} \rangle$ for $R = 0.4$ in the four selected jet p_T bins.

4.6 Correction of the raw data

The data recorded by the detector suffers loss and distortion due to the detector specific effects such as finite tracking efficiency and track momentum resolution. In addition to the obvious impact of these effects on the reconstructed track spectra, they also contribute on the level of charged jet reconstruction. The track p_T resolution of all tracks in the jet results effectively in a smearing of the jet momentum. Similarly, limited tracking efficiency induces loss of tracks at the reconstruction level and softens the reconstructed jet momentum.

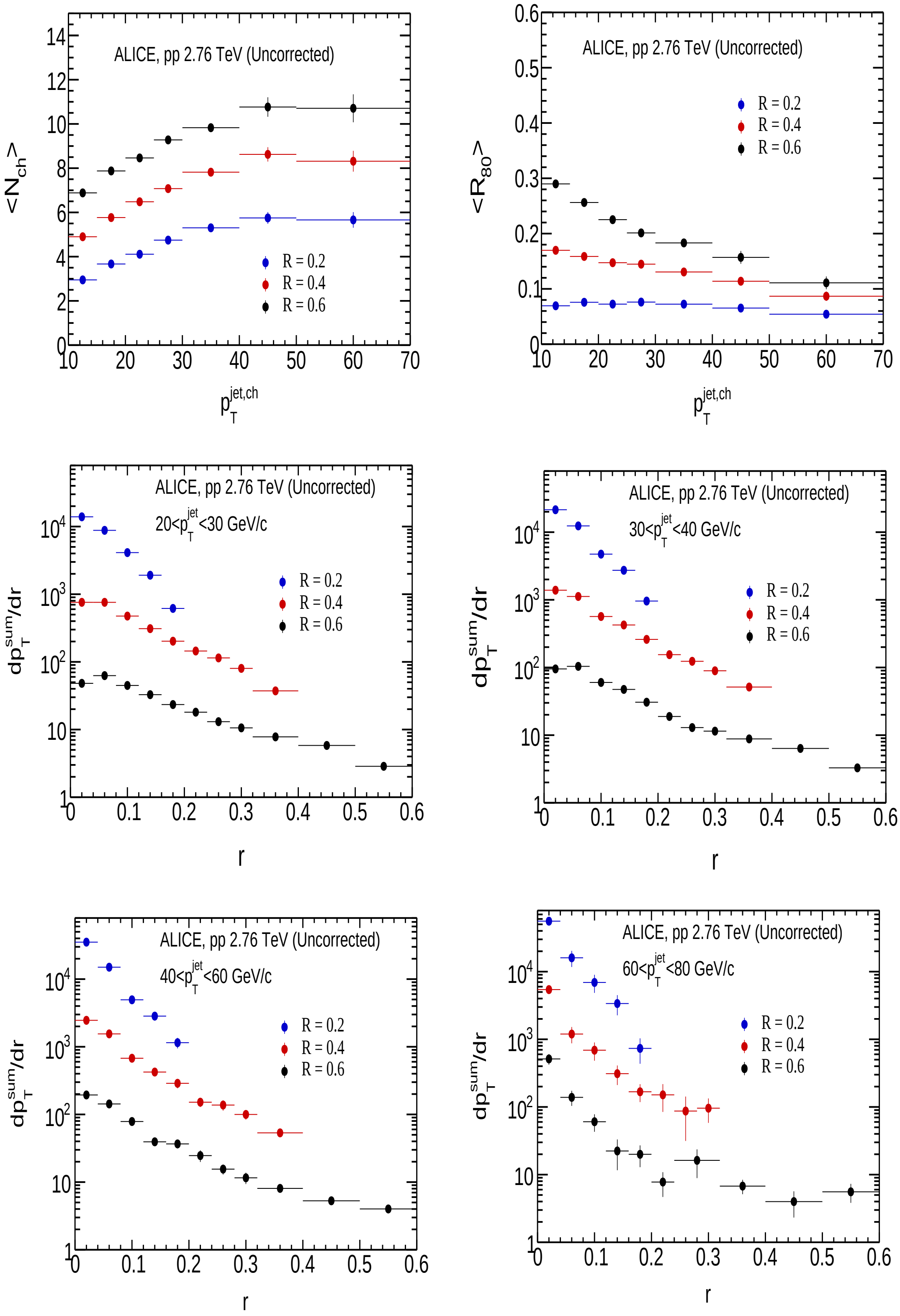

FIGURE 4.7: Measurements with the raw data: $\langle N_{ch} \rangle$ (top left), $\langle R_{80} \rangle$ (top right). Rest four are radial transverse momentum distribution in four different jet p_T bins, 20-30 GeV/c being the lowest jet p_T bin and 60-80 GeV/c is the highest jet p_T bin.

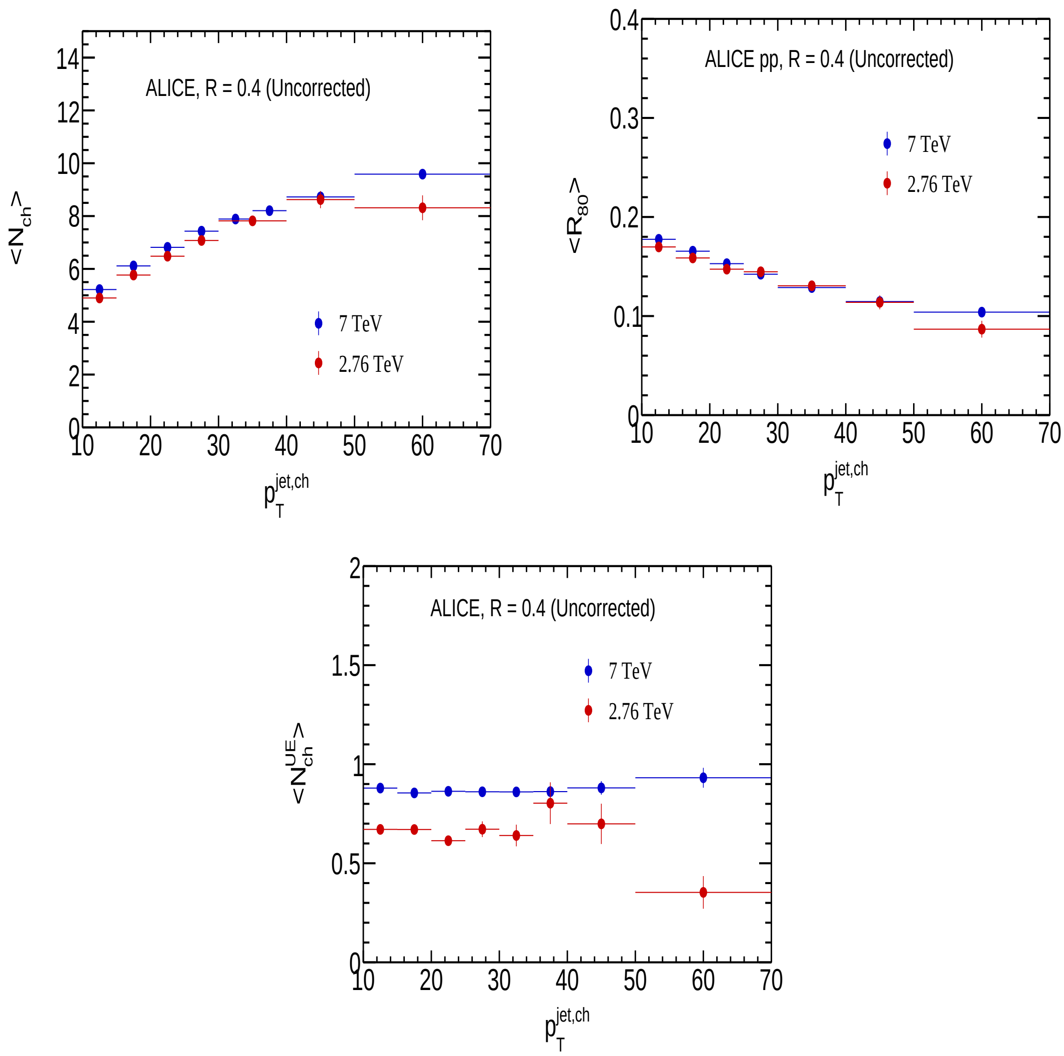

FIGURE 4.8: Comparison of raw measurements of $\langle N_{ch} \rangle$ (top left) and $\langle R_{80} \rangle$ (top right) at $R = 0.4$ for 2.76 and 7 TeV. Comparison of UE for $\langle N_{ch} \rangle$ (bottom) at $R = 0.4$ for 2.76 and 7 TeV.

In order to correct the measurements for the detector responses, here the bin-by-bin correction procedure is adopted, similar to what was introduced by the CDF collaboration [19] and later has been used at LHC experiments [11, 20]. This technique is purely based on the Monte Carlo models, where events are generated with a event generator and full detector simulation is incorporated in the whole process. Here in this analysis PYTHIA6 with tune Perugia0 was used for the event generation and GEANT3 package provided the detector simulation.

In the production, right after the event generation, the production level is called the truth level or particle level and after passing this particle level production through the detector simulation, one obtains the detector level or reconstructed level as it mimics the experimental measurements with detector. Bin-by-bin correction factors are obtained for each observables by taking the ratio of the generated level to the detector level measurements as shown in Figure 4.9 and 4.10. The corrected results are then obtained by multiplying these correction factors with the raw data measurements following the relation:

$$O_{data}^{corrected} = O_{data}^{uncorrected} \frac{O_{mc}^{part}}{O_{mc}^{det}} \tag{4.5}$$

where O_{mc}^{part} is the particle level spectra and O_{mc}^{det} is the detector level spectra.

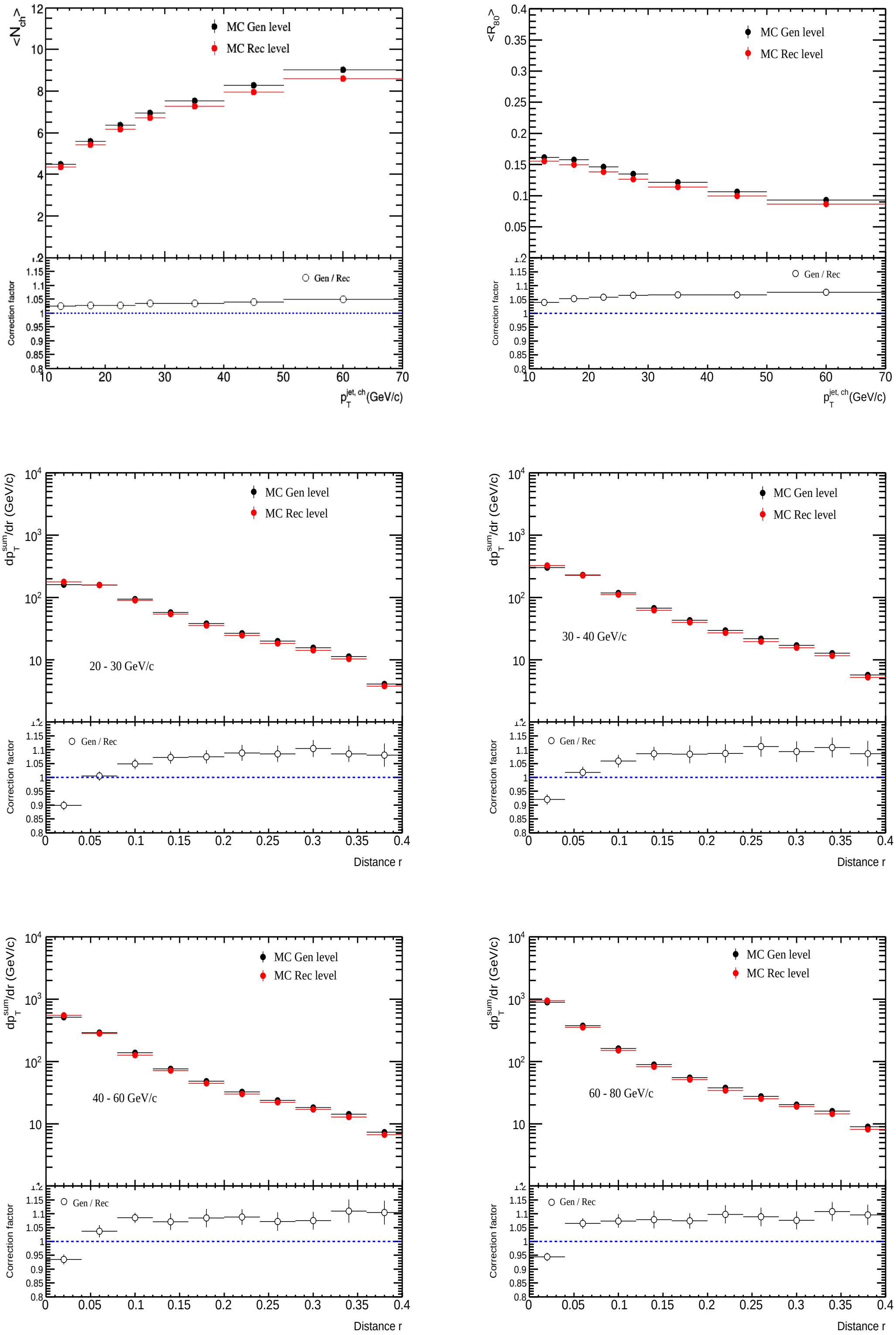

FIGURE 4.9: Correction factors measured at $R = 0.4$ for: $\langle N_{ch} \rangle$ (top left), $\langle R_{80} \rangle$ (top right). Rest four are radial transverse momentum distribution in four different jet p_T bins as indicated.

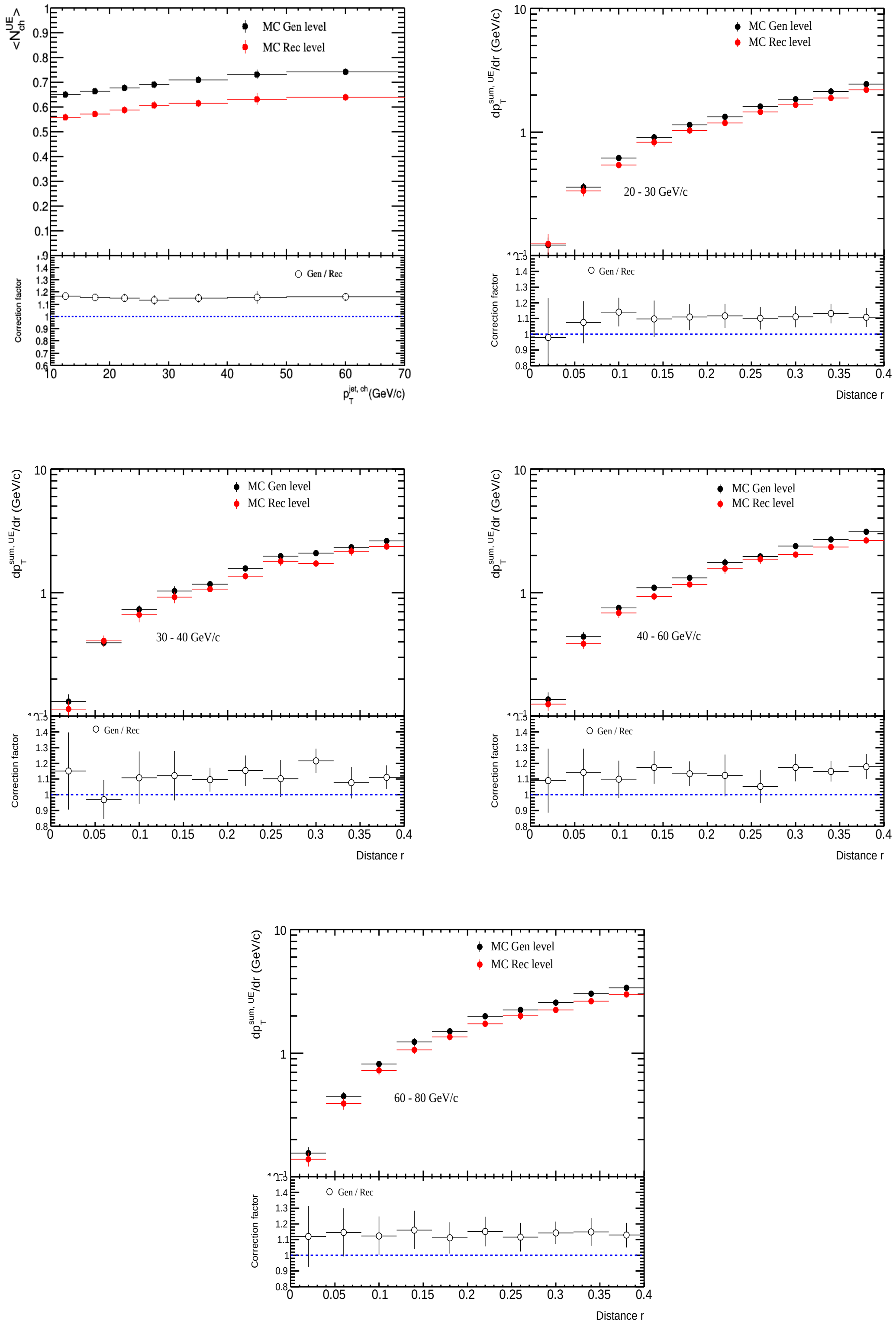

FIGURE 4.10: Correction factors measured at $R = 0.4$ in UE for: $\langle N_{ch} \rangle$ (top left) and rest four are radial transverse momentum distribution in four different jet p_T bins as indicated.

4.7 Underlying event (UE) subtraction

UE distributions for the observables are first measured following the procedure discussed in the previous chapter and then those are also corrected following the bin-by-bin correction procedure described above. The UE is measured over a large number of events and then the average distribution is obtained. After correction of both the measured observables and corresponding UE, the subtraction of UE is done bin-by-bin from the actual observables. The corrected and UE subtracted observables are shown in Figure 4.11.

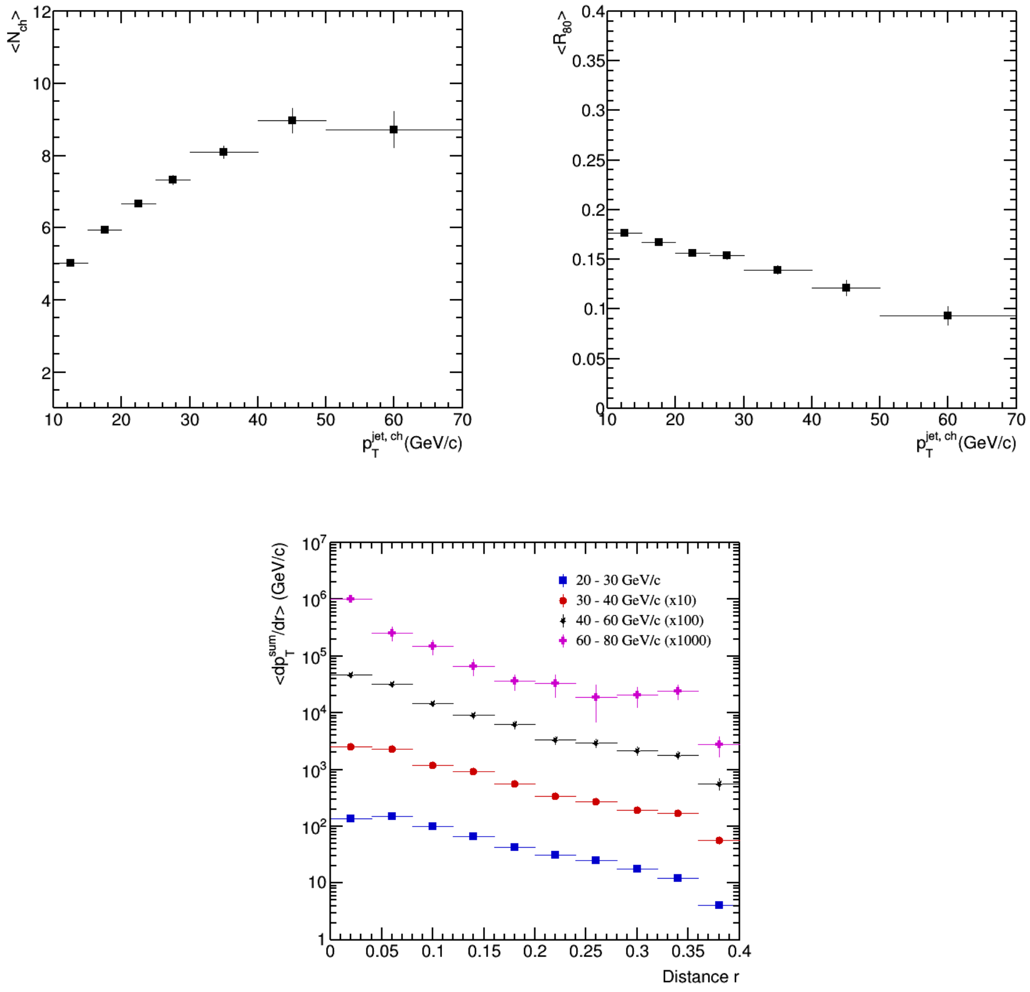

FIGURE 4.11: Observables after bin-by-bin correction and UE subtraction for $R = 0.4$: $\langle N_{ch} \rangle$ (top left), $\langle R_{80} \rangle$ (top right) and $\langle p_T^{sum} \rangle$ (bottom). The distributions in $\langle p_T^{sum} \rangle$ have been scaled, as indicated, for distinguishable display.

4.8 Estimation of systematic uncertainties

Systematic uncertainties stand for the error induced in the measurements due to various systematic effects like detector technology limitation, different methods for estmation of background, correction technique applied in the analysis etc. One really can not have much control over these but one can estimate the band of confidence around the actual data measurements to identify the range in which the values can stay. The sources of systematic uncertainties are analysis specific and for this analysis they are: (i) uncertainties in detector efficiency for track reconstruction, (ii) uncertainties incorporated in the momentum resolution, (iii) uncertainties in the measurement of UE and (iv) uncertainties associated with the correction procedure such as the bias introduced while using different MC models. The main contributors to the total systematic uncertainty are found to be the uncertainty in efficiency and momentum resolution. The estimation process is purely based on MC simulation and described below:

4.8.1 Uncertainties due to finite tracking efficiency and p_T resolution

To estimate the contributions from these two sources, 30 million events with PYTHIA6 Perugia0 tune event generator were produced. An MC based process is adopted which allows to change the detector efficiency and momentum resolution manually as also used in [11].

- Step - 1
  - Plot for track reconstruction efficiency (Figure 4.12) is obtained using GEANT3 full detector simulation. This efficiency is fitted with appropriate functions and particles are removed from the generated events according to this parameterized track reconstruction efficiency.
  - Plot for parameterized momentum resolution is obtained and p_T of the rest of the particles are smeared according to a Gaussian distribution obtaining the width from the parameterized momentum resolution.
  - Jets are reconstructed using these tracks even-by-event using FastJet jet clusterizer.

  - All the observables under consideration are calculated.

- Step - 2
  - The relative track reconstruction efficiency is varied by ±4% (earlier a variation of 5% was considered as in [11]) and two sets of productions are obtained.
  - Step - 1 is repeated.

- Step - 3
  - The relative track momentum resolution is varied by ±20% (following [11]) and two sets of productions are obtained.
  - Step - 1 is repeated.

Taking the production from step - 1 as default, two more sets of productions each for changed efficiency and changed momentum resolution are obtained. The outputs for the same can be found in Figure 4.13 and Figure 4.14 respectively. Then uncertainties for these two effects are obtained on each observable as following:

$$Obs^{sys} = \frac{Obs^{changed\ efficiency/resolution} - Obs^{default}}{Obs^{default}} \tag{4.6}$$

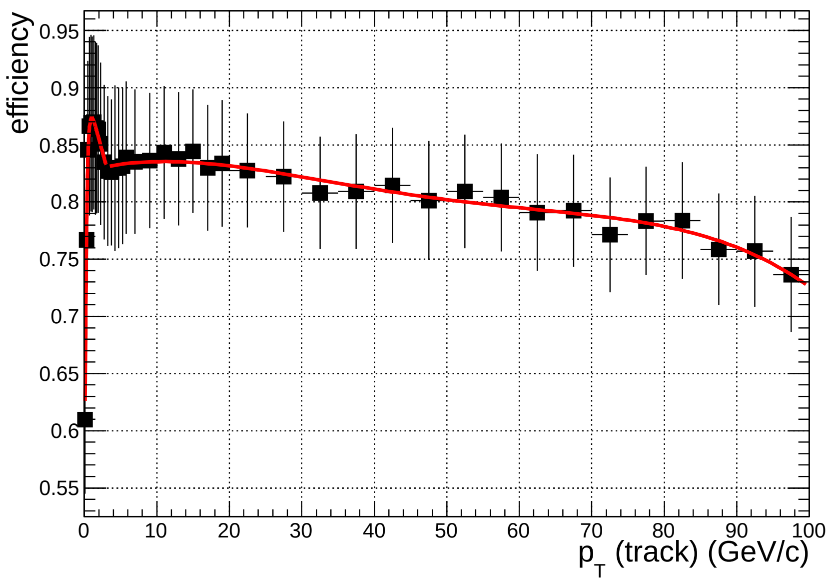

FIGURE 4.12: Tracking efficiency plot from full GEANT simulation with fitting.

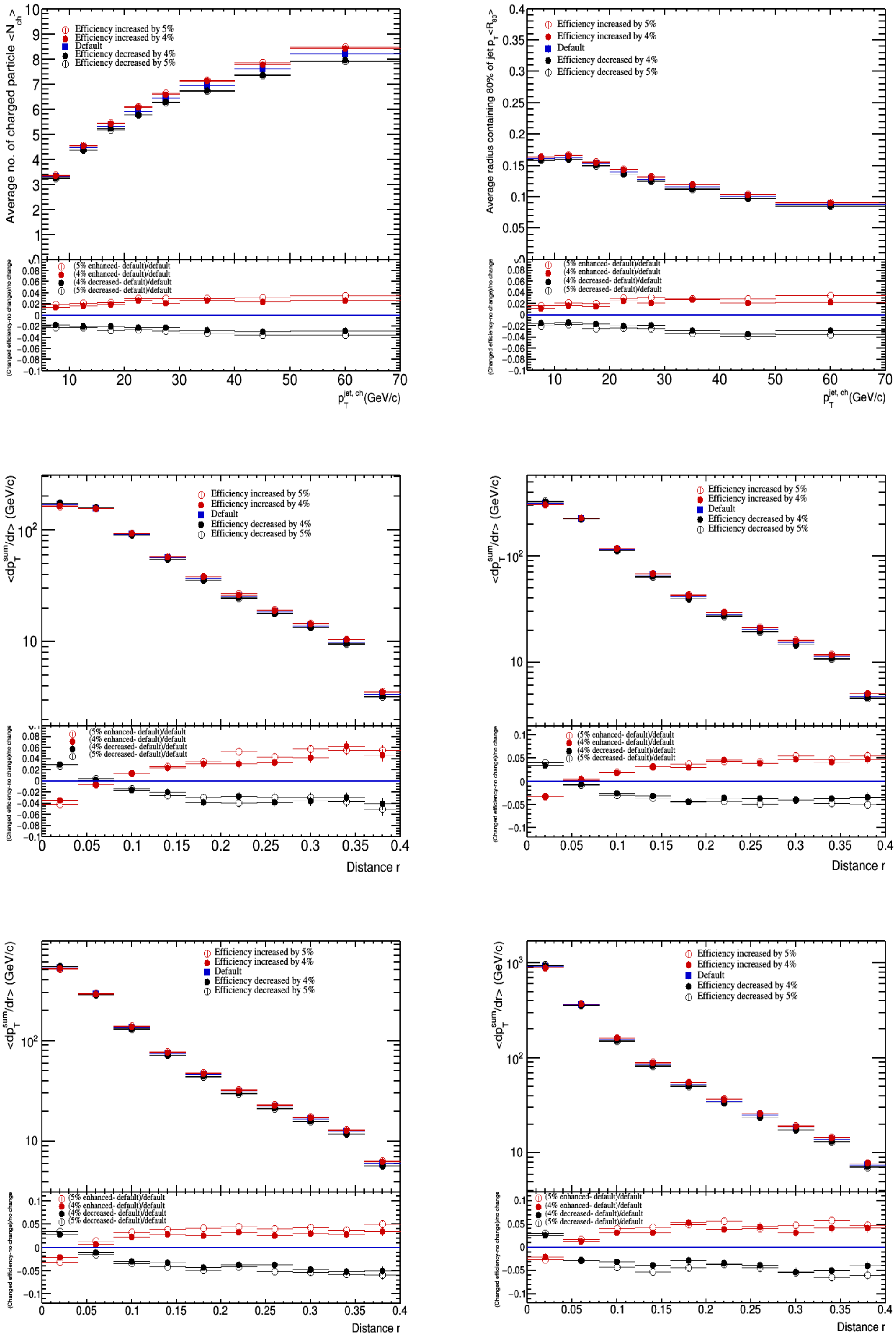

FIGURE 4.13: Estimation of uncertainties for finite tracking efficiency: $\langle N_{ch} \rangle$ (top left), $\langle R_{80} \rangle$ (top right) and rest four are for $\langle p_T^{sum} \rangle$ in four different jet p_T bins as indicated.

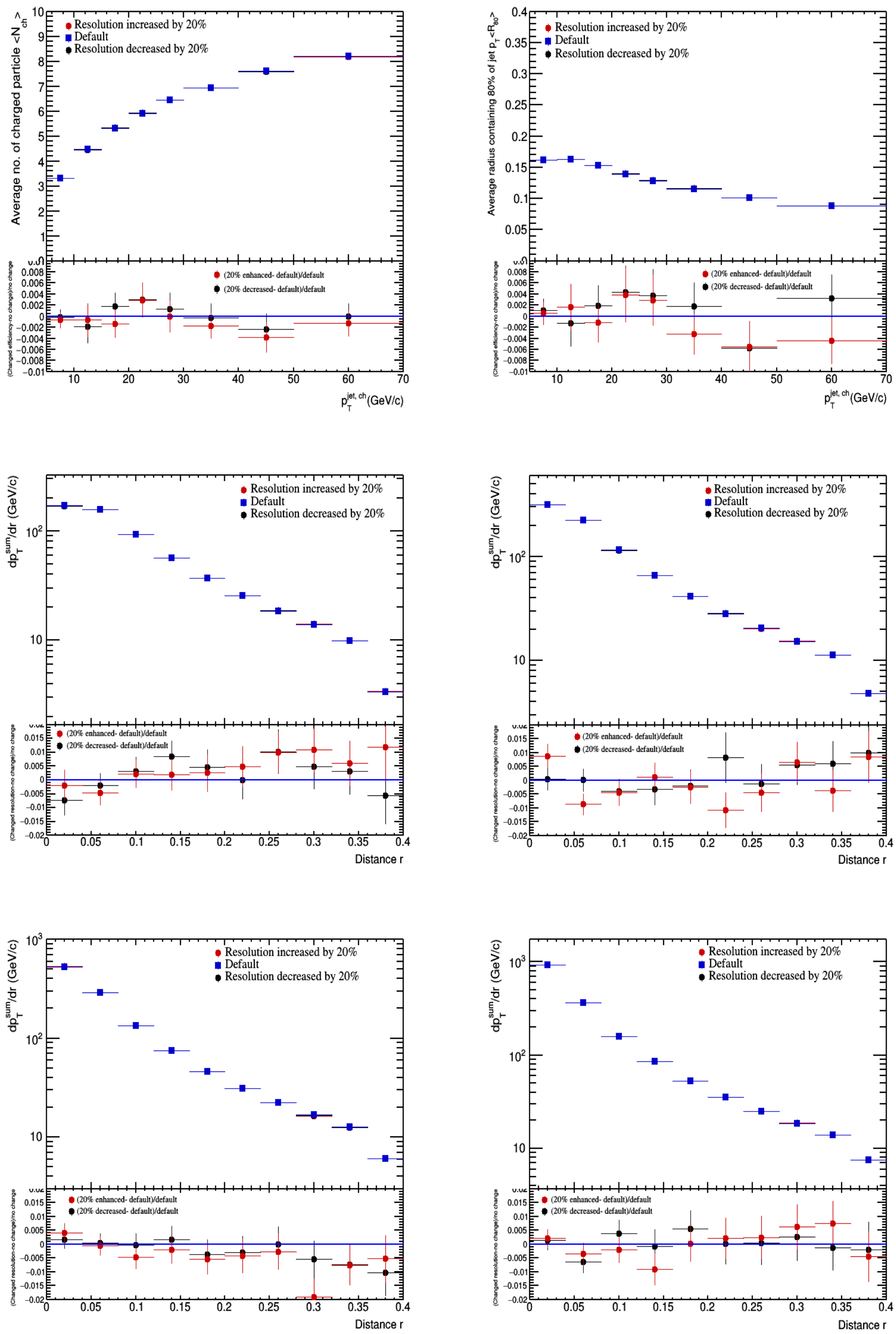

FIGURE 4.14: Estimation of uncertainties for finite momentum resolution: $\langle N_{ch} \rangle$ (top left), $\langle R_{80} \rangle$ (top right) and rest four are for $\langle p_T^{sum} \rangle$ in four different jet p_T bins as indicated.

4.8.2 Uncertainties due to UE estimation technique

There is no unique way to determine the UE, however, the perpendicular cone method as described in the last chapter has been opted in this analysis. In the past, ALICE used a trigger hadron based approach [21] where a geometrically different definition of the transverse cones was adopted. In [22], the UE was estimated from dijet events and imposing an additional veto on a third jet. Additionally, anti-K$_T$ jets are circular and the UE events for the observables are also computed in circular cones. But in reality the cones may get distorted from the circular shape. In individual jets, soft particles might get added to a jet cone around the perimeter and it may produce convex deformation of the cone. Concave deformations may also occur simultaneously.

In this analysis a 5% uncertainty (following [11]) is assigned to account for the difference in evaluating UE through different processes and the possible distortions while measuring with certain process. To evaluate the systematic uncertainties, UE is increased/decreased by 5% and then subtracted from the data. As UE for $\langle R_{80} \rangle$ is not evaluated and UE contribution for $\langle p_T^{sum} \rangle$ for 60-80 GeV/c is negligible, both of them have no associated systematic uncertainties. The outputs can be found in Figure 4.15.

4.8.3 Uncertainties due to MC generator dependence of correction factors (CF)

The bin-by-bin correction technique used in this analysis is based on the PYTHIA6 event generator with Perugia0 tune. Now different event generators may produce different shapes of the jet spectra and that puts some bias in the selection of the MC event generator for correction. Here the structure of jets produced by PYTHIA might conceivably affect the magnitude and dependencies of the correction factors on the jet momentum, particle momentum or even the radial dependence. The possible impact of such event generators have been studied by generating events with different event generators like different tunes of PYTHIA6 (Perugia2010, Perugia2011, AMBT1), HERWIG and PHOJET. The correction factors from each of the MC generators are calculated and then the ratios are taken by dividing Perugia0 production by rest of the MC productions to get the systematic uncertainties. These are presented in Figure 4.16.

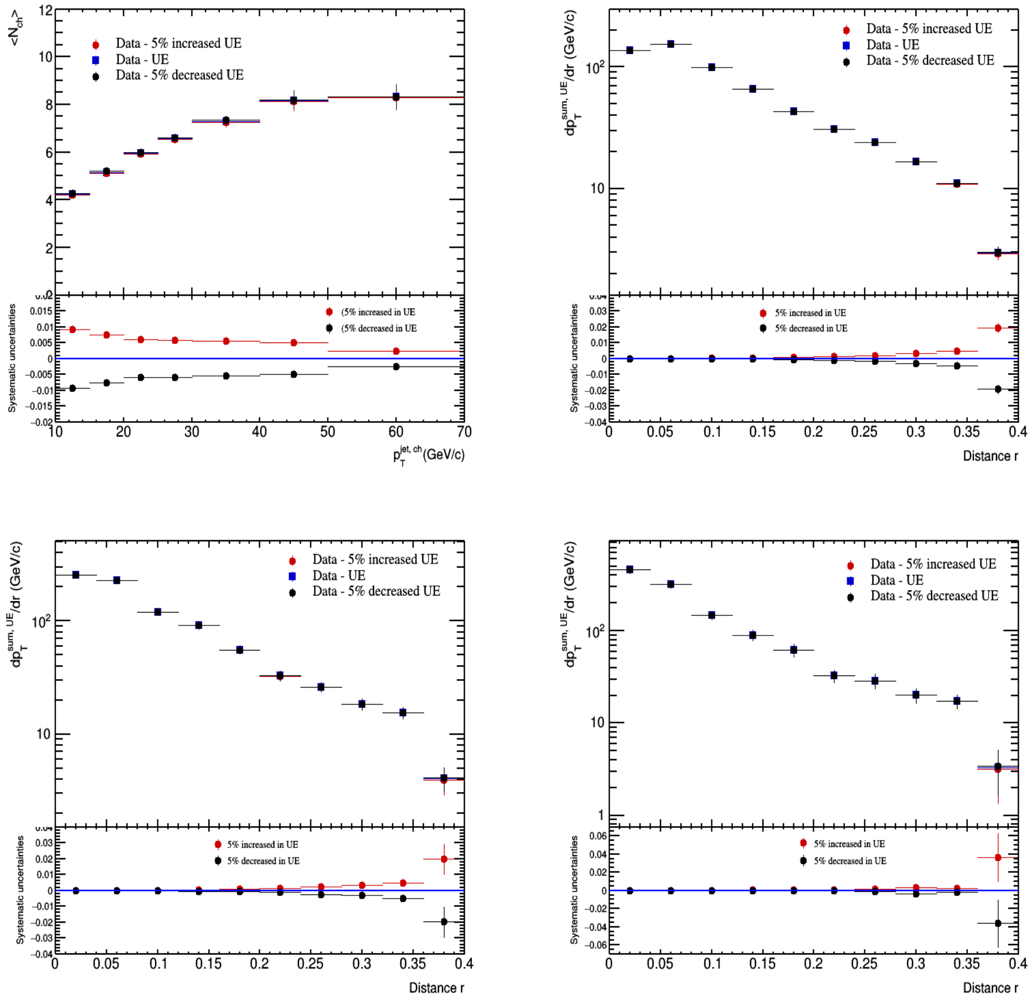

FIGURE 4.15: Estimation of uncertainties from evaluation of UE: $\langle N_{ch} \rangle$ (top left) and rest three are for $\langle p_T^{sum} \rangle$ in three different jet p_T bins as indicated.

Finally the resultant uncertainties are estimated from all the sources for all the observables under consideration. Evaluated systematic uncertainties are tabulated for $\langle N_{ch} \rangle$, $\langle R_{80} \rangle$ and $\langle p_T^{sum} \rangle$ in Table 4.1, Table 4.2, Table 4.3, Table 4.4, Table 4.5 and Table 4.6 respectively.

TABLE 4.1: Systematic uncertainties on $\langle N_{ch} \rangle$ for $R = 0.4$ (in %)

p_T^{jet} bin	Eff: + / -	p_T Res: + / -	CF depend.	UE eval.	Total
10-15	1.71 / -1.97	-0.06 / -0.18	0.17 / -0.17	0.92 / -0.92	1.82 / 2.07
15-20	1.87 / -1.94	-0.13 / 0.18	0.20 / -0.20	0.75 / -0.75	1.98 / 2.04
20-25	2.68 / -2.24	0.29 / 0.29	0.80 / -0.80	0.59 / -0.59	2.87 / 2.46
25-30	2.09 / -2.19	0.00 / 0.01	1.27 / -1.27	0.58 / -0.58	2.50 / 2.59
30-40	2.58 / -2.71	-0.17 / -0.03	1.95 / -1.95	0.54 / -0.54	3.25 / 3.35
40-50	2.34 / -2.96	-0.37 / -0.23	1.54 / -1.54	0.49 / -0.49	2.86 / 3.38
50-70	2.64 / -2.89	-0.12 / 0.00	2.58 / -2.58	0.24 - 0.24	3.69 / 3.87

TABLE 4.2: Systematic uncertainties on $\langle R_{80} \rangle$ for $R = 0.4$ (in %)

p_T^{jet} bin	Eff: + / -	p_T Res: + / -	CF depend.	Total
10-15	1.67 / -1.39	0.16 / -0.11	0.61 / -0.61	1.79 / 1.53
15-20	1.58 / -1.56	-0.11 / 0.19	0.87 / -0.87	1.81 / 1.80
20-25	2.59 / -1.94	0.39 / 0.43	1.49 / -1.49	3.02 / 2.48
25-30	2.19 / -1.85	0.29 / 0.37	1.75 / -1.75	2.82 / 2.58
30-40	2.74 / -2.79	-0.31 / 0.17	2.68 / -2.68	3.85 / 3.88
40-50	2.12 / -3.38	-0.55 / -0.57	2.74 / -2.74	3.51 / 4.39
50-70	2.33 / -2.75	-0.43 / 0.32	3.89 / -3.89	4.55 / 4.77

TABLE 4.3: Systematic uncertainties on $\langle p_T^{sum} \rangle$ for $R = 0.4$ for 20< p_T^{jet} <30 GeV/c(in %)

r bin	Eff: +/-	p_T Res: +/-	CF depend.	UE eval.	Total
0.00-0.04	-3.42/3.05	-0.18/-0.72	3.08/-3.08	-/-	4.64/4.39
0.04-0.08	-0.62/0.22	-0.46/-0.19	0.29/-0.29	-/-	0.83/0.41
0.08-0.12	1.45/-1.62	0.22/0.31	1.20/-1.20	0.01/-0.01	1.90/2.04
0.12-0.16	2.37/-1.89	0.19/0.84	1.63/-1.63	0.03/-0.03	2.89/2.64
0.16-0.20	3.08/-3.73	0.25/0.44	3.04/-3.04	0.06/-0.06	4.34/4.83
0.20-0.24	3.17/-2.65	0.48/-0.01	2.25/-2.25	0.13/-0.13	3.92/3.48
0.24-0.28	3.39/-3.76	0.99/1.02	2.30/-2.30	0.18/-0.18	4.22/4.53
0.28-0.32	4.23/-3.55	1.09/0.49	3.59/-3.59	0.31/-0.31	5.66/5.08
0.32-0.36	6.31/-2.89	0.60/0.31	1.59/-1.59	0.47/-0.47	6.55/3.35
0.36-0.40	4.67/-4.05	1.19/-0.55	1.99/-1.99	1.92/-1.92	5.56/4.94

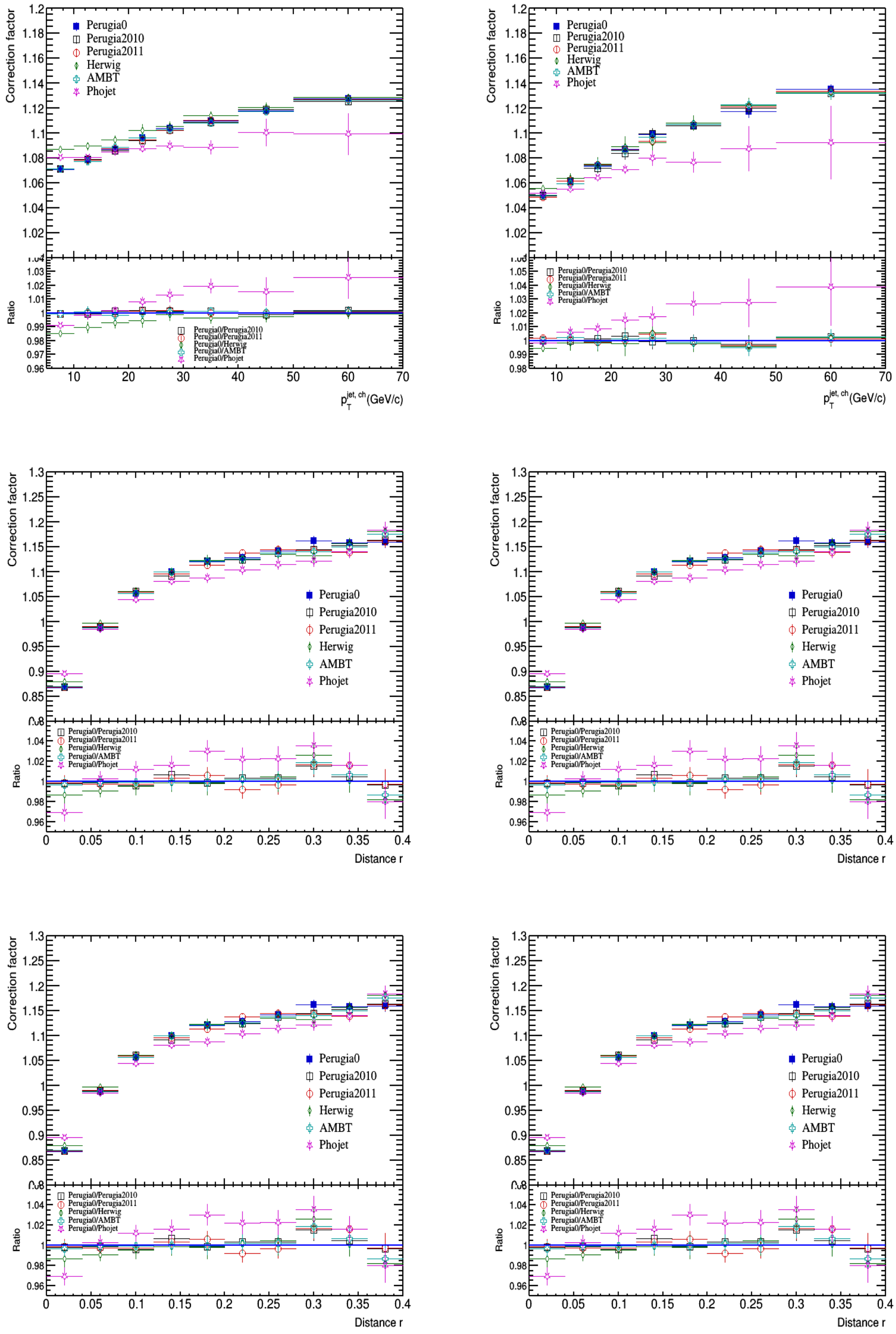

FIGURE 4.16: Estimation of uncertainties from CF dependencies on the choice of MC generator: $\langle N_{ch} \rangle$ (top left), $\langle R_{80} \rangle$ (top right) and rest four are for $\langle p_T^{sum} \rangle$ in four different jet p_T bins as indicated.

TABLE 4.4: Systematic uncertainties on $\langle p_T^{sum} \rangle$ for $R = 0.4$ for 30< p_T^{jet} <40 GeV/c(in %)

r bin	Eff: +/-	p_T Res: +/-	CF depend.	UE sub.	Total
0.00-0.04	-3.21/3.51	0.88/0.05	4.44/-4.44	-/-	5.55/5.66
0.04-0.08	0.50/-0.56	-0.86/0.00	0.94/-0.94	-/-	1.37/1.11
0.08-0.12	1.81/-2.56	-0.45/-0.39	3.36/-3.36	-/-	3.84/4.24
0.12-0.16	3.13/-3.15	0.11/-0.33	4.20/-4.20	0.03/-0.03	5.24/5.26
0.16-0.20	3.04/-4.35	-0.24/-0.20	4.88/-4.88	0.06/-0.06	5.76/6.55
0.20-0.24	4.68/-3.49	-1.08/-0.81	1.75/-1.75	0.13/-0.13	5.11/4.00
0.24-0.28	3.85/-3.64	-0.44/-0.12	5.93/-5.93	0.24/-0.24	7.09/6.97
0.28-0.32	4.70/-3.99	0.65/0.56	3.06/-3.06	0.32/-0.32	5.66/5.07
0.32-0.36	4.18/-3.69	-0.37/0.60	5.04/-5.04	0.48/-0.48	6.58/6.30
0.36-0.40	4.77/-3.33	0.83/0.99	4.63/-4.63	1.97/-1.97	6.99/6.11

TABLE 4.5: Systematic uncertainties on $\langle p_T^{sum} \rangle$ for $R = 0.4$ for 40< p_T^{jet} <60 GeV/c(in %)

r bin	Eff: +/-	p_T Res: +/-	CF depend.	UE sub.	Total
0.00-0.04	-2.04/2.94	0.41/-0.17	1.63/-1.63	-/-	2.64/3.37
0.04-0.08	0.64/-1.12	-0.06/0.04	1.29/-1.29	-/-	1.44/1.71
0.08-0.12	2.30/-2.91	-0.46/-0.02	3.25/-3.25	-/-	4.01/4.37
0.12-0.16	2.87/-3.25	-0.19/0.16	2.76/-2.76	0.02/-0.02	3.99/4.27
0.16-0.20	2.58/-4.29	-0.54/-0.37	0.69/-0.69	0.03/-0.03	2.72/4.36
0.20-0.24	3.27/-3.66	-0.42/-0.30	8.13/-8.13	0.06/-0.06	8.77/8.92
0.24-0.28	2.64/-3.76	-0.26/-0.01	8.96/-8.96	0.11/-0.11	9.34/9.71
0.28-0.32	3.05/-4.72	-1.90/-0.55	0.61/-0.61	0.34/-0.34	3.66/4.80
0.32-0.36	2.90/-5.10	-0.75/-0.72	7.02/-7.02	0.20/-0.20	7.63/8.71
0.36-0.40	3.45/-4.96	-0.52/-1.02	4.61/-4.61	3.64/-3.64	6.83/7.76

TABLE 4.6: Systematic uncertainties on $\langle p_T^{sum} \rangle$ for $R = 0.4$ for 60< p_T^{jet} <80 GeV/c(in %)

r bin	Eff: +/-	p_T Res: +/-	CF depend.	UE sub.	Total
0.00-0.04	-2.10 / 2.60	0.20 / 0.13	0.86 / -0.86	- / -	2.28 / 2.74
0.04-0.08	1.34 / -2.73	-0.35 / -0.64	4.65 / -4.65	- / -	4.85 / 5.43
0.08-0.12	3.21 / -3.12	-0.20 / 0.37	12.86 / -12.86	- / -	13.25 / 13.24
0.12-0.16	3.21 / -3.77	-0.90 / -0.07	10.35 / -10.35	- / -	10.87 / 11.01
0.16-0.20	5.39 / -2.77	0.02 / 0.55	12.50 / -12.50	- / -	13.62 / 12.82
0.20-0.24	3.94 / -3.29	0.21 / 0.01	1.40 / -1.40	- / -	4.19 / 3.58
0.24-0.28	4.52 / -3.81	0.24 / 0.03	10.82 / -10.82	- / -	11.73 / 11.47
0.28-0.32	3.21 / -5.17	0.62 / 0.25	11.20 / -11.20	- / -	11.67 / 12.34
0.32-0.36	4.15 / -4.97	0.75 / -0.13	0.35 / -0.35	- / -	4.23 / 4.98
0.36-0.40	4.19 / -4.00	-0.44 / -0.19	12.24 / -12.24	- / -	12.95 / 12.88

4.9 Results

4.9.1 Average charged particle multiplicity distribution in leading jet ($\langle N_{ch} \rangle$)

The final result for mean charged particle multiplicity distributions, $\langle N_{ch} \rangle$, in the leading jet are shown in Figure 4.17 (left) as a function of p_T^{jet} for $R = 0.4$. It is seen that $\langle N_{ch} \rangle$ rises monotonically with increasing p_T^{jet}. These results qualitatively produce the shape as those reported by the CDF collaboration [5] in $p\bar{p}$ system and in pp system by CMS [9] and ALICE [11].

The result is compared to the predictions from MC models like PYTHIA6 (Perugia0,

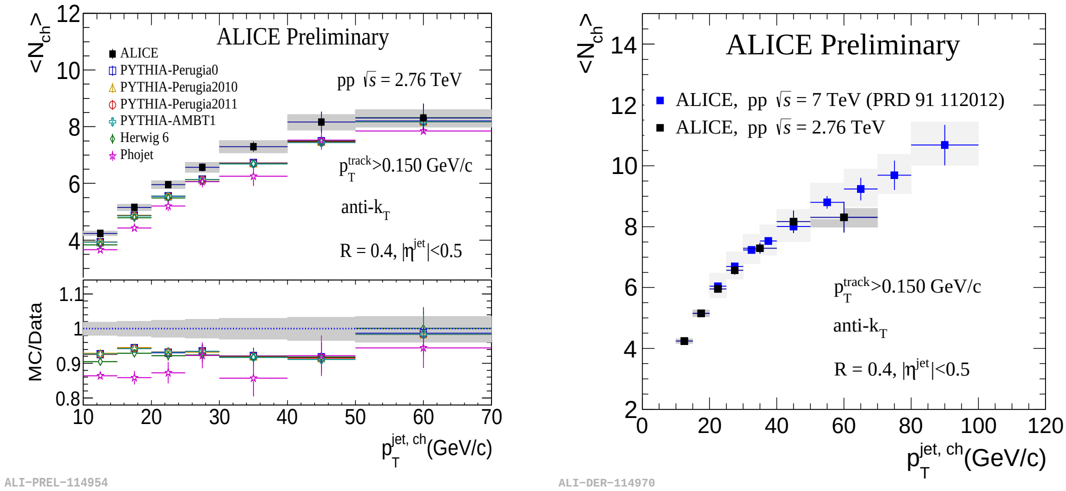

FIGURE 4.17: $\langle N_{ch} \rangle$ (left) distributions for $R = 0.4$ with theoretical predictions from different MC models. The right plot shows the comparison of $\langle N_{ch} \rangle$ from this measurement to the previous 7 TeV measurement by ALICE.

Perugia2010, Perugia2011 and AMBT1), HERWIG and PHOJET. All the models are found to underestimate the experimental measurement and while all the models except PHOJET are within 10% of the measured uncertainty, PHOJET is off to 15% of the measured uncertainty. The used models and their versions for the comparison are not well tuned for this $\surd$ and also for this lower jet p_T reach as this was the first measurement for the same by any LHC experiments. This measurement has also been compared to the previous ALICE measurement at 7 TeV [11]. No $\sqrt{s}$ dependencies has been found for this observable within the measured jet p_T and uncertainties as shown in Figure 4.17

(right).

4.9.2 Average leading charged jet size ($\langle R_{80} \rangle$)

The leading charged jet size, $\langle R_{80} \rangle$, are shown in Figure 4.18 (left) as a function of p_T^{jet} for $R = 0.4$. It is seen that $\langle R_{80} \rangle$ is contained within half of the jet radius for the lowest jet p_T. It also has a decreasing trend with increasing jet p_T. This trend gives the hint that jets with higher p_T are more collimated. This trend is also in qualitative agreement with the previous measurements by ALICE collaboration [11].

This measurement is compared with various model calculations and it is found that all

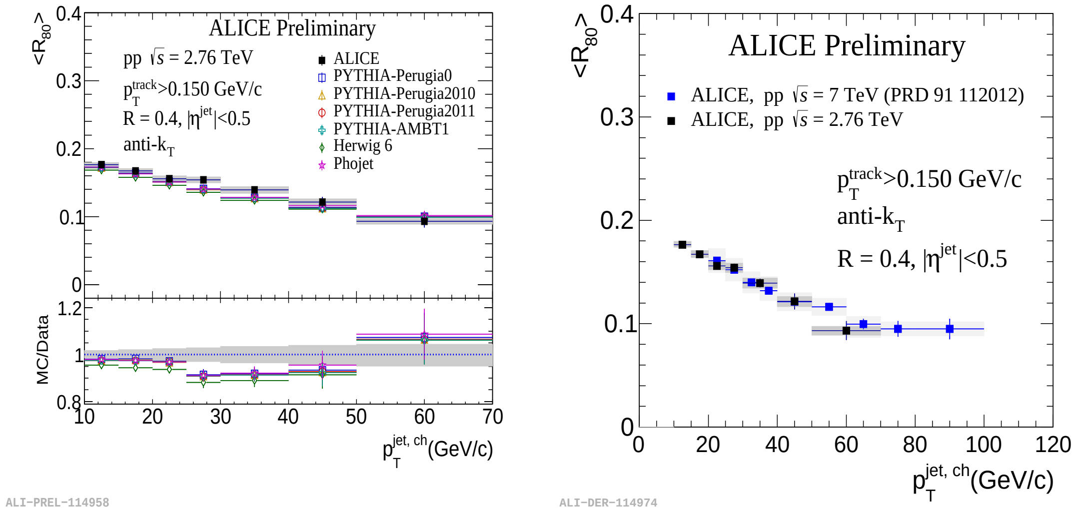

FIGURE 4.18: $\langle R_{80} \rangle$ (left) distributions for $R = 0.4$ with theoretical predictions from different MC models. The right plot shows the comparison of $\langle R_{80} \rangle$ from this measurement to the previous 7 TeV measurement by ALICE.

the models reproduce the trend and they agree within 5% of the measured uncertainties at low and high jet p_T regions. In the intermediate jet p_T, the model predictions agree within 10% of the measured uncertainties. The comparison of this result with that from the 7 TeV measurement by ALICE shows no $\sqrt{s}$ dependencies within the measured jet p_T range and uncertainties as shown in Figure 4.18 (right).

4.9.3 Radial momentum density distribution (dp_T^{sum}/dr)

The radial distribution of average transverse momentum density at $R = 0.4$ for four different jet p_T bins: 20-30, 30-40, 40-60 and 60-80 GeV/c are presented in Figure 4.19 (left). For better visualization, the distributions for the last three jet p_T bins have been scaled with 10, 100 and 1000 respectively. It has been seen that the momentum density is largest near the jet axis for each jet p_T bin and it decreases with increasing distance from the jet axis. It has been further seen that this decrement is steepest for the highest jet p_T bin. This observation also hints that the higher p_T jets are more collimated.

The data measurements are also compared with the predictions from different MC

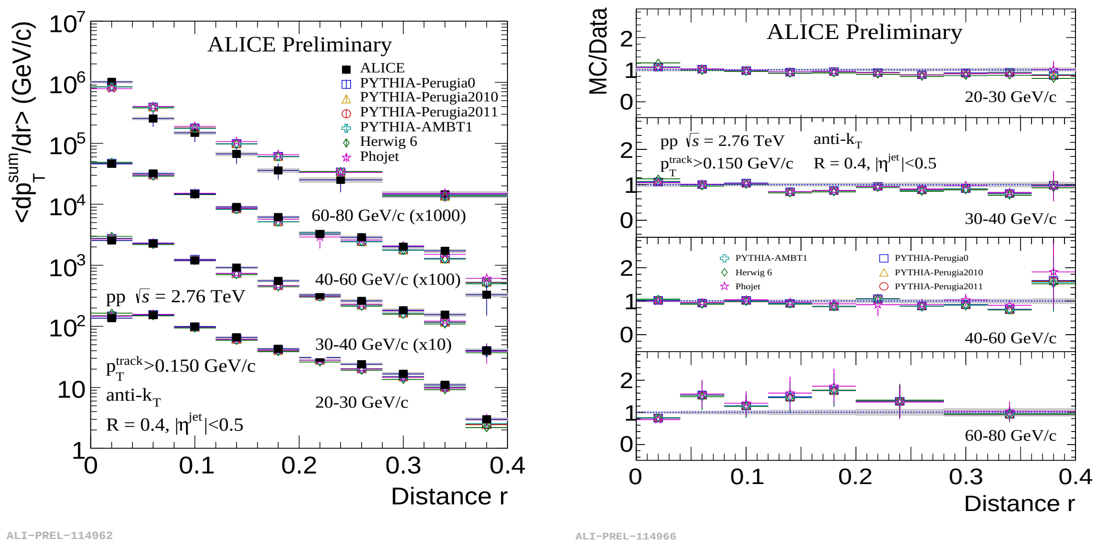

FIGURE 4.19: $\langle R_{80} \rangle$ (left) distributions for $R = 0.4$ with theoretical predictions from different MC models. The right plot shows the comparison of $\langle R_{80} \rangle$ from this measurement to the previous 7 TeV measurement by ALICE.

models and Figure 4.19 (right) gives the quantitative descriptions of the agreement. It is seen that all the models agree well within the uncertainties.

Bibliography

[1] A. Lister, Thesis: Measurement of b-quark jet shapes at CDF (2006)

[2] ZEUS Collaboration, Eur. Phys. J. C 2 (61-75) (1998)

[3] CDF Collaboration, Phys. Rev. D 78 072005 (2008)

[4] CDF Collaboration, Phys. Rev. Lett. 70 (713–717) (1993)

[5] CDF Collaboration, Phys. Rev. D 65 092002 (2002)

[6] CDF Collaboration, Phys. Rev. D 71 112002 (2005)

[7] D0 Collaboration, Phys. Lett. B 357 (500–508) (1995)

[8] ATLAS Collaboration, Phys. Rev. D 83 052003 (2011)

[9] CMS Collaboration, JHEP 1206 160 (2012)

[10] CMS Collaboration, Phys. Lett. B 730 (243–263) (2014)

[11] ALICE Collaboration, Phys. Rev. D 91 112012 (2015)

[12] ALICE Collaboration, Phys. Lett. B 722 (262-272) (2013)

[13] M. Cacciari and G. P. Salam, Phys. Lett. B 641, 57 (2006)

[14] T. Sjöstrand, S. Mrenna and P. Skands, JHEP 0605 026 (2006)

[15] G. Corcella et al., JHEP 0101 010 (2001)

[16] G. Marchesini et al., Comput. Phys. Commun. 67 465508 (1992)

[17] S. Roesler, R. Engel, and J. Ranft, arXiv:hep-ph/0012252 (2000)

[18] R. Brun, F. Carminati and S. Giani, CERN-W-5013, https://cds.cern.ch/record/1082634 (1987)

[19] CDF Collaboration, Phys. Rev. D 65 092002 (2001)

[20] ATLAS Collaboration, Phys. Rev. D 83 052003 (2011)

[21] ALICE Collaboration, JHEP 1207 116 (2012)

[22] CDF Collaboration, arXiv:hep-ph/0510198 (2005)

Chapter 5

Jet properties study in heavy-ion events with JEWEL

In this chapter, the study of inclusive jet yields and different jet shape observables in presence of a dense QCD medium have been presented to reflect the possible modifications of jet in presence of the medium. This study has been conducted with a pQCD based dynamical model namely, Jet Evolution With Energy Loss (JEWEL [1]), which simulates the propagation of jet through the deconfined partonic medium QGP, produced in relativistic heavy-ion collisions. All the measurements have been done at the LHC energies and compared to the available experimental results.

5.1 Prelude

As described in Chapter 2, the energy of a jet in heavy-ion collisions, is substantially reduced in comparison with the pp jet due to the interaction of the jet with the produced dense partonic medium. This phenomena is known as the jet quenching and in its simplest form is manifested as the suppression of the single inclusive cross-sections of high-p_T particles against a scaled pp reference at the same collision energy [2–6]. This suppression actually represents the parton shower modification and partonic energy loss by the produced QGP medium and a common way to quantify it is by the classic observable nuclear modification factor (R_{AA}) [7–10]. Despite giving the clear picture of the macroscopic jet energy suppression, measurement of R_{AA} is unable to give the 'complete descriptive' picture or decipher the complex nature of the jet-medium interaction due to its insensitivity to the microscopic details of the in medium parton evolution and partonic interaction with the QGP constituents [11].

This incompleteness can however, be alleviated from the measurements of fully reconstructed jets that are known to be a reasonable proxy to the shower initiating hard scattered partons. As jet is a composite object made from the final state hadrons, individual partonic energy loss has a subtle difference with the jet energy loss. It is perceived that the modification of jet-yields in a medium not only depends on the energy loss of their individual constituents, but also on how this lost energy is redistributed [12]. This lost energy is the manifestation of the diffusion of the jet constituents into the out-of jet cone. At the same time the medium induced in-cone gluon radiations compensate the energy loss to a certain degree [13–16]. Thus, the medium modifications of jets reflect the multifacet aspect of jet-medium interactions to which inclusive particle spectra are not at all sensitive and R_{AA} is unable to frame all these. This substantiates the necessity for studies with fully reconstructed jets in-order to examine the criticality of jet-medium interactions. This leads to the manifested features of jet-quenching phenomena: the suppression of jet-yields and the modification of intra-jet properties.

RHIC with its limited kinematic reach and LHC with its unprecedented energies have largely facilitated the study of jet-medium interactions with fully reconstructed jets [17–19]. In addition, over the years plenty of theoretical models have come into play in modelling the jet-medium interactions in an evolving QGP [20–25]. The multi-scale nature of the problem also makes the theoretical modelling of the jet-medium interactions highly non-trivial. A complete theoretical framework should address different scales: starting from weak interaction as in ISR to strong interaction with the medium parton. It should also incorporate medium response i.e., the background in a more sophisticated way. To this end, JEWEL [22, 28] has the necessary ingredients to demonstrate its effectiveness in describing variety of inclusive and differential jet observables.

In this chapter a brief description of JEWEL has been given for the reader with the study of inclusive jet yields as well as intra-jet properties to have further insight on the jet-medium interactions and modifications.

5.2 Jet Evolution With Energy Loss (JEWEL)

5.2.1 Introduction to JEWEL

JEWEL offers a dynamical framework to simulate jet quenching phenomena in AA collisions on the basis of QCD evolution of parton showers in presence of a thermalized partonic background. Conceptually, JEWEL uses PYTHIA6 event generator on top-of CTEQ6LL [26] parton distribution function (PDF) for pp events and EPS09 [27] nuclear PDF for heavy-ion collisions. JEWEL used to couple the PYTHIA generated parton showers with Bjorken-type hydrodynamic background. The hydrodynamic expansion in JEWEL follows an ideal-gas equation of state (EOS) with number and energy densities of medium partons being calculated taking local temperature in the medium as an input [33]. For the study of in-medium jet fragmentation, JEWEL implements a virtuality-ordered parton shower similar to the implementation in PYTHIA6.4, i.e., the evolution parameter is the parton virtuality Q^2 . An initial hard parton is taken from a hard scattering provided by PYTHIA. For each hard scattered parton with virtuality sufficiently above the hadronization scale, a shower is started. The kinematics of the splitting gets fixed after every branching, i.e., the two daughters are assigned four-momenta. If the virtuality of the daughters is still high enough they can undergo further splittings in the same way, leading to a shower. A space-time structure is imposed on the parton-shower to demonstrate the interaction with a non-trivial medium by fixing the time between two successive branchings as:

$$\tau = \frac{E}{Q^2} \tag{5.1}$$

One important point is the position of the hard interaction vertex. While it fixes the production of the hard partons, its location is again determined from the collision geometry and, thus, picked in the medium implementation. From PYTHIA, the kinematics of the parton is known and this helps to determine the parton position at a time t_0 after its production at t_0^s as:

$$\overrightarrow{x}_1 = \overrightarrow{x}_0 + (t_0 - t_0^s).\frac{\overrightarrow{p}_0}{E_0} \tag{5.2}$$

These positions give the path traversed and help to evaluate the possibility of a scattering with the medium. The scattering probability per unit path length is given by the cross-section σ and the density of the medium scattering centres.

Interference effects induce a non-trivial interplay between the shower evolution and scatterings of medium recoil centres. A sufficiently hard scattering can result in further splitting by setting the parton shower to a higher scale. Thus, a scattering of a parton in the medium has the potential to modify the projectile virtuality and which in turn affects the shower evolution[22]. In other words, the scatterings are dressed with initial and final state radiation. This also allows for a consistent treatment of the interference between and vacuum and medium-induced radiation, which are treated on the same footing. The formation time plays a pivotal role on the showering process. If no scattering occur during the formation time, the radiation is registered, otherwise the momentum transfer due to the scattering is added coherently to the primary hard scattering and new scale is calculated. This scale defines whether to register an emission or to reject it, based on whether it is lower or higher than the virtual scale i.e. the hardness [22, 29]. Whenever a scattering is encountered a recoil parton from the medium is generated. For a microscopic calculation of the $2 \rightarrow 2$ scattering, the recoil centre must be assigned a parton species, a mass, and a four-momentum. Re-scatterings are terminated once the local temperature drops down to a critical temperature T_c (170 MeV), considered to be the order of QCD phase transition temperature at baryon chemical potential $\mu_B \sim 0$. PYTHIA takes over once all the partons have reached the hadronization threshold and produces the final state particles from the parton shower without acknowledging any underlying event. However, the recoiling scattering centres can be included in the shower evolution. If enabled, they undergo the same shower evolution as the original projectile parton. This endows correlation between jets and recoil partons, likely to be manifested as enhancement in soft hadronic yields at large angles to jet-axis.

In addition to the local temperature and density, the impact parameter (b) is also assigned to the medium to incorporate the overlap region of the nuclei. The probability of the impact parameter, in some range, depends on the assumptions made for the nuclei. The evolution of the parton shower is completely ignorant of the impact parameter and only senses it through the resulting medium. Depending on the medium, b can be fixed or generated randomly in the per-event initialization.

5.2.2 Computing the background

This analysis has been conducted based on standard "recoil-on" JEWEL setup, i.e., keeping record of recoil partons in the event information. These recoil partons serve as the soft uncorrelated background as they are modelled to retain their thermal component, i.e., momentum before scattering. These are sensitive to the measurements of intra-jet observables and needed to be subtracted. The subtraction process plays a tricky role and to overcome it, JEWEL compatible background subtraction techniques were proposed and tested over a variety of jet-observables [30]. A technique, namely, the four momenta subtraction or $4MomSub$ is used in this analysis [30].
In $4MomSub$, a set of neutral particles with very small momenta and positions corresponding to scattering centers, prior to interaction, are included in the final event information. These dummy particles together with others get clustered to a jet. Then all the jet constituents pointing back to the scattering centers (background) are identified and their four momenta are added. Finally, background four momenta is subtracted vectorially from the four momenta of the reconstructed jets. This subtraction technique however, has certain limitations, for example, it is only applicable to full jets and can not be used for charged jets directly [30].

5.2.3 Analysis details

About one million 0-10% central Pb-Pb and pp event sample were generated at $\sqrt{s_{NN}}$ = 2.76 TeV and 5.02 TeV. The initial conditions required to simulate the hydrodynamic background, such as thermalization time (τ_i) and initial temperature (T_i) are tabulated in Table 5.1. Jets are reconstructed with anti-k_T jet-reconstruction algorithm available in the FastJet package.

TABLE 5.1: Details of the parameters used for JEWEL

$\sqrt{s_{NN}}$	σ_{NN}	τ_i	T_i
5.02 TeV	72 mb	0.4	590 MeV[31]
2.76 TeV	64 mb	0.6	485 MeV[32]

5.3 Results

5.3.1 Jet nuclear modification factor, R_{AA}^{jet}

As already introduced in Section 5.1, a standard observable for the study of jet quenching is the nuclear modification factor R_{AA}. It is defined in the case of jet as:

$$R_{AA}^{jet} = \frac{d^2N_{AA}^{jet}/dp_{T,jet}d\eta}{< N_{coll} > d^2N_{pp}^{jet}/dp_{T,jet}d\eta} \tag{5.3}$$

where N_{AA}^{jet} and N_{pp}^{jet} are the number of jets in AA and pp collisions, respectively and $\langle N_{coll}\rangle$ is the number of binary nucleon-nucleon collision averaged over a given collision centrality class. Figure 5.1 shows a comparison of p_T dependence of R_{AA}^{jet} calculated from JEWEL with the recent measurements from ALICE[34, 35], ATLAS[36, 37] and CMS[38] for jet resolution parameter $R = 0.4$ at $\sqrt{s_{NN}}$ = 5.02 TeV (left) and 2.76 TeV (right) and a reasonable agreement is clearly visible.

In heavy-ion events, jet measurement is a little complicated for the large underlying background. To overcome this to some extent, one solution is to reconstruct jet with smaller radius. But this choice comes with the additional shortcoming of missing the partons scattered to large distances from the jet axis and thus suppressing the

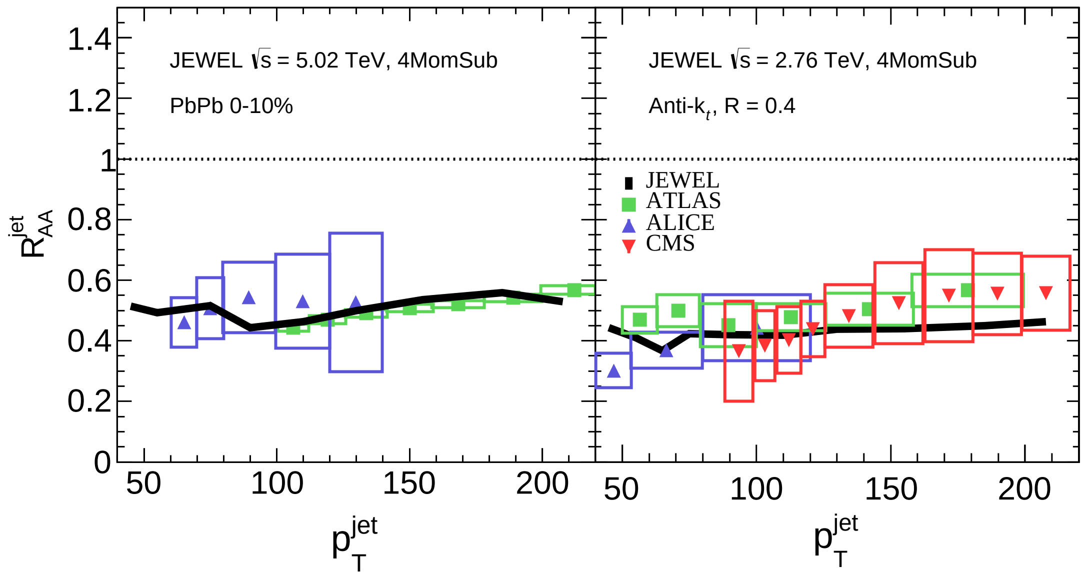

FIGURE 5.1: Transverse momentum dependence of R_{AA}^{jet} from JEWEL at $R = 0.4$ in 0-10% centrality, compared with ALICE [34, 35], ATLAS [36, 37] and CMS [38] measurements. **Left:** $\sqrt{s} = 5.02$ TeV and **Right:** $\sqrt{s} = 2.76$ TeV.

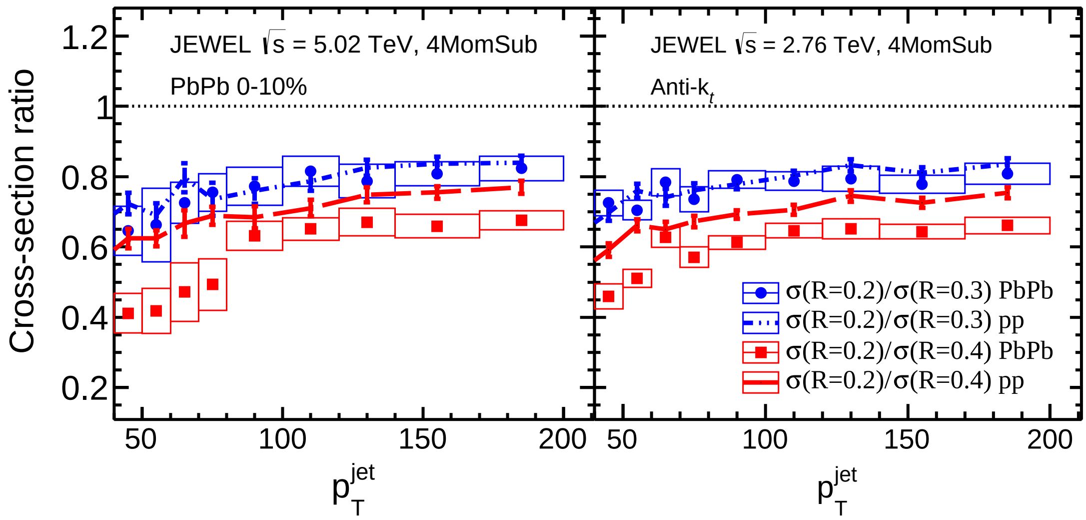

FIGURE 5.2: Ratios of jet p_T spectra at $R = 0.3$ and 0.4 with respect to $R = 0.2$ in pp and Pb-Pb collisions. **Left:** $\sqrt{s} = 5.02$ TeV and **Right:** $\sqrt{s} = 2.76$ TeV.

measured cross-section than the actual production. The expanding medium carries away the energy and momentum transferred to the medium by the propagating jet. This phenomena puts an additional dependence on the jet cone size for the in medium energy loss.

In addition to this, there is also the factor of medium-stimulated radiations which emit at large angles from the jet-axis and this contributes to the resultant jet energy loss. Expectedly, jets reconstructed in AA collisions with smaller cone size will capture only a subset of the full parton shower causing stronger attenuation of jet spectrum relative to pp baseline. To illustrate the effect of R dependence of jet cross sections in pp and AA, the ratio of jet-p_T spectra at $R = 0.2$ with respect to different values of R are shown in Figure 5.2.

This ratio clearly shows the deviation from unity which implies that the jets reconstructed with larger R actually capture the energy deflected in wide angles and in this process compensates the effective lost energy. For the smaller R (0.2 and 0.3), the ratio is consistent in both pp and Pb-Pb which suggest that the redistribution of the jet energy by the medium does not affect the jet structure while going to R = 0.3 from R = 0.2. This is understood by the fact that, these small radii might be representing the unresolved hard jet core.

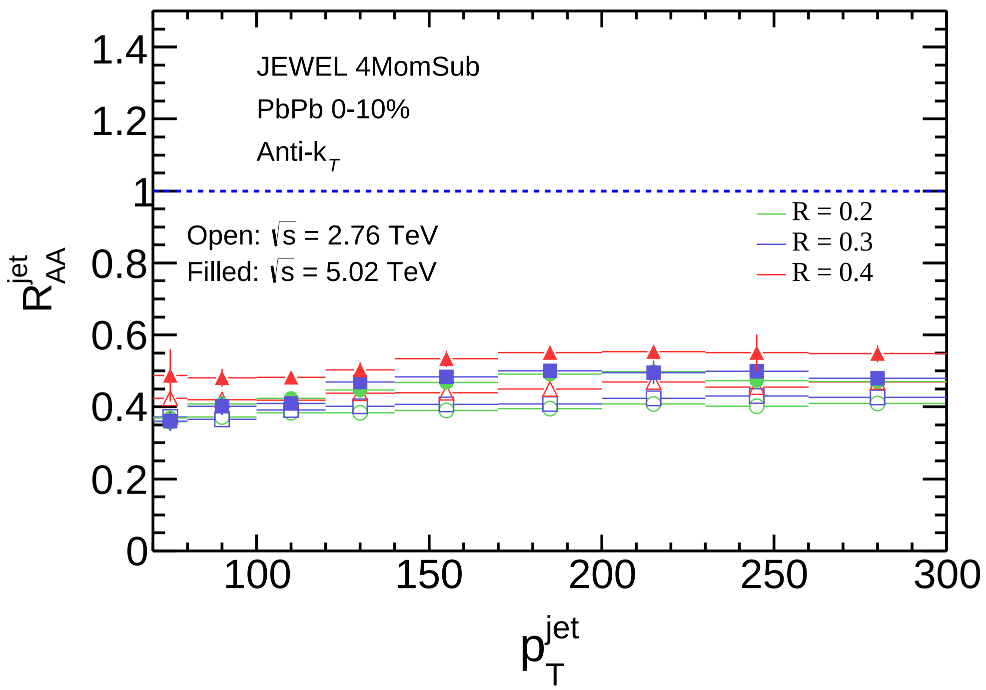

FIGURE 5.3: Transverse momentum dependence of R^{jet}_{AA} at $\sqrt{s}$ = 5.02 and 2.76 TeV for jet radius R = 0.2, 0.3 and 0.4 in 0-10% central events with JEWEL

This R dependence study has also been conducted by the CMS collaboration [38] where due to large uncertainty, the dependence is not clearly established. Just to mention, few model calculations predict a clear hierarchy of R_{AA}^{jet} in measurements for different R [39, 40]. To complement what has been seen in the cross-section measurement, R_{AA}^{jet} has also been studied with jet p_T and it is found that for $R = 0.4$, the suppression is substantially different from $R = 0.2$ or 0.3 as can be seen in Figure 5.3. To complete the R dependence study, R_{AA}^{jet} measured at 2.76 TeV for $R = 0.2$ and 0.4 are overlaid on the same measurements by the CMS collaboration [38] in Figure 5.4. JEWEL has been

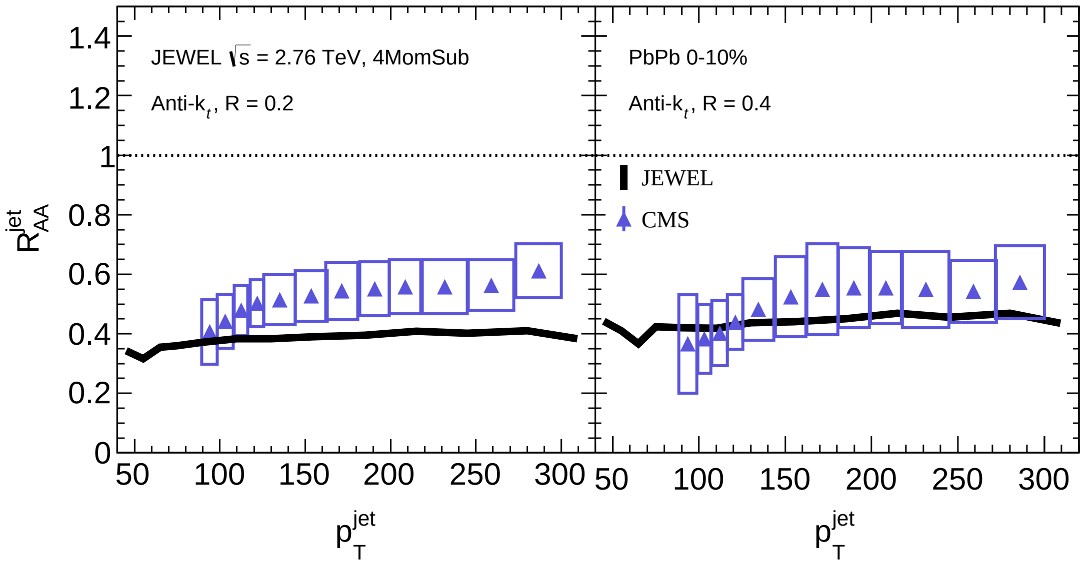

FIGURE 5.4: Transverse momentum dependence of R_{AA}^{jet} from JEWEL in 0-10% centrality Pb-Pb events, compared with CMS [38] measurements. **Left:** $R = 0.2$ and **Right:** $R = 0.4$.

seen to underestimate the data for $R = 0.2$ but at the same time agrees with the result at $R = 0.4$. The possible reason could be found in the implementation of scattering of the recoil partons in JEWEL where they might be getting scattered out to larger angles than the physical expectation. So the large R recovers these wide angle recoil contributions which in turn leads to a better data-to-model agreement.

5.3.2 Fragmentation function distributions, $FF(z)$

As already mentioned, the jet-medium interaction modifies the jet structure and thus the intra-jet properties. One of the most explicit observable, to quantify the changes, is the fragmentation function (FF) by studying the relative changes in it while going to AA from pp system. In this analysis, $FF(z)$ has been defined as is done by the ATLAS collaboration [41]

$$FF(z) = \frac{1}{N_{jet}} \frac{dN}{dz} \tag{5.4}$$

where $z = \frac{p_T \cos\Delta R}{p_T^{jet}}$ refers to the longitudinal momentum fraction of particles relative to a jet of transverse momentum, p_T^{jet}, N_{jet} denotes the number of jets in a given momentum interval and $\Delta R (= \sqrt{(\Delta\eta)^2 + (\Delta\phi)^2})$ corresponds to pseudorapidity and azimuthal separation of particles from the jet-axis. In Figure 5.5 measurement of $FF(z)$ with JEWEL in pp and 0-10% central Pb-Pb collisions at $\sqrt{s_{NN}} = 5.02$ TeV in the p_T^{jet} interval of 126 to 158 GeV/c have been presented along with the ATLAS measurements from [41]. The lines joining the JEWEL points are simple lines for guiding the eyes and are not any type of fitting function.

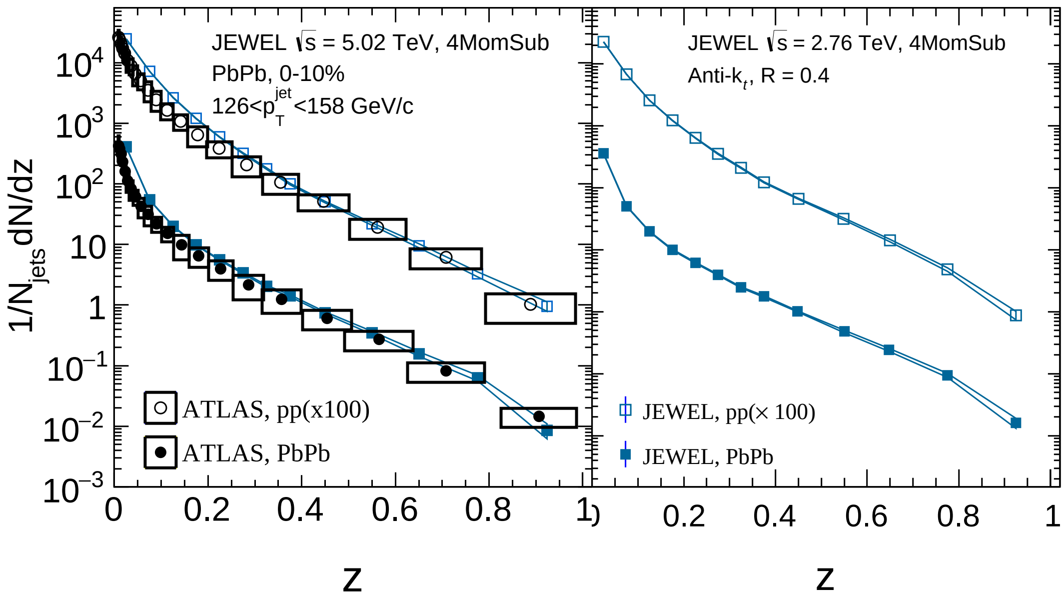

FIGURE 5.5: Fragmentation distributions from JEWEL at $R = 0.4$ in 0-10% Pb-Pb central events compared with ATLAS [42] measurement of the same in pp and Pb-Pb collisions for 126< p_T^{jet} <158 GeV/c. **Left:** $\sqrt{s} = 5.02$ TeV and **Right:** $\sqrt{s} = 2.76$ TeV. Proton-proton data points are scaled by 100 for better visibility.

To quantify the modification of fragmentation functions in heavy ion collisions, ratios of $FF(z)$ in Pb-Pb to that in pp collisions are shown in Figure 5.6 and compared with the ATLAS data for collision energies 5.02 TeV and 2.76 TeV [41, 42].

It has been seen that JEWEL has qualitatively produced the shape with some generic features: enhancement at low z, followed by depletion at the intermediate z and again an enhancement at high z. Lower z stands for the soft particles as per the definition and the enhancement observed at the lower z region stands for an excess yield of low p_T particles implying the softening of the fragmentation functions. In JEWEL this is realized in terms of jet-induced medium response where due to the conservation of the momentum, a component of the jet energy deposited in the medium is directed along the jet-axis. As a result, particles produced from the medium in the vicinity of jets will be endowed with kinematic focussing along the jet-axis. These particles being reconstructed as part of a jet will soften the momentum distributions of hadronic fragments of jets in a medium than in vacuum. In JEWEL, also the modelling of the recoil parton to scatter just once also contribute in this overshooting at low z. In addition, the fact that in JEWEL the background subtraction is done at the inclusive level and not at the track level, also contributes up to few percent in the discrepancy between data and JEWEL measurements at low z.

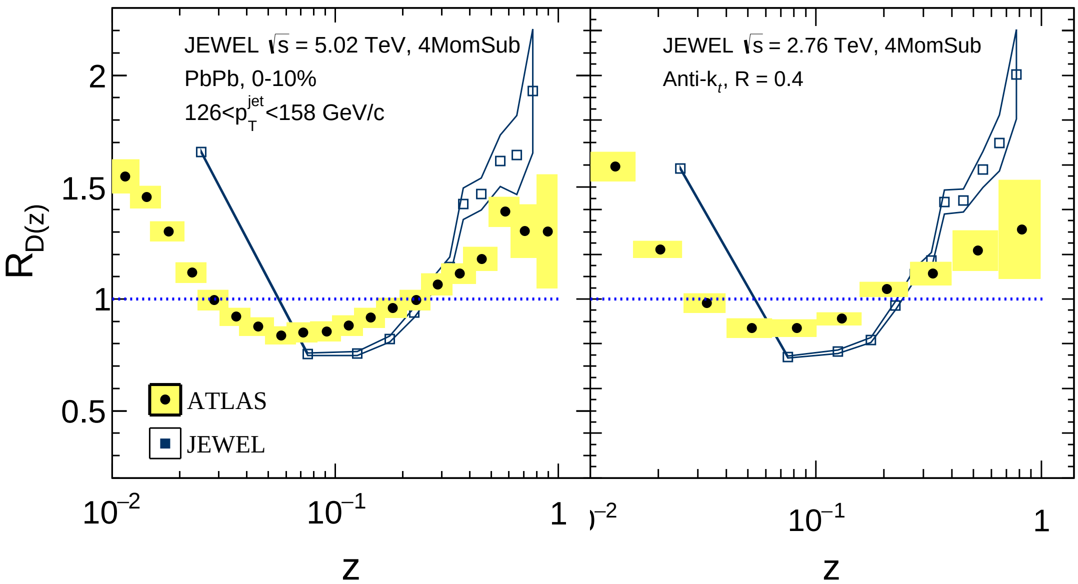

FIGURE 5.6: Ratio of fragmentation distributions from Pb-Pb to pp collisions from JEWEL at $R = 0.4$ in 0-10% centrality compared with ATLAS [41, 42] measurements in 126< p_T^{jet} <158 GeV/c. **Left:** $\sqrt{s}$ = 5.02 TeV and **Right:** $\sqrt{s}$ = 2.76 TeV.

On the other hand, jets get more collimated and hardened after losing energy in the medium. These hardened jets are made of very high p_T particles and this is attributed to the observed enhancement at the high z region. This is supported by the apparent similarity in the fragmentation functions of quenched jets with the jets initiated by the quarks in vacuum. In general quarks have harder fragmentation and thus the quark-jets are more collimated and harder [43]. The enhancement is also expected from the color coherence effect [44, 45], where the partonic fragments with transverse spread less than the coherent length scale of the medium remain unresolved and shielded against the medium modification. For this a quenched jet originally having higher energy, may appear as a low energy jet in comparison with a jet in vacuum with same p_T. A significant percentage of the total jet energy is concentrated within the hard jet core and due to the shielding, modification is negligible. This incident induces a biasness in the ensemble of quenched jets in AA collisions to higher virtuality relative to pp when compared at the same jet-p_T. In JEWEL, the rescatterings of shower partons are modelled according to the virtuality and for this the above mentioned phenomena might have occurred in JEWEL. Now as the rescatterings are softer, the hard core remains unresolved and thus contributes to the observed enhancement at high z region. To study the dependence of

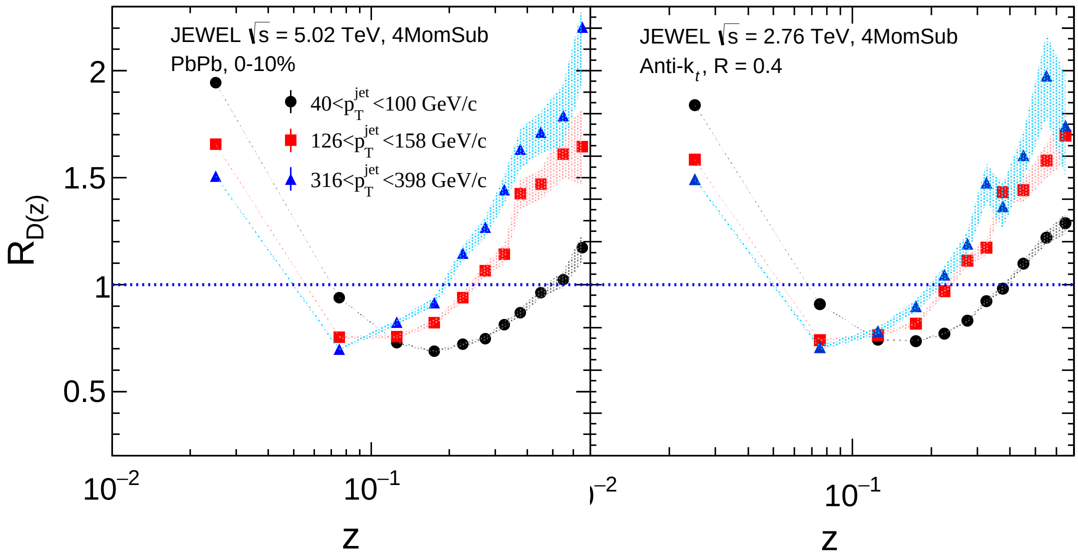

FIGURE 5.7: Ratios of fragmentation distributions from Pb-Pb to pp collisions from JEWEL at $R = 0.4$ in 0-10% centrality for three p_T^{jet} ranges: 40< p_T^{jet} <100, 126< p_T^{jet} <158 and 316< p_T^{jet} <398 GeV/c. **Left:** $\sqrt{s}$ = 5.02 TeV and **Right:** $\sqrt{s}$ = 2.76 TeV. Colored bands show the statistical error in the measurements.

the fragmentation function on the jet p_T, fragmentation functions have been computed in three jet p_T bins: 40 $<p_T^{jet}$ <100 GeV/c, 126 $<p_T^{jet}$ <158 GeV/c and 316 $<p_T^{jet}$ <398 GeV/c. The ratios of the measurements have been presented in Figure 5.7. In all the jet p_T bins, the enhancement at low z region is visible with ordering. While low-z excess is maximum in the lowest p_T^{jet} interval, the high-z enhancement in the same p_T^{jet} range is seen to be least. This might indicate a significant modification to jet substructures at this low p_T^{jet} interval. This measurement has also been extended for three R: 0.2, 0.3 and 0.4 for two jet p_T intervals: 40< p_T^{jet} <100 GeV/c being the low jet p_T bin and 316< p_T^{jet} <398 GeV/c being the high jet p_T bin and presented in Figure 5.8. It is seen that at the low z region, all the R have excess soft yield with an R ordering. The higher R collects more soft yield by opening the cone wider which has also been seen and understood in the R_{AA}^{jet} measurement section above.

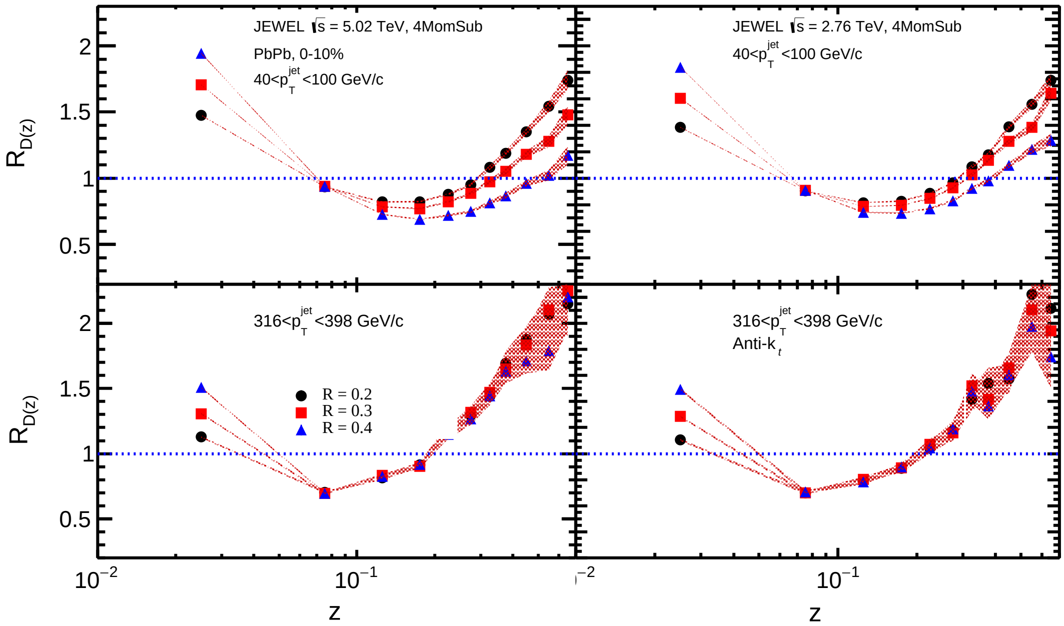

FIGURE 5.8: Ratios of fragmentation distributions from Pb-Pb to pp collisions from JEWEL at R = 0.2, 0.3 and 0.4 in 0-10% centrality for two p_T^{jet} bins: 40< p_T^{jet} <100 and 316< p_T^{jet} <398 GeV/c. **Left:** $\sqrt{s}$ = 5.02 TeV and **Right:** $\sqrt{s}$ = 2.76 TeV.

5.3.3 Radial distribution of transverse momentum density, dp_T^{sum}/dr

This sub-section presents the classic jet shape observables which have already been introduced and defined in the previous chapter. Figure 5.9 shows radial transverse momentum density distributions for $R = 0.4$ for three different jet p_T bins.

The difference in trends in pp and Pb-Pb is clearly visible where the slope in pp is steeper than that in Pb-Pb events. This is due to the fact that a large amount of soft yield is produced by the medium interaction in AA events and when p_T^{sum} is

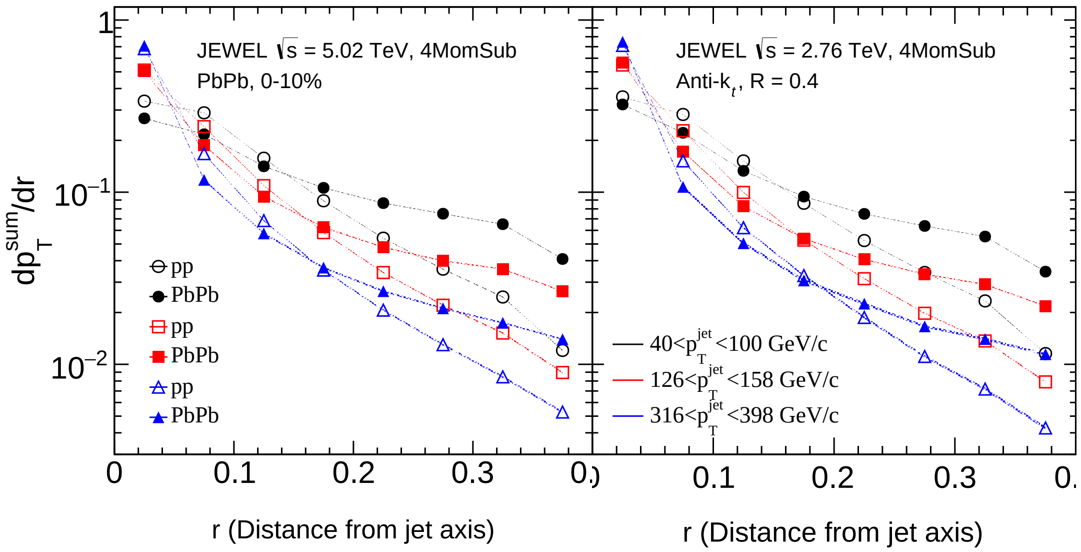

FIGURE 5.9: Radial momentum density distributions in PbPb to pp collisions from JEWEL at $R = 0.4$ in 0-10% centrality are presented for three jet p_T intervals: 40< p_T^{jet} <100, 126< p_T^{jet} <158 GeV/c and 316< p_T^{jet} <398 p_T^{jet}. **Left:** $\sqrt{s} = 5.02$ TeV and **Right:** $\sqrt{s} = 2.76$ TeV. Lines are only to guide the eyes.

calculated in the outward region, these soft particles come into play. Whereas in pp case, the significant amount of p_T is located in close vicinity of the jet axis and p_T^{sum} drops faster when one goes outward.

This is further investigated as a function of R where for a selected jet p_T interval, 40< p_T^{jet} <100, for smaller R, it is found that both the pp and PbPb distributions are consistent with each other as shown in Figure 5.10. Differences arise when one goes to larger R. The pp distribution for $R = 0.4$ is different from PbPb and it fall steeply with r. This happens because, as one opens the cone more and more, it starts to recover the lost energy from the medium in the PbPb case. This has been seen for all the three jet p_T intervals considered here. To quantify and understand the modification in AA collisions, ratio of p_T^{sum} distributions of AA to pp has been presented in Figure 5.11. A depletion at intermediate r and an enhancement at large r is seen in the ratios. However, at very small r, the ratio for jets with p_T^{jet} >100 GeV/c is found to be consistent with unity, implying that jet core remains unmodified or negligibly modified, complementing to what has been understood throughout this study.

In JEWEL, the enhancement at large r is accounted for the inclusion of the

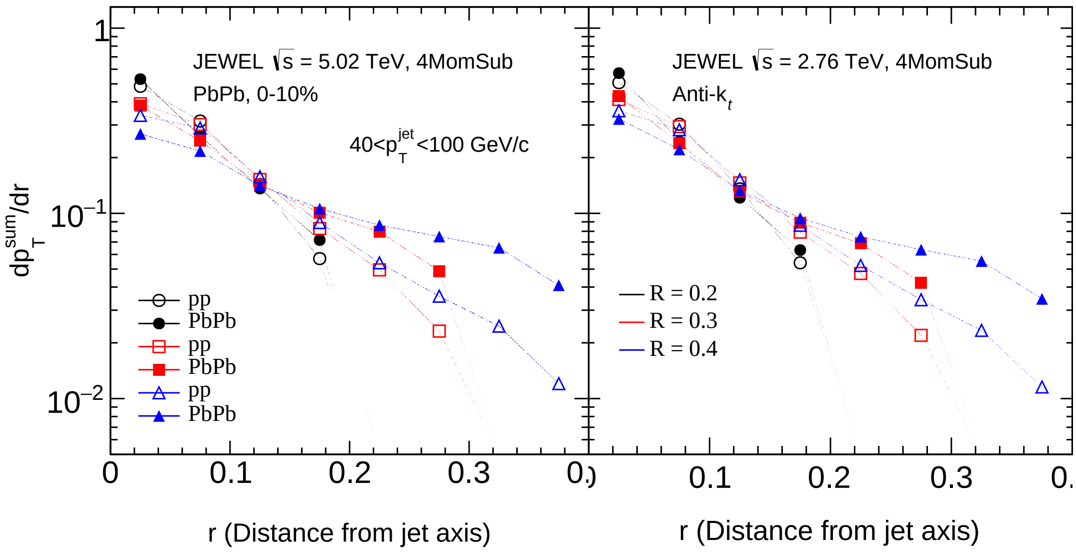

FIGURE 5.10: Radial momentum density distributions in PbPb to pp collisions from JEWEL at R = 0.2, 0.3 and 0.4 in 0-10% centrality are presented for jet p_T interval: 40< p_T^{jet} <100. **Left:** $\sqrt{s}$ = 5.02 TeV and **Right:** $\sqrt{s}$ = 2.76 TeV. Lines are only to guide the eyes.

recoil partons. Interestingly, in the jet-p_T interval 40< p_T^{jet} <100 GeV/c, depletion persists down to very small r. This is consistent with what has been inferred from the modification of fragmentation functions of jets <100 GeV/c. That is, low momentum jets, preferably <100 GeV/c at LHC energies might have their inner core modified by the jet-medium interaction. To be able to have more insights on the large r excess, p_T^{sum} has also been studied as a function of p_T of the constituent particles inside jet cone and is presented in Figure 5.12. It has been seen that the excess is more when the constituent particles considered are very soft: 1 $< p_T <$2 GeV/c in this case. It is consistent with what CMS collaboration has seen in the measurements of jet-track correlations [46]. This confirms one more time in this study, that in jet-medium interaction soft large angle particles are produced in abundance.

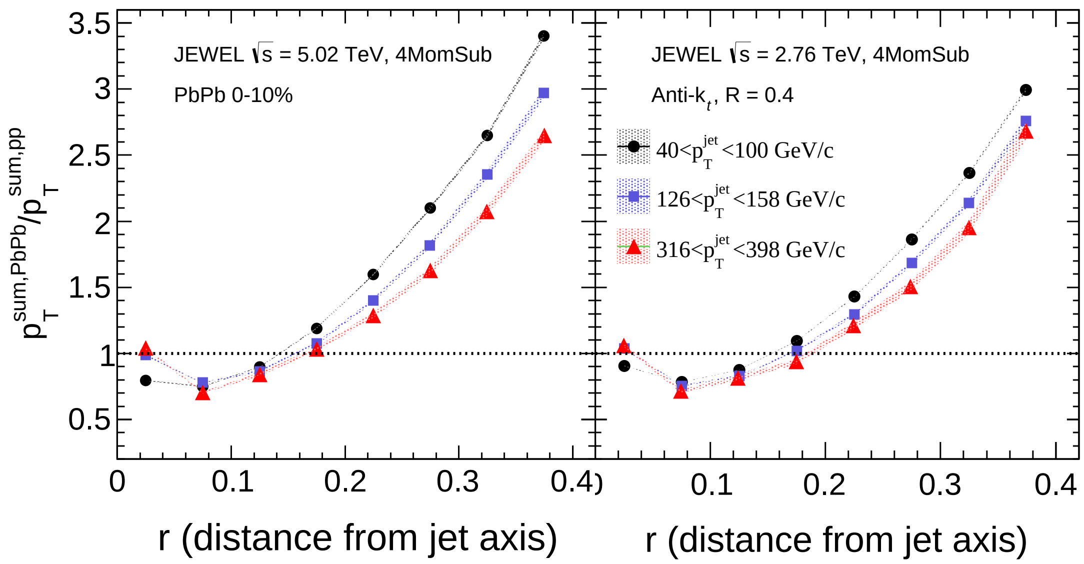

FIGURE 5.11: Ratios of radial momentum density distributions from PbPb to pp collisions from JEWEL at $R = 0.4$ in 0-10% centrality are presented for three jet p_T intervals: 40< p_T^{jet} <100, 126< p_T^{jet} <158 GeV/c and 316< p_T^{jet} <398 p_T^{jet}. **Left:** $\sqrt{s}$ = 5.02 TeV and **Right:** $\sqrt{s}$ = 2.76 TeV.

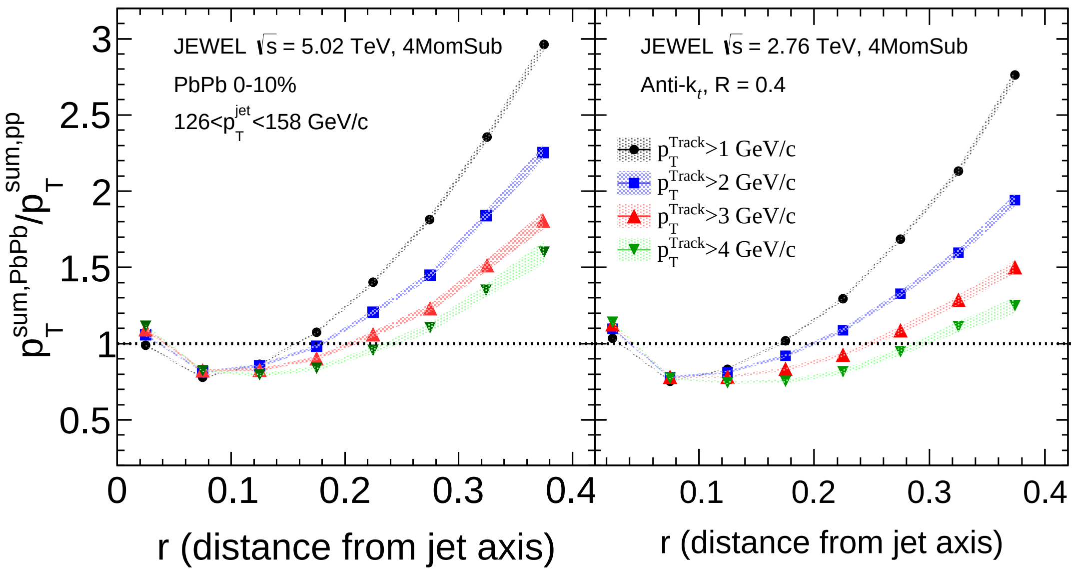

FIGURE 5.12: Ratios of radial momentum density distributions from PbPb to pp collisions from JEWEL at $R = 0.4$ in 0-10% centrality for 126< p_T^{jet} <158 GeV/c, in different ranges of constituent particle's p_T. **Left:** $\sqrt{s}$ = 5.02 TeV and **Right:** $\sqrt{s}$ = 2.76 TeV

Bibliography

[1] K. Zapp, J. Stachel and U. Wiedemann, Proc. of Sc. 09, 022 (2009)

[2] CMS Collaboration, Eur. Phys. J. C 72, 1945 (2012)

[3] PHENIX Collaboration, Phys. Rev. Lett. 101, 232301 (2008)

[4] PHENIX Collaboration, Phys. Rev. C 93, 024904 (2016)

[5] ALICE Collaboration, Phys. Rev. C 93, 034913 (2016)

[6] ALICE Collaboration, JHEP 03, 081 (2016)

[7] JET Collaboration, Phys. Rev. C 90, 014909 (2014)

[8] PHENIX Collaboration, Phys. Rev. C 93, 024911 (2016)

[9] STAR Collaboration, Phys. Rev. Lett. 121, 032301 (2018)

[10] A. Majumder, Phys. Rev. C 75, 021901 (2007)

[11] Y. Mehtar-Tani, J. Milhano and K. Tywoniuk, Int. J. of Mod. Phys. A 28, 1340013 (2013)

[12] I. Vitev, B. Zhang, and S. Wicks, Eur. Phys. J.C 62, 139 (2009)

[13] X. Wang and Y. Zhu, Phys. Rev. Lett. 111, 062301 (2013)

[14] Y. Tachibana and T. Hirano, Phys. Rev. C 93, 054907 (2016)

[15] N. Chang and G. Qin, Phys. Rev. C 94, 024902 (2016)

[16] Y. Chien and I. Vitev, JHEP 05, 023 (2016)

[17] STAR Collaboration, Phys. Rev. Lett. 112, 122301 (2014)

[18] PHENIX Collaboration, Phys. Rev. Lett. 116, 122301 (2016)

[19] STAR Collaboration, Phys. Rev. C 96, 024905 (2017)

[20] Y. He et al., Phys. Rev. C 91, 054908 (2015)

[21] A. Buzzatti and M. Gyulassy, Phys. Rev. Lett. 108, 022301 (2015)

[22] K. Zapp, F. Krauss and U. Wiedemann, JHEP 03, 080 (2013)

[23] T. Renk, Phys. Rev. C 78, 034908 (2008)

[24] B. Schenke, C. Gale and S. Jeon, Phys. Rev. C 80, 054913 (2009)

[25] G. Qin et al., Phys. Rev. Lett. 100, 072301 (2008)

[26] J. Pumplin et al., JHEP 0207, 012 (2002)

[27] K. Eskola, H. Paukkunen and C. Salgado, JHEP 0904, 065 (2009)

[28] K. Zapp, Eur. Phys. J. C 74, 2762 (2014)

[29] S. Floerchinger and K. Zapp, arXiv:1407.1782 [hep-ph]

[30] R. Elayavalli and K. Zapp, JHEP 1707, 141 (2017)

[31] C. Shen and U. Heinz, Phys. Rev. C 85, 054902 (2012)

[32] C. Shen et al., Comput. Phys. Commun. 199, 61 (2016)

[33] K. C. Zapp, Phys. Lett. B 735, 157 (2014)

[34] ALICE Collaboration, Phys. Lett. B 746, 1 (2015)

[35] ALICE Collaboration, arXiv:1812.07681 (2018)

[36] ATLAS Collaboration, Phys. Rev. Lett. 114, 072302 (2015)

[37] ATLAS Collaboration, Phys. Lett. B 790, 108 (2019)

[38] CMS Collaboration, Phys. Rev. C 96, 015202 (2017)

[39] Y. He et al, arXiv:1809.02525 [nucl-th]

[40] Y. Tachibana, N.-B. Chang and G.-Y. Qin, Phys. Rev. C 95, 044909 (2017)

[41] ATLAS Collaboration, Eur. Phys. Jour. C 77, 379 (2017)

[42] ATLAS Collaboration, Phys. Rev. C 98, 024908 (2018)

[43] ALICE Collaboration, JHEP 10, 139 (2018)

[44] J. Casalderrey-Solana et al., Phys. Lett. B 046, 07 (2013)

[45] Y. Mehtar-Tani and K. Tywoniuk, JHEP 04, 125 (2017)

[46] CMS Collaboration, JHEP 02, 156 (2016)

Chapter 6

Summary and discussions

This thesis comprises two main analysis parts: analysis of ALICE pp data at $\sqrt{s} = 2.76$ TeV and analysis of the heavy-ion (Pb-Pb) events as produced by the dynamical jet quenching model JEWEL. This final chapter of the thesis summarises all the analyses conducted and observations found in those analyses.

Jet properties in pp collisions have been studied via long tested jet shape observables with ALICE data at $\sqrt{s} = 2.76$ TeV as well as various MC models like PYTHIA, HERWIG and PHOJET. From data recorded by ALICE detector, 44 million minimum bias events were analyzed after putting event selection cut: -10 cm $< V_z <$ 10 cm. Tracks were selected from combined information of ITS and TPC putting criterion like: $p_T^{track} >$ 150 MeV/c and -0.9 $< \eta^{track} <$ 0.9. This analysis was conducted with only charged jets taking only the jets with the largest p_T^{jet} of each event i.e, with the leading jets. Anti-K_T jet reconstruction algorithm was used and the measurements were conducted for jet radius $R = 0.4$. Raw data were corrected using the bin-by-bin correction procedure whereas UE was estimated using the perpendicular cone method and the average value is subtracted from each observable and the associated systematic uncertainties were also estimated and quoted in this final results.

The average charged particle multiplicity, $\langle N_{ch} \rangle$, shows monotonic rise with increasing jet p_T reaching a plateau. This is consistent with earlier measurements. Experimental results are also compared with theoretical predictions from different tunes of PYTHIA (Perugia0, Perugia2010, Perugia2011 and AMBT1), HERWIG and PHOJET. It has been seen that all the models qualitatively produce the shape and agree within 10% of the estimated uncertainties except PHOJET which stays within 15%. This measurement at 2.76 TeV has also been compared with the measurement from 7 TeV and within the jet p_T reach, no $\sqrt{s}$ dependence has been seen.

Measurement of the average charged jet size, $\langle R_{80} \rangle$, shows that 80% of the p_T found within the jet cone is contained within half of the jet radius for $R = 0.4$. $\langle R_{80} \rangle$ decreases down to even smaller radius with increasing jet p_T. This feature indicates that the higher p_T jets are more collimated around the jet axis. All the MC models shows good agreement with the data measurement. In this case also, the comparison with 7 TeV measurement shows no $\sqrt{s}$ dependence.

The transverse momentum density distributions, $\langle dp_T^{sum}/dr \rangle$ are obtained for four different jet p_T intervals: $20 < p_T^{jet} < 30$ GeV/c, $30 < p_T^{jet} < 40$ GeV/c, $40 < p_T^{jet} <$ 60 GeV/c and $60 < p_T^{jet} < 80$ GeV/c. The transverse momentum density, $\langle p_T^{sum} \rangle$, is found to be maximum near the jet axis and it decreases as one goes radially more outward to the full radius. This is expected as the harder particles sit around the jet axis. It has also been found that the slope of decrement of the jet energy with r gets steeper with higher jet p_T intervals. This is consistent with what have been seen with $\langle R_{80} \rangle$ i.e. higher p_T jets are more collimated. The Monte Carlo models are found to describe the data well within the experimental uncertainties.

The pp 2.76 TeV data set was originally taken as a reference for heavy ion studies at the same $\sqrt{s}$. Nevertheless, this data set also provides an opportunity to narrow the gap in jet measurements from 1.96 TeV at Tevatron to top LHC energies. Together with the measurements at other energies, the present measurement could be useful to improve the constraints on theoretical calculations of several jet properties. The measurement of jet properties like, $\langle N_{ch} \rangle$ or $\langle R_{80} \rangle$ at 2.76 TeV appears to be independent of collision energy, although, p_T dependence of $\langle R_{80} \rangle$ seemingly support hardening of jet-spectra which could be partially because of dominance of quark jets over jets initiated by gluons [1]. A more detailed study of $\langle R_{80} \rangle$ with jet p_T and $\sqrt{s}$ might serve as a promising tool to decipher flavor dependence of jet properties.

Jet properties have also been studied in Pb-Pb events at 2.76 and 5.02 TeV with the framework of a jet-medium interaction model, JEWEL. About 1 million 0-10% most central events produced by JEWEL were analysed. Large background is a very usual for heavy-ion environment and to get rid of the same, a JEWEL compatible subtraction method, 4MomSub, is adopted in this analysis. JEWEL is operated in the standard 'recoil-on' mode. In this analysis, the effect of jet energy loss has been investigated on the single inclusive jet yields and intra-jet properties, namely, the jet fragmentation functions and radial transverse momentum density.

The jet nuclear modification factor, R_{AA}^{jet}, gives the account of the single inclusive jet yields. Comparison with the available experimental results at the LHC energies shows that JEWEL reproduces the data very reasonably. Jet medium interaction tend to redistribute the lost energy within the medium via wide angle radiation. For this, one may expect stronger suppression of jet spectrum when calculated at smaller values of R as it is only able to capture a subset of the total shower. This effect was seen by measuring jet cross-section at different R. The cross-section ratios, $\sigma(R = 0.2)/\sigma(R = 0.3)$ deviates from unity for both pp and Pb-Pb case but they are consistent to each other. But when the ratios $\sigma(R = 0.2)/\sigma(R = 0.4)$ for pp and Pb-Pb were computed, it is seen that the Pb-Pb value is considerably suppressed than the pp. This effect reflects in the study of R_{AA}^{jet} with different jet radius values. It is observed that inclusive jet properties does not change while going from $R = 0.2$ to 0.3 but it changes when we go to larger radius, $R = 0.4$.

Manifestations of jet-medium interactions are not only limited to the suppression of single inclusive jet spectrum but also reflected in the modifications of its transverse and longitudinal energy or momentum profile and are presented here by measuring the fragmentation distributions and radial momentum density distributions. It has been seen that quenched jets have a harder fragmentation pattern than jets in vacuum when compared in the same jet-p_T interval. Medium modification quantified by the ratios of the fragmentation functions in A-A collisions to those in pp exhibit large enhancement at low and high z ($\sim p_T$). This excess yield of soft fragments is generally attributed to wide angle emission of medium-induced soft gluons but in JEWEL soft excess could only be achieved on inclusion of recoil contributions and also from the implementation of background subtraction at the inclusive level and not at the particle level. The enhancement of hard fragments (jet-constituents with relatively large transverse momentum are generally aligned to the jet axis), on the other hand, could be because of quark-like fragmentation pattern on top-of the hardening of the initial energy spectrum of quenched jets when compared to vacuum-jets in the same jet-p_T interval.

Radial momentum density distributions show an enhancement at the high r which stands for the excess yields of soft particles and inclusion of recoil partons in the larger r. To further decompose the scenario, this observable was also studied as a function of constituent particle p_T and it is found that indeed the contribution from the softer particles are the largest. This picture is consistent with what has been seen with fragmentation function study.

The study with JEWEL captures the jet medium interaction to a reasonable agreement by reproducing the wide angle emission to well understood enhancement of the hard fragments. JEWEL shows that all jets are modified but their inner core remains shielded. However, the measurements carried out in this work reveal a potential new finding that at LHC kinematics, the interactions are strong enough to modify the inner core of low p_T jets ($<$ 100 GeV/c) as well. This needs more study from experimental data to follow up.

With ALICE data, jet properties have been studied in the lower jet p_T region. At the LHC energy, this is a unique feature of ALICE compared the other experiments at the LHC to go down to low p_T region with excellent resolution. Although the current measurement ranges between jet p_T 10-70 GeV/c, one can go down in jet p_T up to 5 GeV/c. JEWEL has proven itself to be one of the reliable jet quenching models at the LHC energies. Measurements of inclusive jet properties agrees reasonably well and more intra-jet properties measurements, like those in this thesis, are needed for more accurate prediction in future.

Bibliography

[1] S. Acharya *et al*. (ALICE Collaboration), JHEP 10, 139 (2018)

Appendix A

QA analysis of PMD data

In this chapter, a brief description of the Photon Multiplicity Detector (PMD), the ALICE subsystem that is entirely conceptualised and built in India, has been presented. PMD has a its success stories from the era of WA93 experiment to STAR and then ALICE. In ALICE, PMD was operational for a decade and has successfully taken data at different LHC operating energies and collision systems. In order to provide quality flags to the registered data which the analyser should taken up to physics analysis, it is necessary to do the first hand Quality Assurance (QA) study. This was assigned to me as a service task and in this chapter a description of the QA analysis procedure taken up for PMD data with QA analysis results of few LHC runs have also been presented.

A.1 Photon Multiplicity Detector (PMD)

The PMD [1] is a forward detector in ALICE to measure the photons. It is situated at 363.5 cm away from the interaction point and covers $2.3 < \eta < 3.9$ with full azimuthal coverage.

A.1.1 Physics goals of PMD

PMD helps in the following physics topics:

- Beam energy dependence of average photon multiplicity in forward rapidity region and limiting fragmentation behavior of photons
- Measurement of photons in forward rapidity to determine the reaction plane for measuring the azimuthal anisotropy of the charged particles in midrapidity
- It can probe the thermalization by measuring the azimuthal anisotropy of the inclusive photons
- Critical phenomena near the phase boundary leading to fluctuations in global observables like multiplicity and transverse energy
- Signals of chiral-symmetry restoration (e.g. disoriented chiral condensates) through the measurement of N/N_{ch} in a common part of phase space along with a charged particle detector

A.1.2 Design overview of PMD

PMD consists of two identical active detector planes with a 3 radiation length ($3X_0$) thick Pb plane sandwiched between them. The plane which faces the IP is called Charged Particle Veto (CPV) and the other plane is called Preshower (PRE) plane. A schematic view of the PMD from the IP is shown in the Figure A.1. In Figure A.2 a unit cell of PMD is shown which is hexagonal in shape with an active area of 0.23 cm^2 and a depth of 0.5 cm. A matrix of 48×96 or 96×48 such cells is made using a thin copper sheet (0.2

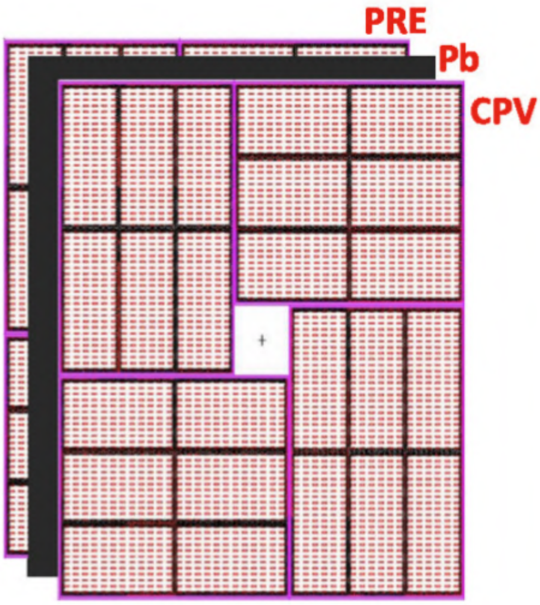

FIGURE A.1: Schematic view of the PMD as installed in ALICE

mm thick) and is known as honeycomb chamber.

There are two types of modules in PMD and each of the planes consist of 24 mod-

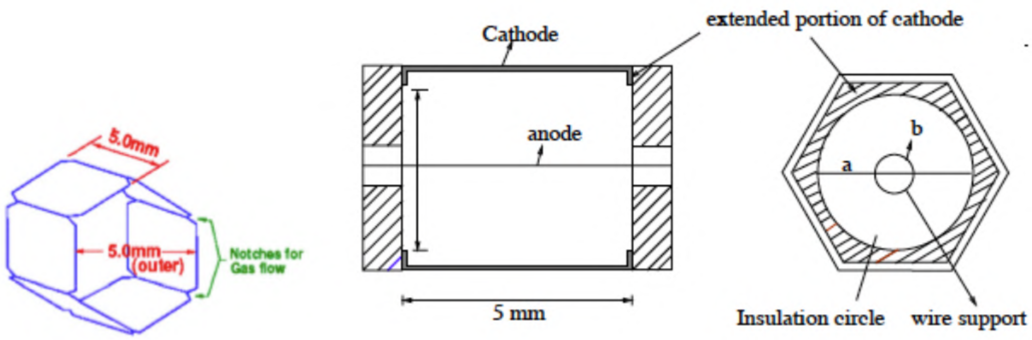

FIGURE A.2: Schematic view of a honeycomb chamber in PMD

ules combining both types. The modules containing 48 rows and 96 column are called short modules whereas the modules containing 96 rows and 48 columns are called long modules. In this way, each module is made up of 4608 numbers of honeycomb cells. Each honeycomb cell acts as an individual and independent detector and this makes each module as an independent gas-tight rectangular unit. The honeycomb chambers are placed between two gold plated Printed Circuit Boards (PCB). Gold plated tungsten wires of diameter 20 μm are inserted through the centre of each cell and a proper tension is applied in the wire during soldering. The top PCB has the solder islands at the centre corresponding to each cell. There are 32 connectors to extract the signal from the 32 cells in the top PCB. The bottom PCB has only soldering islands without signal tracks, serving as anchor points. The inner part of the PCBs are gold plated, with circular islands near the anode wire. Together with the honeycomb wall they form part of an extended cathode going very close to the anode wire. A proper alignment is needed to put the honeycomb plane between the two PCBs. One of the alignment pin is used to provide the high voltage to the honeycomb chamber which is used as a cathode plane. The gold plated tungsten wires are used as anodes. Assembly of a module is shown in the Figure A.3.

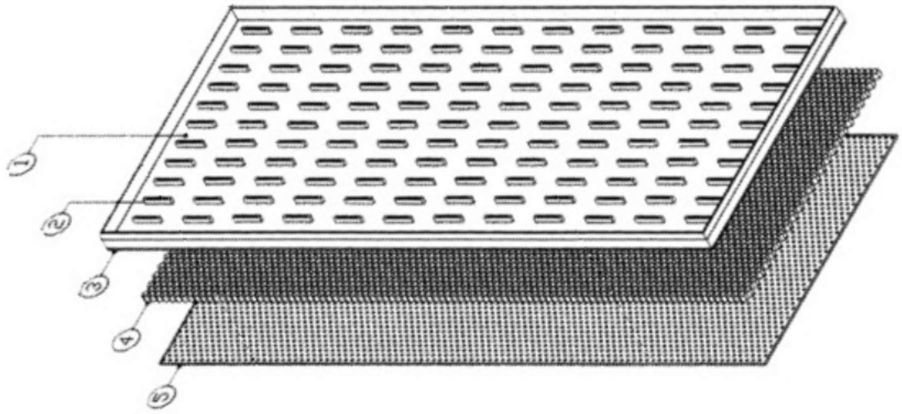

FIGURE A.3: Schematics of a single PMD module: (1) Top PCB, (2) 32-pin connectors, (3) edge frame, (4) honeycomb of 48 × 96 cells, (5) bottom PCB

The modules are kept in 2 mm thick air-tight stainless steel (SS) containers with gas inflow/outflow nozzles. A mixture of Ar and CO_2 with the ratio 70:30 serves as the active detecting medium. Lead converters, of thickness 1.5 cm which is equivalent to $3X_0$, are stacked between the two PMD planes and there are two types of Pb converters depending upon the module configuration: size 49.05 cm × 21.7 cm is the long type and 42.5 cm × 25.15 cm is the short type. PMD has two parts on both sides of beam pipe. SS plate of 5 mm thickness is used to support the lead converter plates and the modules in each half of the PMD. The PMD is supported from a SS girder in such a way that the two halves can be moved on the girder to bring them together for data taking operation or separated for servicing. Figure A.4 shows the installed PMD in ALICE in open and data taking configurations.

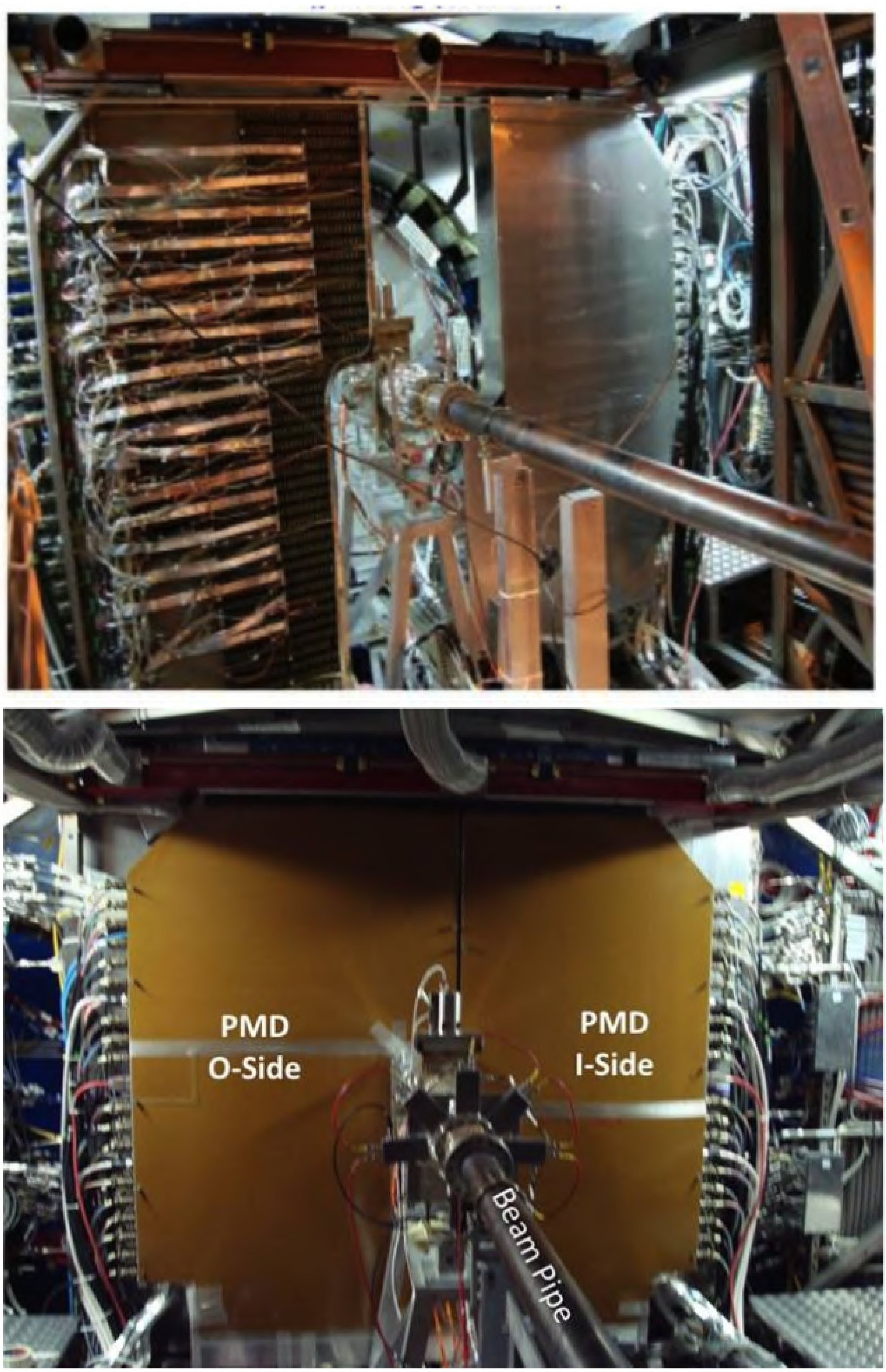

FIGURE A.4: PMD in ALICE: (Top) Open configuration and (bottom) data taking configuration.

A.1.3 Working principle of PMD

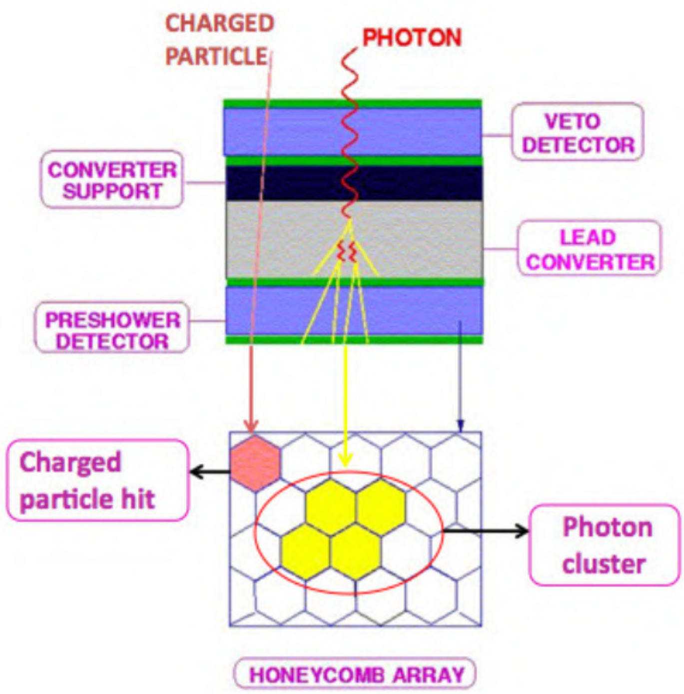

FIGURE A.5: Working principle of PMD

Starting from the interaction point, the produced particles first traverse through the CPV plane. The photon do not produce any signal in the CPV plane. But while traversing through the Pb converter in its way to the preshower plane, it produces shower of photons, electrons and positrons by the combined effect of pair production and bremsstrahlung radiation [2]. A schematic diagram of the working principle is shown in Figure A.5. The thickness of the converter is chosen such a way that conversion probability of photons is high and transverse shower spread is small to minimize shower overlap. The produced shower particles produce signals in large number of cells in the preshower plane [3]. On the other hand, charged hadrons behave like the Minimum Ionizing Particles (MIPs) and produce signal in only one or a few cells both in the CPV and PRE planes since the interaction cross-section of the charged hadrons with the Pb converter is very low. These different responses of the photon and the charged hadrons helps to discriminate charged particles from the photons and on applying a suitable reconstruction algorithm, incident photons are recorded along with their positions. The detector response to different particles is tabulated in Table A.1.

Table A.1: Response of the PMD to different particles

Particle type	CPV plane	PRE plane
Photon	No hit	Shower (several cell hit)
Charged hadrons	few cell hit	few cell hit
Electron	few cell hit	Shower

A.2 QA study of PMD data

The data recorded by the detectors undergo several reconstruction based on different criteria. To begin with, in order to have good physics analysis, the analyser must take up the latest reconstructed data which are free from the hazardous 'hot cells' resulting mostly from electronic noise and calibrated to normalize the gain of each cells. The flow chart of data reconstruction regarding noisy cells and gain normalization has been presented in Figure A.6.

This QA study has been done with all the recorded data by the PMD, but here only analysis of a 7 TeV run in pp collision system has been presented as an example.

A.2.1 Data cleanup: removal of the hot cells

A.2.1.1 Identification of the hot cells

The cells which gets hit or record data above a certain threshold, called the 'noise cut', without any real particle falling on them are known as the noisy or hot cells. There could be various possible reasons for a cell to become noisy: for instance, a cell having some micro level impurities, which under high voltage condition keeps discharging continuously giving rise to a signal above the threshold. The noisy cells can be divided into two categories- ones having signal just above the noise threshold and the ones which have much much larger values. In this QA study, both types of the cells are removed.

The last running configuration of the PMD had 20 modules per plane making the total number of modules to 40 instead of ideal 48. Also with the reduced number of modules, additionally few of the active modules were not running with their full capacity (disabled chains). The empty spaces as seen in Figure A.7 stands for those areas covered

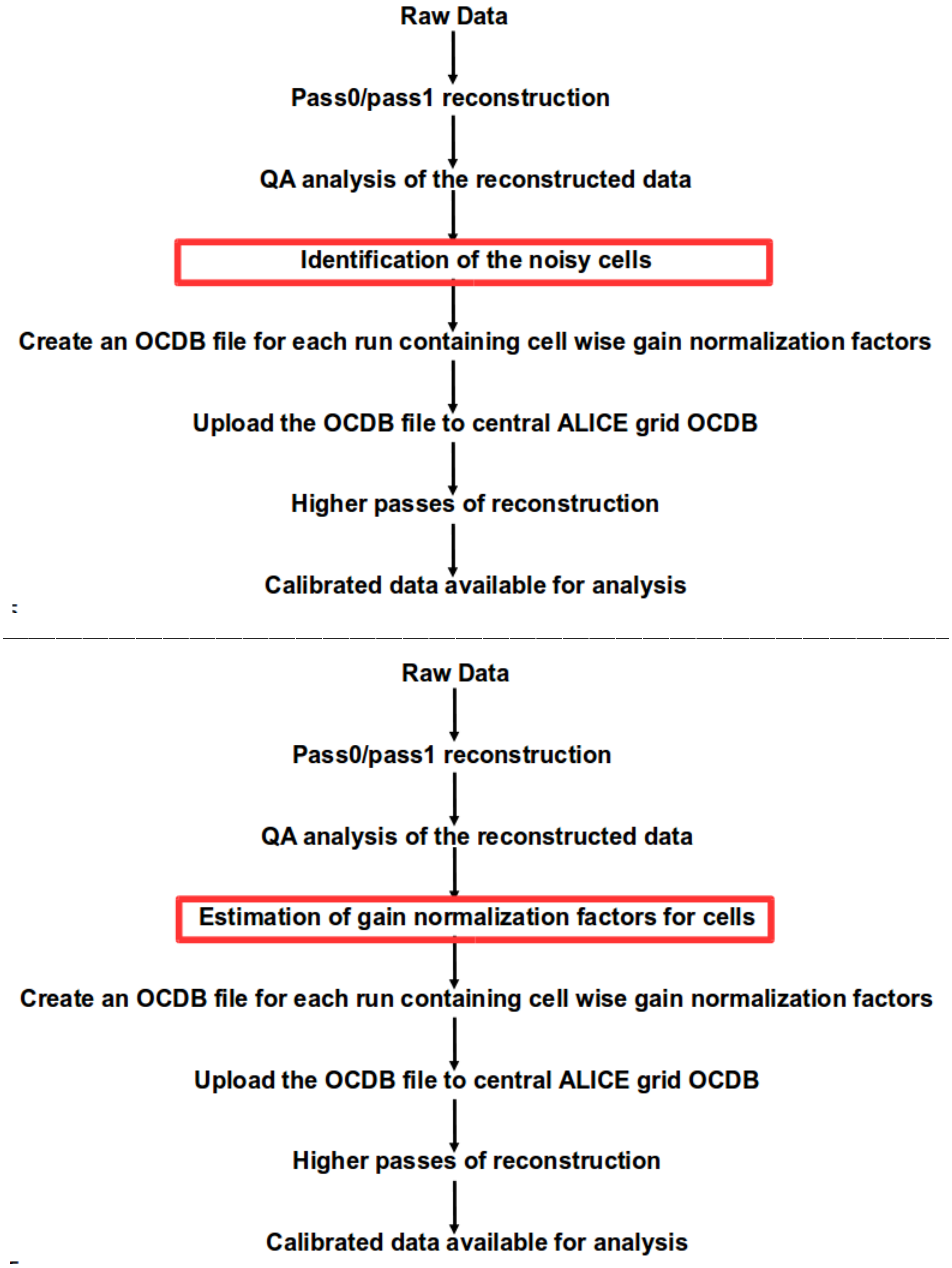

FIGURE A.6: Flow chart of data reconstruction after QA: (Top) hot cell removal and (bottom) gain normalization.

by inactive modules (and chains). One plane (CPV or PRE) has 100 readout chains with each chain comprising 768 cells (channels). This implies that the one PMD plane having 76,800 readout channels covers a pseudorapidity range 2.3< η <3.9 with full azimuthal coverage. Assuming the uniform particle distribution in azimuth one expects same probability of getting hits for each cells. This results in a Gaussian distribution of hit frequency for all the cells in one η slice (or ring, if the whole η coverage is divided into few rings). The cells which have values much larger than the mean of the

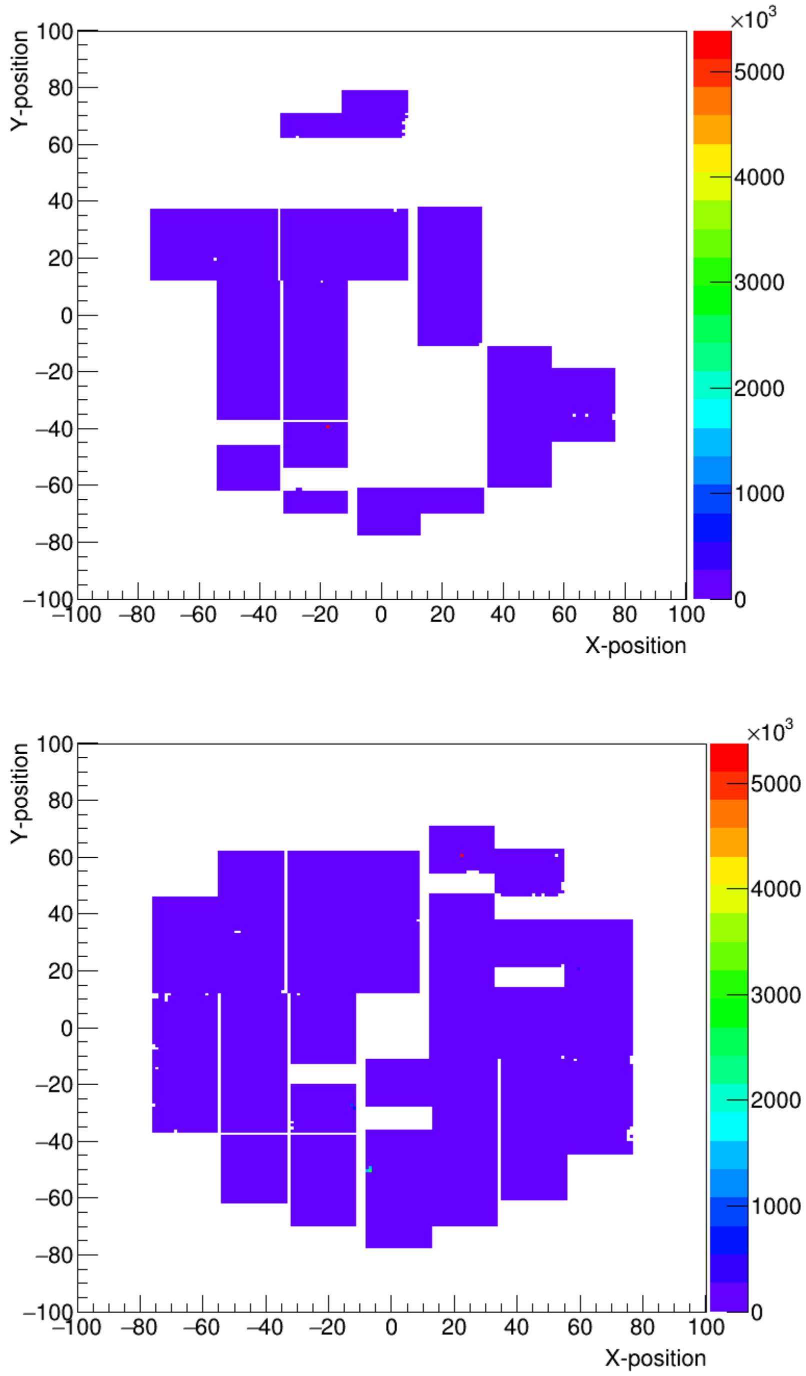

FIGURE A.7: Full occupancy X-Y plots for a representative run number 133006 from the dataset LHC10f: (top) CPV plane (bottom) PRE plane

Gaussian hit frequency distribution, are identified as the hot cells. In reality, if there is any hot cell in CPV or PRE plane, it should be there in the X-Y plane occupancy plots of the same as a scattered concentrated points, as can be seen in Figure A.7.

A.2.1.2 Removal of the hot cells

The whole pseudorapidity range is first divided in 10 rings covering the whole η range. Then the noise threshold is calculated using the mean and sigma from the Gaussian

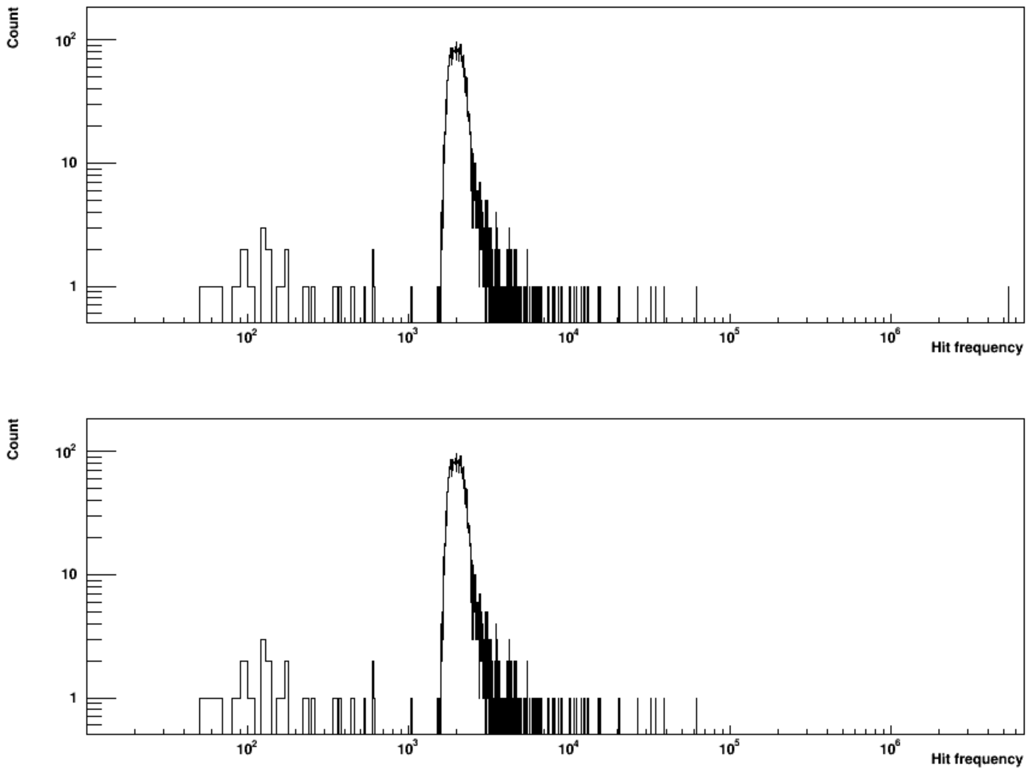

FIGURE A.8: Hot cell removal for a representative run number 133006 from the dataset LHC10f computed on the CPV plane in η ring 3 taking $n = 13$: (top) before hot cell removal and (bottom) after hot cell removal. In this particular case one hot cell was found and removed.

distribution according to the following relation:

$$\text{Noise}_{threshold} = \text{Mean} + \text{n} \times \text{Sigma} \tag{A.1}$$

Any channel showing hit frequency above this threshold is considered as hot cell. In Figures A.8 and A.9 hot cell removal of PRE and CPV plane for a η ring has been presented with before and after removal of the hot cells.

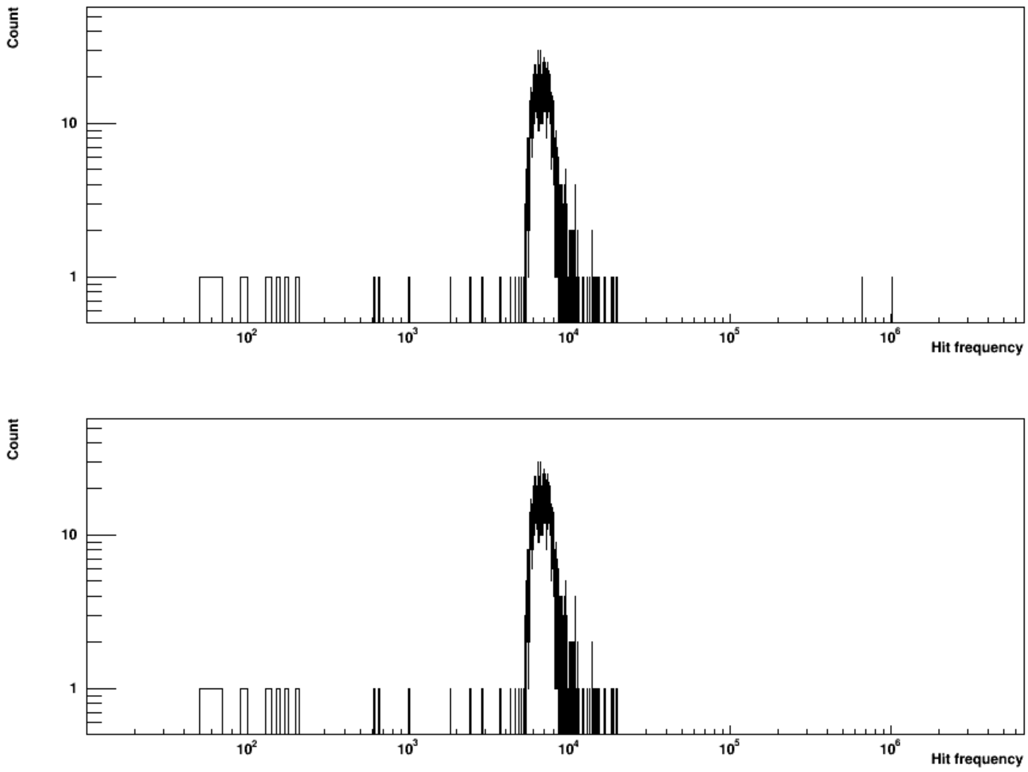

FIGURE A.9: Hot cell removal for a representative run number 133006 from the dataset LHC10f computed on the PRE plane in eta ring 5 taking $n = 13$: (top) before hot cell removal and (bottom) after hot cell removal. In this particular case two hot cells were found and removed.

However, various physical limitations put subjective condition on the selection of 'n', like, limited statistics per η ring in a given run, position of η rings about the beam pipe, finite width of the eta rings etc. Due to these limitations, the distributions get distorted from the Gaussian nature. This complicates the procedure and also rules out the possibility of its automatization. The value of n is thus chosen after looking at the hit frequency and ADC distributions in iterative way and run-wise. In this study it has been seen that the value of n takes mostly 10 or slightly larger than 10.

A.2.2 Calibration: gain normalization

This step is done after the hot cell is removed. As mentioned, one PMD module has 4608 number of cells and as the design, fabrication and all other parameters are identical for all the cells, ideally all the cells should have same gain. However, this is not the practical case and in test beam experiments with PMD modules, a 10% cell-to-cell gain variation has been seen. To remove this discrepancy, a procedure has been adopted to normalize the gain of each cell module wise.

The ADC distribution of all the isolated cells in a module is first obtained and the mean, $\langle m^{ADC} \rangle_n$ (n runs to 4608, total no. of cells in a module), of the distribution is calculated cell wise. Isolated cells are considered because they are expected to get fired by the MIP particles. Next the means of all the cells of a module are taken into consideration which gives the mean ADC value of the total module as can be seen in Figure A.10 and according to the relation:

$$\langle m^{ADC} \rangle_{module} = \sum_{n=1}^{4608} \frac{\langle m^{ADC} \rangle_n}{n} \tag{A.2}$$

The gain factor or the normalization factor (f_n) is then calculated for each cell according to:

$$f_n = \frac{\langle m^{ADC} \rangle_{module}}{\langle m^{ADC} \rangle_n} \tag{A.3}$$

The gain factors are stored and while processing the raw data these factors are multiplied with the cell ADC value before the reconstruction starts. Figure A.11 shows gain factors for module 3 of both PRE and CPV plane for run number 119057 in the LHC10C dataset. For this particular run it has been that the gain varies around 12% for the CPV module and in 10% for the PRE module.

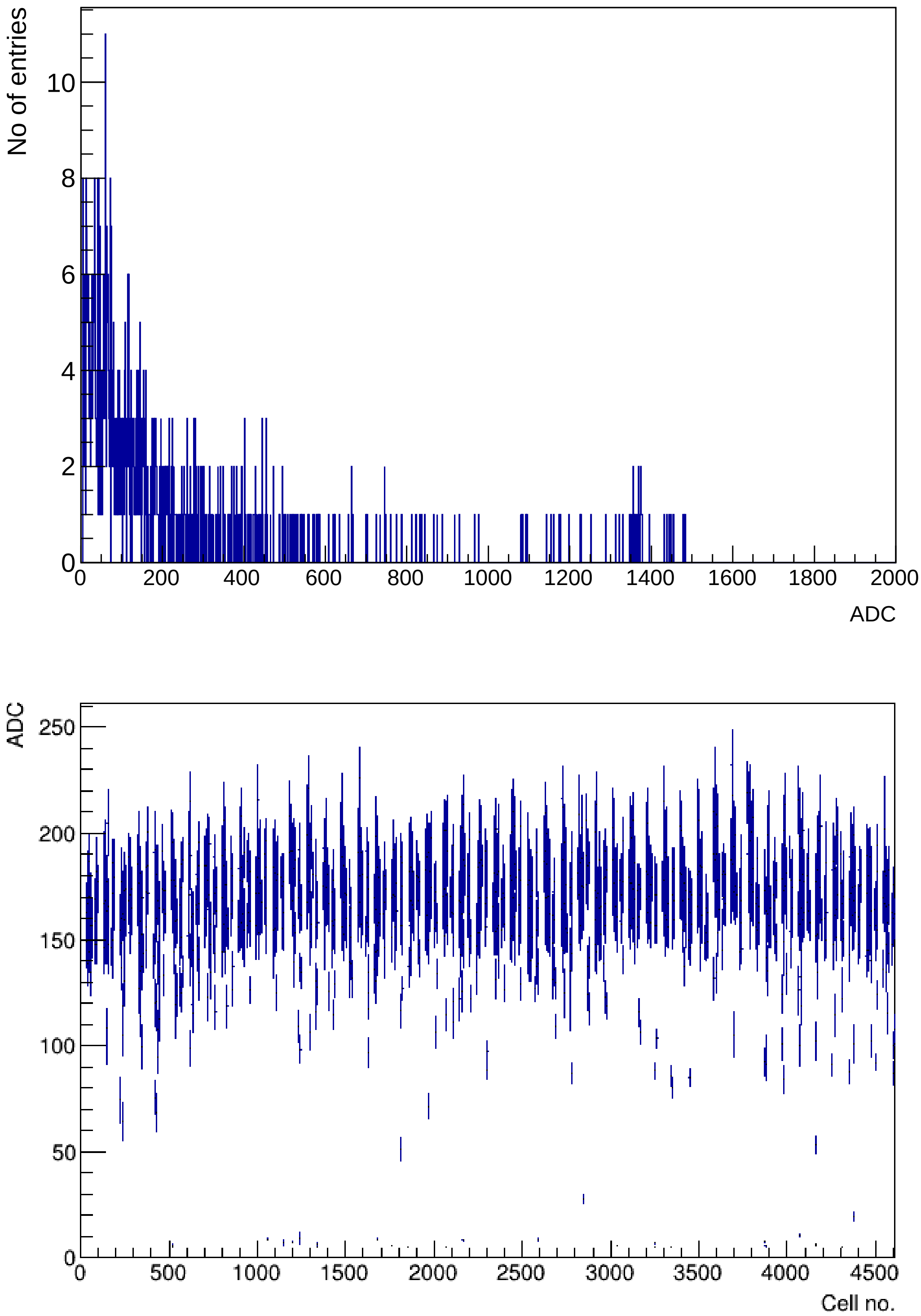

FIGURE A.10: ADC distribution of an isolated cell of module 2 (SM02) for run number 119057 in the dataset LHC10C: PRE plane (top) and the cell-wise mean ADC distribution of the full module which gives the mean ADC of the module (bottom).

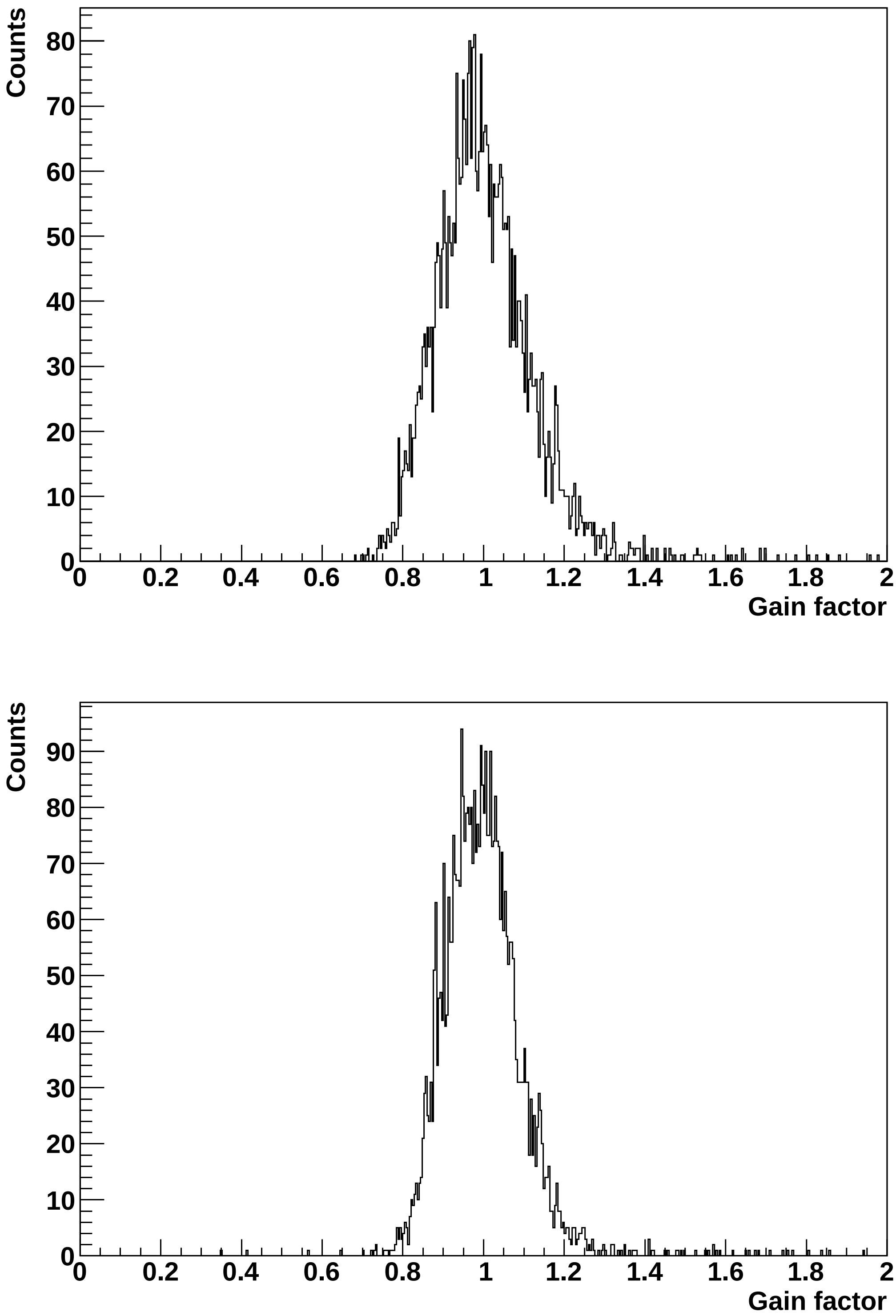

FIGURE A.11: Cell wise gain factors for module 3 (SM03) for run number 119057 in the dataset LHC10C: CPV plane (top) and PRE plane (bottom).

Bibliography

[1] ALICE Collaboration, ALICE Photon Multiplicity Detector (PMD): Technical Design Report, CERN-LHCC-99-032; http://cdsweb.cern.ch/record/451099; ALICE Photon Multiplicity Detector (PMD): addendum to the technical design report, CERN-LHCC-2003-038, http://cdsweb.cern.ch/record/642177

[2] William R. Leo, Techniques for Nuclear and Particle Physics Experiments, First Narosa Publishing House Reprint (1995)

[3] M. M. Aggarwal etal., Nucl. Instr. Meth. A488, 131 (2002)

Appendix B

Monte Carlo event generators

The event generators are computer programs used to simulate the high energy collisions through Monte Carlo (MC) methods. The Monte Carlo methods are stochastic techniques, meaning, they are based on the use of random numbers and probability statistics to investigate problems. Although the event generators are limited by the understanding of the existing underlying physics, it plays very important role in various aspects of the high energy physics. Together with the detector simulations, they can provide real event scenarios with the detector acceptance and efficiency measurement. They are extensively used in optimizing the analysis strategies for real data, in correcting the raw data from the effects of detector acceptance and resolution and in the evaluation of associated uncertainties in the measurement. The main parts of event generators while simulating a high energy collision (hadronic or nucleonic) are following:

- Initial-state component building
- Initial-state showers
- Initial-state hard scattering
- Hard and soft processes
- In-medium energy loss, collectivity (for heavy-ion)
- Final-state showers

- Hadronization and further decays
- Underlying Events

For a large scale experiments like those performed in the LHC, rely on the comprehensive predictions from simulation and this not only helps in realising the design of the experiments but also helps to understand the physics processes out of the recorded data. A general-purpose MC event generator, based on the probability distributions motivated from physics, gives the most complete description of the collisions by generating every intermediate steps starting from the initial interactions to the production final state particles with their respective masses and four-momenta. Starting from the pre-LHC era to latest developments, some review articles on the MC event generators could be found here [1–5].

A schematic diagram of a simple Drell-Yan lepton-pair production is shown in Figure B.1 as an example of MC event generation. The central solid circular red dot presents a high p_T interaction, where the lepton-pair production takes place. As shown in

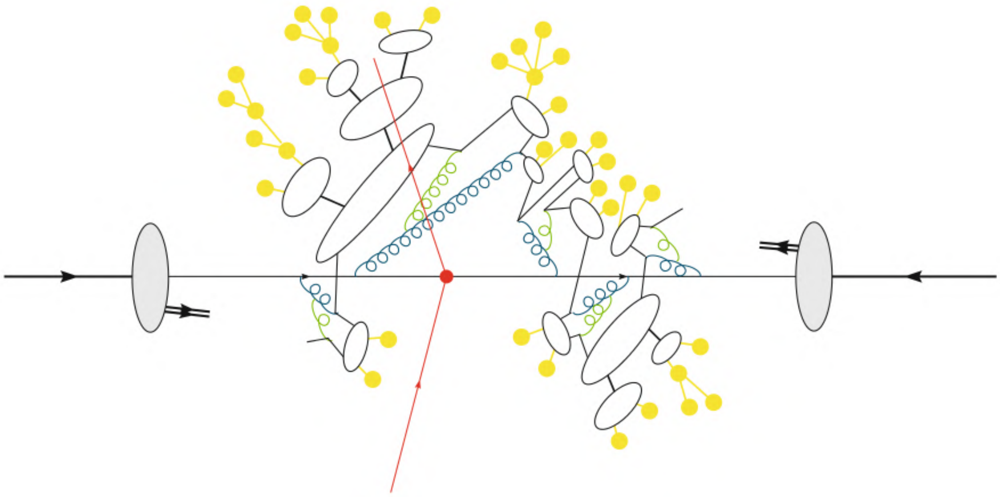

FIGURE B.1: Schematics of a MC event generation. Illustration courtesy: S. Gieseke.

the diagram, the leptons do not take part in further interaction but the event is populated by the emitted gluons from the initial partons and result in cascade of partons, described by the concept of parton showers (PS) [6, 7]. The parton showers represent in their simplest form, a perturbative leading-logarithmic approximation (LLA) to the full event.

The LLA explains the collinear or soft radiation around a parton with a reasonable accuracy. For the general case, The MC event generators combine LO predictions with PS (LO+PS) and this is implemented in different way in different MC generator, taking the freedom to exploit the choice of shower resolution scale and inclusion of color-coherence effects. For example, PYTHIA contains two types: Q^2 and p_T ordered PS [8–10] whereas HERWIG employs angular-ordered showers [11, 12]. Finally, these partons form colorless compounds (hollow ellipses) and they produce hadrons successively, which may in turn decay according to their lifetime. This procedure of fragmentation or in total hadronization is implemented in the MC event generators via some established models, for example, PYTHIA is equipped with Lund String fragmentation for this step while HERWIG uses the cluster model. Figure B.1 is actually presents an event produced by HERWIG. The event also gets messed up by the presence of additional, relatively soft particles which is observed in the hadronic collisions but not included in the theoretical description so far. These are not explained by the combined inputs from ISR, FSR, BBR and it has also been seen that these particles not only depend on the centre-of-mass energy but also on the energy scale of the primary interaction. In phenomenological studies, all the effects excluding the hard scattering are bracketed as the UE and evaluated following the procedure described in Chapter 3.

In this thesis, four Monte Carlo models have been used: PYTHIA, PHOJET, HERWIG and JEWEL. The last one has been described in Chapter 5 and in the following, a glimpse of the rest three event generators have been presented.

B.1 PYTHIA

PYTHIA [13–15] is a pQCD based Monte Carlo event generator, which can collide elementary particles like p, $\bar{p}$, e^+ and e^- and generate simulated events. Currently PYTHIA is considered as a versatile event generator for pp collisions and is widely used in all the hadronic collision experiments all over the world. In PYTHIA total pp cross-section is the combination of elastic, single diffractive (SD), double diffractive (DD) and non diffractive (ND) processes as shown in Figure B.2. Among these, ND processes have the largest contribution to the total cross section. In PYTHIA each beam particle is characterized

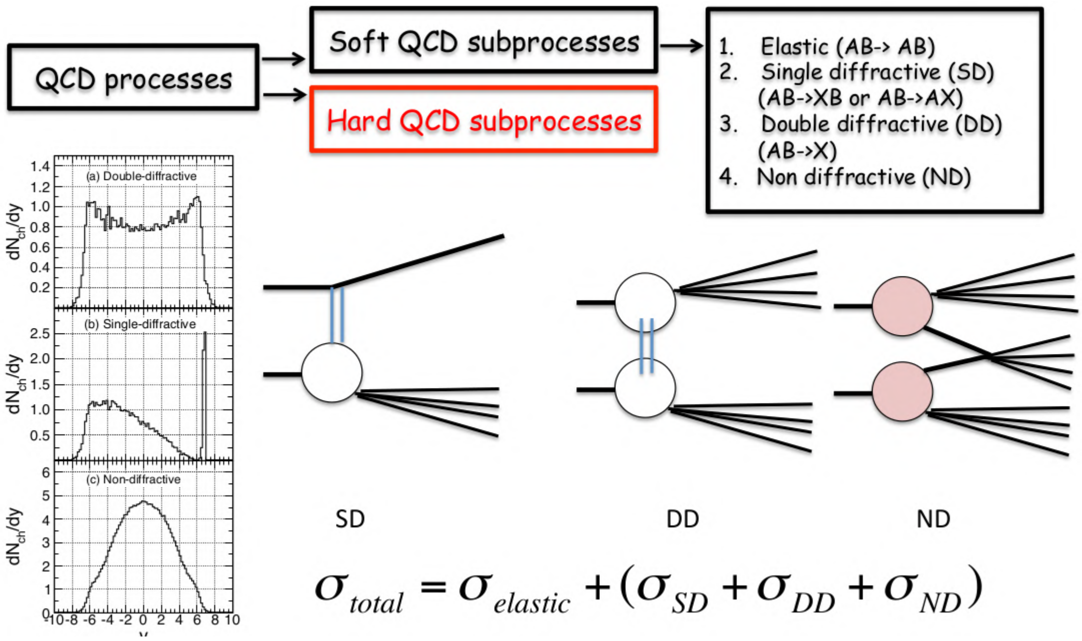

FIGURE B.2: PYTHIA event generator general structure. Figure taken from [16].

by a set of parton (q, $\bar{q}$, g) distribution functions, which defines the partonic substructure in terms of flavor composition and energy sharing. One shower initiator parton from each beam starts off a sequence of branching, such as q → qg, which build up an initial-state shower before interaction. Hard processes such as qg → qg, qg → q take place between the incoming partons and a number of outgoing partons are produced. It is the nature of this process that determines the main characteristics of the event. Figure B.3 presents some of the physics processes among all addressed by PYTHIA. After that the fragmentation of the outgoing partons take place. The fragmentation or hadronization process is governed by the Lund String model according to which, as the q and $\bar{q}$ move apart, the potential energy stored in the string increases and the string may break into the production of a new $q^{'}\bar{q^{'}}$ pair. At this point the system splits into two color-singlet systems $q\bar{q^{'}}$ and $q^{'}\bar{q}$. If the invariant mass of either of these string pieces is large enough, further breaks may occur. At the end, hadrons are produced.

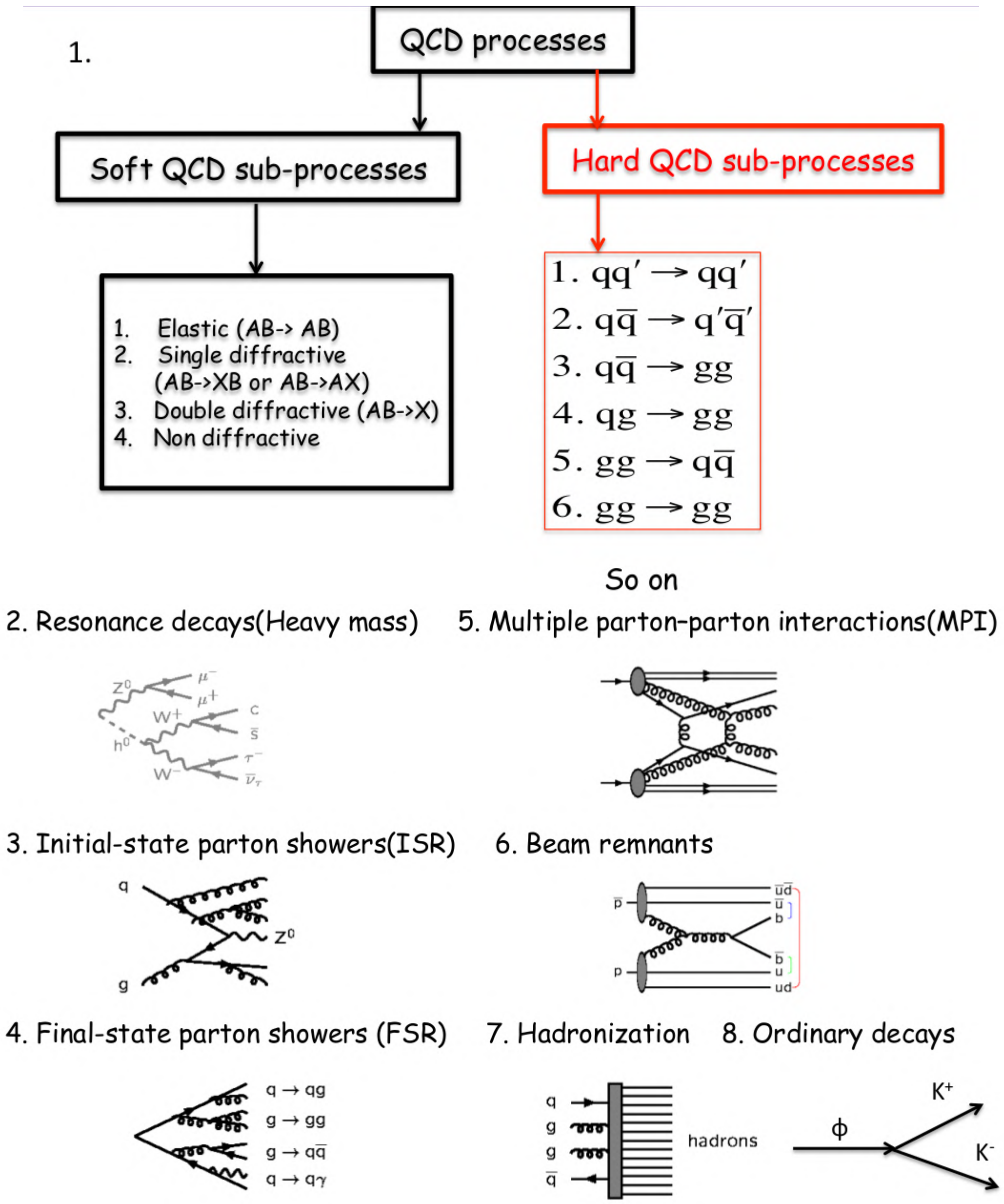

FIGURE B.3: Few of the physics processes addressed by PYTHIA. Figure taken from [16]

B.2 Hadron Emission Reactions With Interfering Gluons, HERWIG

HERWIG [17, 18] is a general purpose event generator which provides full simulation of hard elementary particle (p,$\bar{p}$,e$^+$ and e$^-$) collisions as well as soft hadronic collisions with particular emphasis on the detailed description of the QCD parton showers. A generic hard process simulated by HERWIG has main four components: elementary hard-subprocesses, initial and final state parton shower, heavy object decays and the final hadronization process. Unlike PYTHIA, the fragmentation and hadronization model adopted by HERWIG is the cluster model which has the following special features:

- Initial and final state QCD jet evolution with soft gluon interference taken into account via angular ordering
- Color coherence of (initial and final) partons in all hard subprocesses, including the production and decay of heavy quarks and supersymmetric particles
- Azimuthal correlations within and between jets due to gluon interference and polarization
- A cluster model for jet hadronization based on non-perturbative gluon splitting, and a similar cluster model for soft and underlying hadronic events
- A space-time picture of event development, from parton showers to hadronic decays,with an optional color rearrangement model based on space-time structure

B.3 PHOJET

PHOJET [20–23] is an minimum bias event generator which gives an almost complete picture of high-energy hadron collisions. In principle, it can simulate hadron-hadron, photon-hadron and photon-photon collisions. Hadronic collisions at high energies involve the production of particles with low transverse momenta, the so-called soft multi-particle production. Most of the theoretical models, do not describe these accurately. At this point, PHOJET comes with the unique idea of splitting the total cross-section into two parts: soft and hard processes depending upon the momentum transfer by the partons.

$$\sigma_{total} = \sigma_{soft} + \sigma_{hard} \tag{B.1}$$

Soft processes are governed by the Dual Parton Model [24] (DPM) and the hard part is calculated using pQCD like in PYTHIA. In DPM, high-mass diffraction dissociation exhibits properties similar to hadron production in non-diffractive hadronic collisions at high energies [25]. Hard diffraction is described using leading-order QCD matrix elements together with a parton distribution function for the Pomeron. Pomeron is a color neutral object but not to be confused with ordinary hadrons. It is a theoretical object providing an effective description of the important degrees of freedom of a certain sum of Feynman diagrams in Regge limit (e.g., $\sqrt{s}$ is large compared to the momentum transfer characterizing the scattering process). In this sense, pomeron-hadron or pomeron-pomeron interactions can only be discussed in the framework of collisions of other particles like hadrons or photons. Interactions of hadrons are described in terms of pomeron exchanges. The pomeron exchange is artificially subdivided into soft processes and processes with at least one large momentum transfer (hard processes). Practically, soft and hard processes are distinguished by applying a transverse momentum cutoff $p_{\perp}^{cut}$ of about 3 GeV/c to the scattered partons.

The PHOJET Monte Carlo was the first attempt to build a model which accounts for both effects, multiple soft and hard interactions between the constituents of the projectile and target as well as multiple interactions in the pomeron-projectile, pomeron-target and pomeron-pomeron scattering subprocesses. The model includes also soft color reconnection [26–29] (SCR) in hard scattering processes. The fragmentation process for both soft and hard interactions in PHOJET is governed by the Lund model as in PYTHIA.

B.4 Predictions by the event generators and tuning of them

Predictions, so far are based on the naive picture of only one interacting parton from each colliding hadron to participate in a high p_T reaction. Though at small p_T limit, this fails as the respective cross-sections grow beyond all limits and finally violate unitarity. The UE is simulated by incorporating MPI, depending on the impact parameter of the percolating hadrons, with the primary interaction. Central or head-on collisions produce high p_T physics and large MPI whereas large impact parameter produce only few soft particles. For a better data to theory predictions, these extra activities should be well taken care of along with ISR, FSR and BBR. PYTHIA uses original impact parameter model [30] and few modified versions [10, 31] to take care of these while HERWIG uses eikonal multiple partonic scattering model [32].

The ultimate goal of a event generator is to reach the height of accuracy to describe the experimental data. There exist a number of parameters, to handle the PS, hadronization and decays, which should be optimized with the MPI based phenomenological models employed in the event generator with the help of available experimental results, a process called *tuning* of the model to tune the MC event generator to data. Two such widely used tools for tuning are Rivet [33] and Professor [34]. A comprehensive review on tuning is here [35] and dedicated MC tuning efforts with latest developments can be found here [36–42].

Bibliography

[1] M. Dobbs et al., Proceedings of the 3rd Les Houches Workshop on Physics at TeV colliders, arXiv:hep-ph/0403045 (2003)

[2] A. Buckley et al., Phys. Rept. 504, 145 (2011)

[3] S. Gieseke and Z. Nagy, Book: "Monte Carlo Generators and Fixed-order Calculations: Predicting the (Un)Expected (1st edn.)", Wiley-VCH Verlag GmbH & Co. (2011)

[4] S. Gieseke, Prog. Part. Nucl. Phys. 72, 155 (2013)

[5] S. Höche, Proceedings of Journeys Through the Precision Frontier: Amplitudes for Colliders (TASI 2014), Boulder (2014)

[6] I. Knowles, Comput. Phys. Commun. 58, 271 (1990)

[7] I. Knowles, Nucl. Phys. B 310, 571 (1988)

[8] M. Bengtsson and T. Sjöstrand, Nucl. Phys. B 289, 810 (1987)

[9] M. Bengtsson and T. Sjöstrand, Phys. Lett. B 185, 435 (1987)

[10] T. Sjöstrand and P. Skands, Eur. Phys. J. C 39, 129 (2005)

[11] G. Marchesini and B. Webber, Nucl. Phys. B 310, 461 (1988)

[12] S. Gieseke, P. Stephens and B. Webber, JHEP 12, 045 (2003)

[13] PYTHIA 6.4, Physics and Manual, hep-ph/0603175, FERMILAB-PUB-06-052-CD-T (2006)

[14] T. Sjöstrand, Comput. Phys. Commun. 82, 74 (1994)

[15] T. Sjöstrand, S. Mrenna, P. Skands, JHEP 2006, 05026 (2006)

[16] Event generator session notes, SERC School on Experimental High Energy Physics 2017, NISER

[17] G. Corcella, I. Knowles, G. Marchesini, S. Moretti, K. Odagiri, P. Richardson, M. Seymour and B. Webber, JHEP 0101:010 (2001)

[18] G. Marchesini, B. Webber, G. Abbiendi, I. Knowles, M. Seymour et al., Comput. Phys. Commun. 67 465508 (1992)

[19] B. Webber, Nucl. Phys. B238 492 (1984)

[20] R. Engel, Z. Phys. C 66, 203 (1995)

[21] R. Engel, J. Ranft and S. Roesler, Phys. Rev. D 52, 1459 (1995)

[22] R. Engel and J. Ranft, Phys. Rev. D 54, 4244 (1996)

[23] S. Roesler, R. Engel and J. Ranft, SLAC-PUB-8740, arXiv:hep-ph/0012252

[24] A. Capella et al., Phys. Rep. 236, 225 (1994)

[25] A. Kaidalov and K. Ter-Martirosyan, Nucl. Phys.B 75, 471 (1974)

[26] W. Buchmüller and A. Hebecker, Phys. Lett. B 355, 573 (1995)

[27] A. Edin, G. Ingelman and J. Rathsman, Phys. Lett. B 366, 371 (1995)

[28] J. Amundson, O. Eboli, E. Gregores and F. Halzen, Phys. Lett. B 372, 127 (1996)

[29] O. Eboli, E. Gregores and F. Halzen, hep-ph/9708283

[30] T. Sjöstrand and M. van Zijl, Phys. Rev. D 36, 2019 (1987)

[31] T. Sjöstrand and P.Z. Skands, JHEP 03, 053 (2004)

[32] M. Bähr, S. Gieseke and M. Seymour, JHEP 07, 076 (2008)

[33] A. Buckley et al., Comput. Phys. Commun. 184, 2803 (2013)

[34] A. Buckley et al., Eur. Phys. J. C 65, 331 (2010)

[35] J. Katzy, Prog. Part. Nucl. Phys. 73, 141 (2013)

[36] CMS Collaboration, Eur. Phys. J. C 76, 155 (2015)

[37] CDF Collaboration, Proceedings of The 2013 European Physical Society Conference on High Energy Physics, EPS-HEP2013 P433 (2013)

[38] ATLAS Collaboration, Technical report:ATL-PHYS-PUB-2011-008 (2011)

[39] P. Skands, Phys. Rev. D 82, 074018 (2010)

[40] H. Abramowicz et al., Summary of MPI@LHC2012, arXiv:1306.5413 (2012)

[41] S. Plätzer and M. Diehl (eds.), Proceedings of MPI@LHC2011, DESY-PROC-2012-03 (2011)

[42] P. Bartalini and L. Fanó (eds.), Proceedings of MPI@LHC2008, arXiv:1003.4220 (2008).

Appendix C

Dismantling the PMD from ALICE

After a decade long successfull run from 2009 to 2018, PMD retired from ALICE and was dismantled from the experiment in December 2018, at the commencement of 2nd long shutdown (LS2). I was fortunate enough to be the part of the team responsible for the dismantling. Few photographs during the dispersion of PMD both in the cavern and then on the surface area can be seen here.

FIGURE C.1: Dismantling PMD in the ALICE cavern: removal of power source, cooling mechanics, support girders.

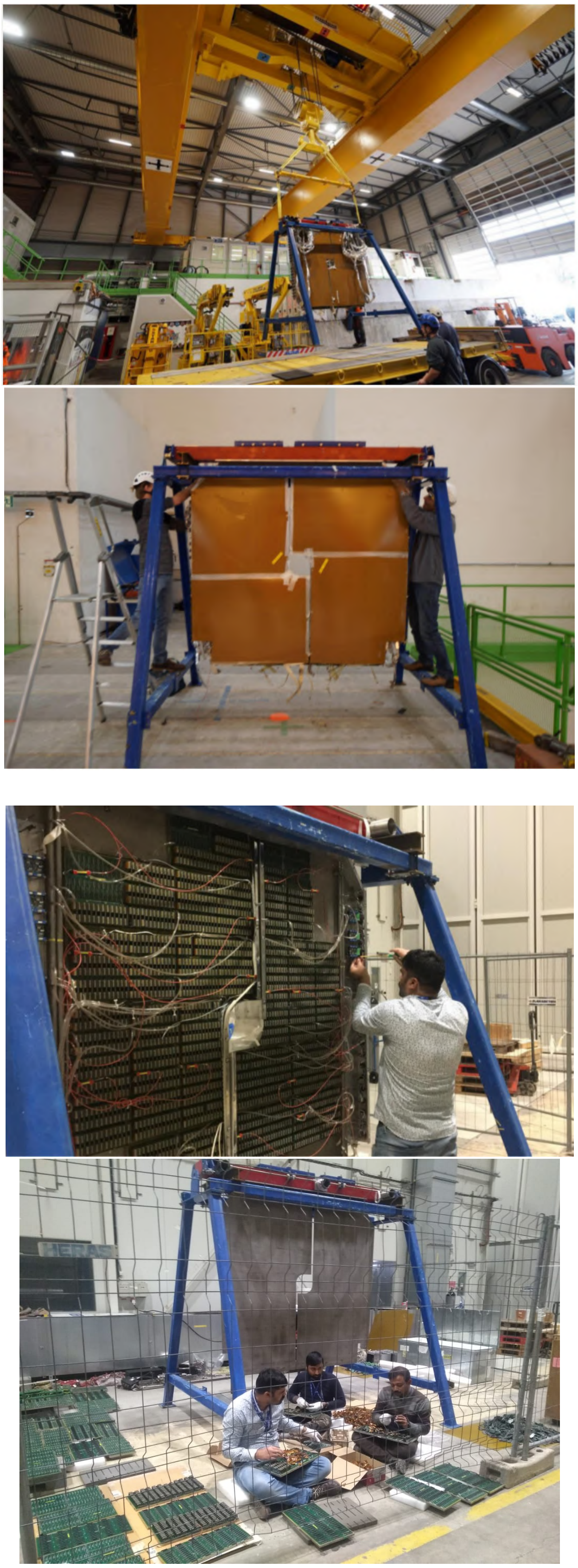

FIGURE C.2: Dismantling PMD at the surface area: (from top to bottom) PMD moved from cavern to surface area by crane, PMD is placed at the surface area (radiation protected zone) with the help of a support structure (blue frame), electrical cables and gas flow tubes removal and finally module wise dismantling.